The University Of Sheffield.

Modelling Spontaneous Motion and Deformation of Active Droplets

By:

Carl A. Whitfield

A thesis submitted in partial fulfilment of the requirements for the degree of Doctor of Philosophy

The University of Sheffield
Faculty of Science
Department of Physics and Astronomy

Submission Date

18/12/2015

Abstract

This thesis investigates symmetry breaking phenomena and motile steady states in droplets driven by stresses generated by active (out-of-equilibrium) liquid crystals. First, we show that in a fluid droplet with active polar liquid crystal an asymmetric polarisation field is sufficient to drive steady state motility. We are able to approximate the forces and flows generated in such a system analytically, and show how the force distribution on the droplet interface is characteristic of this motion. Second, we consider the case of a passive fluid droplet immersed in an active liquid crystal. Here we see that strong anchoring at the droplet interface can create an asymmetric equilibrium configuration, and thus any active stress can drive propulsion of the drop. Third we analytically perform linear stability analysis calculations on two kinds of active droplet to determine how active stresses can make these systems unstable to symmetry breaking events. Finally, we produce 2D simulations of these systems so that we can find the resulting steady states of these systems. We observe a rich phase space of behaviour, with steady state flows in the droplets that result in motion, symmetric deformations and rotation.

Contents

Acknowledgements

Firstly, I would like to thank my supervisor Dr. Rhoda Hawkins, for continual support and guidance from start to finish. Also, I would like to thank my friends and family for their ongoing support. In particular, my parents Karen and Anthony, my girlfriend Rachel, and her parents Julie and Alan, who all had complete faith in my ability, despite not really knowing what I have been studying for the past 3 years.

Nomenclature

Below is a list of definitions of key biological terminology used in this thesis.

Actin - A protein that constitutes part of the **eukaryotic** cell **cytoskeleton**. It can exist in globular form (G-actin) and in polymerised semi-flexible filaments (F-actin).

Actin Cortex - Cytoskeletal structure found in many animal cells. F-actin accumulates and attaches to the inside of the cell membrane into an isotropic filamentous network.

Amoeboid (or Interstitial) Migration - A mode of **cell migration** characterised by a rounded morphology and lack of **focal adhesion** formation.

ATP - Adenosine triphosphate, an organic compound that can be broken down within the cell by hydrolysis. This process results in a release of energy, due to the lower chemical potential energy of the products of the reaction, namely adenosine diphosphate (ADP) plus a phosphate molecule.

Bleb - A swelling of the cell **membrane** due to osmotic pressure equilibration when the membrane is detached from the **actin cortex**.

Cell Motility/Migration - Persistent directed self-propelled motion of a cell. Migration is often used more when describing collective motion of cells.

Centrosome - Radial nucleator of **microtubules** in the cell.

Cytokinesis - The final process in mitosis (cell division) in **eukaryotic cells** where the cell is cleaved in two by a 'ring' of contractile actin in the cell cortex.

Cytoplasm - The composite material of the cell **cytoskeleton** and the **cytosol**.

Cytoskeleton - Polymer network consisting of **actin**, **microtubules** and intermediate filaments. A crucial part of the architecture and dynamics of **eukaryotic** cells.

Cytosol - The fluid solvent that permeates the cell **cytoskeleton**.

Eukaryotic - Referring to the taxon of cells that contain inner compartments enclosed by membranes, such as the nucleus and mitochondria, which contain the genetic material. Animal and plant cells are examples of eukaryotes.

Extra Cellular Matrix (ECM) - Fibrous network consisting mainly of collagen found in most multicellular organisms. This network is secreted by the animal cells themselves and imparts greater structure and rigidity to tissues of cells.

Filopodia - Narrow protrusions of the cell **membrane** formed by polymerisation of tight polar bundles of **actin**.

In vitro - Referring to an experimental system where cells or cell components are removed from their natural environment. Translates from Latin as "within the glass".

Focal adhesion - A protein complex that connects the cell cytoskeleton to its external environment, adhering to specific compounds due to the action of the receptors on the cell surface.

In vivo - Referring to an experimental set up where the cells are observed in their natural living environment. Translates from Latin as "within the living".

Lamellipodia - Thin and flat protrusions of the cell **membrane** formed by polymerisation of the crosslinked **actin** network.

Matrix metalloproteases - Refers to enzymes containing a metallic component that are secreted by some cells to degrade the **ECM** to enable cell **migration**.

Membrane - The lipid bilayer that encloses animal cells.

Metastasis - The process leading up to and including formation of a secondary cancerous tumour within a living host.

Microtubule - A hollow cylindrical polymer consisting of the dimer tubulin. A major component of the cell **cytoskeleton**, much more rigid than **actin** filaments.

Motor proteins - Proteins that can convert chemical energy to work via hydrolysis of a fuel molecule such as **ATP**. The hydrolysis process results in a mechanical conformational change of the protein which can exert a force onto its surroundings.

Nucleus - A compartment (or *organelle*) in eukaryotic cells that contains most of the genetic material (DNA). The relative size of the nucleus compared to that of the cell is very variable between cell types.

Prokaryotic - Referring to the taxon of cells that do not contain any inner compartments. Bacteria and archaea are examples of prokaryotes.

Stress fibres - Bundles of **actin** filaments that can sometimes adhere the substrate beneath a cell and generate contraction forces due to the activity of myosin **motor proteins**.

Preface

A wide range of cells are capable of self-propelled motion through consumption of chemical energy. There are two overarching taxons of cells, eukaryotic and prokaryotic. Eukaryotic cells are defined as containing organelles (or compartments) and in particular a nucleus which contains most of the cell's genetic material, whereas prokaryotes have no such internal structures. Both cell types display a wide range of motility mechanisms which are heavily dependent on their surrounding medium. In single-celled organisms, like bacteria and amoebae, motility is essential for cells to survive enabling them to move towards chemically favourable regions in their environment and, in the case of amoebae, enabling them to capture and consume bacteria [Bray, 2001]. Cell motility is vital in multicellular organisms too, examples include white blood cells 'hunting' foreign bodies and viruses, the organisation and rearrangement of cells during embryonic development, and the healing of wounds through the coordinated migration of epithelial cells. Cell motility also plays a large role in various diseases, a major example being in cancer metastasis, where cancerous cells are able to escape a primary tumour and nucleate a secondary tumour elsewhere in the body.

In this thesis, we will focus on motility driven by the cell cytoskeleton, which appears to be the main component in force generation and dynamics of animal cells during locomotion. The cytoskeleton is a viscoelastic polymer gel which can convert its internal energy (in the form of chemical potential energy) into work. As such, in living cells the cytoskeleton is persistently driven out-of-equilibrium and hence can exhibit interesting behaviour that would be physically impossible in equilibrium systems.

This thesis investigates simplified continuum models of the cell cytoskeleton in confinement, and what these systems can tell us about the physical mechanisms underlying cell polarisation and migration in general. Chapter 1 will summarise the background research that provides the motivation for this project, introducing key biological terminology and concepts. In chapter 2 we will look at models of the cell cytoskeleton and cell motility, and in particular introduce the continuum model employed in chapters 3-6, which will detail my personal research and discuss the results. Finally, chapter 7 will draw all of this together, summarising the discussion and looking ahead at potential areas of continued and future research related to this work.

Chapter 1

Introduction I: The Cell Cytoskeleton and its role in Motility and Polarisation

Abstract

In this chapter we will discuss the biological roles of cell motility and specific molecular biology in the cell that is behind some of these effects. We will introduce some important biological terminology and concepts that will be used throughout. In addition we discuss some early and recent experiments on cell motility that have advanced our understanding of these processes in nature.

1.1 The Cell Cytoskeleton

The cell cytoskeleton consists of a collection of bio-polymers which can be categorised into 3 main types; filamentous actin (F-actin), which consists of monomers of the protein globular actin (G-actin); microtubules (MTs), which consist of dimers of the protein tubulin; and intermediate filaments (IFs), which covers a large range of rope-like protein polymers [Alberts et al., 2008]. Intermediate filaments are generally associated with the mechanical stability of the cell and forming the nuclear lamina, which protects the cell nucleus, rather than cell dynamics. Therefore, we focus instead on the properties of MTs and F-actin in this section as these are more directly relevant to cell migration.

G-actin proteins are folded into an asymmetric morphology, and it is convenient to define the ends of this protein as barbed (+) and pointed (−), where there is a cleft marking the binding site for Adenosine Triphosphate (ATP) at the pointed end. G-actin polymerises with or without the presence of ATP into the 5-9nm width helical filament F-actin (which we will just refer to as actin unless otherwise stated) such that all the subunit ends are pointing the same way. In addition, the actin monomers act as an enzyme hydrolysing ATP into Adenosine Diphosphate (ADP) which remains bound to the actin monomer. This difference in chemical energy between ATP-bound and ADP-bound G-actin gives rise to a difference in polymerisation and depolymerisation rates at the filament barbed and pointed ends. ATP-bound monomers preferentially bind at the filament barbed end, while ADP bound G-actin has a faster depolymerisation rate at the pointed end [Wegner, 1976]. This can lead to various non-equilbrium (or active) processes such as directed polymerisation and treadmilling (see figure 1.1) [Neuhaus et al., 1983]. Thus a non-equilibrium steady state filament length distribution can be observed when the monomer concentration reaches a critical value determined by the ratio of the 'on' and 'off' rates [Hill, 1980], that requires the ATP molecules to be replenished in the system.

Microtubules similarly have distinct polar ends but rather than assembling helically, the monomers arrange to form a hollow cylinder approximately 25nm in diameter. This

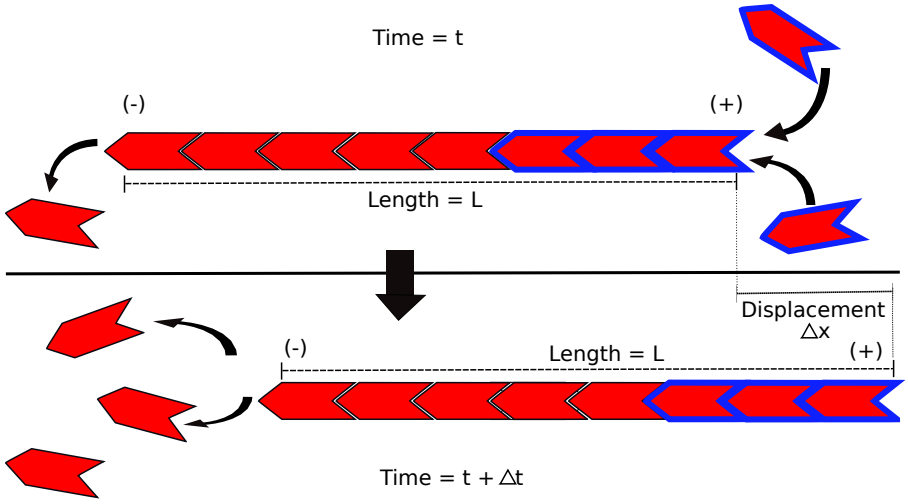

Figure 1.1: Simplified schematic of a filament treadmilling. Above a critical concentration c_c ATP-bound monomers (thick blue outline) attach to the barbed end at rate $k_p c$ (assuming linear dependence on c, the local ATP-bound monomer concentration). The critical concentration for polymerisation at the pointed end is much higher, so depolymerisation generally dominates there. Assuming ADP-bound monomers (black outline) detach at the filament pointed end at rate k_d and that other rates are negligible (polymerisation at pointed end and depolymerisation at barbed end), the filament reaches a steady state length. This happens when $c = k_d/k_p$ and translates in the direction of the (+) end, with average velocity $\Delta x/\Delta t = k_p c L/N$, where N is the number of monomers in the filament.

makes microtubules much more rigid than actin filaments (with a persistence length on the order of $10^3\mu$m rather than $\sim 10\mu$m [Gittes et al., 1993]). Their assembly dynamics are somewhat similar to actin, favouring polymerisation at one end due to Guanosine triphosphate (GTP) hydrolysis, and in certain cases this can also result in filament treadmilling [Rodionov and Borisy, 1997]. However MTs can completely disassemble rapidly, 'unzipping' from the plus end, if there are no GTP bound monomers 'capping' the filament. This is a stochastic process known as microtubule dynamic instability. The complete disassembly of a microtubule is known as a 'catastrophe' event and if it starts to regrow it is known as a 'recovery'. This dynamic instability can lead to coexisting phases of growing and shrinking MTs in bulk [Mitchison and Kirschner, 1984].

1.1.1 Filament binding proteins

A wide range of proteins interact with actin and MTs *in vivo*. Of particular interest are the families of motor proteins that convert chemical energy into mechanical work. The myosin family of motor proteins bind to actin, and these can consist of one or two

'heads' which bind to actin filaments and hydrolyse ATP to change their conformation and effectively walk along the filaments in a given direction. All myosins (except myosin VI) walk towards the barbed end of an actin filament, yet due to their structures they are associated with different functions in the cell [Alberts et al., 2008]. The main motor protein we focus on is myosin II which can bundle to form filaments that interact with actin bundles and networks to generate contraction forces, which are important in cell motility. Interestingly, larger versions of these same myosin filaments, on the order of μm in length, are found interacting within the highly organised array of macroscopic actin bundles in muscles, where they are responsible for muscle contraction [Alberts et al., 2008].

There are two families of motor proteins associated with MTs, kinesins and dyenins. Kinesins have very similar structures to myosins, and walk toward the filament + ends, whereas dyenins walk toward the filament − ends. Generally, in cells these are associated with intracellular transport, pulling cargo through the cytoplasm while walking along a microtubule [Hirokawa, 1998]. However, *in-vitro* experiments have also shown that these motors may be responsible for stabilisation of the microtubule aster [Laan et al., 2012], and interestingly on much larger length scales, kinesins can generate extensile stresses in reconstituted microtubule networks [Sanchez et al., 2012].

A variety of proteins in the cell are also involved in forming the wide range of cytoskeleton structures observed. Often, near the cell leading edge, actin is found to be arranged in a branched network, connected by the actin-related protein 2/3 (ARP2/3), an actin nucleator and branching crosslinker. ARP2/3 has a high affinity for binding to the pointed ends of actin filaments, as well as binding to its sides, thus it provides a nucleation site for new filaments to polymerise from. This leads to the formation of branches with a consistent 70° angle, which continue to polymerise from their barbed end [Mullins et al., 1998]. This branched network appears to be important in generating a pushing force via actin polymerisation at the cell leading edge.

Cofilin proteins sever actin filaments, increasing the number of free barbed ends and

hence polymerisation sites [Chan et al., 2000] while capping proteins can bind to filament barbed ends, preventing further polymerisation [Weeds and Maciver, 1993]. These two types of proteins control the rate actin polymerisation in the cell and hence cells can fluctuate between fast and slow protrusion due to fluctuations in the concentration of these [Ridley et al., 2003].

The protein α-actinin can bundle actin into anti-parallel bundles with enough space between for myosin II filaments to bind, resulting in thick contractile fibres (stress fibres) [Alberts et al., 2008]. These stress fibres can generate long range directed contractile forces which are transmitted to the environment by strong adhesion sites [Pellegrin and Mellor, 2007]. Similarly, fimbrin proteins bind neighbouring filaments to produce tight polar bundles of actin resulting in stiff fibres with directed polymerisation [Alberts et al., 2008].

It is somewhat unsurprising then that the spatial and temporal dynamics of these and other proteins in the cell, regulated by chemical, electrical and mechanical signals, can form complex structures, transiently, persistently or periodically, which can result in overall motility of the cell.

1.1.2 Cytoskeleton structures observed in cells

In living cells, the dynamic nature of these cytoskeleton polymers and their interactions with a wide range of associated proteins mean that they can arrange and rearrange into different structures and patterns. In animal cells it is generally observed that while actin is present throughout the cytoplasm (the fluid medium inside the cell), it is largely concentrated as a gel-like network at the cell periphery, usually referred to as the actin cortex. Actin filaments also bundle to form thicker and stiffer filaments, which depending on their relative orientation can generate strong pushing forces by directed polymerisation (*e.g.* filopodia) or local contractile stress due to the action of myosin motors (*e.g.* stress fibres) [Alberts et al., 2008]. Microtubules are generally much longer than actin filaments *in vivo* and nucleate from a body in the cell known as the centrosome or Microtubule Organising Centre (MTOC), meaning that they generally arrange in a radial structure

(see figure 1.2).

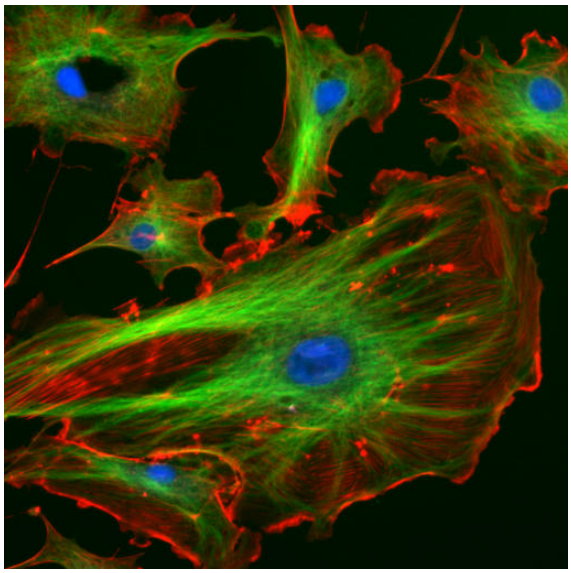

Figure 1.2: The cell cytoskeleton: Endothelial cells with DNA stained blue by DAPI, MTs are tagged green by an antibody bound to Fluorescein isothiocyanate (FITC), and actin is labelled red by phalloidin bound to Tetramethylrhodamine (TRITC). Note the radial structure of the microtubules, and the higher concentration of actin at the cortex, these structures are typical across many animal cell types. Source: http://rsb.info.nih.gov/ij/images/.

A notable example of the fast dynamics of the cell cytoskeleton is observed when animal cells divide on flat substrates. At this stage of the cell cycle the tension in the actin cortex stiffens through active contraction, and the cell rounds up into a sphere. The microtubules are separated around two centrosomes to form a structure known as the mitotic spindle. The division is initiated by cytiokinesis, where actin is observed to concentrate in a ring which squeezes the cell around its middle and eventually cleaves it into two. The position of the two microtubule asters is coupled strongly to the division plane, and any asymmetry in the positioning can lead to asymmetric daughter cell sizes [Robinson and Spudich, 2004, Uyeda et al., 2000].

Experimental approaches to understanding the physical behaviour of the cell cytoskeleton can be broadly split into 'top-down' and 'bottom-up' methods. A 'top-down' approach will generally begin with observations of a living cell, either *in vivo* or *in vitro*, and measure how a particular drug treatment or genetic mutation affects

this. Examples include treating cells with the drug blebbistatin to decrease myosin production [Straight et al., 2003, Kovács et al., 2004] and genetic manipulation of a cell to reduce production of the intermediate filaments that constitute the nuclear envelope [Harada et al., 2014]. The strength of this kind of experiment is that one is able to identify vital ingredients in a particular cell function and those ingredients which do not have such a large effect, in order to narrow down what the mechanism may be.

The 'bottom-up' approach generally involves measuring the mechanical, statistical and/or dynamical properties of reconstituted cytoskeleton networks consisting of a known set of ingredients. A particularly striking example, mentioned briefly earlier in this section, is reported by [Sanchez et al., 2012] who assembled an active microtubule network of bundled microtubules, kinesin motor proteins and ATP which is adsorbed onto the surface of an emulsion droplet. This active network displays strong orientational order and turbulent-like dynamics which can lead to directed motility of the droplet when in contact with a surface. This method of experimental investigation allows one to find out what the bare minimum number of ingredients are necessary to reproduce particular phenomena in a quantifiable way. These two approaches are clearly complimentary to the overall physical understanding of how the cell cytoskeleton works.

1.2 Cytoskeleton Driven Motility

The majority of experimental studies on single-cell motility have historically been performed on cells that crawl along the top of stiff substrates, often referred to as 2-dimensional (2D) migration, and only in recent years have technological advances enabled experiments to study motility in 3-dimensional (3D) environments [Cukierman et al., 2001, Doyle et al., 2013]. Therefore, in the literature when cell migration or motility is discussed, it is often in reference to this 2D migration, despite the fact that this mode of migration may only be observed in a small number of biologically relevant cases.

1.2.1 Crawling motility on flat substrates

Crawling motility is observed in a wide range of animal cells, and different cell types achieve it in different ways resulting with strikingly varied steady state shapes and speeds, however the underlying mechanisms are somewhat similar. It is the actin network in all of these cells that is primarily responsible for the motion [Mitchison and Cramer, 1996], which can be split into distinct stages.

Firstly, protrusions form at the front of the cell due to polymerisation of actin filaments or bundles that are indirectly mechanically linked to the substrate via complexes of proteins that adhere the cell to the surface (known as focal adhesions) [Mogilner and Oster, 1996]. These protrusions can take various forms, the most common being lamellipodia, a flat sheet of branched actin filaments which are oriented with barbed end normal to the leading edge [Small et al., 1978], and filopodia, which are tightly packed polar bundles of actin that protrude from the leading edge also with the filaments oriented barbed end forward [Mitchison and Cramer, 1996] (see figure 1.3). Filaments are observed to nucleate and grow specifically at the leading edge, and depolymerise further back in the cell, causing a retrograde flow of actin relative to the substrate. These protrusions then form new adhesions with the substrate, while older adhesion sites at the cell rear de-adhere.

This de-adhesion in the cell rear is coupled to contractile forces generated by the actin and myosin (or *actomyosin*) network there, which usually consists of stress fibres that can span the width of the cell. This contraction of the cell rear both aids de-adhesion by pulling on the substrate via focal adhesions, and pushes the cell centre of mass forward when these adhesions break [Ananthakrishnan and Ehrlicher, 2007]. Some cells exhibit these different stages continuously, such as fish keratocytes (see figure 1.4), which maintain relatively rounded edges and appear to 'glide' across the substrate, whereas cells such as cultured fibroblasts can adhere very strongly to certain substrates and crawl much more slowly, exhibiting these stages periodically, and displaying much more angular shapes. Interestingly, fragments of keratocyte cells without the cell nucleus or microtubules are

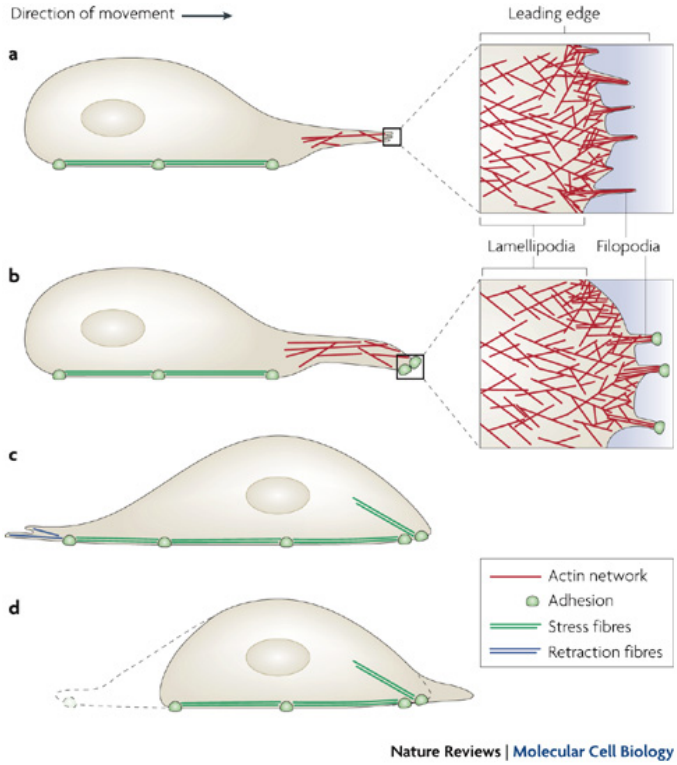

Figure 1.3: Schematic diagram of cell crawling via the formation of protrusions (a) and adhesion sites (b) at the leading edge combined with de-adhesion and contraction at the cell rear (c and d). Note the distinct actin structures at the leading edge, polar bundles of filaments generate narrow protrusions and adhesions at the tip (filopodia) while the flat crosslinked actin network generates a more blunt protrusion of the cell leading edge. Source: [Mattila and Lappalainen, 2008].

observed to migrate across substrates in exactly the same way as whole cells once their symmetry has been broken [Euteneuer and Schliwa, 1984, Verkhovsky et al., 1999]. This suggests it is a physical steady state for this network of molecules, which persists for as long as in the whole cell, even when MTs are removed. A continuum model description of this type of migration is discussed in section 2.3.

1.2.2 Cell polarisation

Of course, in order to migrate, cells must 'choose' a direction to go in by breaking symmetry, unless it is a cell with an intrinsically broken symmetry, such as a sperm cell or various types of bacteria. There are many ways cells can be oriented by the surrounding environment. The most commonly studied is probably chemotaxis, where the cell's surface

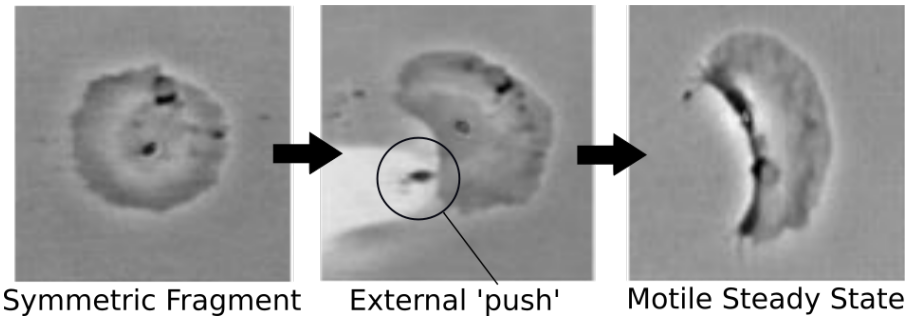

Figure 1.4: A keratocyte cell fragment polarised by an external mechanical stimulus. The motile steady state persists just as long as in the complete cells, even when its microtubules are depolymerised. Source: [Verkhovsky et al., 1999].

receptors detect a chemical gradient over the length of the cell [1], which in response polarises with respect to this gradient. Durotaxis is where the cell aligns with respect to gradients in substrate or environment stiffness, measuring this via the forces it exerts on its environment [Lo et al., 2000, Discher et al., 2005]. In addition, the geometry of the surrounding environment can polarise cells, a particularly interesting example being cells migrating through controlled micro-patterned environments that impose a particular direction on the cell without any chemical cues [Toyota et al., 2012]. In many cell types, when cells polarise, there is a re-organisation of the cell architecture which is highly dependent on the configuration of the microtubule network and centrosome and its position relative to the nucleus [Gomes et al., 2005, Bornens, 2008].

However, we see that even the cell fragments in figure 1.4 can spontaneously form polarised states without much of this cell architecture when their symmetry is broken by mechanically deforming the fragment shape on one side [Verkhovsky et al., 1999]. This suggests a physical instability in the fragment that creates some positive feedback when the symmetry is sufficiently broken.

[1] Small bacteria also respond to chemical gradients but due to their size cannot detect this over the area of its surface. Instead they detect gradients temporally by employing 'run-and-tumble' type motion [Bray, 2001].

1.2.3 Migration in 3D environments

In the context of cell biology, the term 3D environment can refer to any external medium that a cell migrates *through* rather than *on*. In fact there are many types of medium, both *in vivo* and *in vitro* that are referred to as 3D. *In vivo* many cells excrete a variety of proteins which form a fibrous network mostly consisting of collagen known as the extra-cellular matrix (ECM). Also, in most *in vivo* examples cells are confined by neighbouring cells and tissues. These environments constrain the cell motion in all direction, and the result is a range of motility and force generation mechanisms that are qualitatively different from those observed on flat substrates [Ridley et al., 2003, Wolf et al., 2013].

Research into cell migration in 3D is relevant to many biological applications, but one particular focus is in relation to some of the stages of cancer metastasis. Metastasis is the process of secondary tumour formation from cells in an initially isolated primary tumour, it enables cancerous cells to invade distant regions and organs in the body and once the process has successfully occurred treatment becomes much more difficult [Fidler, 2003, Weinberg, 2013]. There are a number of steps in this process, any of which can be rate-limiting, but one important factor is the ability of the cancer cells to migrate persistently and invade tissue. Thus, cancer cells are described as possessing a high 'metastatic potential' if they are very motile and invasive. These highly metastatic cells generally have a lower Young's modulus than their benign counterparts [Guck et al., 2005, Cross et al., 2007], allowing them to migrate through and invade 3D environments more effectively [Wirtz et al., 2011].

Cell motility mechanisms in 3D environments can be broadly split into 2 categories, however there are many differences between types of motion with these categories. Firstly, *amoeboid* (or *interstitial*) modes of migration are characterised by a rounded cell shape with few focal adhesions formed with the surrounding medium. Secondly, *mesenchymal* modes are where the cell elongates and extends protrusions while usually degrading biological barriers with matrix metalloproteases (MMPs) [Webb and Horwitz, 2003]. In addition, it

is observed that structures such as stress fibres and focal adhesions, which are vital to cell migration in 2D, play a much smaller role in 3D migration [Konstantopoulos et al., 2013]. However, there are a range of experimental environments that can be classed as 3D, and the migration observed can depend on the details of these, as well as the type of cell investigated. For example, as well as *in vivo* and reconstituted ECMs which are mostly made of networks of collagen fibres, artificial ECMs are often used, such as polymer hydrogels, so that the properties of the gel can be accurately varied (*e.g.* gel stiffness and MMP susceptibility) [Lutolf and Hubbell, 2005, Ehrbar et al., 2011]. In addition, simpler environments can be fabricated to investigate specific aspects of 3D migration, such a micro-channels with fixed dimensions to mimic cells migrating through different ECM pore sizes [Heuzé et al., 2011, Lautenschläger and Piel, 2013].

Mesenchymal modes of migration share several features with the crawling motion on flat substrates described in section 1.2.1, such as polymerisation driven protrusions and the formation of adhesions with the surrounding environment. When MMPs cannot be used to break down a path for the cell to migrate through, many cells switch to amoeboid migration modes and navigate pores in the matrix by squeezing and pushing through [Even-Ram and Yamada, 2005]. In these cases the formation of adhesion sites appears less important but the cells still need to generate traction forces in order to migrate. Important in this adhesion independent cell migration is a retrograde flow in the actomyosin cortex due to a higher concentration of contractile actomyosin at the cell rear [Poincloux et al., 2011, Bergert et al., 2015]. In this case friction forces alone can give the cell traction to propel forward.

Contraction of the cell cortex can also cause membrane blebbing, where the lipid membrane of the cell detaches from the (much stiffer) actin cortex and swells due to osmotic pressure. These individual 'blebs' tend to survive on the time scale of minutes before reattaching to the cortex, and can play a similar role to lamellipodia in 2D environments, protruding the front of the cell forwards, but in this case not driven by actin polymerisation [Fackler and Grosse, 2008, Charras and Paluch, 2008, Bergert et al., 2015].

1.3 Summary

The cell cytoskeleton is a highly dynamic structure responsible for the majority of animal cell motility phenomena. In this chapter we have seen some of the complex behaviour that the cytoskeleton can exhibit and the variety of ways it can generate force and motion in different environments. In the next section we will take a look at some mathematical models of specific cell motility phenomena, along with generic models for the actin cytoskeleton, and highlight some of the interesting results that provided the motivation for this project.

Chapter 2

Introduction II: Mathematical modelling of the Cell Cytoskeleton

Abstract

In the last 20 years, many physical models of the out-of-equilibrium (or 'active') dynamics of the cell cytoskeleton, from microscopic to continuum level models, have emerged and shown to be successful at characterising a wide range of cell behaviours. In this chapter we will first look at some of the microscopic models proposed to understand active force generation by polymerisation and motor activity. Then we will introduce some continuum models of cytoskeleton as an active gel or fluid, which will be the focus of the rest of this thesis. We will also consider the biological relevance of this model and introduce some examples where these models have been used to explain and predict aspects of cell locomotion.

2.1 Microscopic active mechanisms

While many cell motility phenomena can be qualitatively explained by a combination of protrusions driven by actin polymerisation and contraction of actomyosin to generate forces, modelling the mechanical mechanism for these forces is still an area of ongoing research. There have been several competing theories of how actin polymerisation is able to generate forces and do work inside a cell, however the one that appears to show the best agreement with experiment is the Elastic Brownian Ratchet Model (EBRM) developed by Mogilner and Oster [Mogilner and Oster, 1996] following the original Brownian Ratchet concept introduced by [Peskin et al., 1993].

2.1.1 The Elastic Brownian Ratchet Model

The Brownian Ratchet Model [Peskin et al., 1993] proposes that directed actin polymerisation could push a barrier if the thermal fluctuations of the barrier were large enough to open up a gap that would allow a monomer to bind to the end of the actin filament. Polymerisation of a free monomer would then prevent the barrier moving back to its original centre of mass position, displacing its centre of mass in the direction of polymerisation. This 1D model assumes a fixed filament, that can polymerise and depolymerise at its barbed end. The filament is next to a barrier with diffusion constant D and load force f. It is assumed that if the distance between the filament end and the barrier $x > \delta$ where δ is the monomer size, the filament will polymerise with velocity $\alpha\delta$, where α is the polymerisation rate, otherwise the polymerisation velocity is 0. The depolymerisation rate β is assumed to be constant and independent of distance to the barrier.

Coarse-graining and considering a concentration of filaments $c(x,t)$ at position x and time t one can write a master equation of the system making use of the Heaviside level-set function $H(x-\delta)$ to describe the polymerisation velocity. In the limit of fast diffusion (or slow polymerisation) $\alpha\delta^2/D \ll 1$ one finds an exponentially decaying steady state polymerisation velocity $v = \delta[\alpha \exp(-\omega) - \beta]$ where $\omega = f\delta/(k_B T)$. This leads to a

solution for a stall force, defined as the force for which $v = 0$ given by

$$f_0 = -\frac{k_B T}{\delta} \ln\left(\frac{\beta}{\alpha}\right) . \tag{2.1}$$

Thus, this model makes testable quantitative predictions for the force-velocity curve in actin protrusions and also the diffusion dependence of the velocity. However, one omission of the model is thermal fluctuations of the filaments themselves. In [Peskin et al., 1993] numerical calculations are also used to simulate thermal fluctuations of the filaments too. They find that these play a significant role for filaments over 50 monomers long (given the parameter estimates used). In addition, it does not consider that in filopodia the rate-limiting step to protrusion may be diffusion of monomers to the tip, rather than the load force.

One of the major motivations for this model, as well actin protrusions in cells, is the migration of the bacteria such as *Listeria* and *Shigella* through host eukaryotic cells. These bacteria utilise the host cell's own cytoskeleton attracting a polymerising actin tail at its rear, which propels it through the cell [Tilney and Portnoy, 1989, Goldberg and Theriot, 1995]. This polymerisation is initiated by the ActA protein coating the bacteria's surface, which nucleates actin. In fact, this motion has been reproduced experimentally using beads coated in ActA and WASP (another actin nucleating protein) [Yarar et al., 1999, Cameron et al., 1999]. According to the Brownian Ratchet model, in these systems the bacteria or bead velocity should decrease with its diffusion coefficient, and hence its size. However the results of experiments showed the opposite effect of velocity increasing with size [Cameron et al., 1999], but they also showed that actin tails were not observed for beads over a certain diameter. This suggests that the diffusion of the bead does not determine its propulsion velocity but it may be an important factor in the nucleation of filaments.

Calculations by Mogilner *et al.* [Mogilner and Oster, 2003] show that the Brownian Ratchet model may overestimate the relative importance of diffusion of the bacteria inside

the cell due to the high effective viscosity of the cell cytoplasm plus its contents. Thus, they consider fluctuations of the polymerising filament itself, assuming that it is tethered to the rest of the actin network, which is treated as a rigid object. As the filaments are long and thin, it is bending fluctuations that dominate, and it is supposed in the EBRM that these are the mechanism for the opening of a gap between the filament and membrane [Mogilner and Oster, 1996]. Further, they consider that the filaments therefore are not necessarily perpendicular to the barrier, and hence the force generated by each filament is proportional to $\cos(\theta)$, where θ is the angle between the filament end and surface normal. Similarly, the gap required depends on this angle, and hence the optimal angle of polymerisation varies with load force (see figure 2.1).

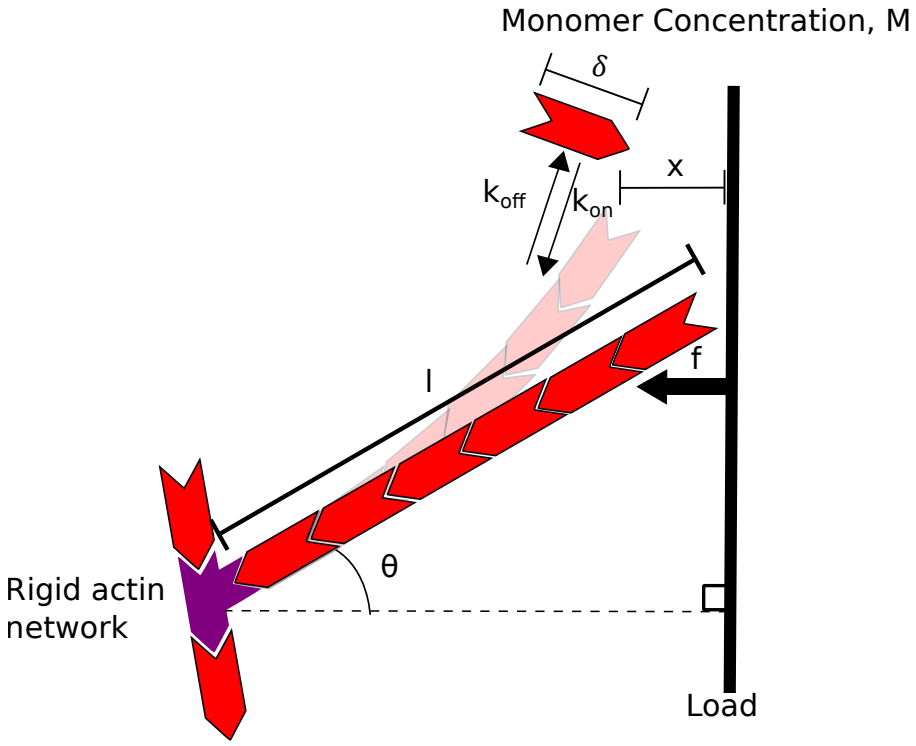

Figure 2.1: Schematic diagram of the EBRM. Filament polymerises and depolymerises at its barbed end against a load force f at an angle θ. The filament is anchored to a rigid actin network at its pointed end. Filaments behave like an elastic spring attached to a particle fluctuating due to Brownian motion to represent filament bending (illustrated by transparent bent filament). When the gap x between filament end and the barrier is greater than the effective monomer size $\delta\cos(\theta)$ a polymerisation event can occur at the tip. Figure based on [Mogilner and Oster, 1996].

Due to the large number of parameters in the EBRM, it's results can be best understood in the context of four parameter limits, given by small/large load forces and low/high

values of filament flexibility l/λ (where l is the length of the filament from its tether point to its free end, and λ is the filament persistence length). In each of these limits one can find the optimal angle (*i.e.* the angle that results in maximum protrusion velocity) and the protrusion velocity corresponding to this angle. In both large load limits, the optimal angle and velocity are the same, with the velocity profiles showing a $1/f$ dependence. For small load forces and flexible filaments, the optimal angle is $\theta = 0$ and the optimal velocity the same as the polymerisation velocity $v = \delta k_{\text{on}} M$, where $k_{\text{on}} M$ is the polymerisation rate assuming a linear dependence on local monomer concentration M. Finally, in the low load force, stiff filament limit, the critical angle increases with filament stiffness ($\theta_c = \tan^{-1}(2\delta\sqrt{\lambda/l^3})$ and the optimal velocity then is simply the net polymerisation speed in the x-direction $v = \delta\cos(\theta_c)(k_{\text{on}} M/l - k_{\text{off}})$. One can estimate the stall force by considering the large load limit when the optimal angle is almost at $\theta_c = \pi/2$, and hence the protrusion force is negligible. They find:

$$f_s \approx \frac{k_B T}{\delta l}\sqrt{l^2 + 4\lambda\delta}. \tag{2.2}$$

The EBRM predicts the velocities of such bacteria and beads to the correct order and magnitude, and provides physical explanations for the force velocity relations observed in these experiments. It also successfully predicts the force velocity relation of growing microtubules *in vitro* next to a barrier [Mogilner and Oster, 1999]. However, while this mechanism may well be incorporated in actin lamellipodia dynamics, these dynamic structures in keratocytes (the 'gliding' cells discussed in chapter 1, see figure 1.4) show force-velocity relations that are not predicted by the EBRM [Prass et al., 2006]. The higher order structure in motile cells, and the tethering of actin filaments to adhesion sites play key roles, and, as discussed in the previous chapter, some of these aspects are highly cell-type dependent. Nonetheless, the physical principal behind this model has proven an effective insight into the polymerisation mechanism. The model has been incorporated into larger scale models of the actin network, adding to it the effects of the ARP2/3 branching proteins, capping proteins, and transient binding events with the barrier, all of which play a role in the formation of cell protrusions [Mogilner, 2009].

2.1.2 Contractile forces in motor-filament interactions

Another key active process to understand in cell motility is the contractile force generated in ordered and disordered actomyosin networks. It is not directly obvious how motors binding and stepping along filaments can result in a macroscopic contraction of the filament bundle or network. One place to start is the mechanism for muscle sarcomere contraction, where an array of bundles of actin filaments are arranged with their pointed ends joined by large myosin filaments. As the myosin walks towards the barbed ends of the bundles they are pulled towards each other contracting the system [Alberts et al., 2008]. These particular networks span a large number of muscle cells that are very precisely ordered.

Actin networks in non-muscle cells lack this level of organisation, however ventral stress fibres (named for their position in crawling fibroblast cells [Small et al., 1998]) appear to have a similar organisation and exhibit contractility. However, experiments show that contractility occurs in more complex or disordered actin networks in crawling cells [Svitkina et al., 1997] suggesting that this is a more generic property of actomyosin. In addition, crosslinked networks of actomyosin with no clear orientational order (such as in the cell cortex) are observed to generate contraction forces in non-adhering cells [Medalia et al., 2002, Paluch et al., 2006]. In this section I will describe some of the microscopic models developed in order to explain the physics behind this phenomena and how they can inform us about continuum descriptions of the cytoskeleton.

Considering pairs of hard rods interacting with a motor in 1-dimension, Kruse *et al.* demonstrated that contractile stresses can be generated in polar bundles if the motor behaviour is different at the filament end [Kruse and Jülicher, 2000, Kruse et al., 2001]. Assuming that a motor transiently binds to both filaments and translates towards their plus end, this results in relative sliding of the filaments in an anti-parallel bundle. In this simple 1D model, it is observed that therefore anti-parallel bundles sort into separate polar bundles, and polar bundles shorten if the motors detach more slowly from the filament tips (see figure 2.2). Coarse graining the system they show that, if this relative contraction of

polar bundles exists it results in an active tension in the bundle. Surprisingly, there is no such tension created by relative sliding of anti-parallel filaments, as due to the symmetry of the top and bottom situations in figure 2.2(a), the filaments are as likely to pull closer together as they are push apart.

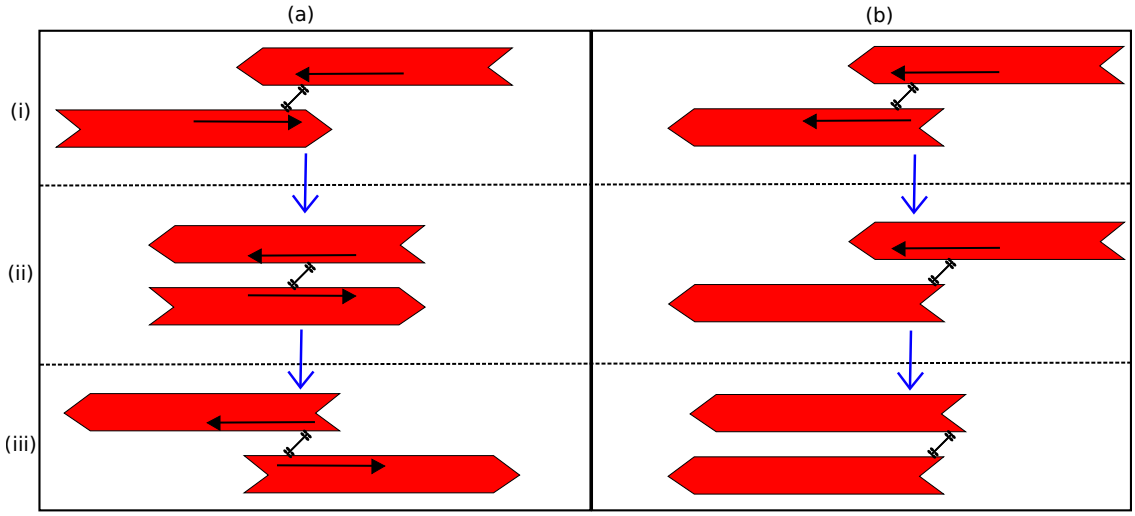

Figure 2.2: Examples of relative filament sliding possible in (a) anti-parallel filaments and (b) parallel filaments by motor generated forces. Force from motor exterted on filaments are demonstrated by the black arrows. In (a) if the motor is bound long enough it will slide the filaments past eachother until their barbed ends are together. In (b) the barbed ends can be brought together if the motor dwells remains bound to the filament barbed end.

Carlsson [Carlsson, 2006] suggests that the state in figure 2.2(a)(i) could be maintained on average by filament treadmilling at the correct rate. In this case, on average the filaments will polymerise away from the motor and the motors will pull the actin filaments together (figure 2.2(a)(i)) in more cases than it will push them apart (figure 2.2(a)(iii)). In this case, anti-parallel filaments on average should contract.

Several important factors are not considered in the simple diagram of figure 2.2 that could also lead to the observed contraction of bundles. For example, more than one motor can bind filaments at the same time, and experiments suggest this may be important for *in vitro* actomyosin bundles which are only contractile above a certain myosin density [Thoresen et al., 2011]. Moreover, crosslinking proteins bind neighbouring filaments on longer time-scales than the motor attachment process, meaning that filaments cannot

slide freely past one another. Liverpool *et al.* show that contraction forces are generated between anti-parallel filaments that have fixed ends [Liverpool et al., 2008]. Because the filaments are fixed, the heads of a bound myosin filament walk in opposite directions, creating an elastic tension in the motor. This results in an extensional force on the part of the actin filament between the bound motor site and the barbed end, and a compression force on the filament between the motor and the pointed end. The actin filaments have non-linear elastic properties, meaning that their elasticity is dependent on the force applied. They require a larger force to stretch than they do to compress, as they buckle easily. This means that there is an overall tension generated in the bundle, which pulls the filament ends towards one another (see figure 2.3). One can model the 1D representation of the situation in figure 2.3 in terms of linear elasticity by considering the actin filaments as two linear springs in series as shown in [Hawkins and Liverpool, 2014]. Then if one assumes that the section of the actin filament undergoing compression has a much smaller elastic constant that the section undergoing extension, net contraction of the bundle results.

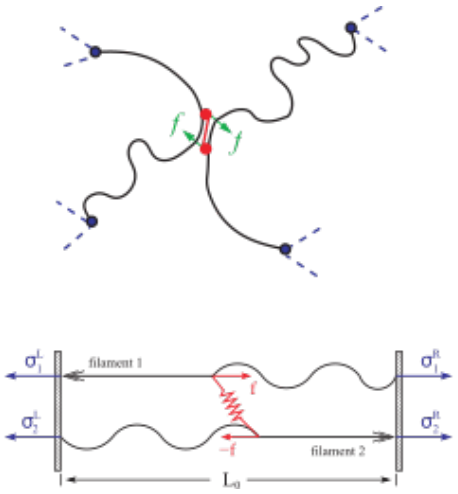

Figure 2.3: Top: Contraction due to myosin binding between two filaments in a crosslinked network, where f is the force exerted by the motor on a single filament. Bottom: 1-dimensional model of a contractile element. The myosin motor in red creates a tension in the actin filament plus ends (straight part of filaments). The minus end buckles providing no resistance to bending and hence the net force on the filaments is contractile. Source: [Liverpool et al., 2008].

In [Hawkins and Liverpool, 2014] this non-linear elasticity model of contraction is incorporated into a statistical model of a 1D contractile fibre. They show that the active

processes and binding rates in the fibre can lead to counter-intuitive force response behaviour at different time-scales The property of non-linear elasticity is also incorporated into the computational model presented in [Wang and Wolynes, 2012]. They simulate a 3D crosslinked actomyosin network by assuming a linear elasticity for filament stretching but zero resistance to filament compression. The crosslinkers form an initially random 3D lattice with some neighbouring crosslinkers joined by filaments [1], to which myosin motors can bind transiently. The motors exert a force on the permanently bound crosslinkers pulling them together as described by the non-linear elasticity. Overall contraction of the network is observed within a certain range of values of motor concentration and network connectivity, which agrees qualitatively with experiments of reconstituted systems of actin, myosin and crosslinkers in [Bendix et al., 2008].

In conclusion, theoretically there are several potential physical mechanisms for contraction in filament-motor systems, however experiments show that anti-parallel bundles generate much larger contractile forces than parallel bundles. Taking this into account, crosslinkers and system connectivity appears to be an important factor in generating contractile stresses, as does the non-linear elasticity of the filaments. It is worth noting that, in reconstituted microtubule-kinesin networks, extensile forces appear to be generated by the motors [Sanchez et al., 2012] and it would be interesting if a single physical model could account for this difference between actin and microtubule networks based on their different physical parameters. As the action of kinesin motors is thought to be somewhat similar to myosin.

2.2 Hydrodynamics of an active polar fluid

In order to gain a physical understanding of cell behaviour, it is useful to develop more coarse-grained models that can study longer length and time scales. Following experiments *in vitro* of long range order and the formation of vortices and asters in microtubule and motor protein solutions [Nédélec et al., 1997, Surrey et al., 1998], sev-

[1] The average fraction of neighbouring crosslinkers bound by filaments is determined by the network connectivity parameter P_c.

eral such course grained models were developed [Lee and Kardar, 2001, Kim et al., 2003, Sankararaman et al., 2004]. However, these particular models did not take into account hydrodynamic interactions of the filaments, which are significant in systems on these length and time scales.

Hydrodynamic models of cytoskeleton filaments were derived in [Kruse et al., 2004, Kruse et al., 2005] (for a gel of polar filaments with long range order) and [Liverpool and Marchetti, 2005] (for an isotropic gels of polar filaments) from symmetry arguments. These were able to capture filament treadmilling and dipole stresses generated by motor activity regulated by phenomenological parameters. These active gel models fall into the more general category of active matter, the study of ensembles of particles individually driven out-of-equilibrium by an internal energy [Ramaswamy, 2010]. A common feature of these models is large fluctuations in density due to interacting particles (know as giant number fluctuations) and patterns in polarisation direction of the constituents. The first active matter models described flocking behaviour of animals using a small number of rules for interaction between a particle and its neighbours [Toner and Tu, 1995, Toner and Tu, 1998]. Similar models have been implemented to describe the collective motions of bacteria and eukaryotes, where physical interactions between neighbours is due to hydrodynamics [Marchetti et al., 2013].

2.2.1 Derivation of hydrodynamic equations

Following [Kruse et al., 2004, Kruse et al., 2005], and [Fürthauer et al., 2012] we can derive hydrodynamic equations for an active polar fluid and then later in the section we will discuss extensions, improvements and simplifications of this model. We consider a fluid containing filaments that polymerise at a rate proportional to the local monomer density and depolymerise everywhere. Then, conservation of mass dictates

$$\frac{\mathrm{d}\rho^{(f)}}{\mathrm{d}t} \equiv \partial_t \rho^{(f)} + \nabla \cdot (\rho^{(f)} \boldsymbol{v}) = k_p \rho^{(a)} - k_d \rho^{(f)} \,, \tag{2.3}$$

where, $\rho^{(f)}$ is the filament density, $\boldsymbol{v}$ is the local centre-of-mass velocity, $\rho_{(a)}$ is the local monomer density and k_p and k_d are constants related to polymerisation and depolymerisation rates respectively (it is assumed that depolymerisation will scale linearly with filament density and polymerisation linearly with monomer density). Note that throughout this thesis we use the notation $\partial_t = \partial/\partial t$ to denote partial derivatives with respect to the time t and $\partial_i = \partial/\partial x_i$ to denote partial derivatives with respect to the coordinates x_i. There is also a reciprocal relation for the monomer density

$$\partial_t \rho^{(a)} + \nabla \cdot \boldsymbol{j}^{(a)} = -k_p \rho^{(a)} + k_d \rho^{(f)} \,. \tag{2.4}$$

As discussed in the previous chapter, the polymerised actin density can reach a steady state, where the polymerisation and depolymerisation balance but the actin filaments treadmill in the direction of their barbed end. The current $\boldsymbol{j}^{(a)}$ denotes the flux of monomers, relative to the (assumed fixed) solvent. In addition, motor proteins can bind and unbind to the filaments so dynamic equations for these two populations of motors can be defined:

$$\partial_t c^{(u)} + \nabla \cdot \boldsymbol{j}^{(u)} = k_{\text{off}} c^{(b)} - k_{\text{on}} c^{(u)} \,, \tag{2.5}$$

$$\partial_t c^{(b)} + \nabla \cdot \left(c^{(b)} \boldsymbol{v} \right) + \nabla \cdot \boldsymbol{j}^{(b)} = -k_{\text{off}} c^{(b)} + k_{\text{on}} c^{(u)} \,. \tag{2.6}$$

Here, $c^{(u)}$ is the concentration of unbound motors, free to diffuse in the solvent, and $c^{(b)}$ is the concentration of bound motors which advect with the filament gel. The constants k_{on} and k_{off} set the binding rates for individual motors and we have assumed for simplicity that these terms are linearly proportional to local concentration.

This can be simplified to a one-component model of an active polar fluid as in [Fürthauer et al., 2012] by considering the conservation of a single mass density ρ, such that $\mathrm{d}\rho/\mathrm{d}t = 0$. In this case we lose the effects of polymerisation and depolymerisation, which for the purposes of the calculations in this thesis is consistent. However for the more general derivation see [Kruse et al., 2005]. Within the framework of this one component

model, conservation of momentum is then given by the single equation:

$$\partial_t(\rho v_i) = \partial_j\left(\sigma_{ij}^{\text{tot}} - P\delta_{ij}\right) + f_i^{\text{ext}}\,, \tag{2.7}$$

where the σ_{ij}^{tot} is the total stress tensor, f_i^{ext} are external force densities, and P is the hydrostatic pressure.[2] We can write the free energy density in the active polar fluid generally as a sum of the kinetic energy and some function of the polarisation $\boldsymbol{p}$ and number density $n = \rho/m$ where m is the particle mass:

$$f = \frac{\rho v_i^2}{2} + f_p(n, \boldsymbol{p}, \nabla\boldsymbol{p})\,. \tag{2.8}$$

We can then write the free energy rate as:

$$\frac{\mathrm{d}F}{\mathrm{d}t} \equiv \frac{\mathrm{d}}{\mathrm{d}t}\int_V f\mathrm{d}V = \int_V \left[\frac{v_i}{2}\partial_t\left(\rho v_i\right) + \frac{\rho v_i}{2}\partial_t(v_i) + \left(\partial_t n\right)\mu_n - \left(\partial_t p_i\right)h_i - r\Delta\mu\right]\mathrm{d}V\,, \tag{2.9}$$

where $\mu_n = \delta F/\delta n$ and $h_i = -\delta F/\delta p_i$ are the functional derivatives of the free energy with respect to the variables. The final contribution $-r\Delta\mu$ is the rate of active energy consumption per unit volume in the system, where $\Delta\mu$ is the chemical potential energy released in the hydrolysis of an ATP molecule. This term implies that the ATP concentration is constant on hydrodynamic time-scales. Substituting the mass and momentum conservation laws into (2.9) we get:

$$\frac{\mathrm{d}F}{\mathrm{d}t} = \int_V \left[v_i\partial_j\left(\sigma_{ij}^{\text{tot}} - P\delta_{ij}\right) + \frac{v^2}{2}\partial_i\left(\rho v_i\right) - \partial_i\left(n v_i\right)\mu - \left(\partial_t p_i\right)h_i - r\Delta\mu\right]\mathrm{d}V\,, \tag{2.10}$$

We can then expand $\sigma_{ij}^{\text{tot}} = \sigma_{ij}^{\text{tot}} - \sigma_{ij}^{e} + \sigma_{ij}^{e}$ where σ_{ij}^{e} is the Ericksen stress given by:

$$\sigma_{ij}^{e} = \left(f_p - \mu n\right)\delta_{ij}\frac{\partial f_p}{\partial(\partial_i p_k)}(\partial_j p_k)\,. \tag{2.11}$$

As demonstrated in [Joanny et al., 2007], one can use this to derive the Gibbs-Dunelm

[2] Often, this hydrostatic pressure is absorbed into the total stress, here we treat it separately as this is consistent with the rest of this thesis.

relation for this system:

$$\partial_j \sigma^e_{ij} = -n\partial_i \mu - h_j \partial_i p_j \,. \tag{2.12}$$

Substituting equation (2.12) into equation (2.10) we can write:

$$\begin{aligned}\frac{\mathrm{d}F}{\mathrm{d}t} = \int_V \Big[& v_i \partial_j \left(\sigma^{\mathrm{tot}}_{ij} - \sigma^e_{ij} - P\delta_{ij}\right) + \frac{v^2}{2}\partial_i\left(\rho v_i\right) - \partial_i\left(n v_i\right)\mu + n v_i\left(\partial_i \mu\right) \\ & - \left(\partial_t p_i + v_j \partial_j p_i\right) h_i - r\Delta\mu \Big] \,\mathrm{d}V \,. \end{aligned} \tag{2.13}$$

Integrating by parts we can re-write this as:

$$\begin{aligned}\frac{\mathrm{d}F}{\mathrm{d}t} = & -\int_V \left[\sigma_{ij}(\partial_j v_i) + \left(\partial_t p_i + v_j \partial_j p_i\right) h_i + r\Delta\mu\right] \mathrm{d}V \\ & + \int_S \left[v_i \sigma_{ij} + v_j(\mu n - P)\right] \mathrm{d}S_j \,, \end{aligned} \tag{2.14}$$

where the surface element vector $\mathrm{d}S_j$ is parallel to the surface normal and we define $\sigma_{ij} = \sigma^{\mathrm{tot}}_{ij} - \sigma^e_{ij} + \rho v_i v_j$. Finally, by considering conservation of angular momentum (as shown explicitly in [Fürthauer et al., 2012]), one can show that the anti-symmetric part of this effective stress $\sigma^a_{ij} = (\sigma_{ij} - \sigma_{ji})/2 = (p_i h_j - h_i p_j)$. Then, substituting $\sigma_{ij} = \sigma^a_{ij} + \sigma^s_{ij}$ into equation (2.14) and using the thermodynamic relation $T\dot{S} = -\dot{F} + J_F + \dot{W}$ for an isothermal fluid, we arrive at the entropy production rate:

$$T\dot{S} = \int_V \left[\sigma^s_{ij} u_{ij} + \frac{Dp_i}{Dt} h_i + r\Delta\mu\right] \mathrm{d}V \,. \tag{2.15}$$

The surface terms from equation (2.14) are absorbed by the surface free energy flux J_F and the work rate from external forces $\dot{W} = 0$ as we assume no external contributions in this derivation. In addition we have introduced the material derivative defined as $D\boldsymbol{p}/Dt = \partial_t \boldsymbol{p_i} + (v_j \partial_j) p_i + \omega_{ij} p_j$ where $\omega_{ij} = (\partial_i v_j - \partial_j v_i)/2$ is the vorticity tensor and $u_{ij} = (\partial_i v_j + \partial_j v_i)/2$ is the strain rate tensor. From equation (2.15) one can read off the thermodynamic fluxes ($\underline{\underline{\sigma}}^{\mathrm{s}}$, $D\boldsymbol{p}/Dt$ and r) and forces ($\underline{\underline{u}}$, $\boldsymbol{h}$ and $\Delta\mu$) in the system. From these, the constitutive equations are derived by expanding the fluxes in terms of allowed

forces by symmetry to give

$$\sigma^{\mathrm{s}}_{ij} = 2\eta u_{ij} + \frac{\nu}{2}\left(p_i h_j + p_j h_i\right) + \bar{\nu} p_k h_k \delta_{ij} - \left(\zeta p_i p_j + \bar{\zeta}\delta_{ij} + \zeta' p_k p_k \delta_{ij}\right)\Delta\mu\,, \tag{2.16}$$

$$\frac{Dp_i}{Dt} = \frac{1}{\Gamma}h_i + \lambda\Delta\mu p_i - \nu p_j u_{ij} - \bar{\nu} u_{jj} p_i\,, \tag{2.17}$$

$$r = \Lambda\Delta\mu + \lambda p_i h_i + \bar{\zeta} u_{ii} + \zeta p_i p_j u_{ij} + \zeta' p_i p_i u_{jj}\,. \tag{2.18}$$

Where η is the dynamic viscosity and Γ the rotational viscosity. The parameters ν and $\bar{\nu}$ are the flow-orientation coupling constants, and ζ, $\bar{\zeta}$, and ζ' are phenomenological parameters describing the active stress. Note that in general these are dependent on filament/motor density. Additionally, λ corresponds to active alignment of filaments and Λ corresponds to a phenomenological ATP consumption.

In this thesis, as we are interested in biological phenomena at very small length scales, we can assume a Reynolds number of effectively $Re \equiv \bar{\rho}\bar{v}L/\eta = 0$. Estimates of the physical parameters of the cytoskeleton are difficult to come by, but if we consider a maximum length scale of $L = 100\mu$m, a velocity scale of $\bar{v} = 0.1\mu\mathrm{ms}^{-1}$ (based on cell migration speeds [Maiuri et al., 2012]), a density approximately that of water $\bar{\rho} = 10^3$kg m^{-3} and a viscosity of 10^3Pas [Gardel et al., 2008], this gives a very crude Reynolds' number approximation of 10^{-12}, justifying the assumption made. Thus, in this limit, viscous forces dominate completely over inertial forces and so the force balance equation (2.7) (in the absence of external forces) can now be written as:

$$\partial_j\left[\sigma^{\mathrm{s}}_{ij} + \frac{1}{2}\left(p_i h_j - p_j h_i\right) + \sigma^{\mathrm{e}}_{ij} - P\delta_{ij}\right] = 0\,. \tag{2.19}$$

The active stresses in equation (2.16) describe generic forces generated by the consumption of a chemical fuel. We can see that $\zeta, \bar{\zeta}, \zeta' < 0$ correspond to contractile stresses, and hence these terms are used to phenomenologically model actomyosin contraction. These terms remain the same with the substitution $\boldsymbol{p} \to -\boldsymbol{p}$ and hence would be the same in a nematic description of orientational order (see section 2.2.3).

To determine the molecular field $\boldsymbol{h}$, we use the free energy for a passive polar liquid crystal to describe distortions in the polarisation field. This energy describes the lower entropy that is achieved by filament alignment relative to disorder. Thus, sufficient active energy can drive the filaments away from their equilibrium state, such that this free energy F is not minimised. Generally we assume that the polarisation field is of fixed magnitude $|p| = 1$, in which case the free energy is given by [de Gennes and Prost, 1993]:

$$F = \int_V \mathrm{d}x^3 \frac{1}{2}\left[K_1(\nabla \cdot \boldsymbol{p})^2 + K_2(\boldsymbol{p} \cdot \nabla \times \boldsymbol{p})^2 + K_3(\boldsymbol{p} \times \nabla \times \boldsymbol{p})^2 - h_{\parallel}^0 \boldsymbol{p}^2\right] + \text{Surface terms} \tag{2.20}$$

Here, the elastic coefficients $K_{1,2,3}$ relate to the splay, twist and bend respectively, while $h_{\parallel}^0$ is a Lagrange multiplier, ensuring that $|\boldsymbol{p}| = 1$. Note that none of these terms are polar (i.e. they obey the $\boldsymbol{p} \to -\boldsymbol{p}$ symmetry, however the surface terms can be polar in nature, depending on the assumptions made.

So far this section has outlined the derivation of the constitutive equations for an active polar fluid. Below, we will describe some of the extensions to this model that have been made to include physics that has been omitted in this simplified case, or some slightly different but related physical cases.

2.2.2 Active Viscoelastic Gel

As described in chapter 1, the cytoskeleton is a viscoelastic gel, which exhibits some exotic rheological properties. In order to capture some of this behaviour, in [Kruse et al., 2004, Kruse et al., 2005] the authors originally derived the constitutive equations (2.16)-(2.18) for a viscoelastic gel using a convected Maxwell model. This assumes that the gel has a single relaxation time $\tau = E/\eta$ (where E is an effective Young's modulus) such that the stress-strain relation is a sum of elastic and viscous responses. Using the same notation as in section 2.2, for a simple isotropic passive gel, this relation is:

$$\left(1 + \tau \frac{D}{Dt}\right) \sigma_{ij} = 2\eta u_{ij} \,. \tag{2.21}$$

Here the convective derivative of a tensor is defined as:

$$\frac{D}{Dt}\sigma_{ij} = \partial_t \sigma_{ij} + v_k \partial_k \sigma_{ij} + z\frac{1}{2}(\omega_{ik}\sigma kj + \omega_{jk}\sigma_{ki}) \tag{2.22}$$

In the limit of $\tau = 0$ (viscosity dominated) we return to the case of a Newtonian fluid, where the stress is proportional to the strain rate. More specifically, this time-scale τ determines the exponential rate at which the shear stress will reduce to zero (in a Newtonian fluid the total shear stress is always zero).

In order to extend this simple model to a complex active fluid, one needs to consider the time symmetry of the different contributions to the forces in the system. The thermodynamic fluxes and forces in the system remain the same as those identified in equation (2.15), however the forces need to be separated into *reversible* (reactive) and *irreversible* (dissipative) contributions based on their time reversal symmetry or asymmetry. This full derivation is presented in [Kruse et al., 2005], however in this thesis we use the fluid limit $\tau = 0$ to make calculations analytically tractable. It is assumed that this represents the long-time behaviour well, but experiments show that the actin cytoskeleton relaxation time can be on the order of tens of seconds [Wottawah et al., 2005], meaning that elasticity in the network may play an important role in cell motility, polarisation and division.

In [Hemingway et al., 2015] the authors develop a model of an active viscoelastic nematic gel that is complementary to these models and show that these extra degrees of freedom can introduce complex new states and damping of some of the active effects.

2.2.3 Anisotropic drag and diffusion

[Liverpool and Marchetti, 2005] derive hydrodynamic equations for active filament solutions starting from a microscopic picture of filament contraction. They consider a pair of hard rods interacting with an active crosslinker that moves to the plus end of the filaments. In this case, if the translational friction coefficients between the rods and external medium are dependent on rod orientation, then the pair of rods can translate

due to the motor activity. They go on to examine a coarse grained system of interacting filament pairs in 2 dimensions, defining a local filament density ρ and polarisation $\boldsymbol{p}$. By then deriving coupled polarisation and density equations, taking into account anisotropic diffusion of the filaments, they derive two active hydrodynamic terms. The first is in the density flux only and acts like a reverse-diffusion term, enhancing density fluctuations, corresponding to filament bundling by motors. The second characterises filament polarity sorting by the motors, which goes to zero when the anisotropic friction coefficients (which gives rise to the anisotropic diffusion tensor) are not considered. Active stresses are not generated from the microscopic interactions between filament motor pairs considered in [Liverpool and Marchetti, 2005] because the filaments are free to slide.

2.2.4 Active nematic fluids

As discussed in section 2.1.2, it may be the case that directed contraction only occurs in anti-parallel bundles of actin filaments. In which case, a theory describing polar contractile rods is not applicable. As in [Hatwalne et al., 2004, Marenduzzo et al., 2007, Edwards and Yeomans, 2009] one can use the nematic orientational order tensor instead $Q_{ij} = (n_i n_j - 1/d)$ where $\boldsymbol{n} = -\boldsymbol{n}$ is the average local orientation direction and d is the dimensionality of the system. The active stress and free energy can then be re-written in terms of $\underline{\underline{Q}}$ although the physical meaning of these terms remains the same (see figure 2.4).

2.2.5 Explicit coupling between densities and polarisation

The coupling between local densities and filament polarisation depends on the number of components included in the model. In section 2.2 we introduced fluxes of motors and filament density but reduced the system to a one component model with fixed density to derive the hydrodynamic equations. [Sarkar and Basu, 2015] show that, from symmetry arguments, this coupling between a one-component density and polarisation can result in

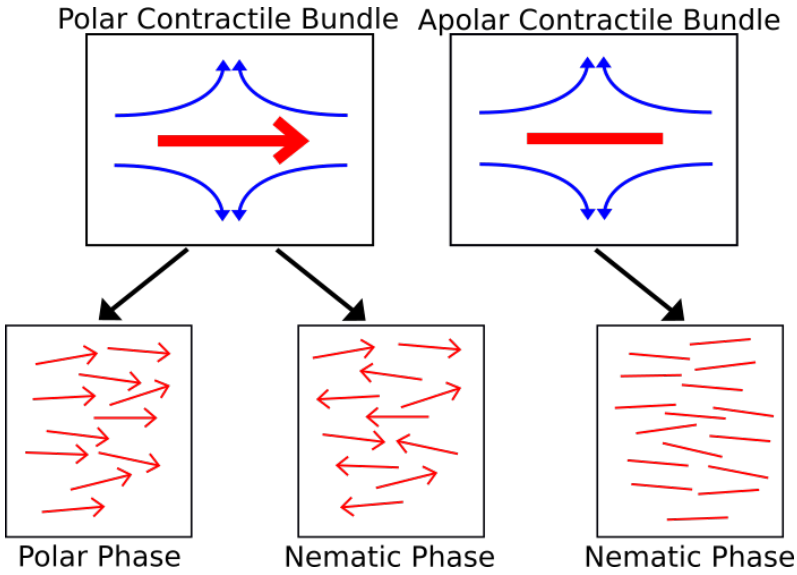

Figure 2.4: A minimal microscopic description of the active stress for $\zeta < 0$. Each polar/nematic particle (red arrow/line) induces a local dipolar flow field (blue arrows), which is the same in the polar and nematic phases. The interaction of all these flow fields results in the macroscopic active stresses in the medium.

new polar terms in the stress and polarisation flux:

$$\underline{\underline{\sigma}}^{\text{coupled}} = -\frac{\epsilon_0}{2}\left[\boldsymbol{p}(\nabla\mu_\rho) + (\boldsymbol{p}(\nabla\mu_\rho))^T\right], \tag{2.23}$$

$$\frac{D\boldsymbol{p}}{Dt}^{\text{coupled}} = -\bar{\lambda}\nabla\bar{\mu}_\rho + \lambda_\rho\Delta\mu\nabla\rho\,, \tag{2.24}$$

$$\boldsymbol{j}_\rho = -\gamma_{\rho\rho}\nabla\bar{\mu}_\rho + \bar{\lambda}\boldsymbol{h} + \kappa_\rho(\rho)\Delta\mu\boldsymbol{p} + w\Delta\mu\nabla\cdot(\rho\boldsymbol{p}\boldsymbol{p}) - \frac{\epsilon_0}{2}(\nabla\boldsymbol{v} - (\nabla\boldsymbol{v})^T)\cdot\boldsymbol{p}\,. \tag{2.25}$$

We see that the extra contribution to the stress is a passive term, it couples the flow and particle current with related coupling constant ϵ_0 where μ_ρ is the chemical potential of the particle density. The active parameter λ_ρ aligns the polarisation field with (or against depending on sign) gradients in the particle density. The constant $\bar{\lambda}$ couples the passive contributions to the density and polarisation. The final equation gives the particle flux $\boldsymbol{j}_\rho$, where the first term is the contribution by its chemical potential and there are two active contributions. The active parameter $\kappa_\rho(\rho)$ implies a flux of particles in the polar direction $\boldsymbol{p}$ corresponding to filament treadmilling, the speed of which in general can depend on filament density. The other active parameter w has a bundling effect leading to banding instabilities in the density.

2.3 Predictions and Applications of Active Gel Models

As we have seen in previous sections, the directional active stress describes a dipolar force that is either contractile or extensile along the filament length. This force can destabilise filaments from their equilibrium state once it is large enough to overcome the equilibrium interactions. In a bulk system the global equilibrium state will be that of aligned filaments as this minimises the free energy in equation (2.20). Ramaswamy [Ramaswamy, 2010] shows that a contractile active stress $\zeta < 0$ leads to splay instabilities in this steady state (and bend instabilities for $\zeta > 0$). This can be seen by considering interactions of the flow fields around constituent particles of the model described by figure 2.4. If the filaments slightly splay outwards relative to one another then a net forward flow is generated, which splays the filaments further. Activity thresholds for these splay instabilities to occur have been predicted under various boundary constraints. [Voituriez et al., 2005] showed analytically that, confined between parallel walls (and assuming the polarisation field is anchored parallel to the walls) this activity threshold scales as the inverse square of the channel width. They are also able to calculate the steady state flow profile for small activities under different flow boundary conditions. Similarly, [Kruse et al., 2004] show that if defects are introduced by boundary conditions, then 2D asters, spirals and vortices will spontaneously rotate above a certain activity threshold.

[Kruse et al., 2006] also apply this model to the lamellipodium of crawling cells, modelling the retrograde flow, height profile and force generated in a thin film of aligned active polar gel with a given linear friction at the substrate interface. They observe that the combined force of active contraction in the bulk and protrusion at the leading edge leads to extension of the layer and also retrograde flow of the actin network relative to this motion. Further, [Ziebert and Aranson, 2014] model symmetry breaking and crawling in keratocyte fragments using a similar continuum model introduced in [Ziebert et al., 2011]. This model describes the cell using a phase field ρ (where $\rho = 1$ inside the cell and $\rho = 0$ outside, corresponding to minima in the phase field free energy). The phase field evolution is coupled to equations describing motor dynamics and polarisation dynamics, assuming

that the actin density is proportional this phase field (*i.e.* constant in the cell). By assuming that (a) the phase field advects with filament polymerisation, (b) motors couple to regions of lower density and (c) motors inhibit average local polarisation of actin, the model recreates several aspects of keratocyte fragment motion including the characteristic cell shape and oscillations in speed.

An active gel description of the cell cortex has also been used to describe some long time-scale phenomena in cells such as rounded motility [Hawkins et al., 2011] and cytokinesis [Turlier et al., 2014]. In [Hawkins et al., 2011] the authors model the cortex as an isotropic active compressible layer with actin filament density ρ and bound motor concentration μ. They assume that the active stress in the layer is proportional to local motor density, and that these motors can interchange between the layer and the contained cell cytosol. Recycling of the actin density is achieved by filament polymerisation and depolymerisation as described in equation (2.3). It is found that this system is linearly unstable for large enough contractile activity. Moreover, approximating biologically relevant parameter values they show that the active steady state in this system produces directed motion and emulates the rounded motion of tumour cells observed in [Poincloux et al., 2011]. In [Turlier et al., 2014] a similar computational model is used to describe the evolution of the cell shape in cytokinesis due to increased contractile activity in the cortex around the cell equator, showing good agreement with experiments.

More recently, a new focus has emerged modelling active fluids at activity ranges much larger than symmetry breaking thresholds. In these limits, the system cannot relax to a steady state and 'turbulent' like states are observed. These are relevant in various biological situations, such as bacterial swarms and reconstituted *in vitro* cytoskeleton networks [Dombrowski et al., 2004, Fielding et al., 2011, Sanchez et al., 2012, Thampi et al., 2014]. In these systems defects in the polarisation field are spontaneously generated by the active stress and interact via distortions in the polarisation field. The topological charge of these defects determines how they interact, and must be conserved in total in the system unless absorbed by a boundary. These defect can be identified in reconstituted microtubule-

kinesin gels and their interaction indicates that the active stresses generated are extensile [Giomi et al., 2013]. These exotic states of matter are fascinating in their own right, and the fact that model systems that display the same behaviour can be constructed in the lab makes them an exciting emerging field in soft matter physics.

2.4 Summary

The hydrodynamic descriptions of active gels introduced in this chapter are derived by considering conservation laws and symmetry arguments. Only in a few cases have the hydrodynamic parameters been directly linked to microscopic properties [Liverpool and Marchetti, 2003, Liverpool and Marchetti, 2005, Ahmadi et al., 2005, Ahmadi et al., 2006]. This shows that we are still some way from a full physical picture of the cell cytoskeleton. Most of the qualitative behaviours predicted in these models (bundling, treadmilling, stress generation *etc.*) are observed in cells, but building a complete model of the dynamic cell cytoskeleton from this approach is not yet feasible. Nonetheless, these models can go some way to understanding aspects of cell behaviour, in particular one can examine the effects of different terms separately to isolate the physics behind specific emergent behaviours or properties.

In this thesis, we focus on modelling active gels in confinement, specifically confined in or around fluid droplets. Modelling symmetry breaking in such a geometry can be more challenging than in quasi 1D systems, but one that is more relevant to cell motility in 3D environments. We aim to quantify motility modes in these systems and establish conditions for symmetry breaking and macroscopic polarisation and motility of the droplets. In addition, we aim to explore how a coupling between droplet shape and filament polarisation can play a role in some of these systems and give rise to characteristic steady state shapes. To do this, we will use both analytical calculations to better understand some of the underlying physics and parameter dependencies, and numerical simulations to quantify more complex behaviour. We also aim to relate these calculations to potential experiments and relevant biological phenomena to gain a better understanding of some of the physical

processes involved.

Chapter 3

Motility in splayed active polar droplets

Abstract

In this chapter we calculate the flows and forces generated in a circular (and spherical in 3D) droplet of active polar fluid with a fixed polarisation field. We consider a droplet with linear friction at the interface and quantify the force moments relating to droplet deformation and motion. Building on these calculations (which were presented in [Whitfield et al., 2014]) we also calculate the flow for the case where the droplet is immersed in an external fluid and show how this relates to its instantaneous velocity.

3.1 Introduction

In this chapter we will present work published in [Whitfield et al., 2014] where we consider a motility mechanism that arises in a droplet of active fluid due solely to active contractile stress from the interaction of myosin II and F-actin. For this case, as in [Kruse et al., 2004] and [Voituriez et al., 2005], we ignore the self-polymerisation of the actin filaments so that we can isolate the effects of the contractile stresses generated by the actomyosin network only. We apply a viscous friction condition at the boundary to address the issue of cell motility in three-dimensional (3D) confinement (such as tissue-like environments), the importance of which was discussed in Chapter 1 and references therein.

We compare our results to the lattice Boltzmann fluid simulations of an active droplet by Tjhung *et al.* [Tjhung et al., 2012], which shows that a droplet of active gel immersed in a Newtonian fluid will display spontaneous symmetry breaking when the intensity of motor activity is above a certain threshold. This symmetry breaking causes the droplet to reach a motile steady state, similar to that discussed in this chapter. The case we present considers a system where the symmetry is already broken by a splayed polarisation of the filaments, which we justify in section 3.2. Imposing the polarisation field allows us to model this system analytically, providing greater insight into the important factors behind this motile steady state. Also the droplet modelled here interacts with the external medium via a linear viscous friction, whereas the simulations in [Tjhung et al., 2012] use a two-phase model with periodic boundary conditions, where the passive viscous properties of the two phases of fluid are identical. Therefore, we are able to predict how the steady state flow in the droplet depends on the effective friction with the external medium.

We first present the two-dimensional (2D) version of the calculation to simplify both the mathematics and graphical representation of the system. This allows for comparison between the analytical results and hybrid lattice Boltzmann simulations of an active droplet that use the source code introduced in [Tjhung et al., 2012]. Finally, in section 3.3.4 we show how the analytical case generalises to 3D.

3.2 Model

We begin with a circular droplet of active fluid of radius R and assume that the boundary remains fixed. This assumption is valid for a droplet with high cortical tension, such that any active pressure gradients in the droplet would have a negligibly small effect on the boundary shape. We discuss the validity of this assumption later in section 3.3.3.

In this calculation, we assume that the density of the active fluid is constant and that the polarisation in the fluid has fixed magnitude $|p| = 1$ describing a highly ordered polar state. In this way, we can calculate specifically how directed contraction can lead to motility without increases in actin or myosin density. Thus simulations in [Tjhung et al., 2012] models the active fluid density with a phase field (see 3.2.2). This effectively fixes the active fluid density inside the droplet to a constant value, and hence the analytical calculations presented here compare well. In real active gels and fluids, actin density and motor concentration fluctuations are often important to contraction based processes, and we consider some of these effects in calculations in chapters 4 and 5.

3.2.1 Constitutive equations

To model the dynamics of the internal active fluid, we use the coarse grained hydrodynamic approach derived in [Kruse et al., 2004, Kruse et al., 2005, Fürthauer et al., 2012] and introduced in chapter 2. We do not consider the viscoelastic nature of the active cytoskeleton, assuming that the time-scales we consider are long enough to observe fluid-like behaviour. We can split the constitutive equation for the stress in the active gel into viscous, distortion and active components as follows:

$$\sigma_{ij}^{\mathrm{tot}} = \sigma_{ij}^{\mathrm{visc}} + \sigma_{ij}^{\mathrm{dist}} + \sigma_{ij}^{\mathrm{act}} \,. \tag{3.1}$$

The viscous stress is assumed to be the same as a Newtonian fluid, proportional to the strain rate in the fluid:

$$\sigma_{ij}^{\text{visc}} = 2\eta u_{ij} = \eta \left(\partial_i v_j + \partial_j v_i\right) , \tag{3.2}$$

where η is the shear viscosity and $\boldsymbol{v}$ is the fluid velocity. Next, the stress caused by distortions in the filament alignment is

$$\sigma_{ij}^{\text{dist}} = \frac{\nu}{2}\left(p_i h_j + p_j h_i\right) + \frac{1}{2}\left(p_i h_j - p_j h_i\right) + \sigma_{ij}^{\text{e}} , \tag{3.3}$$

where the molecular field $\boldsymbol{h} = -\left(\delta F\right)/\left(\delta \boldsymbol{p}\right)$ and F_d is the distortion free energy for a network of polar filaments in the passive regime with $|\boldsymbol{p}| = 1$. We simplify the free energy from equation (2.20) by taking the one-constant approximation $K = K_1 = K_2 = K_3$, to match the simulations in [Tjhung et al., 2012]. However, as we consider a fixed polarisation, these parameters could be included in this calculation. In addition, we do not include surface terms, as the instability is driven by bulk behaviour, however we consider these in Chapters 4 and 5 in some detail. The distortion stress from equation (3.3) depends also on ν, which is a dimensionless constant that relates to the coupling between the polarisation field and the flow (negative for rod-like particles; the value and sign of ν however have no qualitative bearings on our results). The second term in equation (3.3) is the anti-symmetric component of the distortion stress and the final term is the contribution from the Ericksen stress:

$$\sigma_{ij}^{\text{e}} = f\delta_{ij} - \frac{\partial f}{\partial\left(\partial_j p_k\right)}\partial_i p_k \, . \tag{3.4}$$

The final contribution to equation (3.1) is from the active stress. Note this has a non-zero trace, whereas it is taken to be traceless in the Lattice-Boltzmann simulations. However in an incompressible drop the trace of the active stress can be absorbed into the internal pressure and makes no difference to the calculation here,

$$\sigma_{ij}^{\text{act}} = -\zeta \Delta\mu p_i p_j \, . \tag{3.5}$$

Again, we should note that in general ζ is a function of actin and myosin density, which we assume to be constant. The assumption of constant ζ means that we potentially miss some interesting effects due to gradients in the activity. On hydrodynamic time scales the motors would be advected by the flow which could lead to a feedback mechanism (*e.g.* as calculated in [Hawkins et al., 2011] for a compressible cortical layer of active gel), but we would not expect this effect to occur in incompressible systems. In addition density fluctuations can occur when the density is coupled to the polarisation field [Joanny et al., 2007, Giomi et al., 2012, Sarkar and Basu, 2015] which can occur microscopically due to filament treadmilling (for actin density) or motor clustering (for motor density). However we do not consider this here, but instead focus on the effects of contraction in such a splayed state and the effect of filament orientation.

When the system is in steady state, the total stress will satisfy the force balance equation:

$$\partial_i \left(\sigma_{ij}^{\mathrm{tot}} - P\delta_{ij} \right) = 0 \,, \tag{3.6}$$

where P is the hydrostatic pressure. Finally, we also impose the incompressibility condition on the fluid:

$$\nabla \cdot \boldsymbol{v} = 0 \,. \tag{3.7}$$

We do not include evolution of the polarisation vector $\boldsymbol{p}$ in this calculation, so the equation (2.17) from the previous chapter is omitted. This means that we will essentially find the steady state flow from a polarisation field that is not at steady state. Hence this will be an approximation to the steady state motion observed in [Tjhung et al., 2012], which will be discussed in the section 3.2.3.

3.2.2 Hybrid lattice Boltzmann simulations of an active droplet

The lattice Boltzmann simulations, used to obtain fig. 3.1, are adapted from [Tjhung et al., 2012]. This section summarises the governing equations in these simulations.

Firstly, the free energy functional, which completely governs the behaviour of the system in the passive limit, in summation notation is as follows:

$$F\left[\phi, p_i\right] = \int d^3r \left\{ \frac{a}{4\phi_{cr}^4}\phi^2(\phi-\phi_0)^2 + \frac{k_\phi}{2}\left|\nabla\phi\right|^2 - \frac{a}{2}(\phi-\phi_{cr})p_i p_i + \frac{a}{4}\left(p_i p_i\right)^2 + \frac{K}{2}\left(\partial_i p_j\right)^2 \right\} . \tag{3.8}$$

In this model, ϕ is the activity concentration, and so $\phi = 0$ in the passive phase and $\phi > \phi_{cr}$ in the active phase. The first term in equation (3.8), with coefficient a, gives free energy minima for ϕ at $\phi = 0$ and $\phi = \phi_0 > \phi_{cr}$. The coefficient k_ϕ contributes to the interfacial tension, and a characterises the isotropic to nematic transition (this term couples $|\boldsymbol{p}| = 0$ to the passive phase and $|\boldsymbol{p}| = 1$ to the active phase). The final term is the distortion free energy contribution from (2.20) where K is the elastic constant in the one constant approximation $K_1 = K_2 = K_3 = K$ and we assume no specific anchoring at the boundary.

The total activity in the system is conserved, so the time evolution of ϕ is calculated using a convective-diffusion equation at each time step:

$$\frac{\partial\phi}{\partial t} + (v_i\partial_i)\phi = M\partial_i^2\frac{\delta F}{\delta\phi}\,, \tag{3.9}$$

where M is related to the diffusion of the phase field. The polarisation dynamics are then governed by equation (2.17) with $\lambda = 0$, as this term only has an effect when $|p| \neq 1$ in the active phase.

Lattice Boltzmann techniques (see [Chen and Doolen, 1998] for a review) are used to satisfy the incompressible Navier-Stokes equations (the generic version of equations (3.6)

and (3.7), applicable for all Reynolds' number values),

$$\rho\left(\frac{\partial}{\partial t}+v_k\partial_k\right)v_i=\partial_j\left(\sigma^p_{ji}-P\delta_{ij}\right)\,. \tag{3.10}$$

$$\partial_i v_i=0 \tag{3.11}$$

The tensor $\boldsymbol{\sigma}^{\mathrm{p}}=\sigma^{\mathrm{tot}}+\sigma^{\mathrm{int}}$ is the total stress from the active gel plus an extra interfacial term related to the surface tension:

$$\sigma_{ij}^{\mathrm{interface}}=-\phi\frac{\delta F}{\delta\phi}\delta_{ij}-\frac{\partial f}{\partial(\partial_j\phi)}\partial_i\phi\,, \tag{3.12}$$

where f is the free energy density in equation(3.8).

We initialise the simulation by assuming an aligned polarisation field $\boldsymbol{p}=\hat{\boldsymbol{x}}$ inside a circular droplet in the active phase. The initial radius of the droplet is set to approximately 1/5 of the total grid size so that the drop is isolated and the boundaries are periodic to allow the droplet to migrate freely.

3.2.3 Imposed filament polarisation

In previous analytical studies, it has been shown that contractile active fluids are unstable to splay defects. Firstly, in studies of quasi one-dimensional active gels [Voituriez et al., 2005] and semi-infinite thin films [Voituriez et al., 2006], a finite polarisation gradient and spontaneously flowing state is calculated, indicating that such a splayed polarisation field is a natural steady state in the active contractile phase. This generic splay instability in active contractile systems of filaments and motors is explained in detail in [Edwards and Yeomans, 2009] and [Ramaswamy, 2010] as due to long wavelength splay fluctuations, which perturb the balance of flow by pulling fluid along the axes of the filaments, creating a shear. This shear results in an amplification of the splay fluctuation, causing a feedback loop.

Furthermore, using lattice Boltzmann simulations of the full dynamic equations (with

the same source code as in [Tjhung et al., 2012]), we find that a 2D droplet of contractile active fluid (with no filament self-advection) is unstable to splay defects in the polarisation. The simulations use a phase field to define the active and passive phases of the fluid, as outlined in section 3.2.2. The results in 2D show that, above a certain critical value of ζ, the droplet reaches a splayed steady state, which is plotted in fig. 3.1(c). This splayed steady state is stable despite the fact that it results in vortices in the flow (fig. 3.1(d)).

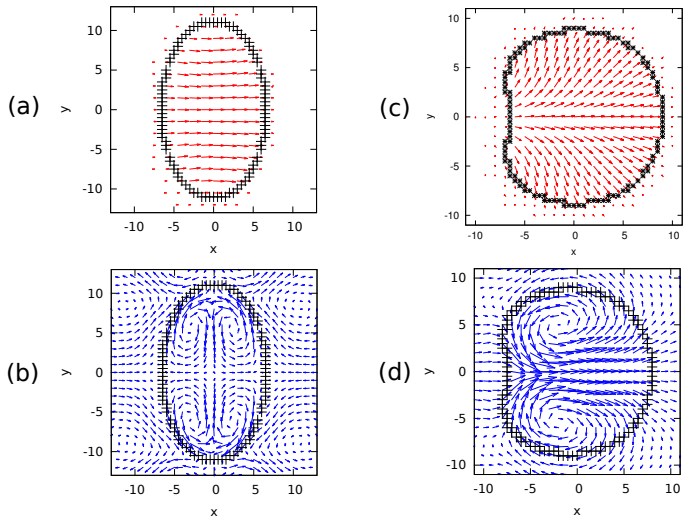

Figure 3.1: Lattice Boltzmann simulations of an active contractile droplet with the following parameter values in simulation units: $K = 0.04$, $\nu = -1.1$, $\eta = 1$, $\Gamma = 1$ and $\zeta\Delta\mu = -0.005$. Also, a higher value of surface tension was used than in [Tjhung et al., 2012]: $k_\phi = 0.3$ (see section 3.2.2). **(a)** Polarisation field before symmetry breaking. **(b)** Velocity profile before symmetry breaking. **(c)** Splayed polarisation field in motile steady state **(d)** Velocity profile of the motile steady state in the droplet reference frame. Reproduced from [Whitfield et al., 2014]

In the case of confinement in a droplet, boundary effects become important and these can promote splay in the filament polarisation depending on the specific anchoring conditions at the boundary. However, we do not consider any anchoring at the boundaries in the lattice Boltzmann simulations presented in fig. 3.1.

Based on the results of these simulations, we investigate the effects of polarisation splay in an active fluid droplet by imposing a splayed polarisation field. We then treat $\boldsymbol{p}$ as fixed in time, modelling only the steady state flow. As we are working in the $|\boldsymbol{p}| = 1$ limit, we can assume without loss of generality that $p_x = \cos(\alpha)$ and $p_y = \sin(\alpha)$ where α is the angle between the filament polarisation and the x-axis. Then, we can arbitrarily choose

a direction for the splay to occur, in this case we specify that the polarisation should splay outwards from the x-axis. The simplest example of this is if α is an anti-symmetric function of y only. If we take α to be linear in y then this choice gives the smallest change in free energy, and hence is what we might expect near to the transition from stationary to motile. Therefore we consider the polarisation:

$$\boldsymbol{p} = \cos\left(\frac{\pi c_s y}{2R}\right)\hat{\boldsymbol{x}} + \sin\left(\frac{\pi c_s y}{2R}\right)\hat{\boldsymbol{y}}\,, \tag{3.13}$$

where c_s is a unitless parameter that sets the length-scale of the polarisation deformation (see fig. 3.2). The relative amount of splay and bend in the polarisation can be calculated by finding the ratio of the magnitudes of the 'splay' and 'bend' terms in the distortion free energy (from equation (5.40)). Taking the one constant approximation $K_1 = K_2 = K_3 = K$, this ratio is:

$$\varepsilon = \frac{(\nabla\cdot\boldsymbol{p})^2}{[\boldsymbol{p}\times(\nabla\times\boldsymbol{p})]^2} = \cot^2\left(\frac{\pi c_s y}{2R}\right)\,. \tag{3.14}$$

This shows that splay is the dominant distortion everywhere ($\varepsilon > 1$) in the droplet when $c_s < 1$ and so we take this as a minimum value. Note that the 'twist' term, $[\boldsymbol{p}\cdot(\nabla\times\boldsymbol{p})]^2$, is always zero in the 2D case, only contributing in 3D. For small values of c_s we can use this parameter as an effective measure of splay in the droplet.

In [Whitfield et al., 2014] we presented the calculation in Cartesian coordinates, however with the benefit of hindsight we will present it here in polar coordinates as this makes the calculation clearer. In polar coordinates the polarisation is:

$$\boldsymbol{p} = \cos\left(\frac{\pi c_s}{2R} r\sin(\theta) - \theta\right)\hat{\boldsymbol{r}} + \sin\left(\frac{\pi c_s}{2R} r\sin(\theta) - \theta\right)\hat{\boldsymbol{\theta}} \tag{3.15}$$

For this polarisation, we calculate the molecular field

$$\boldsymbol{h} = -\left(K\frac{\pi^2 c_s^2}{4R^2} + h_\parallel^0\right)\boldsymbol{p}\,. \tag{3.16}$$

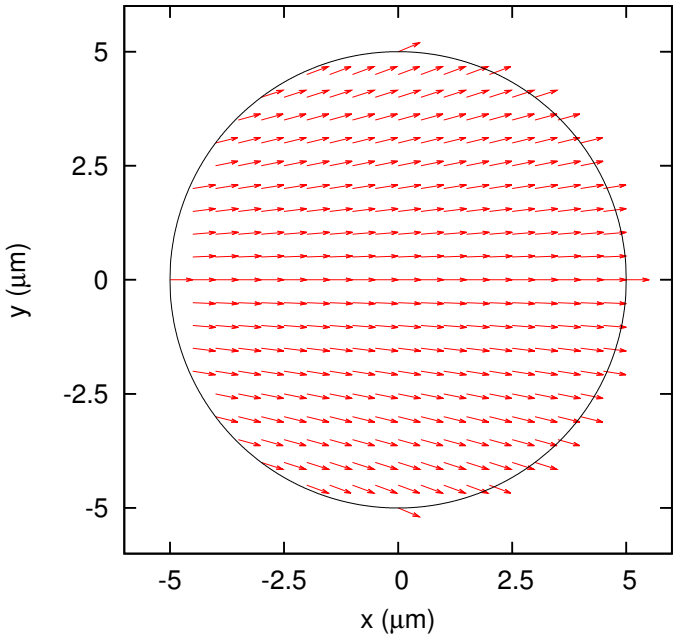

Figure 3.2: Vector plot of the polarisation field $\boldsymbol{p}$ of equation (3.13) with $c_s = 0.25$ imposed on a circular droplet of radius $R = 5\,\mu$m. Reproduced from [Whitfield et al., 2014]

In general, the Lagrange multiplier $h_\parallel^0$ is a function of space and time, and can be calculated by solving $\partial\,|\boldsymbol{p}|\,/\partial t = 0$. However, this is only possible analytically in more simplified geometries because this equation is coupled to the flow. Thus, we consider here that $h_\parallel^0$ is a constant. Substituting equations (3.15) and (3.16) into (3.1), we find the total stress in component form is

$$\sigma_{rr}^{\text{tot}} = 2\eta u_{rr} + K\frac{\pi^2 c_s^2}{8R^2}\cos(2\theta) - \nu\frac{h_\parallel^0}{2} - \frac{\tilde{\zeta}\Delta\mu}{2}\left[\cos\left(\frac{\pi c_s}{R}r\sin(\theta) - 2\theta\right) + 1\right] \tag{3.17}$$

$$\sigma_{r\theta}^{\text{tot}} = \sigma_{\theta r}^{\text{tot}} = 2\eta u_{r\theta} - K\frac{\pi^2 c_s^2}{8R^2}\sin(2\theta) - \frac{\tilde{\zeta}\Delta\mu}{2}\sin\left(\frac{\pi c_s}{R}r\sin(\theta) - 2\theta\right) \tag{3.18}$$

$$\sigma_{\theta\theta}^{\text{tot}} = -K\frac{\pi^2 c_s^2}{8R^2}\cos(2\theta) - \nu\frac{h_\parallel^0}{2} + \frac{\tilde{\zeta}\Delta\mu}{2}\left[\cos\left(\frac{\pi c_s}{R}r\sin(\theta) - 2\theta\right) - 1\right] \tag{3.19}$$

where $\tilde{\zeta}\Delta\mu = \zeta\Delta\mu - \nu K\pi^2 c_s^2/\left(4R^2\right) + \nu h_\parallel^0$. Substituting these into the force balance equations (3.6) along with the incompressibility condition (3.7) we have 3 partial differential

equations (PDEs) describing the system for the three variables v_r, v_θ and P:

$$\eta\left[\frac{\partial}{\partial r}\left(\frac{1}{r}\frac{\partial(rv_r)}{\partial r}\right)+\frac{1}{r^2}\frac{\partial^2 v_r}{\partial\theta^2}-\frac{2}{r^2}\frac{\partial v_\theta}{\partial\theta}\right]=\frac{\tilde{\zeta}\Delta\mu\pi c_s}{2R}\cos\left(\frac{\pi c_s}{R}r\sin(\theta)-\theta\right)+\frac{\partial P}{\partial r}\,, \tag{3.20}$$

$$\eta\left[\frac{\partial}{\partial r}\left(\frac{1}{r}\frac{\partial(rv_\theta)}{\partial r}\right)+\frac{1}{r^2}\frac{\partial^2 v_\theta}{\partial\theta^2}+\frac{2}{r^2}\frac{\partial v_r}{\partial\theta}\right]=\frac{\tilde{\zeta}\Delta\mu\pi c_s}{2R}\sin\left(\frac{\pi c_s}{R}r\sin(\theta)-\theta\right)+\frac{1}{r}\frac{\partial P}{\partial\theta}\,, \tag{3.21}$$

$$0=\frac{1}{r}\left[\frac{\partial\left(rv_r\right)}{\partial r}+\frac{\partial v_\theta}{\partial\theta}\right]. \tag{3.22}$$

Finally, we can express this as a single PDE using the stream function Φ defined by

$$v_r=\frac{1}{r}\frac{\partial\Phi}{\partial\theta}\qquad\text{and}\qquad v_\theta=-\frac{\partial\Phi}{\partial r}\,. \tag{3.23}$$

Then, by taking $[\partial(3.20)/\partial\theta-(1/r)\partial(r(3.21))/\partial r]$, (the numbers in brackets indicating equations) we arrive at the inhomogeneous biharmonic equation:

$$\left(\nabla^2\right)^2\Phi(r,\theta)=-\frac{\tilde{\zeta}\Delta\mu}{2\eta}\left(\frac{\pi c_s}{R}\right)^2\sin\left(\frac{\pi c_s}{R}r\sin(\theta)\right)\,. \tag{3.24}$$

A partial solution to this equation is

$$\Phi_{\text{par}}=-\frac{\tilde{\zeta}\Delta\mu}{2\eta}\left(\frac{R}{\pi c_s}\right)^2\sin\left(\frac{\pi c_s}{R}r\sin(\theta)\right)\,. \tag{3.25}$$

We see that this solution leads to non-physical flows for $c_s=0$, which physically should be cancelled out by the boundary conditions (which will be introduced in section 3.2.4). We find that we cannot explicitly write equation (3.25) as an infinite sum of increasing modes of $\sin(\theta)$, however we can write the full solution generally in integral form:

$$\Phi=\sum_{k=1}^{\infty}\left(f_k(r)+a_k r^{k+2}+b_k r^k\right)\sin(k\theta) \tag{3.26}$$

$$\text{where}\quad f_k(r)=-\frac{\tilde{\zeta}\Delta\mu}{2\pi\eta}\left(\frac{R}{\pi c_s}\right)^2\int_0^{2\pi}\sin\left(\frac{\pi c_s}{R}r\sin(\theta)\right)\sin(k\theta)\mathrm{d}\theta\,, \tag{3.27}$$

where the terms multiplied by the constants a_k and b_k represent the general solution in polar coordinates to the homogeneous biharmonic equation. We have omitted the

contributions to the general solutions with r^{-k} and r^{-k+2} dependencies as these give infinite flows at the origin. In addition, we have dropped general solutions proportional to $\cos(k\theta)$ by symmetry.

3.2.4 Boundary conditions

We confine the solutions to a fixed circular droplet with the following boundary conditions:

$$v_r(R,\theta) = 0\,, \tag{3.28}$$

$$\sigma_{r\theta}(R,\theta) = -\xi v_\theta(R,\theta)\,. \tag{3.29}$$

Equation (3.28) ensures that there is no fluid entering or leaving the droplet and equation (3.29) applies an effective viscous friction at the boundary (with friction coefficient ξ). This friction condition is general as it infers little about the external medium, only that it will create some linear resistance to flow at the interface. If the droplet is embedded in a solid, then ξ will determine the slip between the fluid and the boundary. Alternatively, if the external medium is a viscous fluid, and we assume non-slip between the internal and external fluid, then the friction coefficient ξ will be related to the viscosity of the external fluid. Therefore we call ξ the *effective* friction coefficient. It is important to note that in a biological context the conditions at the cell boundary would be more complicated, depending also on the adhesion between the membrane and the surrounding environment, the elastic/viscoelastic properties of the external medium and the active processes of the membrane itself. Including these effects would require more general boundary conditions that could be space and/or time dependant and in general would invalidate the assumption of a fixed boundary.

The boundary conditions equations (3.28) and (3.29) are distinctly different from those used in lattice Boltzmann simulations of an active contractile droplet (as used to obtain fig. 3.1; and introduced in [Tjhung et al., 2012]). In these simulations, a phase field parameter is used to discern between the active and passive phases of the fluid, and this parameter is advected with the fluid velocity. Therefore the shape of the droplet is coupled to the flow,

however the boundary between the two phases is diffuse and is defined by the gradient of the phase field. This also means that the external fluid in the simulations is assumed to have the same passive properties as the droplet. We also compute the flow in the specific case of the drop immersed in a Newtonian fluid medium in section 3.2.6 to show how these relate.

Applying the boundary conditions in equations (3.28) and (3.29) for the stream function in equation (3.26), we find that:

$$a_k = -\frac{R^{-(k+2)}}{2(\xi R + 2k\eta)}\left[R^2\eta f_k''(R) + R(\xi R - \eta)f_k'(R) - k(\xi R + (k-2)\eta)f_k(R) - R^2 g_k(R)\right] \tag{3.30}$$

$$b_k = \frac{R^{-k}}{2(\xi R + 2k\eta)}\left[R^2\eta f_k''(R) + R(\xi R - \eta)f_k'(R) - (k+2)(\xi R + k\eta)f_k(R) - R^2 g_k(R)\right] \tag{3.31}$$

$$\text{where} \quad g_k(r) = \frac{1}{2\pi}\int_0^{2\pi} \tilde{\zeta}\Delta\mu \sin\left(2\theta - \frac{\pi c_s r \sin\theta)}{R}\right)\sin(k\theta)\mathrm{d}\theta - K\frac{\pi^3 c_s^2}{8R^2}\delta_{2,k}\,. \tag{3.32}$$

In order to approximate the flows and forces analytically, in the next section we expand these solutions for leading orders of c_s, which is valid in the small distortion limit of $c_s \ll 1$.

3.2.5 Approximation of Steady State Flow and Pressure

In the limit $c_s \ll 1$ bend deformations are negligible relative to splay, and the partial stream function solution (from equation (3.25)) to third order in c_s is:

$$\begin{aligned}\Phi_{\text{par,s}} = &-\frac{\tilde{\zeta}\Delta\mu r^2}{\eta}\left\{\frac{R}{2\pi c_s r}\left[1 - \frac{1}{8}\left(\frac{\pi c_s r}{R}\right)^2 + \frac{1}{384}\left(\frac{\pi c_s r}{R}\right)^4\right]\sin(\theta)\right. \\ &\left. + r^2\frac{\pi c_s r}{48R}\left[1 - \frac{1}{16}\left(\frac{\pi c_s r}{R}\right)^2\right]\sin(3\theta) + \frac{1}{3840}\left(\frac{\pi c_s r}{R}\right)^3\sin(5\theta)\right\} + O(c_s^4)\,.\end{aligned} \tag{3.33}$$

To account for larger values of c_s, we are able to solve for Taylor series of arbitrarily high order, as discussed in section 3.2.5. In this small c_s limit, we can assume that the distortion contributions to the stress and flow equations should be small compared to the active contribution and hence $\tilde{\zeta} < 0$ regardless of the value of ν.

We can then satisfy the boundary conditions for each mode separately so that the solutions are consistent to the order we have expanded to. These algebraic solutions are lengthy and can be found in appendix 3.A. We see from the boundary condition equations that to third order in c_s the coefficients $a_k = b_k = 0$ if $k > 5$. This maximum mode increases by 1 for each extra order of c_s included.

As expected, the leading order term in c_s, proportional to $1/c_s$, vanishes and hence the flow does not diverge at small c_s. We also check that these approximate solutions satisfy the original PDE to the correct order such that:

$$\left(\nabla^2\right)^2 \Phi(r,\theta) = -\frac{\tilde{\zeta}\Delta\mu}{2\eta}\left(\frac{\pi c_s}{R}\right)^3 r\sin(\theta) + O\left(c_s^5\right) . \tag{3.34}$$

Note that the leading order term in this equation is proportional to c_s^3 and hence the lower order terms in the solution for Φ_s (equation (3.64)) are generated at the boundary. This means that, in the approximation of small c_s the polarisation direction at the boundary determines the flow, unless the friction coefficient is large (see section 3.3.2).

The pressure P can be calculated by substituting the flow solutions back into the force balance equation (3.21). We also give the full expression for this in appendix 3.A equation (3.66). This pressure is only defined to a constant P_0, which ensures area conservation (volume conservation in 3D) of the droplet via force balance at the interface. If we assume an average external pressure of P_0^{ext} then P_0 can be determined by Laplace's law:

$$\oint f_r(R,\theta)\mathrm{d}\theta \equiv \oint \left[\sigma_{rr}^{\text{tot}} - P - P_0^{\text{ext}} - \frac{\gamma}{R}\right]\mathrm{d}\theta\Big|_{\text{r=R}} = 0\,, \tag{3.35}$$

where γ is the surface tension of the droplet. Solving equation (3.35) for P_0 gives

$$P_0 = \frac{\gamma}{R} + P_{\text{ext}}^0 - \frac{\tilde{\zeta}\Delta\mu}{2}\left(1 + \frac{(\pi c_s)^2}{8}\right) + \frac{h_{\|}^0}{2}\,. \tag{3.36}$$

3.2.6 External fluid boundary conditions

By changing the boundary conditions in section 3.2.4 we can consider the flow in the case where the droplet is immersed in a fluid. In this case, rather than a condition of no flow across the boundary, we set a condition of flow continuity. Further, rather than a friction condition we use a force balance condition at the interface. These conditions read:

$$\boldsymbol{v}(R,\theta) = \boldsymbol{v}^{\text{ext}}(R,\theta)\,, \tag{3.37}$$

$$\sigma_{rr}^{\text{tot}} - P + P^{\text{ext}} + \frac{\gamma}{R} = 2\eta_1 u_{rr}^{\text{ext}}\,, \tag{3.38}$$

$$\sigma_{r\theta}^{\text{tot}} = 2\eta_1 u_{r\theta}^{\text{ext}}\,, \tag{3.39}$$

where η_1 is the viscosity of the external fluid. In order to satisfy these conditions, we require expressions for the flow in the external fluid. These can be found by assuming that the flow obeys the incompressible Stokes' equation (with no external forces). Then the general solutions in polar coordinates (in terms of the stream function) are:

$$\Phi^{\text{ext}} = \sum_{k=1}^{\infty} \left[a_k^* r^{-k+2} + b_k^* r^{-k}\right] \sin(k\theta)\,. \tag{3.40}$$

We now have 4 constants to solve for each value of k, and 4 boundary conditions. We solve these boundary conditions simultaneously for each order of k and find again that all constants are zero for orders of $k > 5$, if we expand terms up to third order in c_s. We also set $b_1^* = 0$, as this is equivalent to the velocity of the external fluid in the limit $r \to \infty$. The full flow solutions are given in appendix 3.A (equations (3.67) and (3.68)) and are plotted in figure 3.6.

In the actual droplet steady state, forces at the boundary would be balanced and there would be no flow normal to the interface. However, because we have assumed a circular droplet, the normal flow here shows how the droplet shape would change in order for the surface tension force to cancel it out. Similarly, in the previous case where we set $v_r = 0$ at the boundary, the forces at the interface are not balanced (see the analysis in section 3.3.3). Hence, as mentioned previously, these calculations are only a good estimate if the

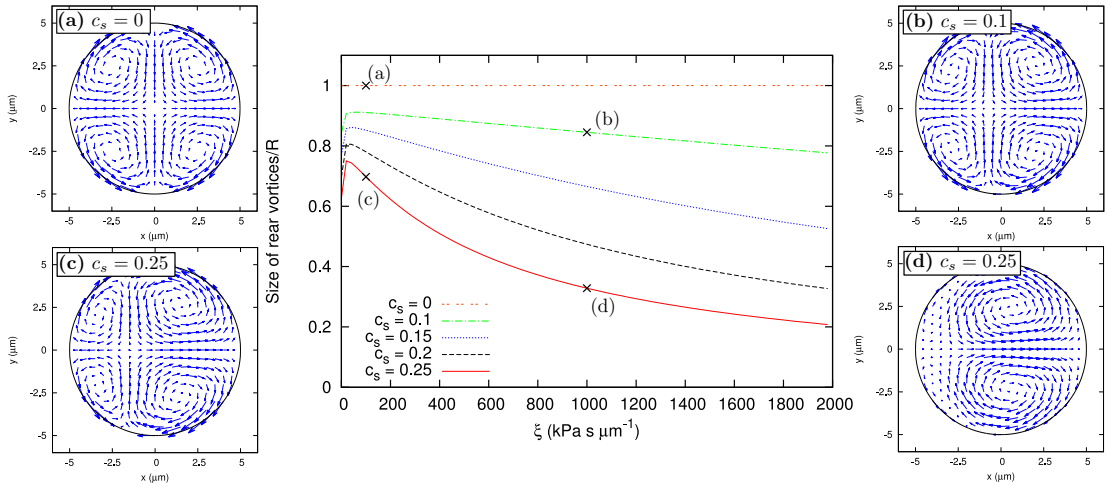

Figure 3.3: Graph of the width of the two rear vortices in the droplet against the effective friction coefficient ξ, plotted for various values of the splay parameter c_s. Other parameter values are $\tilde{\zeta}\Delta\mu = -1\,\mathrm{kPa}$ [Kruse et al., 2006], $K = 1\,\mathrm{kPa}\,\mu\mathrm{m}^2$, $R = 5\,\mu\mathrm{m}$, and $\eta = 10\,\mathrm{kPa\,s}$ [Wottawah et al., 2005]. Corresponding flow profiles at the points labelled **(a)**, **(b)**, **(c)**, and **(d)** are also shown. For these, the velocity arrow lengths are scaled independently for visibility by a scale factor S such that a velocity magnitude of v corresponds to an arrow length of Sv. The values of S for each plot are: **(a)** and **(b)** $S = 300$, **(c)** $S = 3000$, and **(d)** $S = 1200$. Reproduced from [Whitfield et al., 2014].

surface tension is very large, and hence small deformations to the boundary would cancel out the forces acting on it.

3.3 Results and Analysis

3.3.1 Flow at zero splay

Figure 3.3 shows profiles of the velocity $\boldsymbol{v}$ for different values of the effective friction coefficient ξ and the splay parameter c_s. The velocity profile generally has 2 pairs of opposing vortices for lower values of ξ and c_s, and as ξ or c_s is increased (the upper limit of c_s is bound by the third order approximation in c_s) the front pair of vortices occupy more of the droplet. In the limit of zero splay, $c_s \to 0$ for fixed R, the vortices become completely symmetric and the solutions are (plotted in figure 3.3(a)):

$$\boldsymbol{v} = \frac{\tilde{\zeta}\Delta\mu r}{2R^2(R\xi + 4\eta)}\left[-\left(R^2 - r^2\right)\cos(2\theta)\hat{\boldsymbol{r}} + \left(R^2 - 2r^2\right)\sin(2\theta)\hat{\boldsymbol{\theta}}\right] \tag{3.41}$$

The source of the flow in this case is the remaining active terms in the boundary condition equation (3.29), since in this limit there are no active terms present in the force balance equations (3.20) and (3.21). This shows that even when the polarisation field is completely aligned, the confinement of the active fluid to a droplet results in a flow (see fig. 3.3(a)), which is not found in studies of bulk active fluids. This observation is in agreement with the lattice Boltzmann simulations of a droplet prior to symmetry breaking, which maintains an (approximately) aligned polarisation field (figures 3.1(a) and (b)). Therefore the splay directly imposes the preferred direction in the flow, and hence the asymmetry of the vortices increases with c_s. The rear vortices only completely disappear mathematically in the infinite friction limit $\xi \to \infty$, because this destroys the boundary effects that induce the symmetric part of the flow.

We can measure this asymmetry by finding the turning point where $\boldsymbol{v} = 0$ along $y = 0$. This equates to solving a sixth order polynomial in x, which we solve numerically for various of c_s and ξ. The results are plotted in 3.3 where the *size* of the rear vortices refers to the distance of the turning point relative to $x = -R$.

3.3.2 Non-slip solutions

In the limit of infinite friction, the boundary condition in equation (3.29) becomes $v_\theta(R, \theta) = 0$. This means that the stress at the boundary does not contribute to the flow, and (in the approximation of small c_s) only the coefficients a_1 and b_1 are non-zero. Hence, the flow profile is given simply by

$$\boldsymbol{v} = \frac{\tilde{\zeta}\Delta\mu}{384\eta}\left(\frac{\pi c_s}{R}\right)^3 (R^2 - r^2)\left[-(R^2 - r^2)\cos(\theta)\hat{\boldsymbol{r}} + (R^2 - 5r^2)\sin(\theta)\hat{\boldsymbol{\theta}}\right]. \tag{3.42}$$

This flow is plotted in figure 3.5(a).

3.3.3 Force moment analysis and migration speed

Figure 3.4 plots the pressure difference inside the droplet for the same parameters as used in fig. 3.3(b). It shows that the variation in pressure across the boundary is

approximately 1 kPa with these estimated values. This means that, for our fixed boundary approximation to be valid, $\gamma/R \gg 1\,\mathrm{kPa}$ meaning that $\gamma \gg 5\,\mathrm{kPa}\,\mu\mathrm{m}$. For comparison, experimental evidence suggests that the effective cell membrane tension (the combination of the bare membrane tension and the cortex tension) is $\gamma \approx 0.3\,\mathrm{kPa}\,\mu\mathrm{m}$ [Thoumine et al., 1999, Dai and Sheetz, 1999]. Thus, the high surface tension limit assumed in this calculation is not valid for the majority of cells or vesicles. However, emulsion droplets in water and oil generally have a much higher surface tension, so this may be a good approximation for *in vitro* experiments on cytoskeleton networks confined to or on droplets (*e.g.* [Sanchez et al., 2012]).

The solutions simplify greatly in the infinite friction limit $\xi \to \infty$, which is equivalent to applying the non-slip boundary condition, $v_\theta = 0$ at $r = R$. Therefore, in this section we use these solutions to clarify the analysis and to keep the resulting equations brief. This analysis does generalise to the finite friction case, and we show how the results depend on the friction graphically. The force density on the interface (as used in equation (3.35)) is

$$f_j = \hat{r}_i \cdot \left[\left(P - P^0_{\mathrm{ext}} - \frac{\gamma}{R} \right) \delta_{ij} - \sigma^{\mathrm{tot}}_{ij} \right] . \tag{3.43}$$

Then, the total force (note in 2D this still has units of force per unit length as it is implicitly averaged over the third dimension) on the droplet is

$$F^{(1)}_i = \int_0^{2\pi} f_i R \mathrm{d}\theta = 0. \tag{3.44}$$

This force is zero for $i = x, y$ as expected at low Reynolds' number. However, it can be shown that there is spatial separation of the equal and opposite forces at the droplet boundary. We show this by taking successive moments of the force at the boundary. As for the force monopole (equation (3.44)), increasing moments of the force can be expressed by tensors of increasing order, the dipole and quadrupole moments form the following

second and third order tensors respectively:

$$F_{ij}^{(2)} = \int_0^{2\pi} f_i r_j R \, \mathrm{d}\theta \,, \tag{3.45}$$

$$F_{ijk}^{(3)} = \int_0^{2\pi} f_i r_j r_k R \, \mathrm{d}\theta \,. \tag{3.46}$$

The dipole moment gives:

$$F_{ij}^{(2)} = F_0 \left(\delta_{ix}\delta_{jx} - \delta_{iy}\delta_{jy}\right) \tag{3.47}$$
$$\text{where} \quad F_0 = \frac{\tilde{\zeta}\Delta\mu\pi R^2}{2}\left(1 - \frac{(\pi c_s)^2}{8}\right) - \frac{K\pi^3 c_s^2}{8} \,.$$

The coefficient F_0 is always negative (in the finite friction case too) and hence the droplet is contractile along the x-axis and equally extensile along the y-axis. This force dipole is due to the alignment and contraction of the filaments along the x-axis, and this can be shown by taking the limit of zero splay, $c_s \to 0$, where all of the filaments in the droplet are completely aligned. In this limit the dipole moment is maximised, and this explains the behaviour observed in the lattice Boltzmann simulations of an active droplet that is below the threshold concentration of activity to break symmetry. In those simulations, the filaments remain approximately aligned in one direction and the droplet squeezes itself, shortening in the direction of alignment and extending in the perpendicular direction (fig. 3.1(a)) [Tjhung et al., 2012].

For a circular droplet at low Reynolds' number, a non-zero force dipole distribution is insufficient for motion [Yoshinaga, 2014] and in this case it does not vanish in the symmetric limit $c_s \to 0$. However, the quadrupole moment is directly dependent on the symmetry breaking,

$$F_{ijk}^{(3)} = F_1 \left(-\delta_{ix}\delta_{jx}\delta_{kx} + \delta_{ix}\delta_{jy}\delta_{ky}\right) + F_2\delta_{iy}\delta_{jx}\delta_{ky} \tag{3.48}$$
$$\text{where} \quad F_1 = \frac{\tilde{\zeta}\Delta\mu\pi^2 R^3 c_s}{4} + O\left(c_s^3\right) \quad \text{and} \quad F_2 = 0 \,.$$

Note that the F_2 parameter is non-zero in the finite friction case. In the non-slip case the forces that make up the quadrupole moment only act in the x-direction (shown by the non-zero components of the quadrupole tensor both having $i = x$). It shows that the net normal forces at the front and back of the droplet act in the positive x direction (as $F_1 < 0$) and the shear forces at the sides are equal and opposite, as sketched in fig. 3.5(a). In the no-splay limit, $c_s \to 0$, the quadrupole moment disappears along with the asymmetry in x.

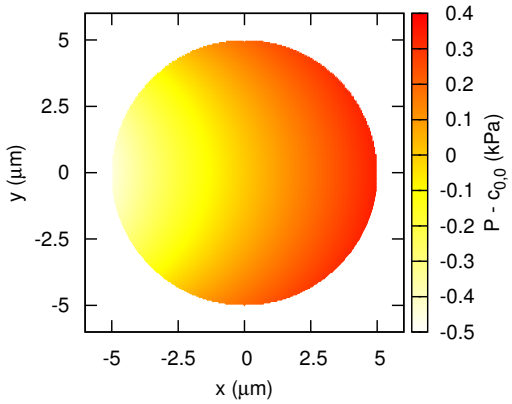

Figure 3.4: Relative pressure inside the droplet for $\xi = 100\,\mathrm{kPa\,s\,\mu m^{-1}}$. Other parameter values are $\tilde{\zeta}\Delta\mu = -1\,\mathrm{kPa}$, $K = 1\,\mathrm{kPa\,\mu m^2}$, $R = 5\,\mu\mathrm{m}$, $\eta = 10\,\mathrm{kPa\,s}$, and $c_s = 0.25$. Reproduced from [Whitfield et al., 2014].

The quadrupole moment characterises the motility mechanism because of the force distribution it indicates. The shear forces at the sides of the droplet arise from the friction between the fluid and the external medium and hence act to propel the droplet forwards (or the medium rearwards in the droplet rest frame). The normal forces however act to deform the front and back of the droplet asymmetrically in the positive x-direction. The magnitude of these shear and normal forces can be calculated by integrating the corresponding elements of the total stress tensor at the boundary,

$$\boldsymbol{F}^{(\mathrm{norm})} = -\int_0^{2\pi} f_r \boldsymbol{r}\,\mathrm{d}\theta\,\Big|_{r=R} \quad \text{where } i \neq j\,, \tag{3.49}$$

$$\boldsymbol{F}^{(\mathrm{shear})} = -\int_0^{2\pi} f_\theta r\hat{\boldsymbol{\theta}}\,\mathrm{d}\theta\,\Big|_{r=R}\,. \tag{3.50}$$

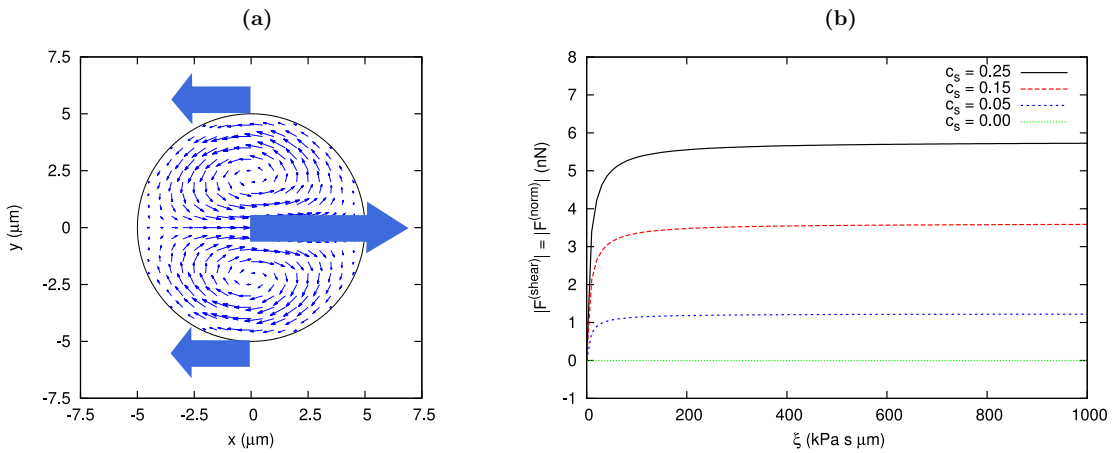

Figure 3.5: **(a)** Sketch of the droplet motility mechanism in 2D. The large arrows represent the spatially separated forces exerted by the active droplet on a surrounding medium, where the central arrow is the sum of the normal forces in the x-direction and the arrows at the top and bottom each contribute half of the total shear force in the x-direction. The smaller arrows show the flow profile of the motile droplet in the case of a solid non-slip boundary. **(b)** Magnitude of the shear and normal forces (which are equal and opposite) plotted against the effective friction coefficient ξ for several values of the splay parameter c_s. Note that in the no-splay case these forces are zero, as is the quadrupole moment. Parameter values used are $R = 5\,\mu$m, $\eta = 10\,$kPa s and $\tilde{\zeta}\Delta\mu = -1\,$kPa. Reproduced from [Whitfield et al., 2014].

These forces only act in the x direction and, for the case of finite friction is given by

$$F_x^{(\text{shear})} = -F_x^{(\text{norm})} = \frac{1}{4}\frac{\tilde{\zeta}\Delta\mu c_s \pi^2 R\xi}{R\xi + 2\,\eta} + O(c_s^3) \tag{3.51}$$

As one would expect there is no force generated at zero friction, and the force plateaus for large values of ξ. In the infinite friction limit, they are given by

$$\lim_{\xi\to\infty} F_x^{(\text{shear})} = -\lim_{\xi\to\infty} F_x^{(\text{norm})} = \frac{\tilde{\zeta}\Delta\mu\pi^2 R c_s}{2} + O\left(c_s^3\right). \tag{3.52}$$

and shows that the magnitude of the forces plateaus at large friction, with the maximum at the infinite friction limit given by equation (3.52).

It is useful to compare this analysis to the calculation of an active fluid droplet immersed in a external fluid from section 3.2.6 (see figure 3.6). In this case the forces on the boundary are balanced by the boundary conditions, and hence it is the velocity distribution at the interface that is interesting. As mentioned, in the true steady state,

the droplet shape would deform in order that the forces and velocities balance at the interface and (subject to reference frame) these two solutions would converge for the correct parameters. We can describe the initial deformation of the droplet immersed in an external fluid by the fluid velocity normal to the interface $v_n = v_r(R, \theta)$. The different modes of this velocity correspond to different modes of deformation, which will be discussed in detail in Chapter 5. The first (normalised) mode we consider corresponds to the droplet centre of mass velocity:

$$\boldsymbol{V} = \frac{1}{2\pi}\int_0^{2\pi} v_n \hat{\boldsymbol{r}} \mathrm{d}\theta = \left[-\frac{\tilde{\zeta}\Delta\mu\pi c_s R}{32(\eta+\eta_1)} + O(c_s^3)\right]\hat{\boldsymbol{x}} \tag{3.53}$$

which clearly shows motion in the positive x-direction for leading order c_s and contractile activity.

Relating this to the graph in fig. 3.5(b) we see that while a high friction with an external medium allows maximum force generation, the droplet will move most quickly through a low viscosity medium, as one would expect. It should be noted that in the limit $\eta_1 \to \infty$ the flow field is identical to the $\xi \to \infty$ and the droplet cannot move.

To summarise, the dipole moment shows that this droplet behaves like a *puller* (contractile along axis of motion) [Ramaswamy, 2010], however this is not sufficient for motility in this case. It is the quadrupole moment that characterises the motility mechanism and symmetry breaking in our system, and the resulting picture resembles the motility mechanism of a *squirmer* (a particle propelled by coordinated beating of cilia on its surface) [Blake, 1971].

3.3.4 3D generalisation

In ref. [Tjhung et al., 2012], it is found through lattice Boltzmann simulations of the dynamic equations that in 3D, as in 2D, above a certain activity threshold the system stabilises to a splayed steady motile state. However, this motile state becomes unstable at a second higher activity threshold, above which a non-motile aster configuration becomes

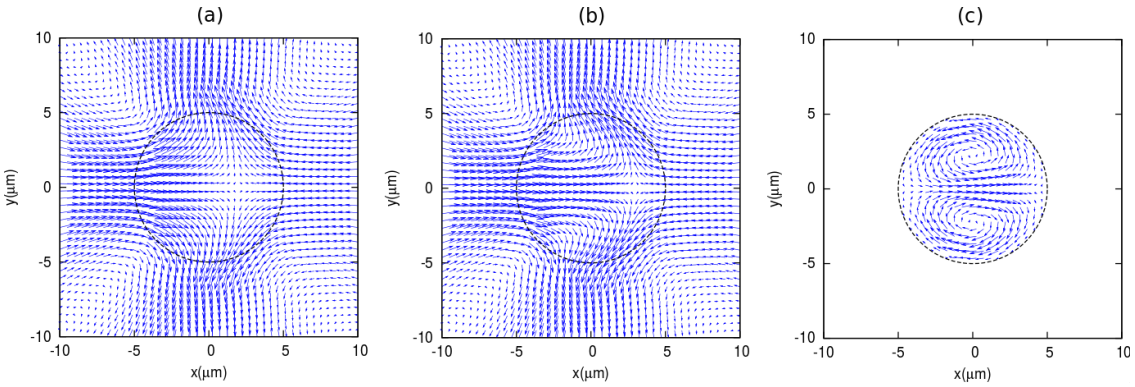

Figure 3.6: Flow field for a droplet immersed in an external fluid for increasing values of external viscosity: **(a)** $\eta_1 = \eta$, **(b)** $\eta_1 = 100\eta$, **(c)** $\eta_1 \to \infty$. Other parameters used are $c_s = 0.25$, $\zeta\Delta\mu = -1$k Pa, $K = 0$, $\eta = 10$k Pa s and $R = 5\mu$m. The velocity vectors are scaled for visibility.

stable. Therefore, to model the system in 3D, we consider that the activity is between these two thresholds.

By applying appropriate symmetry rules, the calculation for the motile splayed state can be easily extended to 3D for the case of a spherical droplet with radius R and centre at $r = 0$. If we assume that the polarisation is now splayed around the z-axis uniformly (for convenience using spherical coordinates) then the polarisation can still be written $\boldsymbol{p} = \cos(\beta)\hat{\boldsymbol{r}} + \sin(\beta)\hat{\boldsymbol{\theta}}$ where now $r = \sqrt{x^2 + y^2 + z^2}$ is the radial distance in 3D and θ is the angle that $\boldsymbol{r}$ makes with the z-axis such that $\theta = \{0 : \pi\}$. The angle β is

$$\beta = \frac{\pi c_s}{2R} r \sin(\theta) - \theta \,. \tag{3.54}$$

This means, taking a slice through the z-axis for any value of the azimuthal angle φ the polarisation will look the same as the 2D case. In order to see this more clearly, this polarisation in Cartesian coordinates is:

$$\boldsymbol{p} = \frac{x}{\rho} \sin\left(\frac{\pi c_s}{2R}\rho\right) \hat{\boldsymbol{x}} + \frac{y}{\rho} \sin\left(\frac{\pi c_s}{2R}\rho\right) \hat{\boldsymbol{y}} + \cos\left(\frac{\pi c_s}{2R}\rho\right) \hat{\boldsymbol{z}} \,, \tag{3.55}$$

where $\rho = \sqrt{x^2 + y^2}$ is the projection of the radial distance in the x-y plane. Using this polarisation we find that there is no force contribution in the φ direction, and that there is no φ dependence, thus we argue that the flow field can be given by $\boldsymbol{v} = v_r(r, \theta)\hat{\boldsymbol{r}} + v_\theta(r, \theta)\hat{\boldsymbol{\theta}}$.

Thus we can yet again reduce the problem to 3 partial differential equations (which are too long to be meaningful written in full). In 3D it is easier to work in terms of velocities than a stream function at this point. However it is still useful to take the curl of the force balance equations so that we are left with only 2 PDEs, which to third order in c_s read:

$$-\left[\nabla\times\left(\nabla^2\boldsymbol{v}\right)\right]\cdot\hat{\boldsymbol{\varphi}}=-\frac{2}{3}\zeta'\Delta\mu\left(\frac{\pi c_s}{R}\right)^3 r\sin(\theta) \tag{3.56}$$

$$\nabla\cdot\boldsymbol{v}=0\,, \tag{3.57}$$

where $\zeta'\Delta\mu=\zeta\Delta\mu-\nu h_{\parallel}^0$. If we first consider the inhomogeneous contribution to the solutions, we see from equation (3.56) that we can write $\boldsymbol{v}^{\text{inh}}=a(r)\cos(\theta)\hat{\boldsymbol{r}}+b(r)\sin(\theta)\hat{\boldsymbol{\theta}}$. Then solving these equations as simultaneous ODEs for $a(r)$ and $b(r)$ gives:

$$\boldsymbol{v}^{\text{inh}}=\frac{\zeta'\Delta\mu r^4}{210}\left(\frac{\pi c_s}{R}\right)^3\left[-\cos(\theta)\hat{\boldsymbol{r}}+3\sin(\theta)\hat{\boldsymbol{\theta}}\right]. \tag{3.58}$$

Thus we can then add the general solutions for flow inside a sphere (known as Lamb's solutions [Lamb, 1945]) in the case of no φ dependence to give the full solutions:

$$\boldsymbol{v}=\boldsymbol{v}^{\text{inh}}+\sum_{l=1}^{\infty}\left[\left(a_l r^{l+1}+b_l r^{l-1}\right)Y_0^l(\theta)\hat{\boldsymbol{r}}+\frac{1}{l(l+1)}\left(a_l(l+3)r^{l+1}+b_l(l+1)r^{l-1}\right)\left(\partial_\theta Y_0^l(\theta)\right)\hat{\boldsymbol{\theta}}\right], \tag{3.59}$$

where $Y_0^l(\theta)$ is the spherical harmonic function where the index $m=0$ indicating no φ dependence. Expanding the tangential stress $\sigma_{r\theta}^{\text{tot}}$ to third order in c_s we can once again apply the boundary conditions from equations (3.28) and (3.29) to define the coefficients a_l and b_l. We find that for this approximation $a_l=b_l=0$ if $l>5$. The full solutions are plotted for example cases in figure 3.7. Once again we find that, for $c_s=0$ there are four vortices in the flow:

$$\boldsymbol{v}\Big|_{c_s=0}=\frac{\zeta'\Delta\mu r}{4R^2(R\xi+5\eta)}\left[-(R^2-r^2)(1+3\cos(2\theta))\hat{\boldsymbol{r}}+(3R^2-5r^2)\sin(2\theta)\right]. \tag{3.60}$$

Plus the non-slip case also provides simple two-vortices solutions:

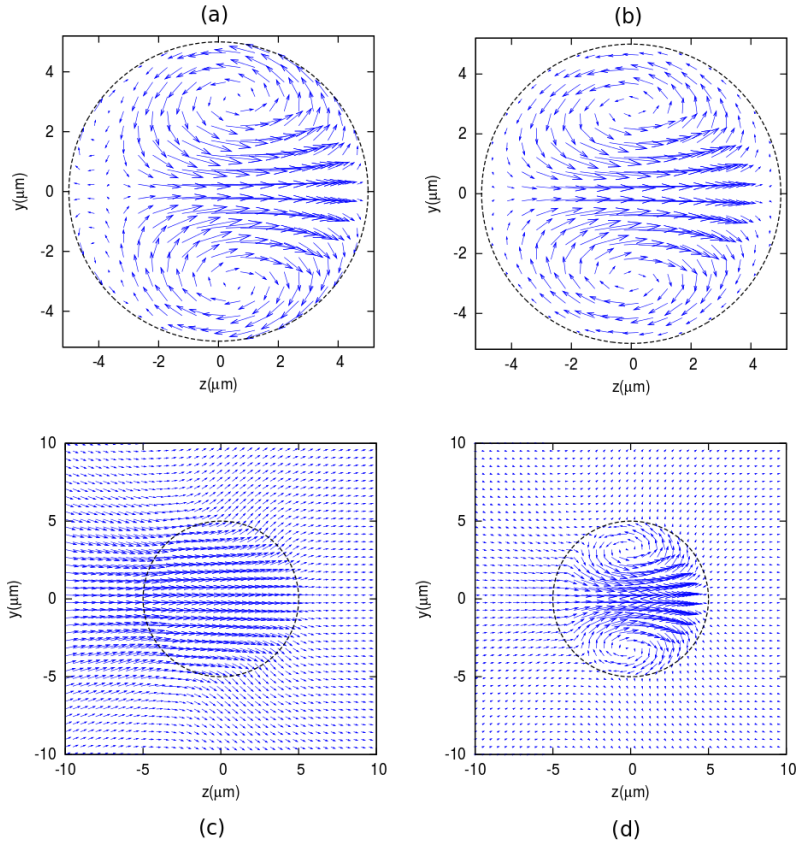

Figure 3.7: Vector plots of the 3D flow profile in the y-z plane. Figures **(a)** and **(b)** show the flow in the droplet with an impermeable boundary for friction coefficients of $\xi = 100$k Pa sμm and $\xi \to \infty$ respectively. Figures **(c)** $\eta_1 = \eta$ and **(d)** $\eta_1 = 100\eta$ show the flow profile if the droplet is immersed in an external fluid. The splay parameter $c_s = 0.25$ in all plots and all other parameters are the same as figure 3.3

.

$$\lim_{\xi\to\infty} \boldsymbol{v} = \frac{\zeta'\Delta\mu}{210}\left(\frac{\pi c_s}{R}\right)^3 (R^2 - r^2)\left[-(R^2 - r^2)\cos(\theta)\hat{\boldsymbol{r}} + (R^2 - 3r^2)\sin(\theta)\hat{\boldsymbol{\theta}}\right] . \quad (3.61)$$

We can also solve the equations of motion using an external fluid boundary condition, as in the 2D case. The general solutions for the (φ independent) flow of the external fluid are

$$\boldsymbol{v}^{\text{ext}} = \sum_{l=1}^{\infty}\left[\left(a_l^* r^{-l} + b_l^* r^{-l-2}\right) Y_0^l(\theta)\hat{\boldsymbol{r}} - \frac{1}{l(l+1)}\left(a_l^*(l-2)r^{-l} + b_l^* l r^{-l-2}\right)\partial_\theta Y_0^l(\theta)\hat{\boldsymbol{\theta}}\right] . \quad (3.62)$$

The boundary conditions to solve in this case are the same as those in section 3.2.6. From

this we can calculate the centre of mass velocity of the 3D droplet in an external fluid:

$$\boldsymbol{V}^{3\mathrm{D}} = \frac{1}{4\pi}\int_0^{2\pi}\int_0^{\pi} v_r\hat{\boldsymbol{r}}\sin(\theta)\mathrm{d}\theta\mathrm{d}\varphi = \left[-\frac{\zeta'\Delta\mu\pi c_s R}{15(3\eta+2\eta_1)} + O(c_s^2)\right]\hat{\boldsymbol{z}} \tag{3.63}$$

3.4 Summary and Conclusions

The model we have presented here demonstrates analytically how self-propelled motion can be generated in a finite active polar droplet, purely by the internal circulation of material driven by active contractile stresses. By imposing an asymmetric splayed polarisation on the droplet, we have analytically calculated the hydrodynamic steady state of the system. The resulting internal fluid flow coupled with a viscous interaction at the boundary causes a non-zero force quadrupole and leads to self-propulsion of the droplet.

In addition, our model predicts flow in the droplet even when the filaments are completely aligned and the droplet is not motile, which is also seen in simulations. In this limit the filament alignment results in a symmetric force dipole moment, which is responsible for the 'squashing' of the droplet that is seen in simulations, prior to the development of splay instabilities [Tjhung et al., 2012], but does not result in overall motility of the droplet.

Our model shows that according to the friction at the boundary and the amount of splay, the intra-droplet flow can undergo transitions between several different patterns. For infinite friction, we observe a transition from zero flow in the no-splay limit to 2 directed vortices for finite splay. In the finite friction case, we observe a transition from 4 symmetric vortices in the no-splay limit to 4 asymmetric vortices for finite splay. This means that for finite splay there is a transition from 4 asymmetric vortices to 2 vortices as the friction goes to infinity. The 4 symmetric vortices are due to the interaction between the active gel and the boundary and consequently the flow is zero in the infinite friction limit due to the boundary condition $v_\theta(R,\theta) = 0$. The 2 directed vortices are generated by the active stress due to the splay. The 4 asymmetric vortices are a combination of these two effects.

Our results predict and explain both the non-motile and motile states observed in lattice Boltzmann simulations of active contractile droplets [Tjhung et al., 2012]. Importantly, as we consider a confined active fluid and control the flow field at the boundary, our calculations can extend those of [Tjhung et al., 2012] to the case of a more general external medium that can be applied to more biologically relevant cases.

Previous theoretical studies using a coarse grained hydrodynamic approach on active gels in bulk and confinement have predicted individual vortices in the flow due to rotationally invariant filament polarisations [Kruse et al., 2004, Woodhouse and Goldstein, 2012]. Similar aster and vortex type defects in the filament orientation have been observed to self-organise [Aranson and Tsimring, 2006] and rotate [Nédélec, 2002, Head et al., 2011] in discrete microscopic models and also experimentally for microtubule filaments [Nédélec et al., 1997, Surrey et al., 2001]. An important distinction of our model is that the pairs of directed vortices we predict only form in confinement. Experimentally probing *in vitro* active gels in confinement is now becoming feasible due to new techniques. Recent examples include confinement of active microtubule-kinesin networks inside micro-chambers [Laan et al., 2012] to measure the forces exerted in these systems and inside fluid droplets in emulsions of water and oil using microfluidic devices [Sanchez et al., 2012].

The results presented here are complementary to the case of a spherical cell migrating due to the flow of an active gel cortical layer [Hawkins et al., 2011]. In that case, a similar force distribution is generated to propel the droplet forwards, only the asymmetry is driven by activity concentration rather than filament polarisation. In this paper we have not explicitly enforced a cortical layer of active gel, but rather we have modelled a complete droplet of active gel, with similar findings. Therefore, it is likely that coupling aspects from both of these simplified systems will lead to greater understanding of friction dependent cell migration in confinement.

This analytical study explains how motility can occur in a *in-vitro* active droplet of

contractile actomyosin when confined in a 3D environment. Experimental studies of this nature in the future will be important in understanding actomyosin dynamics in cells and also how real active gels differ from the linear model used in these calculations. The motion that we predict is heavily friction dependent, but does not rely on the droplet being adhered to the surrounding medium. In this way the work is also relevant to the study of migration mechanisms in environments where cells are unable to form adhesion complexes that connect the cytoskeleton to the external medium.

Finally, this work provides an insight into coupling between the internal polarisation field and a confining boundary. In the next chapters we will extend this more generally to cases where the polarisation is anchored to a dynamic interface, which will draw upon much of the mathematics presented in this chapter.

3.A Appendix: Approximate Analytical Solutions

In equation (3.33) we approximate the general solution for the stream function of equation (3.26) to leading order terms in the splay parameter c_s and apply the friction boundary conditions given by equations (3.28) and (3.29). This leads to two simultaneous equations to be solved for the constants a_k and b_k for each order $1 \leq k \leq 5$. The resulting solutions in terms or the stream function and the pressure are:

$$\begin{aligned}\Phi_s = &-\tilde{\zeta}\Delta\mu\left(R^2-r^2\right)\left\{\frac{\pi c_s r}{8(\xi R+2\eta)R}\left[1-\frac{(\pi c_s)^2}{24}\left(\left(1+\frac{r^2}{R^2}\right)-\frac{\xi R}{2\eta}\left(1-\frac{r^2}{R^2}\right)\right)\right]\sin(\theta)\right.\\
&+\frac{r^2}{(\xi R+4\eta)R^2}\left[1-\frac{(\pi c_s)^2}{4}\left(1+\frac{K}{\tilde{\zeta}\Delta\mu R^2}\right)\right]\sin(2\theta)\\
&-\frac{\pi c_s r^3}{8(\xi R+6\eta)R^3}\left(1-\frac{(\pi c_s)^2}{8}\right)\sin(3\theta)+\frac{(\pi c_s)^2 r^4}{32R^4(\xi R+8\eta)}\sin(4\theta)\\
&\left.-\frac{(\pi c_s)^3 r^5}{192(\xi R+10\eta)R^5}\sin(5\theta)\right\}, \qquad (3.64)\end{aligned}$$

$$P = P_0 - \tilde{\zeta}\Delta\mu\eta \left\{ \frac{\xi R}{2\eta} \frac{\pi c_s r}{(\xi R + 2\eta)R} \left[1 - \frac{(\pi c_s)^2}{12} \right] \cos(\theta) \right. \tag{3.65}$$

$$- \frac{3r^2}{(\xi R + 4\eta)R^2} \left[1 - \frac{(\pi c_s)^2}{12} \left(1 - \frac{\xi R}{2\eta} + \frac{3K}{\tilde{\zeta}\Delta\mu R^2} \right) \right] \cos(2\theta)$$

$$+ \frac{2(\pi c_s) r^3}{(\xi R + 6\eta)R^3} \left[1 - \frac{(\pi c_s)^2}{16} \left(1 - \frac{\xi R}{6\eta} \right) \right] \cos(3\theta)$$

$$\left. - \frac{5(\pi c_s)^2 r^4}{8(\xi R + 8\eta)R^4} \cos(4\theta) + \frac{(\pi c_s)^3 r^5}{8(\xi R + 10\eta)R^5} \cos(5\theta) \right\} . \tag{3.66}$$

In section 3.2.6, we consider the case where there is an external fluid, and the conditions at the interface ensure velocity and stress continuity. In this case the approximate solutions that we use to plot figures 3.6 are given explicitly by the stream functions:

$$\Phi_f^{\text{int}} = -\frac{\tilde{\zeta}\Delta\mu r^2}{8(\eta + \eta_{\text{ext}})} \left\{ \frac{\pi c_s R}{2r} \left[\left(2 - \frac{r^2}{R^2} \right) - \frac{(\pi c_s)^2}{8} \left(1 - \frac{r^4}{3R^4} - \frac{\eta_{\text{ext}}(R^2 - r^2)^2}{3\eta R^4} \right) \right] \sin(\theta) \right.$$

$$- \left[1 - \frac{(\pi c_s)^2}{4} \left(\frac{K}{\tilde{\zeta}\Delta\mu R^2} + \frac{r^2}{3R^2} \right) \right] \sin(2\theta) + \frac{\pi c_s r}{6R} \left[1 - \frac{(\pi c_s r)^2}{16R^2} \right] \sin(3\theta)$$

$$\left. - \frac{(\pi c_s r)^2}{48R^2} \sin(4\theta) + \frac{(\pi c_s r)^3}{480R^3} \sin(5\theta) \right\} , \tag{3.67}$$

$$\Phi_f^{\text{ext}} = -\frac{\tilde{\zeta}\Delta\mu R^2}{8(\eta + \eta_{\text{ext}})} \left\{ \frac{\pi c_s R}{2r} \left(1 - \frac{(\pi c_s)^2}{12} \right) \sin(\theta) \right.$$

$$+ \frac{R^2}{r^2} \left[\left(1 - \frac{2r^2}{R^2} \right) - \frac{(\pi c_s)^2}{6} \left(1 - \frac{3r^2}{2R^2} + \frac{3K}{2\tilde{\zeta}\Delta\mu R^2} \left(1 - \frac{2r^2}{R^2} \right) \right) \right] \sin(2\theta)$$

$$- \frac{\pi c_s R^3}{3r^3} \left[1 - \frac{3r^2}{2R^2} - \frac{3(\pi c_s)^2}{32} \left(1 - \frac{4r^2}{3R^2} \right) \right] \sin(3\theta)$$

$$\left. + \frac{(\pi c_s)^2 R^4}{16r^4} \left(1 - \frac{4r^2}{3R^2} \right) \sin(4\theta) - \frac{(\pi c_s)^3 R^5}{120r^5} \left(1 - \frac{5r^2}{4R^2} \right) \sin(5\theta) \right\} . \tag{3.68}$$

In order to make the stream function solutions more readable in equations (3.67) and (3.68), we have factorised the solutions so that the quantities inside the curly parentheses are all unitless.

Chapter 4

Active propulsion of a passive fluid droplet

Abstract

In this chapter we will consider the inverted physical situation from that discussed in chapter 3, of a passive fluid droplet immersed in an active polar fluid. Based on the results of simulations in [De Magistris et al., 2014] we make approximations in order to calculate the active forces and flows in such a system for small values of the active stress. We compare these results quantitatively to those observed in simulations and discuss what this analytical analysis adds to this discussion. We also consider experimental realisation of such a system and the limits of this analysis.

4.1 Introduction

In this chapter we will investigate the behaviour of a passive fluid droplet immersed in an active liquid crystal medium. In reference [De Magistris et al., 2014] our collaborators used hybrid Lattice Boltzmann simulations to show that spontaneous motion of the fluid droplet can occur in this system. Two cases are investigated; normal and tangential anchoring of the active liquid crystal at the droplet interface. Here we will explain the motion observed as far as possible in analytical terms, making approximations when necessary.

These novel states of matter are interesting from a purely theoretical point of view, but also there is some scope for these to be repeated experimentally *in vitro* as outlined in [De Magistris et al., 2014] and discussed in section 4.5 here. While these systems are far removed from the complex environment of the *in vivo* cytoskeleton, we hope that this study can give insight into the role that interactions with internal boundaries can play on cytoskeletal organisation. In real cells the cytoskeleton organisation is strongly influenced by the nucleus, via protein complexes that connect the filaments to the nuclear lamina. In addition, as discussed in chapter 1 the position of a nucleus in the cell appears to be coupled to the cell polarisation and in particular the organisation of the microtubule network.

We will begin our analysis applying the calculations in [Lubensky et al., 1998] which calculate the polarisation in an infinite passive liquid crystal containing a passive fluid drop. Then we go on to approximate this polarisation field for this system with confining walls. We then introduce the active terms and analyse the forces that these generate on the droplet, which was the part of the work that we contributed to [De Magistris et al., 2014]. Finally, we will see how expanding these forces can allow us to estimate the flow in certain regions and compare our results to the simulations, these calculations are not included in [De Magistris et al., 2014].

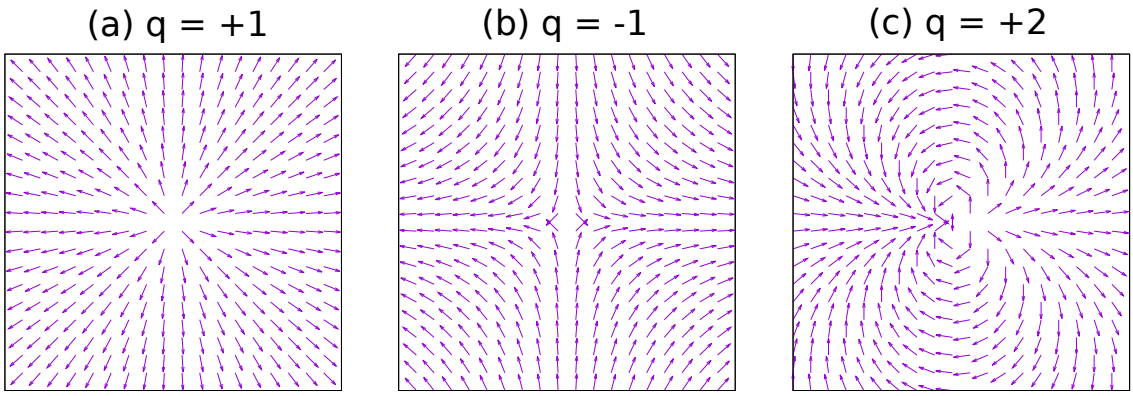

Figure 4.1: Three examples of topological defects in 2D with their respective charge (or winding number) q.

4.2 Fluid droplet in a 2D infinite passive polar liquid crystal

In a passive polar liquid crystal, the insertion of a fluid droplet or colloid will lead to different polarisation steady states depending on the favoured anchoring direction at the interface. [Lubensky et al., 1998] showed that, in a nematic liquid crystal, if the particles favour normal (homeotropic) anchoring the equilibrium orientation field can take one of three configurations depending on the elastic response in the nematic to different deformations. However, this is reduced to one for a polar liquid crystal with directed anchoring, namely a state known as a 'hyperbolic hedgehog' where a charge $q = -1$ defect forms in the liquid crystal near to the drop. In 2D the 'topological charge' q of a defect is simply equal to $q = (\oint \mathrm{d}\alpha)/2\pi$ where alpha is the polarisation (or director) angle to the x-axis, and the integral is performed in a closed loop around the defect [Selinger, 2015]. This charge q is also sometimes referred to as a winding number, as it counts the number of times the polarisation or director rotates by 2Π in a closed loop around the defect. See figure 4.1 for some examples of topological defects in 2D. In the tangential anchoring case, two equally spaced surface defects, known as 'boojums' in 3D (see figures 4.2 and 4.3 for 2D plots of the polarisation fields for homeotropic and tangential anchoring respectively).

If we consider a polar liquid crystal far from the isotropic to nematic transition such that $|\boldsymbol{p}| = 1$, then in two dimensions the polarisation can be determined by a single angle

α, such that $p_x = \cos(\alpha)$ and $p_y = \sin(\alpha)$. It is then useful to split the molecular field into parallel and perpendicular contributions where $h_{\parallel} = h_x \cos(\alpha) + h_y \sin(\alpha) + h^0_{\parallel}(x, y, t)$ and $h_{\perp} = h_x \sin(\alpha) - h_y \cos(\alpha)$, where $h^0_{\parallel}(x, y, t)$ is a Lagrange multiplier that fixes $|\boldsymbol{p}| = 1$. Then, the Euler-Lagrange equation for this system can be written as $h_{\perp} = K\nabla^2\alpha = 0$ [de Gennes and Prost, 1993]. In the following two sections we will solve the bulk Euler-Lagrange equation for homeotropic and tangential anchoring at the droplet interface, as outlined by [Lubensky et al., 1998].

4.2.1 Homeotropic anchoring

The main difference assumed here between a polar liquid crystal and a nematic is that the perpendicular anchoring boundary condition will have a preferred direction, as well as orientation. Thus the 2D free energy on the droplet boundary l for this anchoring can be written as:

$$F_l = \frac{1}{2} W_1 \int_l (\boldsymbol{p}.\hat{\mathbf{n}}) \mathrm{d}l \tag{4.1}$$

where $\hat{\mathbf{n}}$ is the surface normal and hence this term is minimised for $\boldsymbol{p}$ anchored inwards (for positive W_1) or outwards (for negative W_1). For most liquid crystal emulsions the limit of high surface tension $\gamma \gg W_1 + K/a$ (where a is the droplet radius) is applicable and so we can assume that, as in the simulations in [De Magistris et al., 2014], deformation of the droplet with be negligible. However, it is worth noting that animal cells are generally much more deformable than these emulsion droplets. For example, [Dai and Sheetz, 1999] measure the membrane tension in two types of animal cells, taking measurements from blebs (which are detached from the actomyosin cortex) to find the bare membrane tension, and in bleb free parts of the cell surface. The values range from 5×10^{-3}mN m^{-1} for the bare membrane to 5×10^{-2}mN m^{-1} in cortex-attached membrane. In context these values are $3 - 4$ orders of magnitude lower than oil-water emulsions and liquid crystal emulsions.

In the following we also assume that W_1 is negative (outward anchoring) and that anchoring effects dominate near to the interface. This way we can impose a strong anchoring

condition such that $\alpha = \theta$ at $r = a$ (for a circular drop), where r and θ are the standard polar coordinates.

The far field polarisation will be dominated by the bulk free energy, and so will be in a completely aligned state. We take this to be $\boldsymbol{p} = \hat{\boldsymbol{x}}$ (or $\alpha = 0$) to match the simulations, but this direction is arbitrary. This leads to the creation of a 'hyperbolic hedgehog' defect in the negative x-direction relative to the droplet. This is a defect of topological charge $q = -1$, which cancels the topological charge of $q = +1$ imposed by the droplet boundary condition so that the polarisation is aligned in the far field. A defect can be represented by $\alpha = q \tan^{-1}((y - y_0)/(x - x_0))$ where (x_0, y_0) are the coordinates of the defect centre. Note that this defect satisfies the Euler-Lagrange equation, and in 2D solutions are additive. Thus, as in [Lubensky et al., 1998] we can analytically represent the equilibrium polarisation profile by assuming that the hyperbolic hedgehog defect (charge $q = -1$) is centred at $(-l_0 a, 0)$, where l_0 is the defect distance from the droplet centre in units of droplet radius a. Then to satisfy the boundary conditions and the Euler-Lagrange equation we also define another $q = -1$ defect inside the droplet at $(-a/l_0, 0)$ and a $q = +2$ defect at the origin (the droplet centre). These defects inside the droplet are not real but they ensure that the polarisation field in the liquid crystal satisfies all of its constraints. Hence, we can write the polarisation field in terms of α as:

$$\alpha_{\text{hom}} = \begin{cases} 2\theta - \tan^{-1}\left(\frac{y}{x+l_0 a}\right) - \tan^{-1}\left(\frac{y}{x+a/l_0}\right) & \text{if} \quad \sqrt{x^2+y^2} \geq 1 \\ 0 & \text{if} \quad \sqrt{x^2+y^2} < 1\,. \end{cases} \tag{4.2}$$

This polarisation is plotted in figure 4.2 and one can show that this configuration gives the desired $\alpha = \theta$ at $r = a$ and $\alpha = 0$ as $r \to \infty$. Note however that this method is only valid in 2D, since solutions to the Euler Lagrange equation are not additive in the 3D case.

4.2.2 Tangential anchoring

In the case of tangential anchoring in 2D, if we assume the droplet surface to be homogeneous, then there should be no preferred polarisation direction along the interface

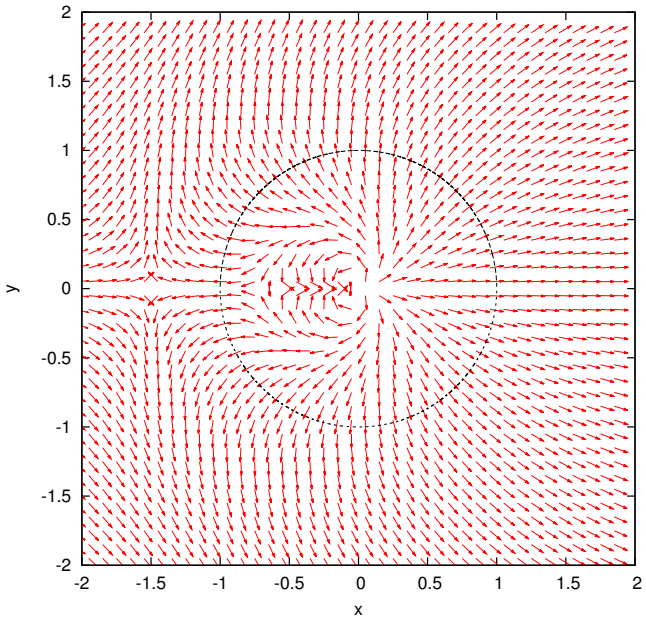

Figure 4.2: Equilibrium polarisation profile for a droplet of radius $a = 1$ and strong radial anchoring at the interface. We have set the constant $l_0 = 1.5$ which determines the position of the hyperbolic hedgehog defect. The polarisation inside the droplet is zero but we plot the external solution everywhere to demonstrate how the field is constructed.

(clockwise or anti-clockwise), and so it is identical to the nematic case. Thus the surface free energy is given by:

$$F_S = \frac{1}{2} W_2 \int \mathrm{d}S (\boldsymbol{p}.\hat{\mathbf{n}})^2 \tag{4.3}$$

where W_2 is always positive and again we assume that it is large enough that we can take this anchoring as a boundary condition. In this case, if we again assume that $\boldsymbol{p} = \hat{\mathbf{x}}$ in the far field, then the polarisation profile can be represented by a pair of $q = -1$ defects at $(\pm a, 0)$ and a $q = +2$ defect at the origin. Hence:

$$\alpha_{\tan} = \begin{cases} 2\theta - \tan^{-1}\left(\frac{y}{x+a}\right) - \tan^{-1}\left(\frac{y}{x-a}\right) & \text{if} \quad \sqrt{x^2+y^2} \geq 1 \\ 0 & \text{if} \quad \sqrt{x^2+y^2} < 1\,. \end{cases} \tag{4.4}$$

which is plotted in figure 4.3.

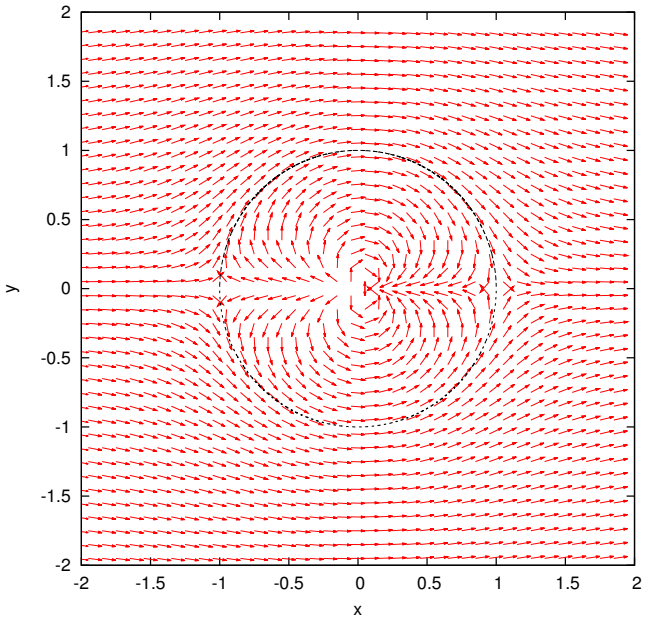

Figure 4.3: Equilibrium polarisation profile for a droplet of radius a = 1 and with tangential anchoring. Again the interior is plotted for demonstrative purposes.

4.3 Fluid droplet in a confined 2D passive polar liquid crystal

Confinement is important at cell length scales, and the cell cytoskeleton is confined by the external environment and internal organelles such as the nucleus. In the simulations presented in [De Magistris et al., 2014] the active liquid crystal is confined to a channel of width approximately twice that of the droplet diameter [1]. For these reasons we consider the case where a polar liquid crystal is confined in a channel such that the polarisation is parallel with the walls at $y = \pm L$. To approach this analytically we assume that the polarisation is parallel to the x-direction at a radius $r = L$ from the droplet. This gives some radial symmetry to the problem so that we can work in polar coordinates. Here, we define the polarisation angle with respect to the $\hat{\boldsymbol{r}}$ direction $\beta(r, \theta)$ such that $p_r = \cos(\beta)$ and $p_\theta = \sin(\beta)$. This is related to the polarisation angle with respect to $\hat{\boldsymbol{x}}$ direction α simply by $\beta = \alpha - \theta$.

[1] In the tangential case the resulting droplet diameter is approximately 1/3 of the width of the channel in the simulations. This is due to the competition between the phase field and liquid crystal parts of the free energy. In order to minimise the free energy some of the phase field that is at $\phi = \phi_0$ changes to $\phi = 0$ (see section 3.2.2) [De Magistris et al., 2014].

We can approach this problem in a number of ways, the simplest is using the symmetry of the system assuming $\beta \propto \theta$ where $\theta = \{-\pi \dots \pi\}$. This supposes that the θ dependence of the angle β is linear, to match the external boundary condition $\beta = -\theta$ at $r = L$. In the following two sections we will use this assumption to approximate this polarisation in confinement for the two anchoring cases and compare these to simulations. Then we will also show an alternative way to solve the Euler-Lagrange equation in this geometry using a Fourier series approach.

4.3.1 Homeotropic anchoring

Substituting $\beta(r, \theta) = \theta\beta_1(r) + \beta_0(r)$ into the one-constant approximation of $h_\perp = 0$ and comparing coefficients we get,

$$\theta\left(\frac{\mathrm{d}^2\beta_1}{\mathrm{d}r^2} + \frac{1}{r}\frac{\mathrm{d}\beta_1}{\mathrm{d}r}\right) = 0 \qquad \rightarrow \qquad \frac{\mathrm{d}\chi}{\mathrm{d}r} = -\frac{\chi}{r}\,, \tag{4.5}$$

$$\left(\frac{\mathrm{d}^2\beta_0}{\mathrm{d}r^2} + \frac{1}{r}\frac{\mathrm{d}\beta_0}{\mathrm{d}r}\right) = 0 \qquad \rightarrow \qquad \frac{\mathrm{d}\xi}{\mathrm{d}r} = -\frac{\xi}{r}\,, \tag{4.6}$$

where $\chi = (\mathrm{d}\beta_1)/(\mathrm{d}r)$ and $\xi = (\mathrm{d}\beta_0)/(\mathrm{d}r)$. From (4.5) we can see that $\chi = ar^{-1}$ where a is a constant of integration and so $\beta_1 = a_1 \ln(r) + b_1$ and similarly $\beta_0 = a_0 \ln(r) + b_0$. Applying the two boundary conditions we find that $a_1 = -1/(\ln(L/a)$, $b_1 = \ln(a)/\ln(L/a)$ and $a_0 = b_0 = 0$ and so,

$$\beta(r, \theta) = \beta_{\mathrm{hom}} \equiv -\theta\frac{\ln(r/a)}{\ln(L/a)}\,. \tag{4.7}$$

It is important to note that this angle does not obey the periodic condition $\beta(r, \theta + 2\pi) = \beta(r, \theta)$ and so there is a discontinuity at the interface between $\theta = -\pi$ and $\theta = \pi$ (see figure 4.4).

Comparing this to Lattice-Boltzmann hybrid simulations of an active polar liquid crystal, we see that the results are characteristic of the zero activity case, despite the assumptions in arriving at equation (4.7) (see figure 4.5). We see that there is a point

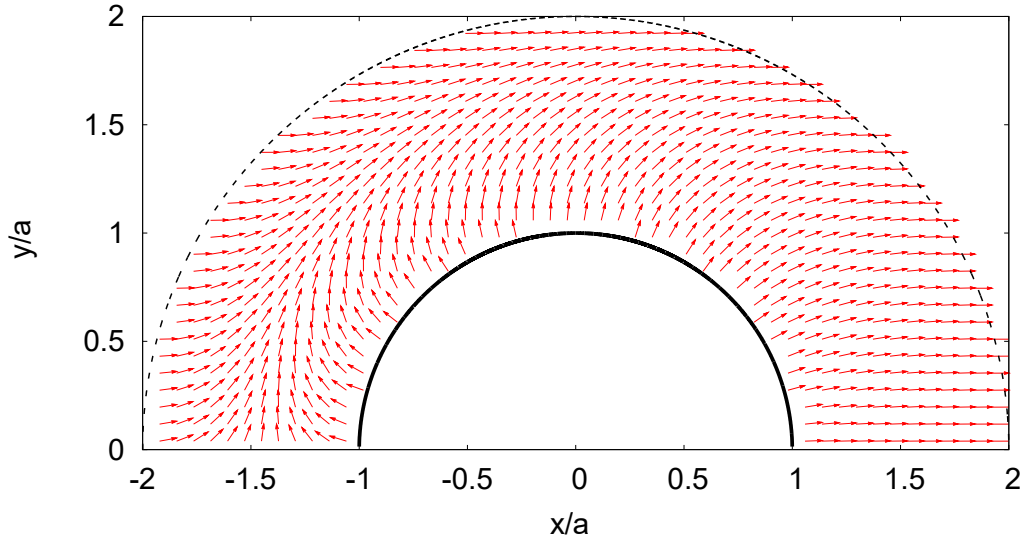

Figure 4.4: Vector plot of the polarisation field in equation (4.7) around a passive droplet with strong normal anchoring at the interface, plotted for $L = 2a$ in units of the radius.

defect in the polarisation at the point where the analytical solution is discontinuous.

In the simulations (figure 4.5(b)), it would appear that the distance from the droplet at which the polarisation returns to the bulk minimum is proportional by the distance from the droplet to the y-boundaries. Comparing this to the infinite solution we see that the polarisation decays over a much shorter distance, even in the non-confined x-direction. This suggests that our assumption of $\beta = 0$ at $r = L$ is a reasonable one.

4.3.2 Tangential anchoring

In the tangential anchoring case the boundary conditions we use are $\beta = 0$ at $r = a$ and $\beta = -\theta$ at $r = L$. We can again assume $\beta \propto \theta$ and thus the differential equations to be solved are given by equations (4.5) and (4.6) and so we have the same general solutions $\beta = \theta(a_1 \ln(r) + b_1) + a_0 \ln(r) + b_0$. Applying the boundary conditions we find that, $a_1 = -1/(\ln(L/a))$ and $b_1 = \ln(a)/(\ln(L/a))$ for all θ. Then $a_0 = \pi/(2\ln(L/a))$ and $b_0 = -\pi \ln(L)/(2\ln(L/a))$ when $\sin(\theta) > 0$ and the negative of these values when

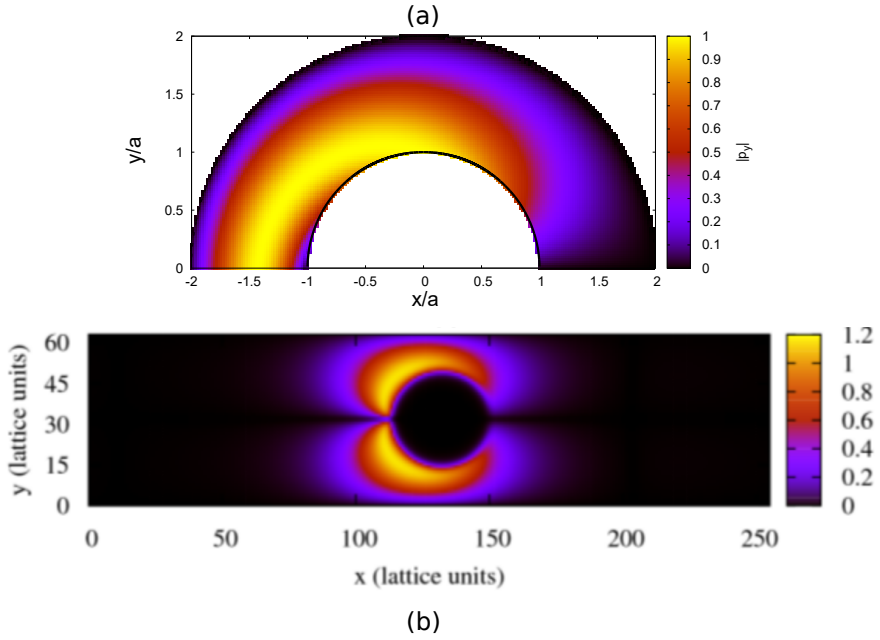

Figure 4.5: Comparison between equilibrium polarisation profile with homeotropic anchoring from **(a)** the analytical approximation of the polarisation angle in equation (4.7) **(b)** lattice-Boltzmann hybrid simulations in a periodic channel from [De Magistris et al., 2014]. The colour scale corresponds to the magnitude of the y component of the polarisation. In order to fit the simulation length scale we set $L = 2a$.

$\sin(\theta) < 0$. Therefore, $\beta(r, \theta)$ is given by:

$$\beta(r,\theta) = \beta_{\tan} \equiv \begin{cases} -\theta \frac{\ln(r/a)}{\ln(L/a)} - \frac{\pi}{2} \frac{\ln(L/r)}{\ln(L/a)} & \text{when} \quad \sin(\theta) > 0\,, \\ -\theta \frac{\ln(r/a)}{\ln(L/a)} + \frac{\pi}{2} \frac{\ln(L/r)}{\ln(L/a)} & \text{when} \quad \sin(\theta) < 0\,. \end{cases} \tag{4.8}$$

It is clear that again this polarisation is not periodic and this time there are two discontinuities, one at $\theta = 0$ and another when $\theta = \pm\pi$ (see figure 4.6). We can again compare this to the Lattice-Boltzmann simulations at zero activity and show that they compare well everywhere except near to the defects.

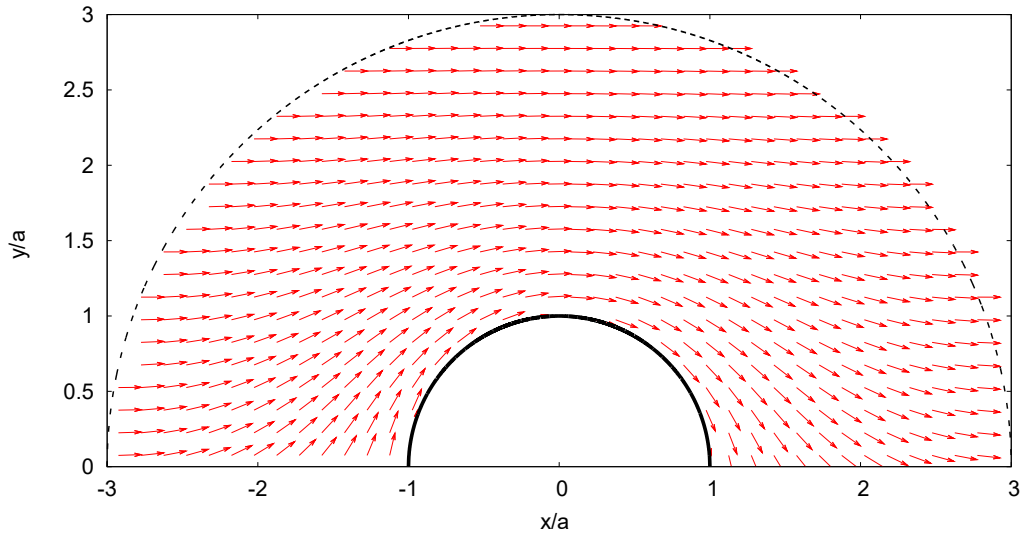

Figure 4.6: Vector plot of the polarisation field in equation (4.8) around a passive droplet with strong tangential anchoring at the interface, plotted for $L = 3a$.

4.3.3 A Fourier approach to calculating the confined polarisation field

An alternative way to approximate the polarisation in 2D such that the discontinuity at $\theta = \pm\pi$ is properly accounted for is to express the angle β in terms of a Fourier series:

$$\beta = \sum_{k=1}^{\infty} b_k(r) \sin(k\theta)\,. \tag{4.9}$$

We do not include $\cos(k\theta)$ terms since the boundary conditions are odd in θ. We can then solve the Euler-Lagrange equation for each mode of this equation separately, as the solutions are additive, so we find that $b_k(r)$ at $r = L$ must satisfy the differential equation:

$$\left[b_k''(r) + \frac{1}{r} b_k'(r) - \frac{n^2}{r^2} b_k(r)\right] \sin(n\theta) = 0\,. \tag{4.10}$$

In both anchoring cases, the boundary condition at $r = L$ is $\beta = -\theta$. Thus, the boundary condition for $b_k(r)$ is

$$b_k(L) = -\frac{1}{\pi} \int_{-\pi}^{\pi} \theta \sin(k\theta) = \frac{2(-1)^n}{n} \tag{4.11}$$

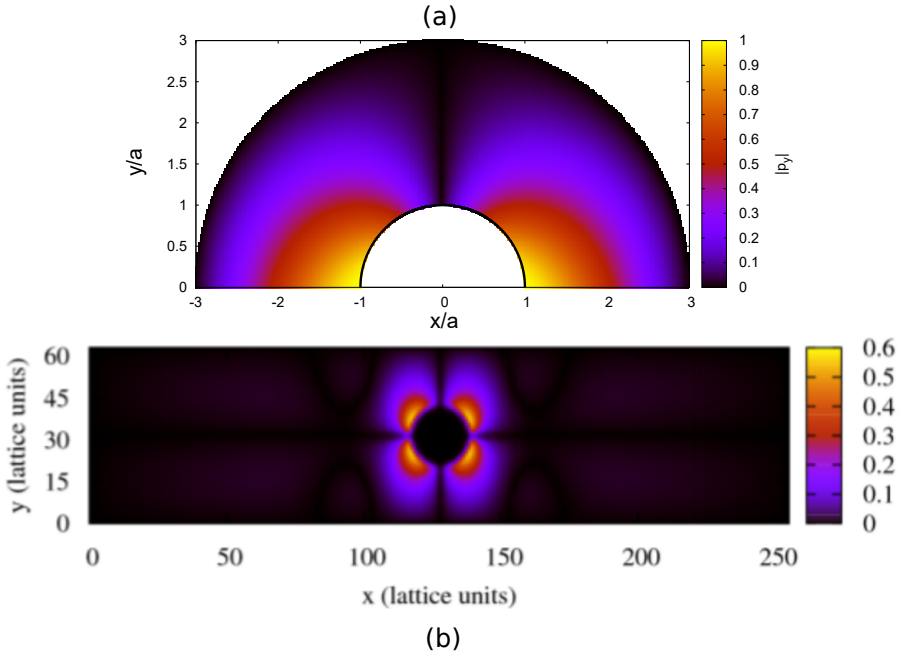

Figure 4.7: Comparison between equilibrium polarisation profile with tangential anchoring from **(a)** the analytical approximation in equation (4.8) and **(b)** Lattice-Boltzmann hybrid simulations in a periodic channel from [De Magistris et al., 2014]. The colour scale corresponds to the magnitude of the y component of the polarisation. In order to fit the simulation length scale we set $L = 3a$.

Solving equation (4.10) for the boundary condition in (4.11) yields

$$\frac{1}{(a/L)^n - (L/a)^n}\left\{\frac{2(-1)^n}{n}\left[\left(\frac{a}{r}\right)^n - \left(\frac{r}{a}\right)^n\right] + b_k(a)\left[\left(\frac{r}{L}\right)^n - \left(\frac{L}{r}\right)^n\right]\right\} \tag{4.12}$$

where $b_k(a)$ is the boundary condition at $r = a$. For homeotropic anchoring $b_k(a) = 0$ and in the tangential anchoring case $b_k(a) = \pm(-1)^n/n$ for the boundary conditions $\beta = \pm\pi/2$. For large n these solutions approach those observed in the simulations, but they are significantly more difficult to deal with analytically so in the following sections we only work with the solutions presented in sections 4.2, 4.3.1 and 4.3.2.

4.4 Fluid droplet in an active polar liquid crystal

Now we extend the analysis of the previous sections to consider the flows and forces created if the polar liquid crystal generate contractile or extensile active stresses. In order to do this we consider that the activity magnitude is very small ($|\zeta\Delta\mu| \ll K/a^2$) such that we can assume that the polarisation remains approximately unchanged from the

equilibrium case. Since the flow should be zero at thermodynamic equilibrium, the flows and forces generated in this small activity limit can be estimated just by considering the terms proportional to $\zeta\Delta\mu$.

In the simulations presented in [De Magistris et al., 2014] we observe that, in the homeotropic anchoring case the droplet migrates at a steady speed for all non-zero values of activity. There is no activity threshold, as the symmetry of the system is already broken in the equilibrium case, which is clear from the polarisation field in figure 4.5. In the contractile activity case ($\zeta\Delta\mu < 0$) the droplet moves to the right (given that the defect forms on the left) and the opposite direction in the extensile case ($\zeta\Delta\mu > 0$). Therefore, in this section we look at the active forces in this low activity limit for the polarisations calculated in equations (4.2) and (4.7) for the homeotropic anchoring case. We then go on to approximate the flows in the system using far and near field expansions of the infinite polarisation solution.

In this section we do not consider flows in the tangential anchoring case as this remains symmetric in the low activity limit. The simulations of [De Magistris et al., 2014] do predict thresholds of the activity above which the tangential anchoring case breaks symmetry (discussed in section 4.5). However, we are unable to predict these thresholds or steady states accurately from analytical calculations due to this difficult geometry.

4.4.1 Active forces around the drop in an infinite active polar liquid crystal

In general an infinite active liquid crystal will have infinite total active energy and so we just consider forces local to the droplet using the local active force. In any experimentally realisable system the length scale will be important as it will determine the total active energy in the system, but one could feasibly create a large enough system such that the solutions for the polarisation field in section 4.2 would be valid near to the drop. We also consider local active forces in the confined case and show that these show similar qualitative behaviour.

In general we can write the active force density (using the active stress from equation (3.5)) as:

$$\nabla \cdot \underline{\underline{\sigma}}^{\text{act}} = \zeta \Delta\mu \left\{ \left[\frac{\partial \alpha}{\partial r} \sin(2\alpha) - \frac{1}{r} \left(1 + \frac{\partial \alpha}{\partial \theta} \right) \cos(2\alpha) \right] \hat{\mathbf{r}} - \left[\frac{\partial \alpha}{\partial r} \cos(2\alpha) + \frac{1}{r} \left(1 + \frac{\partial \alpha}{\partial \theta} \right) \sin(2\alpha) \right] \hat{\boldsymbol{\theta}} \right\} . \tag{4.13}$$

Using the passive polarisation in equation (4.2) in section 4.2.1 for an infinite polar liquid crystal; we see that at $r = a$ we have $\alpha = 0$, $\partial_\theta \alpha = 0$ and (after a little algebra) $\partial_r \alpha = -2\sin(\theta) c_0 / [a(1 + 2c_0 \cos(\theta) + c_0^2)]$. This means that, at $r = a$:

$$(\nabla \cdot \underline{\underline{\sigma}}^{\text{act}}) \cdot \hat{\mathbf{x}} = -\frac{\zeta \Delta\mu}{a} \left[\cos(\theta) + \frac{2c_0 \sin^2(\theta)}{1 + 2c_0 \cos(\theta) + c_0^2} \right] \tag{4.14}$$

We can then calculate the average force density on the droplet boundary in the x-direction as:

$$F_x^{\text{act}} = \frac{1}{2\pi} \int_{-\pi}^{\pi} (\nabla \cdot \underline{\underline{\sigma}}^{\text{act}}) \cdot \hat{\mathbf{x}} \mathrm{d}\theta = -\frac{\zeta \Delta\mu}{a c_0} \tag{4.15}$$

Hence, the total active force on the droplet interface will be the result of equation (4.15) multiplied by the droplet area, i.e. $f_x^{\text{act}} = -(\zeta \Delta\mu \pi a)(c_0)$. This implies that in the contractile case ($\zeta \Delta\mu < 0$) the droplet will be pushed in the positive x direction, and the opposite for the extensile case, as seen in the simulations.

We can do a similar analysis for the approximation to a confined droplet from equation (4.7) section 4.3.1 where:

$$\alpha_{\text{hom}} = \beta_{\text{hom}} + \theta = \theta \left[1 - \frac{\ln(r/a)}{\ln(L/a)} \right] . \tag{4.16}$$

Then we get that $F_x^{\text{act}} = -(\zeta \Delta\mu \pi a)/(\ln(L/a))$, suggesting qualitatively similar behaviour. The higher the distortion near to the droplet (either when $c_0 - 1$ is small or $(L - a)/a$ is small) the larger the active force acting on it.

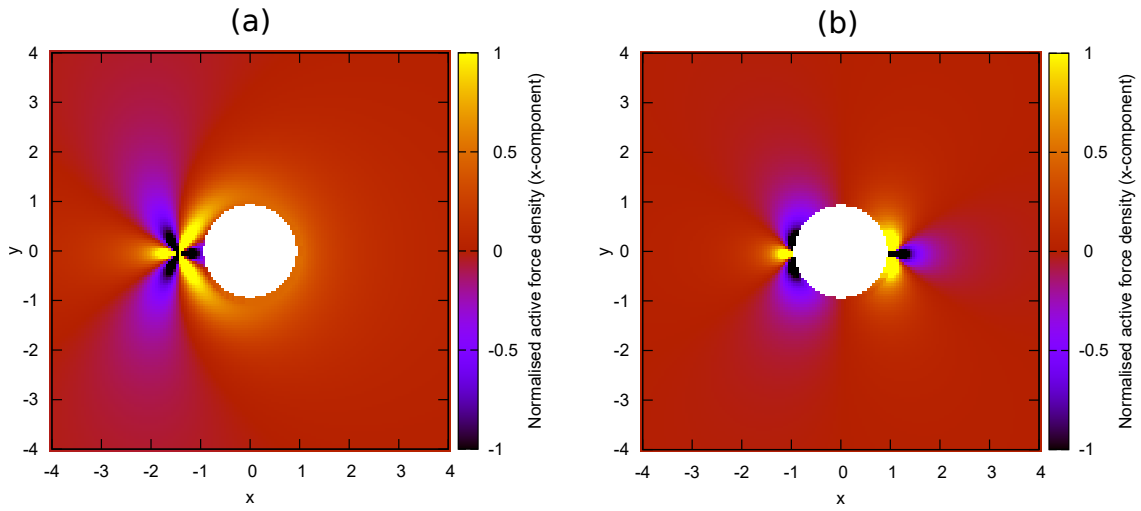

Figure 4.8: Active force density plots in **(a)** the homeotropic anchoring case and **(b)** the tangential anchoring case for a droplet in an infinite active polar fluid at low activity. The colour gradient measures the x-component of the active force density and the scale is 'capped' for visibility.

In the case of tangential anchoring the equilibrium polarisation is symmetric and the net active force at the interface is zero in the x-direction. This is reflected in the simulations which show that at low activity values the droplet is stationary. In this case there is both contractile and extensile activity thresholds above which the system breaks symmetry.

4.4.2 Far and near-field approximations to the activity induced flow

We see that using the expressions derived for the polarisation fields calculated in equations (4.2) and (4.7) we cannot calculate active flows analytically. However, we can improve our understanding of this steady state by expanding the expression for the bulk polarisation from equation (4.2) in terms of a Taylor series at the hyperbolic hedgehog defect and at $r \to \infty$. First we need to redefine the origin such that it is positioned at the centre of the hyperbolic hedgehog defect, this means the polarisation angle α in our new reference frame is transformed from (4.2) to:

$$\alpha'_{\text{hom}} = -\theta + 2\tan^{-1}\left(\frac{y}{x - l_0 a}\right) - \tan^{-1}\left(\frac{y}{x - a(l_0 - 1/l_0)}\right). \tag{4.17}$$

As outlined by Lubensky *et al.* [Lubensky et al., 1998] the polarisation can be approximated far away from the droplet by expanding around $r \to \infty$ in a Taylor series. Here, since we are interested in the active flows, we expand the active force density around $r \to \infty$ to leading order:

$$\boldsymbol{f}_{\infty}^{\text{act}} = \zeta \Delta\mu \frac{a(1+l_0^2)}{l_0 r^2} \left[-\cos(3\theta)\hat{\boldsymbol{r}} + \sin(3\theta)\hat{\boldsymbol{\theta}} \right] + O\left(r^{-3}\right) \tag{4.18}$$

We can then also expand the force density about $r = 0$ (the defect centre) to leading order:

$$\boldsymbol{f}_{\text{defect}}^{\text{act}} = \frac{\zeta \Delta\mu}{r} \left[\cos(4\theta)\hat{\boldsymbol{r}} - \sin(4\theta)\hat{\boldsymbol{\theta}} \right] + O(r^0) \tag{4.19}$$

We can substitute (4.18) into the Stokes' equation for an infinite fluid (ignoring the presence of the droplet) and find that, as $r \to \infty$ the velocity goes to:

$$\boldsymbol{v}_{\infty} = \frac{\zeta \Delta\mu a(1+l_0^2)}{16\eta l_0} \left[-3\cos(3\theta)\hat{\boldsymbol{r}} + \sin(3\theta)\hat{\boldsymbol{\theta}} \right] . \tag{4.20}$$

To obtain equation (4.20) we used the boundary condition that $\boldsymbol{v}$ is finite at $r \to \infty$ and $r \to 0$. One can check that including more terms into the expansion in equation (4.18) does not change the expression for the flow in this limit. The x-component of this flow is plotted in figure 4.9(a) which shows that at large values of y (around $\theta = \pm\pi/2$) this flow is negative (*i.e.* to the left), and at small values of y (around $\theta = \pm\pi$) this flow is positive (to the right). This qualitatively agrees with the flow at the edges of the simulation, even though this is in confinement.

The expansion of the force around the defect at $r = 0$ shows that at leading order it is identical a $q = -1$ defect and so makes a symmetric contribution to the force at the origin. This can be seen in the force plot in 4.8(a) by the anti-symmetric x-component of the force (reflecting in the $y = -l_0$ axis). If we consider this symmetric defect in isolation with force density given by equation (4.19) then we find that the flow field around it is

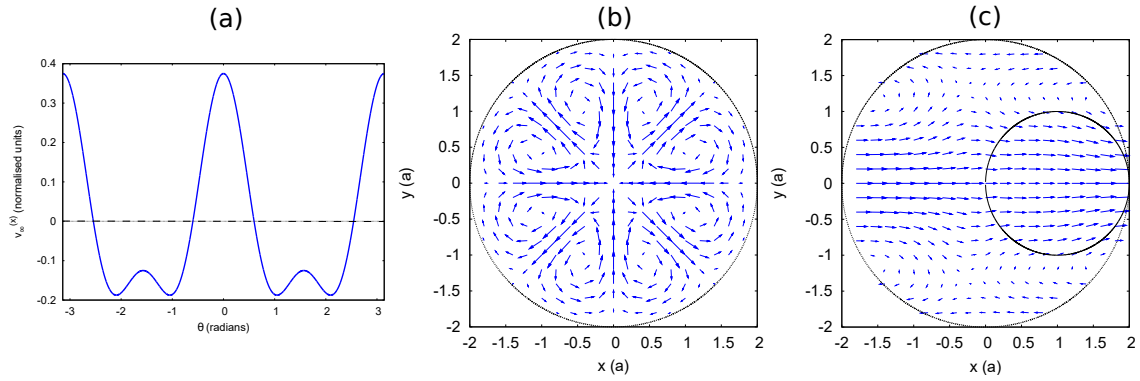

Figure 4.9: **(a)** The x-component of the far-field flow solution in (4.20) plotted against the polar angle θ. **(b)** Flow around an isolated $q = -1$ defect with a no-slip condition at $r = 2a$ (dotted line). **(c)** Flow around an isolated $q = -1$ defect with boundary condition at $r = 2a$ given by the flow in figure (a). The inner circle identifies where the passive droplet interface would be.

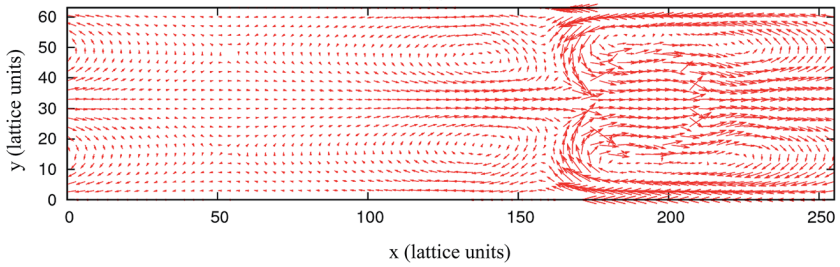

Figure 4.10: Active flow simulated in [De Magistris et al., 2014] with small contractile activity $\zeta\Delta\mu < 0$ and homeotropic anchoring at the droplet interface.

given by

$$\boldsymbol{v}_{\text{defect}} = \frac{\zeta\Delta\mu r}{24\eta}\left[2\left(1-\frac{r}{R_1}\right)^2\left(1+\frac{r}{R_1}\right)^2\cos(4\theta)\hat{\boldsymbol{r}} - \left(1-4\frac{r^2}{R_1^2}+3\frac{r^4}{R_1^4}\right)\sin(4\theta)\hat{\boldsymbol{\theta}}\right] \tag{4.21}$$

where we have applied the boundary condition $\boldsymbol{v} = 0$ at some distance $r = R_1$. This velocity is plotted in figure 4.9(b).

We can combine these two effects on the flow field and approximate what happens in the simulations by solving for the velocity again using the force from equation (4.19) but this time applying the boundary condition $\boldsymbol{v} = v_\infty^{(x)}\hat{\boldsymbol{x}}$ at $r = R_1$ instead. The simulations are confined in the y-direction, which is applied by the $v^{(y)} = 0$ condition at the boundary, as is (approximately) observed in the simulations. Then, applying just the x-component of the far-field velocity from equation (4.20) as a boundary condition we find that the

solution (plotted in figure 4.9(c)) is very similar to the simulations (plotted in figure 4.10). A quantitative analysis of this flow in the region of the droplet shows that this very simple analysis gives a reasonable estimate of the droplet speed, even though we have not modelled the droplet interface. If we transform back to the frame with the droplet centre at the origin, we can estimate the droplet velocity by integrating the velocity vector normal to the interface:

$$\boldsymbol{v}_{\text{drop}} = \frac{1}{2\pi}\int_{-\pi}^{\pi} v_r'\hat{\boldsymbol{r}}\,\mathrm{d}\theta = -\frac{\zeta\Delta\mu a}{32\eta}\left(l_0 + \frac{1}{l_0}\right)\left[2 - \frac{a^2}{L^2}\right]\hat{\boldsymbol{x}}\,. \tag{4.22}$$

If we use the parameter values in the simulation and assume that $L \approx 2a$ and $l_0 \approx 1$ we see that for small values of $\zeta\Delta\mu < 0$ this agrees well with the observed velocity in the simulation. Our estimate from equation (4.22) gives a velocity approximately 90% the values observed in the simulations. It would be interesting therefore to see whether the prediction of scaling with droplet radius and confinement length scale is observed in simulations or whether this agreement is coincidental. Further simulations changing the confinement scale and droplet size would need to be performed to test this.

4.5 Summary and Conclusions

It is clear from this chapter and the work in reference [De Magistris et al., 2014] that the presence of a passive fluid drop, can cause symmetry breaking in an active fluid depending on the conditions at the interface. In the case of homeotropic anchoring the droplet moves for any non-zero activity as this system has broken symmetry. At low activities the droplet velocity is steady along the x-direction and increases linearly with the magnitude of $\zeta\Delta\mu$. In the case of tangential anchoring the resulting polarisation field is symmetric around the droplet and so the drop is not propelled. At larger values of activity the polarisation field is no longer dominated by the elastic energy terms and cannot be approximated by the equilibrium polarisations derived. This is because the activity can deform the polarisation field and if the activity is strong enough there can be positive feed back between this deformation and flow which promotes further deformation. This leads to several different transitions in the simulations for the cases corresponding to the different combinations of

tangential and homeotropic anchoring and contractile and extensile activity. However, in the analytical work we present here we are only able to consider the low activity case.

We have used equilibrium polarisation profiles derived by Lubensky *et al.* for a droplet in an infinite liquid crystal as well as those we derive in section 4.3 for a confined system to estimate the active force on the droplet. We see that these two cases give comparable results and show a force acting at the droplet interface that is directed away from the defect for $\zeta\Delta\mu < 0$, and towards the defect for $\zeta\Delta\mu > 0$ in the homeotropic anchoring case. We then expand around this force near to the defect and in the far field to estimate the droplet speed. Despite this crude approximation to the system we find that the asymmetry of the far-field flow (from the infinite liquid crystal analysis) applied as a boundary condition to a confined system containing a symmetric defect gives a reasonable physical approximation to the flow observed in the simulations.

As discussed in reference [De Magistris et al., 2014], this system could be realised experimentally using *in vitro* techniques to reconstruct an actin or microtubule based active gel [Sanchez et al., 2012, Soares e Silva et al., 2011, Tsai et al., 2011]. Controlling the amount of ATP in the system and confining to length scales of a few micrometres it should be possible to prevent the system from generating the pseudo-chaotic states observed in microtubule-kinesin systems and bacterial active gels and many active fluid simulations [Marchetti et al., 2013]. With the addition of a stabilising surfactant, emulsion droplets of oil or water could be inserted into this medium. The observed anchoring will depend on the nature of the active gel and the surface chemistry of the drop. An important distinction between the calculations presented here and an experimental system is the dimensionality, however the symmetry of the set-up suggests that similar behaviour would be observed in 3D.

Inside the cell cytoskeleton there are many proteins that govern bundling and anchoring of filaments, including those in LINC (Linker of Nucleoskeleton and Cytoskeleton) complexes that connect filaments to the nuclear lamina and the centrosome that nucleates

directed microtubule growth. Therefore, these internal boundaries constrain and order the filaments and hence it is unsurprising that in many cell types their positions correlate in some way with cell polarisation as discussed in Chapter 1. The calculations presented here are far removed from any biological system but the questions of symmetry breaking and internal boundaries are a common theme. Thus they provide an interesting insight into these novel physical states of matter.

It would also be interesting in future to observe how internal constraints on the flow field can affect the symmetry of the system. If one considers a hard colloid immersed in an active fluid, a condition of non-slip at the colloid interface could induce a flow in the system, regardless of anchoring. In [Foffano et al., 2012] for example, Foffano *et al.* show through simulation that a colloid pulled though an active fluid by an external force experiences anomalous drag forces due to the distortion of the filaments around it.

To conclude, in chapter 3 we discussed the importance of a confining boundary on an active polar fluid but we have seen in this chapter that internal constraints can generate similar directed moving states as well. These two chapters have a common theme of splay driven flow in contractile systems that lead to an ordered steady state with broken symmetry. In the following chapters we will consider deforming boundaries and explicit coupling between the active gel and the interface shape.

Chapter 5

Instabilities and Boundary Effects in Active Droplets

Abstract

In this chapter we consider two limiting cases of active fluid droplets. Firstly, we consider a fluid drop with an isotropic contractile active fluid dispersed on its interface. The active contraction changes the droplet surface tension and gradients in concentration of the active material can result in flow. We perform a linear stability analysis on the droplet to calculate the threshold activity values for which the system will break symmetry, and compare these predictions to 2D simulations of such a droplet.

Next, we consider an active polar fluid confined inside a deformable droplet with a large anchoring energy at the interface. We show that in general we cannot perform a linear stability analysis on this complete system. However, with appropriate approximations we are able to show that contractile activity should give rise to symmetric deformation of the droplet if the polarisation is strongly coupled to the boundary deformation. This is observed in 2D simulations of the system. We also find from the simulations that extensile activity gives rise to motility and droplet rotation in the parameter ranges studied.

5.1 Introduction

As mentioned in Chapter 2, there are many examples of calculations of instabilities and non-equilibrium steady states in active liquid crystals; in thin or 2D flat films ([Kruse et al., 2004], [Voituriez et al., 2005], [Voituriez et al., 2006], [Kruse et al., 2006], [Sarkar and Basu, 2015]), in a thin cortical layer ([Zumdieck et al., 2005], [Hawkins et al., 2011], [Joanny et al., 2013]), confined inside emulsion droplets or vesicles ([Callan-Jones et al., 2008], [Tjhung et al., 2012], [Joanny and Ramaswamy, 2012], [Giomi and DeSimone, 2014], [Whitfield et al., 2014], [Marth et al., 2014]), and in simplified models of animal and plant cells ([Hawkins et al., 2009], [Woodhouse and Goldstein, 2012], [Callan-Jones and Voituriez, 2013], [Kumar et al., 2014]). This chapter will investigate the stability of two contrasting cases of active droplets in order to quantify the activity threshold for symmetry breaking in these simplified systems. First, we look at the case of a fluid drop with an isotropic active gel dispersed on the droplet interface. The active stress generated alters the interfacial tension, which we find can lead to translation and deformation instabilities if the active material is contractile. Secondly, we consider a fluid drop with a fixed density and concentration of active matter in the droplet interior. In this case we see that when the polarisation of the filaments at the interface is strongly aligned with the interface normal direction, we observe rotation, translation and deformation instabilities. These two cases show how coupling to a moving boundary can affect stability in two simplified extremes of the active liquid crystal model, one where the concentration of active material can vary but there is no alignment between filaments, and one where the concentration is considered as fixed but there is long range order between filaments.

In order to test the prediction of our analytical calculations, we perform finite difference simulations of these systems in 2-dimensions using an immersed boundary method for the fluid-fluid interface [Peskin, 2002]. For the active interface model, we treat the active particles as analogous to a concentration of surfactant which alters the surface tension, as in [Lai et al., 2008], and we extend this to consider the case where this "active surfactant" can bind and unbind and diffuses in the droplet bulk. In order to model a polar active

fluid in the droplet bulk, we define a vector field $\boldsymbol{p}$ that is coupled to the droplet bulk by a numerical level-set function H. Details of these simulations will be discussed in depth in chapter 6, for this section we just consider the results and compare these to analytical calculations. With these simulations we are able to build phase diagrams of the two systems, and using the analytical calculations we can qualitatively explain the wide range of phase behaviour observed.

5.2 Fluid droplet with an active interface

First, we will consider the case of an isotropic active liquid crystal dispersed on the interface of a fluid droplet. In chapter 2 the active stress was introduced, which has an isotropic component and a nematic component (zero in this case). For an incompressible active fluid, this isotropic component is absorbed into the hydrostatic pressure, and does not contribute to the flow. However, if we consider an active liquid crystal dispersed on a droplet interface, we can assume that all stresses will be in the plane of the interface. More specifically while there is no alignment in the filaments, we assume that none are orientated normal to the boundary, and so the isotropic stress only acts in the plane of the interface. This set-up is comparable to *in vitro* experiments of microtubule networks and kinesin motors dispersed on the surface of an emulsion droplet [Sanchez et al., 2012] or vesicle [Keber et al., 2014]. However in those experiments the filaments show strong nematic order and so defects play an important role, potential experimental realisation of the model presented here will be discussed in the conclusions of this section.

This model is simpler than models of the actin cortex found in many cell types, which is generally modelled as a thin viscous active layer [Hawkins et al., 2011, Joanny et al., 2013, Turlier et al., 2014]. This is because we do not consider thickness or density dynamics, which allows us to model the shape dynamics analytically. Therefore, this model is not intended as a model of a cell's actin cortex, but does show very similar instabilities as these models with coupling to droplet deformation. Mathematically, it is identical to the more general models of droplets with surface tension gradients which can be either passive

or active in origin [Ohta and Ohkuma, 2009, Shitara et al., 2011, Yabunaka et al., 2012, Yoshinaga, 2014], however, to my knowledge there has not been full stability analysis published of one of these active systems.

5.2.1 Model

We consider a fluid droplet described by an interfacial surface Σ separating the contained fluid domain Ω_0 and external fluid domain Ω_1. We take the Reynolds' number $Re = 0$ as inertia plays practically no role at cellular length scales. Therefore the fluid flow (which we assume to be incompressible, *i.e.* $\nabla \cdot \boldsymbol{v} = 0$) can be described by the Stokes' equation:

$$\eta \nabla^2 \boldsymbol{v} + \boldsymbol{f}^{\text{ext}} - \nabla P = 0 \,, \tag{5.1}$$

where η is the viscosity, $\boldsymbol{v} = \boldsymbol{v}(r, \theta, \phi)$ is the fluid velocity, $\boldsymbol{f}^{\text{ext}} = \boldsymbol{f}^{\text{ext}}(r, \theta, \phi)$ denotes any external force densities acting on the fluid and $P = P(r, \theta, \phi)$ is the hydrostatic pressure. We use standard spherical polar coordinates to describe the system such that they map to Cartesian coordinates by the relations $x = r\sin(\theta)\cos(\phi)$, $y = r\sin(\theta)\sin(\phi)$ and $z = r\cos(\theta)$. The only forces acting on the system originate at the droplet surface Σ, the position of which we describe with the vector $\boldsymbol{R} = R(\theta, \phi)\hat{\boldsymbol{r}}$ assuming that this is monotonic with respect to the angular coordinates (θ,ϕ) (however this constraint is removed in the simulations presented in full in chapter 6). Thus, we can write $\boldsymbol{f}^{\text{ext}} = \boldsymbol{F}\delta\left[r - R(\theta, \phi)\right]$ where $\boldsymbol{F} = \boldsymbol{F}(\theta, \phi)$ is the surface force density.

Active stresses change the surface tension $\gamma = \gamma(\theta, \phi)$, and so the force from a fluid-fluid interface is

$$\boldsymbol{F} = \kappa\gamma\boldsymbol{n} + \left[\nabla_s \gamma\right]\boldsymbol{t}_i \,, \tag{5.2}$$

where $\nabla_s = (\boldsymbol{t}_i \cdot \nabla)$ is the surface gradient, $\kappa = \kappa(\theta, \phi)$ is the curvature, $\boldsymbol{n} = \boldsymbol{n}(\theta, \phi)$ is the surface normal and $\boldsymbol{t}_i = \boldsymbol{t}_i(\theta, \phi)$ are the orthogonal surface tangent vectors. Equation (5.2) is the general form of Laplace's law for a spatially varying surface tension. We assume

here that to first order in the concentration of active material $c = c(\theta, \phi)$ the surface tension scales with the contractile activity, but that there is a repulsive second order term proportional to $B \geq 0$:

$$\gamma = \gamma_0 - \zeta_c \Delta\mu c - \frac{B}{2} c^2 \,, \tag{5.3}$$

where γ_0 is the bare surface tension, $\zeta_c \Delta\mu$ is the activity coefficient, and B is a constant. This assumption is similar to that made in [Joanny et al., 2013] where a higher order repulsive term is employed to represent passive pressure in the active fluid. Defining the effective activity $\tilde{\zeta}\Delta\mu = \zeta\Delta\mu + Bc_0$ where c_0 is the stationary state concentration, we can see that the interface will be contractile for $\tilde{\zeta}\Delta\mu < 0$ or $\zeta_c\Delta\mu < Bc_0$ and hence increase the net surface tension. The concentration of active material at the interface c is governed by the rate equation:

$$\frac{\partial c}{\partial t} = -\nabla_s \cdot (c\boldsymbol{V}) + D\nabla_s^2 c - k_{\text{off}} c + k_{\text{on}} \rho_b \,. \tag{5.4}$$

The first term in equation (5.4) describes advection of the active material along the interface where $\boldsymbol{V} = \boldsymbol{V}(\theta, \phi) \equiv \boldsymbol{v}(r, \theta, \phi)\big|_{r=R} = \int_\Omega \boldsymbol{v}(r, \theta, \phi)\delta(r - R)\mathrm{d}^3\boldsymbol{r}$ is the fluid velocity at the interface. The second term describes 2D diffusion along the interface and k_{on} and k_{off} denote the rates of binding and unbinding to the interface of the active material respectively. The concentration $\rho_b = \rho_b(\theta, \phi) \equiv \int_\Omega \rho\delta(r - R)\mathrm{d}^3\boldsymbol{r}$ is the concentration of active matter in the bulk fluid $\rho = \rho(r, \theta, \phi)$ that are in the proximity of the interface. Note that c is a surface concentration and ρ a bulk concentration so k_{on} has dimensions of velocity.

Similarly, the concentration of active matter in the fluid ρ is governed by the equation:

$$\frac{\partial \rho}{\partial t} = -(\boldsymbol{v}.\nabla)\rho + D_b \nabla^2 \rho \tag{5.5}$$

with the boundary condition at the moving interface Σ:

$$D_b(\boldsymbol{n}\cdot\nabla)\rho_b = k_{\rm on}\rho_b - k_{\rm off}c\,. \tag{5.6}$$

Finally, the equation of motion of the interface is simply given by

$$\frac{\partial \boldsymbol{R}}{\partial t} = \boldsymbol{V} \tag{5.7}$$

such that the boundary moves with the velocity of the surrounding fluid. Note that the difference between this model and models of a viscous active layer is that there can be no thickness or density change in the cortex as it is treated as a 2D interface. Thus, the flow of the interface is enslaved to the flow of the fluid, which enables us to analyse fluctuations in the droplet shape analytically. Note that we imply here that the active matter is only contractile when bound to the interface. This makes little difference practically as any isotropic contractile stresses are absorbed by the hydrostatic pressure (since the fluid is incompressible) and do not alter the flow.

5.2.2 Linear Stability Analysis

For the system described in the section above, a stationary steady-state is observed if $c = c_0$, $\rho = (k_{\rm off}c_0)/k_{\rm on}$ and $\boldsymbol{R} = R_0\hat{\boldsymbol{r}}$. In this case the steady-state pressure in the drop is $P_0 = P_0^{\rm ext} + 2\gamma_0'/R_0$, where $P_0^{\rm ext}$ is the initial pressure in the external fluid and $\gamma_0' = \gamma_0 - \tilde{\zeta}\Delta\mu c_0 - Bc_0^2$.

First, we will consider the case where $k_{\rm on} = k_{\rm off} = 0$ for simplicity. We apply a general

spherical harmonic perturbation to the system of the form:

$$c = c_0 + \sum_{l=1}^{\infty} \sum_{m=-l}^{l} \delta c_{lm} Y_l^m(\theta, \phi)\,, \tag{5.8}$$

$$\boldsymbol{v} = \sum_{l=1}^{\infty} \sum_{m=-l}^{l} \left[\delta v_{lm}^{(1)}(r) Y_l^m(\theta,\phi)\hat{\boldsymbol{r}} + \delta v_{lm}^{(2)}(r) r(\nabla Y_l^m(\theta,\phi)) + \delta v_{lm}^{(3)}(r)\left(\boldsymbol{r} \times \nabla Y_l^m(\theta,\phi)\right) \right] \tag{5.9}$$

$$\boldsymbol{R} = R\hat{\boldsymbol{r}} = \left\{ R_0 + \sum_{l=1}^{\infty} \sum_{m=-l}^{l} \delta R_{lm} Y_l^m(\theta,\phi) \right\} \hat{\boldsymbol{r}}\,, \tag{5.10}$$

$$P = P_0 + \sum_{l=1}^{\infty} \sum_{m=-l}^{l} \delta P_{lm}(r) Y_l^m(\theta,\phi)\,, \tag{5.11}$$

where Y_l^m are the spherical harmonics and we assume the perturbations $\delta f_{l,m} \ll 1$ for $f = c$, $v^{(i)}$, and R. Note that all real perturbations will satisfy the constraint $\delta f_{lm} = (-1)^m \delta f_{l,-m}^*$. This is demonstrated by figure 5.1, which plots the set of linearly independent perturbations to the droplet shape possible when $l = 2$, as plotted also in [Yoshinaga, 2014].

As the external force $\boldsymbol{f}^{\text{ext}}$ is only non-zero at the interface, one can see that equation (5.1), along with the incompressibility equation $\nabla \cdot \boldsymbol{v} = 0$, is satisfied to first order by Lamb's solutions [Lamb, 1945] when we consider the perturbations in equations (5.8)-(5.11). Thus

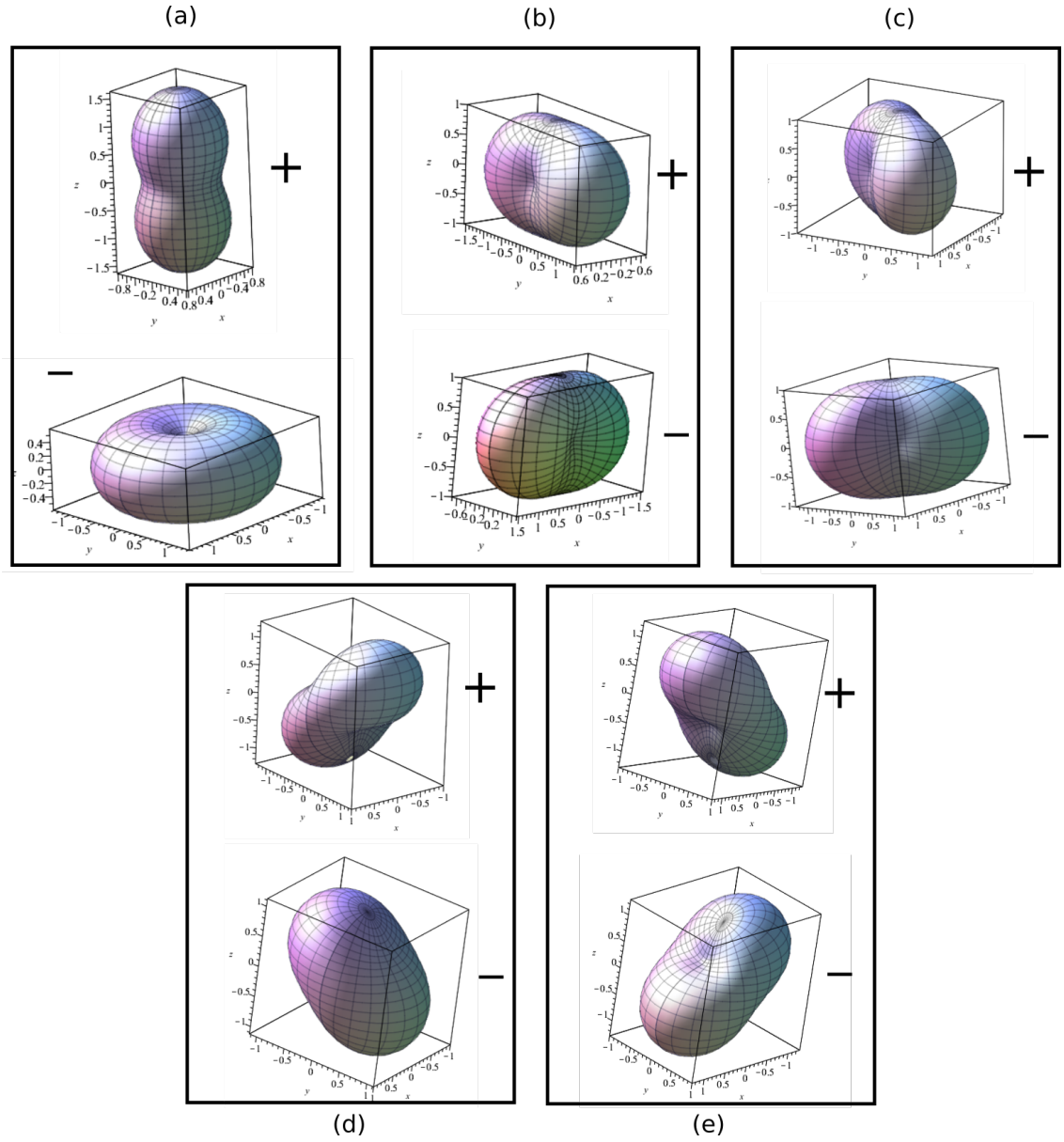

Figure 5.1: Visualisation of perturbation modes of the surface $R(\theta, \phi)$ from equation 5.10 with $R_0 = 1$ and $|\delta R_{lm}| = 1$. The plots show all of the linearly independent modes for the $l = 2$ case, corresponding to the following values for $\delta R_{2,m}$: **(a)** $\delta R_{2,0} = \pm 1$ **(b)** $\delta R_{2,2} = \delta R_{2,-2} = \pm 1/\sqrt{2}$ **(c)** $\delta R_{2,2} = -\delta R_{2,-2} = \pm i/\sqrt{2}$ **(d)** $\delta R_{2,1} = -\delta R_{2,-1} = \pm 1/\sqrt{2}$ **(e)** $\delta R_{2,1} = \delta R_{2,-1} = \pm i/\sqrt{2}$. Where the plus and minus in the figures correspond to the $\pm$ in these definitions. The x, y and z axes have approximately consistent orientations for all plots, with the x-axis forming the front-right base of the box, the y-axis forming the front-left base of the box, and the z axis in the vertical plane.

we can write these first order solutions as:

$$\delta v_{lm}^{(1)}(r) = \begin{cases} a_{lm}^{(0)} r^{l+1} + a_{lm}^{(1)} r^{l-1} & \text{if} \quad r < R \\ b_{lm}^{(0)} r^{-l} + a_{lm}^{(1)} r^{-l-2} & \text{if} \quad r > R \end{cases} \tag{5.12}$$

$$\delta v_{lm}^{(2)}(r) = \begin{cases} \left(a_{lm}^{(0)} (l+3) r^{l+1} + a_{lm}^{(1)} (l+1) r^{l-1} \right) / \left[l(l+1) \right] & \text{if} \quad r < R \\ - \left(b_{lm}^{(0)} (l-2) r^{-l} + b_{lm}^{(1)} l r^{-l-2} \right) / \left[l(l+1) \right] & \text{if} \quad r > R \end{cases} \tag{5.13}$$

$$\delta v_{lm}^{(3)}(r) = \begin{cases} a_{lm}^{(2)} r^{l} & \text{if} \quad r < R \\ b_{lm}^{(2)} r^{-l-1} & \text{if} \quad r > R \end{cases} \tag{5.14}$$

$$\delta P_{lm}(r) = \begin{cases} 2\eta a_{lm}^{(0)} r^{l} (2l+3)/l & \text{if} \quad r < R \\ 2\eta^{\text{ext}} b_{lm}^{(0)} r^{-l-1} (2l-1)/(l+1) & \text{if} \quad r > R \end{cases} \tag{5.15}$$

where η^{ext} is the viscosity of the external fluid, and the constants $a_{l,m}^{(i)}, b_{l,m}^{(i)}$ are determined by the boundary conditions:

$$\boldsymbol{v}^{\text{ext}}\big|_{r=R} - \boldsymbol{v}\big|_{r=R} = 0 \tag{5.16}$$

$$2\hat{\boldsymbol{n}} \cdot \left[\eta \underline{\underline{u}} - \eta^{\text{ext}} \underline{\underline{u}}^{\text{ext}} \right] \big|_{r=R} = \boldsymbol{F}_{lm} + (P - P^{\text{ext}}) \hat{\boldsymbol{n}} \big|_{r=R} \tag{5.17}$$

where $\underline{\underline{u}} = (\nabla \boldsymbol{v} + (\nabla \boldsymbol{v})^{\text{T}})/2$ is the strain rate tensor. From equation (5.10) we can calculate the perturbed normal and tangential vectors to first order in δR_{lm}:

$$\hat{\boldsymbol{n}} = \hat{\boldsymbol{r}} - \sum_{l=1}^{\infty} \sum_{m=-l}^{l} \left[\delta R_{lm} \frac{\partial Y_l^m}{\partial \theta} \hat{\boldsymbol{\theta}} - \delta R_{lm} \frac{1}{\sin(\theta)} \frac{\partial Y_l^m}{\partial \phi} \hat{\boldsymbol{\phi}} \right] \tag{5.18}$$

Substituting (5.8) and (5.10) into (5.2) gives the boundary force:

$$\begin{aligned} \boldsymbol{F}_{lm} = & - \frac{1}{R_0} \left\{ 2\gamma_0' + \left[2\delta c_{lm} \tilde{\zeta} \Delta\mu + \delta R_{lm} \gamma_0' (l+2)(l-1) \right] Y_l^m \right\} \hat{\boldsymbol{r}} \\ & + \frac{1}{R_0} \left[2\delta R_{lm} \gamma_0' - \tilde{\zeta} \Delta\mu \delta c_{lm} \right] \frac{\partial Y_l^m}{\partial \theta} \hat{\boldsymbol{\theta}} \\ & + \frac{1}{R_0 \sin(\theta)} \left[2\delta R_{lm} \gamma_0' - \tilde{\zeta} \Delta\mu \delta c_{lm} \right] \frac{\partial Y_l^m}{\partial \phi} \hat{\boldsymbol{\phi}} \end{aligned} \tag{5.19}$$

to first order in the perturbations. From these forces we can calculate the boundary

conditions for the flow, and the resulting expressions for the constants $a_{l,m}^{(i)}$ and $b_{l,m}^{(i)}$ (outlined in appendix 5.A). Substituting these solutions for the flow into equations (5.4) and (5.7) gives:

$$\frac{\mathrm{d}(\delta c_{lm})}{\mathrm{d}t} = -\frac{l(l+1)c_0}{\eta R_0(2l+1)(2l+3)(2l-1)}\left[3(l+2)(l-1)\gamma_0'\frac{\delta R_{lm}}{R_0} + (2l^2+2l-3)\tilde{\zeta}\Delta\mu\delta c_{lm}\right] - \frac{D}{R_0^2}l(l+1)\delta c_{lm} \tag{5.20}$$

$$\frac{\mathrm{d}(\delta R_{lm})}{\mathrm{d}t} = \frac{l(l+1)}{\eta(2l+1)(2l+3)(2l-1)}\left[-2(l+2)(l-1)\gamma_0'\frac{\delta R_{lm}}{R_0} + \tilde{\zeta}\Delta\mu\delta c_{lm}\right] \tag{5.21}$$

To test the stability, we find the eigenvalues of the stability matrix $\underline{\underline{T}}$ defined as

$$\frac{\mathrm{d}}{\mathrm{d}t}\begin{pmatrix}\delta c_{lm}\\ \\ \delta R_{lm}\end{pmatrix} = \underline{\underline{T}}\begin{pmatrix}\delta c_{lm}\\ \\ \delta R_{lm}\end{pmatrix} \tag{5.22}$$

When either of the eigenvalues $\lambda_{1,2}$ of $\underline{\underline{T}}$ are positive, the steady state is unstable. As one would expect, the eigenvalues are always negative for $\zeta\Delta\mu = 0$, and remain stable if

$$-\frac{D(\eta+\eta^{\mathrm{ext}})}{R_0c_0}(2l+1) < \tilde{\zeta}\Delta\mu < \frac{\gamma_0}{c_0}\,. \tag{5.23}$$

The upper limit suggests an extensile instability, but this corresponds to an effective surface tension of $\gamma_0' < 0$ which is unphysical for a droplet. The lower limit of this range shows there is an instability for contractile activity. Note that the threshold for this contractile instability is independent of the bare surface tension γ_0. The eigenvalues $\lambda_{1,2}$ are plotted for specific parameters in figure 5.2.

Attempting to find the mode number $l_{\max}$ that maximises the unstable eigenvalue λ_1 results in having to solve a polynomial that is too high order to solve analytically. However, since the instability does not depend on the surface tension, we can approximate $l_{\max}$ by solving equation $(\mathrm{d}\delta R_{lm})/(\mathrm{d}t) = 0$ for δR_{lm}, hence assuming that the shape is

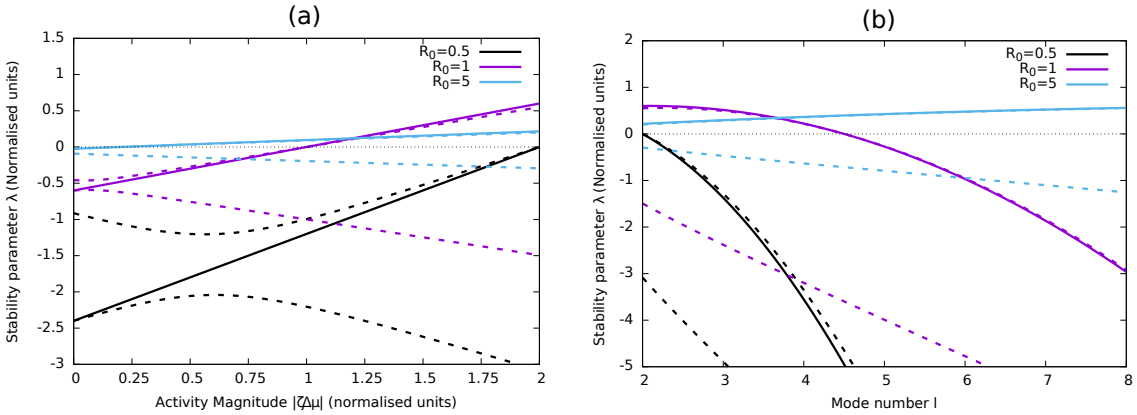

Figure 5.2: Eigenvalues λ_1 and λ_2 (dashed lines) plotted against (a) activity and (b) mode number and approximate solution λ^* (solid lines) for three values of the initial droplet radius R_0. We normalise the units by setting $\gamma_0 = 1$, $c_0 = 1$ and $\eta = 1$. In both figures we assume a diffusion constant of $D = 0.1$. In figure (b) we take $\tilde{\zeta}\Delta\mu = -2$. Note that, in the cases where only one dotted line is visible, the other is obscured by the approximate solution λ^*.

quasistatic. From equation (5.21) we can read off the solution:

$$\delta R^*_{lm} = \frac{\tilde{\zeta}\Delta\mu R_0 \delta c_{lm}}{2\gamma_0'(l+2)(l-1)}\,. \tag{5.24}$$

Substituting this for δR_{lm} in equation (5.20) we find:

$$\frac{\mathrm{d}\delta c^*_{lm}}{\mathrm{d}t} = -\frac{l(l+1)}{R_0^2}\left[\frac{\tilde{\zeta}\Delta\mu c_0 R_0}{2(2l+1)\eta} + D\right]\delta c^*_{lm} \equiv \lambda^* \delta c^*_{lm}\,. \tag{5.25}$$

Comparing this approximate stability parameter λ^* to the full solutions in figure 5.2, we see that it is a very good approximation to the maximum stability parameter, especially for larger droplets, where the deformations result in small contributions to the flow. In smaller droplets the results deviate more because the surface tension force is more significant, and so any deformation will create flow which couples to the evolution of the concentration field. Nonetheless, this approximate solution always leads to the same contractile activity threshold from equation (5.23) as before but now the stability parameter λ^* is only an approximation. We can get an approximate analytical expression for the maximum mode $l_{\max}$ by solving $(\partial\lambda^*)/(\partial l) = 0$, which gives the cubic equation:

$$16D\eta l^3 - 2(\tilde{\zeta}\Delta\mu R_0 c_0 + 12D\eta)l^2 - 2(\tilde{\zeta}\Delta\mu R_0 c_0 + 6D\eta)l - (\tilde{\zeta}\Delta\mu R_0 c_0 + 2D\eta) = 0 \tag{5.26}$$

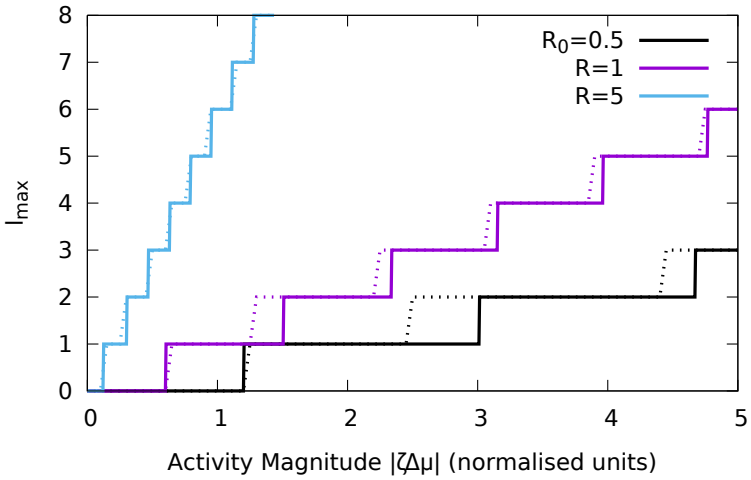

Figure 5.3: Maximum mode number $l_{\max}$ rounded to nearest integer value for several values of R_0. Numerical solutions to the full expression for $l_{\max}$ (dotted line) and analytical approximation (solid line) from equation (5.26) is plotted. The same parameter values are used as in figure 5.2.

The real solution of this equation is plotted in figure 5.3 where the value of $l_{\max}$ is rounded to the nearest integer, since only integer values of l are physically allowed. We see from figure 5.3 that this maximum mode number increases marginally more quickly in the numerical solutions for $l_{\max}$. This suggests that while the surface tension force does not affect the threshold, the coupling between boundary evolution and concentration evolution can result in greater instability of the higher perturbation modes.

We can extend this to consider the case when the active concentration can bind and unbind from the interface and is soluble only in the droplet interior. In order to solve this we assume that we can take the bulk concentration ρ to be quasistatic, such that $\partial\rho/\partial t = 0$. We can then solve equation (5.5) assuming a generic spherical perturbation to ρ of the form:

$$\rho = \frac{k_{\text{off}} c_0}{k_{\text{on}}} + \delta\rho(t) f(r) Y_l^m(\theta, \phi) \tag{5.27}$$

From this, solving $\partial\rho/\partial t = 0$ given the boundary condition in (5.6) gives:

$$f(r) = \frac{\delta c(t)}{\delta\rho(t)} \frac{k_{\text{off}} R_0}{D_\rho l + k_{\text{on}} R_0} \left(\frac{r}{R_0}\right)^l . \tag{5.28}$$

We can see from this solution that if the diffusion is dominant $D_\rho \gg k_{\mathrm{on,off}}$, the function $f(r)$ is close to zero and the concentration inside the droplet will be approximately unchanged from ρ_0. However, if the binding rates are fast then the concentration in the droplet bulk will be coupled to the concentration on the interface. Substituting this in we see that this extra coupling alters the activity threshold from equation (5.23). Now the system will be unstable for a contractile active fluid when:

$$\tilde{\zeta}\Delta\mu < -\frac{(2l+1)(\eta+\eta^{\mathrm{ext}})}{c_0}\left(\frac{D}{R_0}+\frac{D_\rho R_0 k_{\mathrm{off}}}{(l+1)(D_\rho l + k_{\mathrm{on}}R_0)}\right). \tag{5.29}$$

Clearly, with this assumption the coupling to a bulk concentration always increases the activity required to break symmetry, assuming that the stationary state concentration c_0 is the same in both cases. This is because the active fluid unbinds at areas of higher concentration, damping any peaks in the concentration profile on the surface. This effect is much less significant when diffusion in the bulk of the droplet is low compared to the binding rate k_{on}, because then the motors are more likely to rebind at the same location before diffusing away. The dispersion relation is also shifted by this term. In all cases the stability eigenvalues are reduced by the introduction of this coupling, and the dispersion relation shifted down with the introduction of non-zero binding rates.

5.2.3 Results in 2D and comparison with simulations

We have performed 2-dimensional numerical simulations of both systems (the active boundary and active droplet) using an Immersed Boundary method to model the moving interface between the internal and external fluid. Generalising the simulations to 3D is non-trivial and goes beyond the scope of this work (see section 6.6.3).

In order to compare the results of analytical calculations in section 5.2.2 to these simulations we need to recalculate in two dimensions. We repeat the calculation in plane polar coordinates with a perturbation to the concentration of the form $c = c_0 + \delta c_k(t)\exp(ik\theta)$ where $\delta c_k(t)$ is in general a complex function. In 2-dimensions we find that the droplet shape is stable to all perturbations, because the normal components of the

flow at the interface, due to a gradient in the surface tension, always cancel (as calculated for the reaction-diffusion system in [Yoshinaga, 2014]). This makes the 2D case a much simpler analogue of the 3D system, as it is only governed the partial differential equation for c given in equation (5.4). Therefore we only have to consider perturbations to the concentration c and the flow components v_r, v_θ and the pressure P. The flow and pressure once again is given by (the 2D analogue of) Lamb's solutions around a circular drop of radius $R = R_0$:

$$v_r = \begin{cases} \sum_{k=1}^{\infty} \left(a_k^{(0)} r^{k+1} + a_k^{(1)} r^{k-1} \right) \mathrm{e}^{ik\theta} & \text{if} \quad r < R_0 \\ \sum_{k=1}^{\infty} \left(b_k^{(0)} r^{-k+1} + b_k^{(1)} r^{-k-1} \right) \mathrm{e}^{ik\theta} & \text{if} \quad r > R_0 \end{cases} \tag{5.30}$$

$$v_\theta = \begin{cases} i \sum_{k=1}^{\infty} \left[(k+2) a_k^{(0)} r^{k+1} + k a_k^{(1)} r^{k-1} \right] \mathrm{e}^{ik\theta}/k & \text{if} \quad r < R_0 \\ -i \sum_{k=1}^{\infty} \left[(k-2) b_k^{(0)} r^{-k+1} + k b_k^{(1)} r^{-k-1} \right] \mathrm{e}^{ik\theta}/k & \text{if} \quad r < R_0 \end{cases} \tag{5.31}$$

$$P = \begin{cases} P_0 + 4\eta \sum_{k=1}^{\infty} (k+1) a_k^{(0)} r^k \mathrm{e}^{ik\theta}/k & \text{if} \quad r < R_0 \\ P_0^{\mathrm{ext}} + 4\eta \sum_{k=1}^{\infty} (k-1) b_k^{(0)} r^{-k} \mathrm{e}^{ik\theta}/k & \text{if} \quad r > R_0 \,. \end{cases} \tag{5.32}$$

Applying the perturbation to the concentration and solving the boundary conditions of continuous velocity and force balance at the interface we can solve for the constants $a(i)_k, b_k^{(i)}$ and find:

$$a_k^{(0)} = -\delta c_k(t) \frac{\tilde{\zeta} \Delta\mu k}{4 R_0^{k+1} (\eta + \eta^{\mathrm{ext}})} \tag{5.33}$$

$$a_k^{(1)} = \delta c_k(t) \frac{\tilde{\zeta} \Delta\mu k}{4 R_0^{k-1} (\eta + \eta^{\mathrm{ext}})} \tag{5.34}$$

$$b_k^{(0)} = -\delta c_k(t) \frac{\tilde{\zeta} \Delta\mu k R_0^{k-1}}{4 (\eta + \eta^{\mathrm{ext}})} \tag{5.35}$$

$$b_k^{(1)} = \delta c_k(t) \frac{\tilde{\zeta} \Delta\mu k R_0^{k+1}}{4 (\eta + \eta^{\mathrm{ext}})} \tag{5.36}$$

Substituting this back into the equation for $\partial c/\partial t$ (taking the binding constants as

$k_{\text{on}} = k_{\text{off}} = 0$) then we find:

$$\delta c'(t) = s\delta c(t) \equiv -k\delta c(t) \left[\frac{\tilde{\zeta}\Delta\mu}{2R_0\left(\eta + \eta^{\text{ext}}\right)} c_0 + \frac{kD}{R_0^2} \right] . \tag{5.37}$$

Thus, the threshold for the effective activity in this case can just be read off as

$$\tilde{\zeta}\Delta\mu < -\frac{2kD\left(\eta + \eta^{\text{ext}}\right)}{c_0 R_0} . \tag{5.38}$$

From equation (5.37) we can find the mode k which maximises the stability parameter s:

$$k_{\text{max}} = -\frac{\tilde{\zeta}\Delta\mu R_0 c_0}{4D(\eta + \eta^{\text{ext}})} . \tag{5.39}$$

The resulting phase diagram that we acquire is plotted in figure 5.4. We see that the analytical calculations predict the thresholds for the maximum perturbation mode well. Using the analytical expression for k_{max} we find that the second mode should only be dominant in the simulations tested when $D = 0.1$ and $\tilde{\zeta}\Delta\mu < -1.5$. We measure this in the simulations by plotting the modes in the concentration profile (calculation of these is outlined in section 6.5.1) and observe that only in these two simulation runs does the second mode evolve faster than the first, resulting in the initial formation of two peaks. When we observe these 2 peaks form on the droplet interface, we see that these are themselves unstable, and at later time in the simulations these coalesce to form a single peak (see figure 5.5 and section 6.5.2 in chapter 6).

We see that the simulations actually appear to break symmetry only for activity values slightly larger than the threshold. One might expect this here because the velocity at the interface that determines the convergence of active concentration is maximum exactly at the boundary. In the simulations the interface velocity is approximated by interpolating the flow at the surrounding fluid points by a numerical analogue of the Dirac delta function (see section 6.3.2). Therefore, the velocity at the interface may be slightly underestimated compared to the analytical calculation since the neighbouring fluid points will have slightly smaller viscosities. Furthermore, as the stability parameter becomes very small we expect

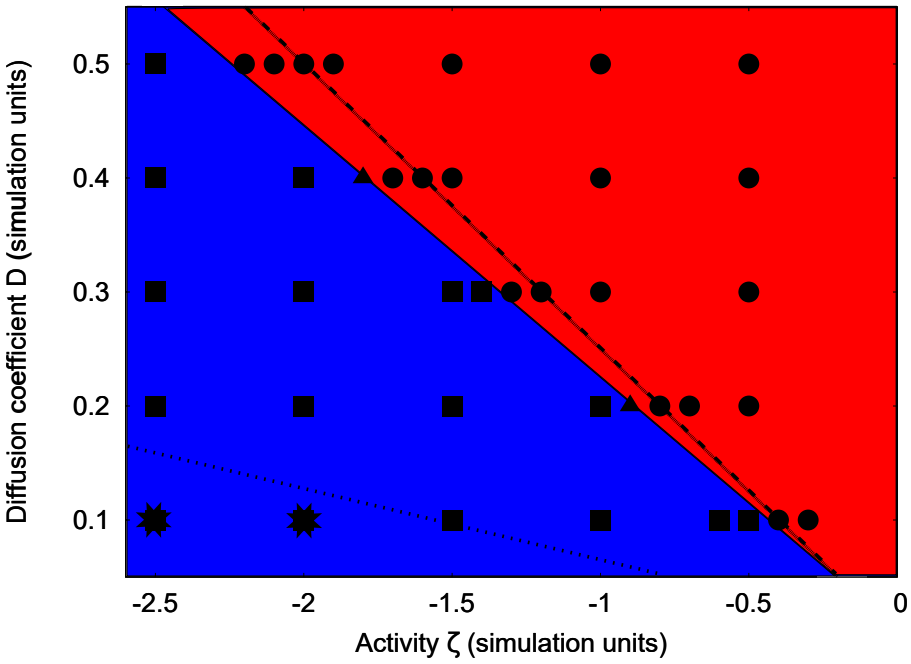

Figure 5.4: Phase diagram showing symmetry breaking in the simulations of an active droplet. The red region (circular dots) are simulations where the boundary was stable and the concentration remains constant. The blue region (square dots) is where the droplet reaches a motile steady state. Triangular points indicate simulations where it the droplet profile neither completely homogenises or continues to break symmetry over the simulation time. Star shaped dots indicate cases where the concentration profile initially broke symmetry into two peaks, before coalescing to one (see figure 5.5). The black dashed line indicates the prediction of activity threshold for the $k = 1$ mode in 2D. The black dotted line shows where the threshold above which the $k = 2$ mode should be dominant, calculated by solving equation (5.39) for $k_{\max} = 2$. We again use the same parameters as in figure 5.2.

the system to evolve very slowly, and so the system may take a very long time to break symmetry near to the activity threshold.

5.3 Active polar fluid droplet

We will now consider the contrasting case of a droplet of active polar fluid immersed in a passive fluid medium. We assume the active liquid crystal has constant polarisation magnitude $|\boldsymbol{p}| = 1$ and constant concentration and density. The free energy for a finite

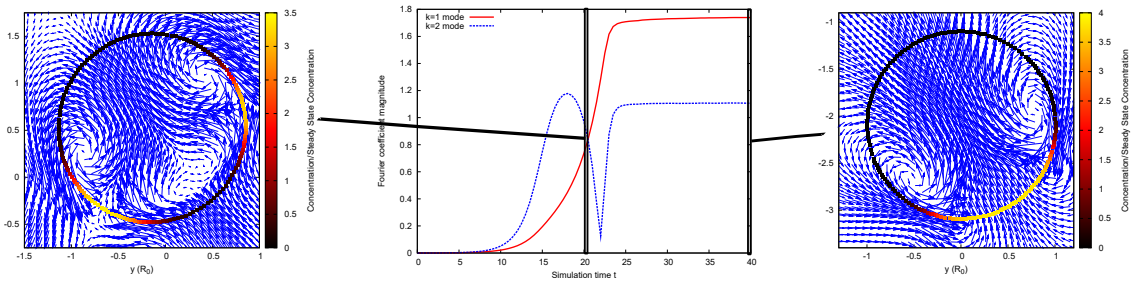

Figure 5.5: Centre plot shows the evolution of the magnitude of the first two Fourier modes of the concentration for a simulations with $\tilde{\zeta}\Delta\mu = -2.5$, $B = 2$ and $D = 0.1$. These Fourier modes track the shape of the concentration profile, we see that initially two peaks form (see $k = 2$ mode and left figure) then later these coalesce to form one ($k = 1$ mode dominant and right figure). The droplet profiles are plotted at simulation times $t = 20$ and $t = 100$. After $t = 40$ the steady state is constant hence the central figure is only plotted to $t = 40$ for visibility.

passive polar liquid crystal with constant particle concentration is given by:

$$F = \frac{1}{2}\int_{\Omega_0}\left[K(\nabla \boldsymbol{p})^2 + K_S \nabla\cdot\boldsymbol{p} - h_{\parallel}^0 \boldsymbol{p}^2\right]\mathrm{d}^3\boldsymbol{r} + \frac{1}{2}\int_{\Sigma}\left[W_1\left[\boldsymbol{p}\pm\hat{\boldsymbol{n}}\right]^2 + W_2(\boldsymbol{p}.\hat{\boldsymbol{n}})^2\right]\mathrm{d}A \tag{5.40}$$

where K is the elastic constant for distortions in the liquid crystal using the "one constant approximation", and W_1 and W_2 are positive coefficients for the normal and tangential anchoring terms respectively. Note that the lowest order allowed surface term is actually proportional to $\boldsymbol{p}\cdot\hat{\boldsymbol{n}}$, but this can be minimised for $|p| > 1$ and hence can cause instabilities, both for the linear stability analysis and numerical calculations, as the anchoring strength is increased. In this way the anchoring terms we used are similar to those commonly used to describe a nematic liquid crystal [Nobili and Durand, 1992]. In this chapter we consider the case of outward normal anchoring such that the $\pm$ sign in equation (5.40) is evaluated as a minus sign and $W_2 = 0$. Thus the surface free energy is minimised now for $\boldsymbol{p} = \hat{\boldsymbol{n}}$. The molecular field governs the equilibrium contribution to the dynamics of the polarisation field and is given by $\boldsymbol{h} = -\delta F/\delta\boldsymbol{p}$ and the Lagrange multiplier $h_{\parallel}^0$ ensures $|\boldsymbol{p}| = 1$. K_s is the spontaneous splay coefficient, allowed by symmetry for a polar liquid crystal. Note that this term can be rewritten as a surface term using Gauss's divergence theorem, which, depending on the sign of K_s, acts to promote inward or outward normal anchoring of the polarisation.

As outlined in chapter 2, the out-of-equilibrium nature of active forces means that they cannot be described using a free energy formalism, however equations for the active stress can be derived via an Onsager approach as shown in [Kruse et al., 2004] and introduced in chapter 2. With a constant concentration of filaments inside the droplet the active stress can be written as:

$$\underline{\underline{\sigma}}^{\mathrm{act}} = -\zeta\Delta\mu\left(\boldsymbol{pp} - \frac{\mathbb{I}}{d}\right), \tag{5.41}$$

where we have used the traceless form here and d is the dimensionality of the system. In this chapter we ignore the effect of active polymerisation of the filaments which can exert polar forces at the boundary, we focus on the effect of active contraction ($\zeta\Delta\mu < 0$) and extension ($\zeta\Delta\mu > 0$).

The free energy in equation (5.40) generates a stress related to the relative orientation of filaments in the active fluid, known as the distortion stress, which is given by

$$\underline{\underline{\sigma}}^{\mathrm{dis}} = \frac{\nu}{2}\left(\boldsymbol{ph} + \boldsymbol{hp}\right) + \frac{1}{2}\left(\boldsymbol{ph} - \boldsymbol{hp}\right) + \underline{\underline{\sigma}}^{\mathrm{e}} \tag{5.42}$$

where ν is a liquid crystal constant coupling the molecular field $\boldsymbol{h}$ to the flow, the second term is the antisymmetric stress and the final term is the Ericksen stress, which is essentially an extension of the hydrostatic pressure for complex fluids, as detailed in chapter 2. Considering force balance, we can derive the equations of motion for an incompressible active fluid at low Reynolds' number given these internal stresses,

$$0 = \eta\nabla^2\boldsymbol{v} + \nabla\cdot\left(\underline{\underline{\sigma}}^{\mathrm{act}} + \underline{\underline{\sigma}}^{\mathrm{dis}}\right) - \nabla P \tag{5.43}$$

$$0 = \nabla\cdot\boldsymbol{v} \tag{5.44}$$

which is the incompressible Stokes' equation as in (5.1) with extra source terms due to the internal stresses. It is worth noting that calculation of the Ericksen stress can be simplified by the relation $\partial_\beta\sigma^e_{\alpha\beta} = -h_\gamma\partial_\alpha p_\gamma$ (in the case of constant concentration), which can be substituted directly into equation (5.43). We use the same boundary conditions

for the flow and the stress as given by equations (5.16) and (5.17) except that now the interface is passive and so we take the surface tension γ to be constant. The interface dynamics are again given by equation (5.7).

Finally, the evolution of the polarisation field $\boldsymbol{p}$ is given by:

$$\frac{\partial \boldsymbol{p}}{\partial t} = -\left(\boldsymbol{v}\cdot\nabla\right)\boldsymbol{p} - \underline{\underline{\omega}}\cdot\boldsymbol{p} - \nu\underline{\underline{u}}\cdot\boldsymbol{p} + \frac{\boldsymbol{h}}{\Gamma} + \lambda\Delta\mu\boldsymbol{p} \tag{5.45}$$

where $\underline{\underline{u}} = \left[(\nabla\boldsymbol{v}) + (\nabla\boldsymbol{v})^T\right]/2$ is the strain rate tensor, $\underline{\underline{\omega}} = \left[(\nabla\boldsymbol{v})^T - (\nabla\boldsymbol{v})\right]/2$ is the vorticity tensor and Γ is the rotational viscosity. The parameter λ is an active terms which promotes filament alignment, however, this can be absorbed into the Lagrange multiplier $h_\parallel^0$ so it does not enter into the linear stability analysis.

5.3.1 Linear Stability Analysis

For the case of outward normal anchoring at the interface, and taking $K_s = 0$, we find that a non-moving steady state for this system is just given by a spherical droplet with an aster in the polarisation field:

$$\begin{aligned} &\boldsymbol{p} = \hat{\boldsymbol{r}}\,, \quad \boldsymbol{R} = R_0\hat{\boldsymbol{r}}\,, \quad \boldsymbol{v} = 0\,, \quad h_\parallel^0 = -\frac{2K}{r^2} \\ &\text{and} \quad P_0^{\text{int}} = P_0^{\text{ext}} + 2\frac{\gamma}{R_0} + \frac{K}{R_0^2} - 2\zeta\Delta\mu\left[\frac{1}{3} + \ln\left(\frac{r}{R_0}\right)\right]\,, \end{aligned} \tag{5.46}$$

where P_0^{ext} is the hydrostatic pressure in the external medium (assumed constant). The continuum approximation breaks down near the defect at $r = 0$ and so we can find unphysical behaviour such as infinite hydrostatic pressure as in [Kruse et al., 2004].

Unlike in the active boundary perturbation, here we omit the $l = 1$ mode perturbation as this does not agree with the assumptions we make in the following analysis (see the end of this section for details). The rest of the perturbation modes ($l > 1$) can be applied

as follows:

$$\boldsymbol{p} = \hat{\boldsymbol{r}} + \sum_{l=2}^{\infty}\sum_{m=-l}^{l} a_{lm}(r)\left[\delta p_{lm}^{(1)}(t)\left(\frac{\partial Y_l^m}{\partial\theta} - \frac{1}{\sin(\theta)}\frac{\partial Y_l^m}{\partial\phi}\right)\hat{\boldsymbol{\theta}} + \delta p_{lm}^{(2)}(r)\left(\frac{\partial Y_l^m}{\partial\theta} + \frac{1}{\sin(\theta)}\frac{\partial Y_l^m}{\partial\phi}\right)\hat{\boldsymbol{\phi}}\right], \tag{5.47}$$

$$\boldsymbol{v} = \sum_{l=2}^{\infty}\sum_{m=-l}^{l}\left[\delta v_{lm}^{(1)}(r)Y_l^m\hat{\boldsymbol{r}} + \delta v_{lm}^{(2)}(r)r(\nabla Y_l^m) + \delta v_{lm}^{(3)}(r)\left(\boldsymbol{r}\times\nabla Y_l^m\right)\right] \tag{5.48}$$

$$\boldsymbol{R} = R\hat{\boldsymbol{r}} = \left\{R_0 + \sum_{l=2}^{\infty}\sum_{m=-l}^{l}\delta R_{lm}Y_l^m(\theta,\phi)\right\}\hat{\boldsymbol{r}}\,, \tag{5.49}$$

$$P = P_0 + \sum_{l=2}^{\infty}\sum_{m=-l}^{l}\delta P_{lm}(r)Y_l^m(\theta,\phi)\,. \tag{5.50}$$

Note that the constraint $|\boldsymbol{p}| = 1$ does not permit a first order perturbation of p_r. The form of the function $a_{lm}(r)$ of the polarisation perturbations affects the calculation a great deal, and cannot be solved for analytically from equation (5.45) due to the coupling between the polarisation and the flow. As a simplification, we consider the case where the polarisation perturbation has no r-dependence, effectively assuming that all the filaments along a radial spoke are perturbed by the same angle. This means that the predicted behaviour will only be observed if we are in the regime where distortions in the bulk of the active fluid are strongly coupled to the behaviour at the interface. This approximation is only valid if the anchoring energy is large ($W_1 \gg \zeta\Delta\mu$). In addition, this approximation also breaks down for small values of K, where the polarisation field can be distorted by the activity near the droplet centre. This will be discussed further in section 5.3.2 and chapter 6.

Due to the internal stress of the droplet, the general solutions to the Stokes equation from equations (5.12)-(5.15) are only complete solutions for the case $r > R$. Inside the droplet we need to add the specific solutions from the internal stress. Assuming $a_{lm}(r) = 1$, we find that the bulk free energy density from equation (5.40) to first order in the perturbation reads

$$f_{lm}^b = -\frac{K}{r^2}l(l+1)\delta p_{lm}^{(1)}Y_l^m \tag{5.51}$$

where $F_d = \int_{\Omega_0} \left[\sum_{l=2}^{\infty}\sum_{m=-l}^{l} f_{lm}^b\right] \mathrm{d}^3\boldsymbol{r} + \int_{\Sigma} \left[\sum_{l=2}^{\infty}\sum_{m=-l}^{l} f_{lm}^s\right] \mathrm{d}A$, then the molecular field reads:

$$\begin{aligned}\boldsymbol{h}_{lm} =& \frac{K}{r^2}\left\{2l(l+1)\delta p_{lm}^{(1)} Y_l^m \hat{\boldsymbol{r}} - (l+2)(l-1)\left(\delta p_{lm}^{(1)}\frac{\partial Y_l^m}{\partial\theta} - \frac{\delta p_{lm}^{(2)}}{\sin(\theta)}\frac{\partial Y_l^m}{\partial\phi}\right)\hat{\boldsymbol{\theta}}\right.\\ &\left.-(l+2)(l-1)\left(\delta p_{lm}^{(2)}\frac{\partial Y_l^m}{\partial\theta} + \frac{\delta p_{lm}^{(1)}}{\sin(\theta)}\frac{\partial Y_l^m}{\partial\phi}\right)\hat{\boldsymbol{\phi}}\right\}. \end{aligned} \tag{5.52}$$

The surface free energy density $f_{lm}^s = 0$ to first order in the perturbations (as the term is squared), however there are leading order contributions to the surface molecular field:

$$\begin{aligned}\boldsymbol{h}_{lm}^s =& -\left[\left(\delta p^{(1)} + \frac{\delta R_{lm}}{R_0}\right)\frac{\partial Y_l^m}{\partial\theta} - \frac{\delta p_{lm}^{(2)}}{\sin(\theta)}\frac{\partial Y_l^m}{\partial\phi}\right]\hat{\boldsymbol{\theta}}\\ &-\left[\delta p_{lm}^{(2)}\frac{\partial Y_l^m}{\partial\theta} + \frac{1}{\sin(\theta)}\left(\delta p^{(1)} + \frac{\delta R_{lm}}{R_0}\right)\frac{\partial Y_l^m}{\partial\phi}\right]\hat{\boldsymbol{\phi}}. \end{aligned} \tag{5.53}$$

Note that $\boldsymbol{p} = \hat{\boldsymbol{n}}$ at the interface to first order if $\delta p_{lm}^{(1)} = -\delta R_{lm}/R_0$ and $\delta p_{lm}^{(2)} = 0$. We are then able to substitute in the bulk expressions for free energy and molecular field into equations (5.41) and (5.42) to acquire the specific part of the flow solutions from equation (5.43). We then add the boundary contributions to the distortion stress from (5.53) to the stress balance boundary condition from (5.17) to account for total force balance at the interface.

We have not considered here a perturbation to the Lagrangian multiplier $h_{\parallel}^0$ which would be necessary to satisfy the radial component of equation (5.45). If this is included we cannot solve for the flow analytically, so we omit this equation from our analysis and only consider the angular components of equation (5.45). This means that in this analysis $(\partial\,|\boldsymbol{p}|\,/\partial t) = 0$ is not satisfied. Due to the spherical harmonic identity, we can decompose the angular components of the polarisation evolution equation (5.45) into equations for

the perturbations $\delta p_{lm}^{(1)}$ and $\delta p_{lm}^{(2)}$ as follows:

$$\frac{\mathrm{d}}{\mathrm{d}t}\left(\delta p_{lm}^{(1)}\right) = -\frac{\nabla\cdot}{l(l+1)Y_l^m}\frac{\mathrm{d}}{\mathrm{d}t}(\boldsymbol{p}-\hat{\boldsymbol{r}}) \tag{5.54}$$

$$\frac{\mathrm{d}}{\mathrm{d}t}\left(\delta p_{lm}^{(2)}\right) = -\frac{1}{l(l+1)Y_l^m}\hat{\boldsymbol{r}}\cdot\left[\nabla\times\frac{\mathrm{d}}{\mathrm{d}t}(\boldsymbol{p}-\hat{\boldsymbol{r}})\right]. \tag{5.55}$$

An important note here is that the polarisation is defined throughout the drop, however as we are considering strong coupling between the deformation and polarisation field, we calculate just the evolution at $r = R$. Substituting in the expressions for the flow, we can construct the stability matrix $\underline{\underline{T}}$ such that:

$$\frac{\mathrm{d}}{\mathrm{d}t}\begin{pmatrix}\delta R_{lm}\\ \delta p_{lm}^{(1)}\\ \delta p_{lm}^{(2)}\end{pmatrix} = \underline{\underline{T}}\begin{pmatrix}\delta R_{lm}\\ \delta p_{lm}^{(1)}\\ \delta p_{lm}^{(2)}\end{pmatrix} \qquad \text{at} \quad r = R \tag{5.56}$$

We find that $T_{31} = T_{32} = T_{13} = T_{23} = 0$, and so $\underline{\underline{T}}$ is block diagonal. Thus, one of the eigenvalues is $\lambda_3 = T_{33}$ and the other two are the solutions to $(T_{11}-\lambda)(T_{22}-\lambda) - T_{12}T_{21}$. The eigenvalue λ_3 can be expressed as the following linear sum:

$$\lambda_3 = -a_K(\nu, l, \Gamma, \eta, \eta_{\text{ext}}, R_0)K - a_W(\nu, l, \Gamma, \eta, \eta_{\text{ext}}, R_0)W_1 + a_Z(\nu, l, \Gamma, \eta, \eta_{\text{ext}}, R_0)\zeta\Delta\mu \tag{5.57}$$

where a_K and a_W always positive for physical values of the parameters (*i.e.* $\Gamma, \eta, \eta_{\text{ext}}, R_0 > 0$). The coefficients $a_{K,W,Z}$ are lengthy expressions so we omit them here. We see that $\lambda_3 > 0$ for $\zeta\Delta\mu < \zeta\Delta\mu_{c3} < 0$ if $\nu > 1$ and $\zeta\Delta\mu > \zeta\Delta\mu_{c3} > 0$ otherwise. Hence, the liquid crystal coupling parameter determines whether this state is unstable to contractile or extensile activity. However, $|\zeta\Delta\mu_{c3}|$ scales linearly with the anchoring coefficient W_1, so as the anchoring strength increases this particular eigenmode becomes more stable, for all values of l. We can see this clearly when we consider the strong anchoring limit, whereby the polarisation $\boldsymbol{p} = \hat{\boldsymbol{n}}$ at the boundary, and hence $\delta p_{lm}^{(2)} = 0$. This means that in this limit $\delta p_{lm}^{(2)}$ perturbations are disallowed.

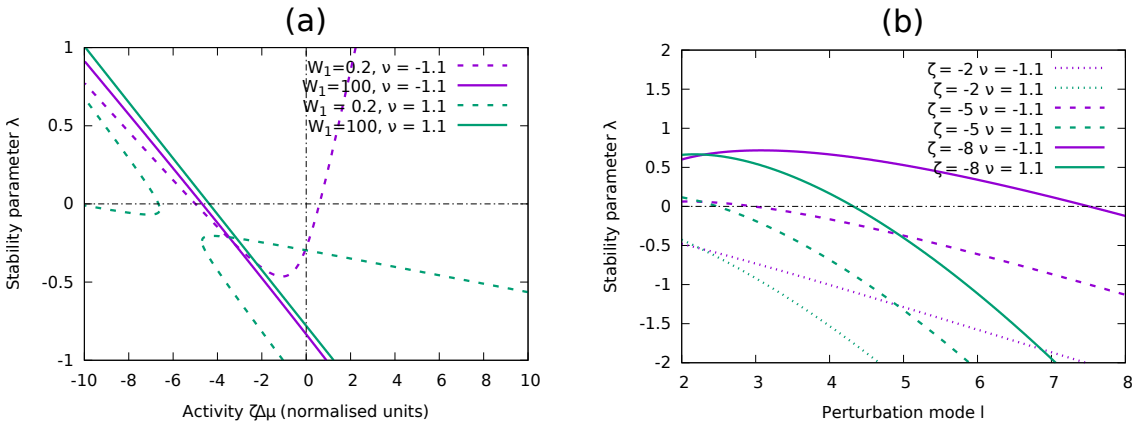

Figure 5.6: Eigenvalues λ_1 and λ_2 in the rod-like ($\nu < -1$ magenta lines) and disc-like ($\nu > 1$ cyan lines) plotted against: **(a)** activity for low (dotted lines) and high (solid lines) anchoring cases and perturbation mode $l = 2$; **(b)** mode number l for three values of the activity with $W_1 = 100$. Other parameters $\eta = \eta_{\text{ext}} = \Gamma = 1$, $K = 0.1$, $\gamma = 1$, $R_0 = 1$.

The eigenvalues $\lambda_{1,2}$ come from the coupled dynamics of the boundary and the polarisation perturbation $\delta p_{lm}^{(1)}$. The expressions for these are lengthy and have non-linear dependence on $\zeta\Delta\mu$, K and W_1 unlike the value of λ_3 so we characterise their behaviour here via the plots in figures 5.6. We can see from figure 5.6(a) that for low anchoring the maximum eigenvalue can be unstable for two activity thresholds, one contractile and one extensile threshold. The extensile threshold, which we will label $\zeta\Delta\mu_{c2}$, scales linearly with W_1 again, and so does not contribute in the strong anchoring case where $\delta p_{lm}^{(1)} = -\delta R_{lm}/R_0$. This is because it corresponds to the case where the polarisation perturbation at the boundary acts in the opposite direction to the perturbation in the normal vector.

The other threshold $\zeta\Delta\mu_{c1}$ does not scale linearly with W_1. This can be seen in figure 5.6(a), where the contractile threshold is actually reduced slightly for large anchoring values. Interestingly, we see that this threshold is always for contractile activity and its value plateaus at large anchoring. So, when the polarisation and normal vector are strongly coupled, we find that the system is only unstable for an active contractile fluid. This can be explained by considering the splay distribution in the droplet, as shown in figure 5.7 for a 2D projection. We see that, if we perturb the boundary shape and assume that $\delta p_{lm}^{(2)} = -\delta R_{lm}$ and $\delta p_{lm}^{(3)} = 0$, then there is increased outward splay where the curvature

increases and vice versa. As discussed in previous chapters, in an active contractile liquid crystal, splay deformations in the alignment lead to outward flow, this outward flow promotes an increase in curvature at the bulges of the droplet, and corresponding inward flow at areas of decreased splay perpetuating the instability. This competes with the stabilising effect of the elastic free energy parameter K and the surface tension γ.

In the limit of strong anchoring at the interface, we see that the eigenvalues λ_2 and λ_3 are always negative, and so only λ_1 can be positive. Hence, if we consider the case where the polarisation vector $\boldsymbol{p}$ is fixed to be in the normal direction (and continue with the assumption that it has no r dependence), the only degree of freedom remaining is R. Explicitly, we substitute $\delta p_{lm}^{(1)} = -\delta R_{lm}/R_0$ and $\delta p_{lm}^{(2)} = 0$ into our equations, and the stability parameter in this limit is λ_1' where $\delta\dot{R}_{lm} = \lambda_1'\delta R$. We can plot λ_1' and λ_1 against the rotational diffusion and we see that they agree for large W_1 if $\Gamma \ll \eta$, such that the polarisation responds to the strong anchoring on shorter time-scales than from active flow. However, we note that there is still good agreement when $\Gamma \approx \eta$ (see figure 5.7(b)) and many values of $\Gamma > \eta$. An analytical expression for the mode number l_{max} corresponding to the maximum of the stability parameter, is still unobtainable analytically even in this simplified case of strong anchoring as $(\partial\lambda_1')/(\partial l) = 0$ gives a polynomial of 11th order in l. λ_1' does give a simpler expression for the activity threshold however $\zeta\Delta\mu_c'$ that is linear in K and γ. In the case where $\eta_{\text{ext}} = \eta$ (which we take for brevity), we find

$$\zeta\Delta\mu_c' = -\frac{K(l+3)}{2(l+1)(4l^2+3l-6)R_0^2}\left[4(\nu+1)l^4+2(3\nu+11)l^3+(37-11\nu)l^2+(17-25\nu)l\right.$$
$$\left.-2(3\nu+4)\right]-\frac{\gamma(l+3)(l+2)(l-1)}{(4l^2+3l-6)R_0}\,. \tag{5.58}$$

The above calculation does extend to the $l = 1$ mode of deformation, and predicts similar contractile thresholds, but we have to be more careful with our assumptions in this case. For small perturbations there is no deformation in the droplet interface for the $l = 1$ mode, we can see this by calculating the change in curvature of the boundary due to

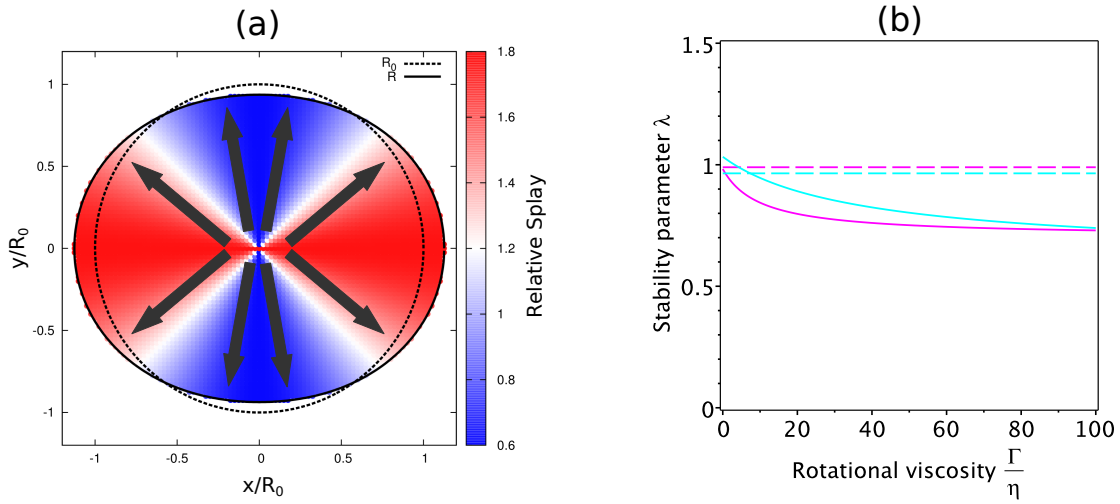

Figure 5.7: **(a)** Sketch of the instability mechanism for the $l = 2$ mode (2D projection at $\theta = 0$). The solid line plots the perturbed shape, while the dotted line is the original circle and the shading shows the corresponding change in splay if we use the assumptions outlined in the text. This relative splay is calculated as $(\nabla \cdot \boldsymbol{p})^2/(\nabla \cdot \hat{\boldsymbol{r}})^2$, with blue shading indicating a decrease in splay and red showing an increase. The black arrows illustrate the polarisation direction (exaggerated for clarity). **(b)** λ_1 at high anchoring value of $W_1 = 100$ (solid line) and λ^* dotted line against the relative rotational viscosity Γ/η in the rod-like (magenta lines) and disc-like (cyan lines) cases. We see that only when Γ is very large does the real values diverge much from the approximation. Other values used are $K = 0.1$, $\zeta\Delta\mu = -10$, $R_0 = 1$, $\eta = \eta^{\text{ext}} = 1$ and $\gamma = 1$.

the generic perturbation δR from equation (5.49):

$$\Delta\kappa = \kappa_p - \kappa_0 \equiv (-\nabla \cdot \hat{\boldsymbol{n}})\Big|_{r=R} - (-\nabla \cdot \hat{\boldsymbol{r}})\Big|_{r=R_0} = \sum_{l,m} \frac{\delta R(t)}{R_0^2}(l+2)(l-1)Y_l^m(\theta,\phi) \tag{5.59}$$

$\Delta\kappa = 0$ for $l = 1$ and so this perturbation mode corresponds to a pure translation of the droplet. Thus, if we consider remaining in the droplet reference frame ($R = R_0$) and just perturb the polarisation, we see that the interesting dynamics is no longer stronger coupled to the interface, but rather is around the defect. An $l = 1$ mode of perturbation breaks the symmetry and so we can no longer assume that the flow around the defect is symmetric and hence it's position relative to the droplet centre of mass could change. Therefore, to consider this stability properly we need to have an expression for the r-dependence of the polarisation perturbation, which we cannot acquire analytically, and the simple assumption that we made (of the polarisation being strongly coupled to the interface deformation) is no longer relevant for this mode. Thus we are unable to make analytical

predictions about symmetry breaking of the system in this mode.

5.3.2 Results in 2D and comparison with simulations

As in section 5.2.3 the simulations are of a 2D circular drop immersed in a 2D fluid. Therefore we repeat the linear stability analysis in 2D using the same assumptions in order to compare with the simulations. In 2D plane polar coordinates the system stationary state is given by:

$$\boldsymbol{R} = R_0\hat{\boldsymbol{r}} \qquad \boldsymbol{p} = \hat{\boldsymbol{r}} \qquad \boldsymbol{v} = 0 \qquad h_{\parallel}^0 = -\frac{K}{R_0^2}$$
$$P = P_0^{\text{ext}} + \frac{\gamma}{R_0} - \zeta\Delta\mu\left[\ln\left(\frac{r}{R_0}\right) + \frac{1}{2}\right] + K(\frac{1}{R_0^2} - \frac{1}{r^2})\,. \tag{5.60}$$

Then we assume perturbations of the form:

$$\boldsymbol{p} = \hat{\boldsymbol{r}} + \sum_{k=2}^{\infty}\frac{r}{R_0}\delta p(t)\exp(ik\theta)\hat{\boldsymbol{\theta}} \tag{5.61}$$

$$\boldsymbol{R} = (R_0 + \sum_{k=2}^{\infty}\delta R(t)\exp(ik\theta))\hat{\boldsymbol{r}}\,. \tag{5.62}$$

Note that if we assume the polarisation has no r-dependence (the $a_{lm}(r) = 1$ approximation in the 3D calculation) then the solutions contain division by 0 for the $k = 2$ case. Instead therefore we assume linear r-dependence in the polarisation and find that the results of this are qualitatively very similar to those in the 3D case. Again, we only take perturbations of order $k > 1$ so that we can use the same assumptions as before.

We repeat the calculations and find the eigenvalues of the stability matrix $\underline{\underline{T}}_{2D}$ where:

$$\frac{\mathrm{d}}{\mathrm{d}t}\begin{pmatrix}\delta R_k\\ \delta p_k\end{pmatrix} = \underline{\underline{T}}_{2D}\begin{pmatrix}\delta R_k\\ \delta p_k\end{pmatrix} \qquad \text{at} \quad r = R\,. \tag{5.63}$$

From this we can solve $\lambda_{1,2} = 0$ for the activity to find the threshold values and again see that for large anchoring, only contractile thresholds remain. Thus, if we take the polarisation perturbation again to be enslaved to the normal vector ($\delta p_k(t) = \delta R_k(t)k/R_0$),

then we can reduce the stability problem to a single equation for $\frac{\mathrm{d}\delta R_k}{\mathrm{d}t} = s\delta R_k(t)$. Solving for s we get:

$$s = \frac{1}{\eta + \eta^{\mathrm{ext}}}\left[-\frac{\gamma}{2R_0}k - \zeta\Delta\mu\frac{k^2}{(k+1)(k+3)} - \frac{K}{2R_0^2}\frac{k^2\left(k^2(\nu+1)+(2k+1)(1-\nu)\right)}{k^2-1}\right]. \tag{5.64}$$

Solving $s = 0$ to find the critical activity in this limit:

$$\zeta\Delta\mu^*_{c2D} = -\frac{1}{2}\left[\frac{\gamma}{R_0}\frac{(k+1)(k+3)}{k} + \frac{K}{R_0^2}\frac{(k+3)(k^2(\nu+1)+(2k+1)(1-\nu))}{k-1}\right] \tag{5.65}$$

We perform simulations for $\nu = \pm 1.1$, such that we can compare the rod-like ($\nu < 0$) and disc-like cases ($\nu > 0$) in the flow-aligning regime $|\nu| > 1$. We choose $W_1 \gg K$ so that the stationary steady state is approximately given by equation (5.46). Furthermore, we fix $R_0 = 1$ and $\eta = 1$ in simulation units as our length and time scales (see section 3.3 for simulation values and SI equivalent values).

We run the simulations for enough time to reach the stationary steady state then apply a small random perturbation to the interface. By running numerous simulations and varying certain parameters, we are able construct the phase diagrams in figure 5.8 which show the parameter ranges for which the droplet breaks symmetry. We can see that for both values of ν the droplets show a deformation instability corresponding to the $k = 2$ mode for contractile activity, as predicted by the analytical calculations. We compare the threshold observed with that predicted in equation (5.65). We see that the analytical analysis do lead us to a reasonable understanding of this behaviour in the simulations, but we lack quantitative agreement due to the assumptions. We see an approximately linear dependence on surface tension for the $k = 2$ mode, but we do not observe any discernible difference for the different values of ν. An example snapshot from the simulations of this instability is shown in figure 5.9(a).

Furthermore, we see that for extensile activity ($\zeta\Delta\mu > 0$) there is a transition to a

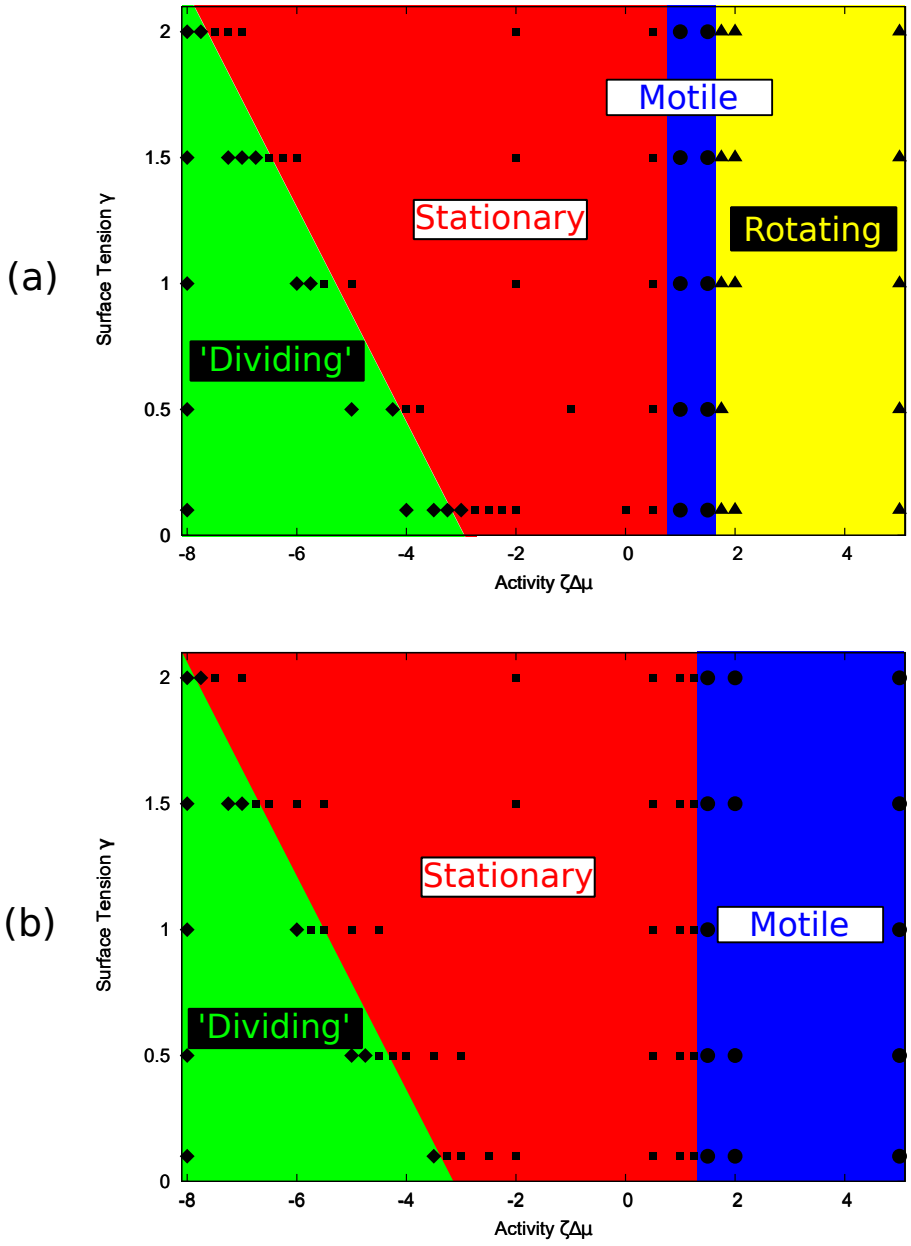

Figure 5.8: Phase diagram of simulation results for parameters $K = 0.1$, $\eta_{\text{ext}} = \Gamma = 1$, $W_1 = 50$ and **(a)** $\nu = -1.1$ and **(b)** $\nu = 1.1$. Blue corresponds to a $k = 2$ mode deformation (see figure 5.9(b)), green corresponds to a rotating state (see figure 5.9(a)) and red corresponds to a swimming ($k = 1$ mode) state (see figure 5.9(c)). Purple corresponds to states that initiated a $k = 2$ mode deformation then returned to circular. Black corresponds to the droplet stationary state being stable.

motile mode that appears to have no dependence on surface tension. We would expect from our considerations of the $k = 1$ (or $l = 1$ in 3D) mode perturbation that any instability in this mode would be independent of surface tension. While we were not able to predict the instability, the lack of boundary deformation when we apply a perturbation of this mode does suggest that its stability should not depend on the surface tension. A plot of this motile state is shown in figure 5.9(b)This symmetry breaking does depend on the elastic constant K, however investigating the behaviour with changing K is beyond the scope of this chapter. Preliminary tests show the K dependence can be fairly complex, because for much lower values of K we enter the limit where distortions can be decoupled from the shape, which we do not consider in the analytical calculations here.

Finally, as predicted in [Kruse et al., 2004] we see a rotational instability for extensile activity when $\nu = -1.1$. The threshold for such rotational symmetry breaking, as recalculated in [Kruse et al., 2005], is:

$$\zeta\Delta\mu_c^{\mathrm{ROT}} = -\frac{1}{2}\left(\frac{z_0}{R_0}\right)^2 \frac{4\eta + \Gamma(\nu-1)^2}{2\Gamma(\nu-1)}K \tag{5.66}$$

in the one-constant approximation and where z_0 is the positive root of the Bessel function $J_0(z)$. Using the parameter values in the simulation, we see this gives (to 1 decimal place) a threshold of $\zeta\Delta\mu_c^{\mathrm{ROT}} = 1.2$ when $\nu = -1.1$ and $\zeta\Delta\mu_c^{\mathrm{ROT}} = -11.6$ when $\nu = 1.1$. This fits with our observations, the droplet changes from motile to rotating when $\nu = -1.1$ when $\zeta\Delta\mu > \zeta\Delta\mu_c^{\mathrm{ROT}}$. This tells us that as we increase the activity, this rotational mode become more unstable than the motile mode, and hence the rotational mode dominates. Furthermore, we don't see this for $\nu = 1.1$ because the threshold activity is too high. This rotational instability is caused by a angularly independent rotation of the polarisation field away from the radial axis, which is not clear from the plot in figure 5.9(c), but one can see that the defect and boundary remain in the same position. We cannot predict from this however how this rotational mode would manifest in 3D.

The qualitative agreement of the analytical calculations and simulations is only achieved

for the parameter range in which we reasoned it to be valid. In simulations where K is an order of magnitude smaller, we observe that the polarisation defect is often deformed into line defects, or occasionally new defects are created. This corresponds to the case where $|\zeta\Delta\mu| \gg K/R_0^2$ where much higher levels of distortion are achievable in the bulk of the droplet, that are somewhat decoupled from the boundary dynamics. This is a very interesting regime as in a bulk active fluid it corresponds to the onset of turbulent-like states driven by activity, where polarisation defects can be created and annihilated [Marchetti et al., 2013, Giomi et al., 2013]. When confined to a droplet with strong anchoring, as in this case, one can observe more complex behaviours such as swimming droplet with several flow vortices generated inside driven by the interaction of defects. Analysis of these states is left for future work.

5.4 Summary and Conclusions

In this chapter we have probed analytically the stability of two types of active droplet. First, in section 5.2 we considered a fluid droplet with a concentration of active material dispersed on its interface. We use a simple one component model to describe the active fluid on the interface and assume that the active stress generated scales linearly with concentration. We show by applying general spherical harmonic perturbations that there exists a threshold value of contractile activity, above which the system will break symmetry. The lowest energy mode, corresponding to a single peak in the concentration profile of the active material, requires the least activity to occur, and the threshold scales linearly with mode number l. We also see that coupling with the boundary shape does not affect this threshold, and so it is only affected by diffusion of the concentration field, the phenomenological passive pressure term that we include proportional to c^2 and binding rates between the interface and fluid. However, we do see that coupling with the shape increases the evolution rate of the instability (the stability matrix eigenvalues are larger than if we consider a fixed spherical boundary). These calculations compare well to Immersed Boundary simulations on the system in 2D, which show symmetry breaking above the predicted threshold and steady state swimming behaviour. However, as shown

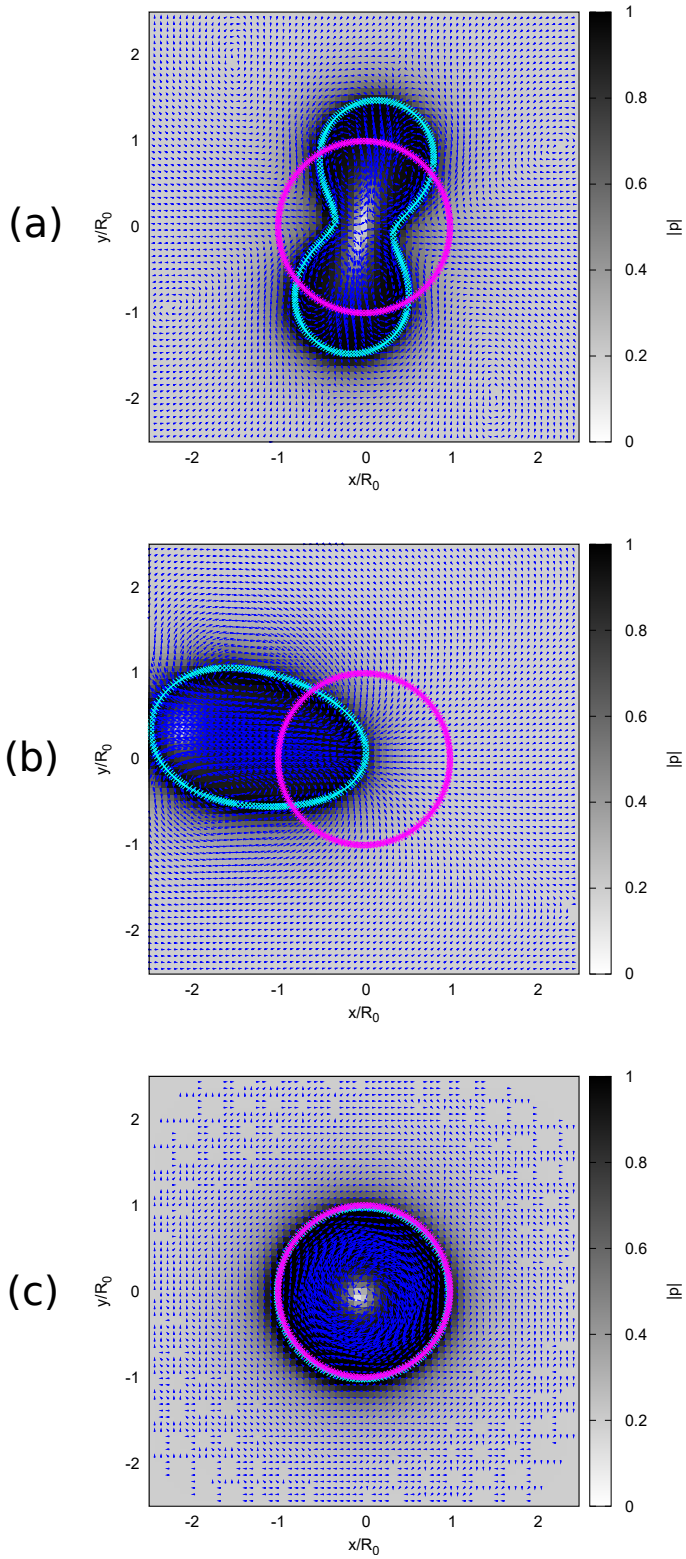

Figure 5.9: Snapshots of the active droplets during symmetry breaking in the simulations. Parameters used are the same as in figure 5.8 with $\gamma = 1$ and the activity and ν values stated: **(a)** Deformation ($k = 2$) instability ($\zeta\Delta\mu = -6$ and $\nu = 1.1$) **(b)** Motility ($k = 1$) instability ($\zeta\Delta\mu = 5$ and $\nu = 1.1$) **(c)** Rotational instability ($\zeta\Delta\mu = 5$ and $\nu = -1.1$). Blue arrows indicate velocity (scaled for visibility), magenta points indicate the boundary at time $t = 0$ and cyan points mark the boundary position current time in the simulation. Shading indicates polarisation magnitude from 0 to 1.

in the analytical calculation, there can be no deformation of the droplet in 2D due to surface tension gradients alone. Furthermore we see that, as predicted by the analytical approximation of the maximum mode number $k_{\max}$, at larger values of contractile activity the instability results in the formation of 2 peaks at the droplet interface. We observe that these two peaks are always unstable in simulations, and coalesce to form one. This is physically very similar to the stability problem of cytokinesis discussed in [Sedzinski et al., 2011].

This fluid drop with varying surface tension shares several properties with cortex of animal cells. [Hawkins et al., 2011] show that contractile activity in the cell cortex can lead to instabilities that result in a self-propelled moving steady state. Despite our simplification of an infinitely thin layer of one component active material, we also see that the resulting steady state consists of a single peak in concentration on the interface and a self-propelled drop. Our 3D analysis suggests that this would couple to deformation in the cortex, however this cannot occur in the 2D simulations that we perform here.

In section 5.3 we instead consider a droplet of active polar fluid with normal anchoring at the droplet interface. We show that, if we consider the limit where the deformation of the polarisation is strongly coupled to that of the interface, then we can predict a contractile threshold for instabilities in the droplet shape. The lowest order mode of deformation instability corresponds to the set of second order spherical harmonic deformations (see figure 5.1). We observe this in the 2D immersed boundary simulations, where the droplet deforms into a 'dumbbell' shape for large enough activity. Using these analytical approximations we are unable to predict motile symmetry breaking corresponding to the $l = 1$ (or $k = 1$ in 2D) mode of perturbation. The immersed boundary simulations however show that this does occur for extensile activity where the $q = +1$ defect in the droplet becomes asymmetrically positioned in the drop near its leading edge. Note the difference between these observations and those made in [Giomi and DeSimone, 2014] for a droplet of active nematic fluid. In those simulations [Giomi and DeSimone, 2014] apply large normal anchoring at the interface, but due to the nematic nature of the liquid crystal the stationary state consists of two $q = +1/2$ defects rather than one $q = +1$ defect. This means that

the droplet has only two axes of symmetry (infinite axes of symmetry for the stationary state observed in the calculations presented here) and elongates under contractile activity. In this case the droplet becomes motile at large enough contractile activity and swims in the direction perpendicular to its long axis. This shows that the system geometry alone can affect the steady states possible in the system. In addition, the 2D simulations show a rotational steady state, as predicted in [Kruse et al., 2004, Kruse et al., 2005]. Our analytical calculations predict that the 'division' instability that we observe would be observed in 3D, although to leading order in the perturbations all of the set of deformations in 5.1 have the same energy cost and hence are equally likely. However, we are unable to predict how the other instabilities will manifest in 3D, and leave this to investigate in future work.

The two systems we present here are highly idealised, and could only be reproduced experimentally by the synthesis of active gels *invitro*. However, surface chemistry and density of the active gels would be a big factor in determining whether active polar fluid droplets could be synthesised with these properties. This is because in many cases the filaments will adsorb to the interface if immersed in an emulsion droplet or vesicle. However, this suggests that experiments on a fluid droplet with an isotropic contractile active gel dispersed on its interface could potentially be achieved.

A case we have not studied here is that of an active polar gel with strong orientational order confined to a fluid interface. This has been studied experimentally and theoretically in [Keber et al., 2014] for a microtubule and kinesin based active gel. The geometrical constraint in that system means that several defects can be formed on the droplet surface. This may be a good candidate system for study via these immersed boundary method simulations, but the simulations would need to be generalised to 3D, as discussed in chapters 6 and 7.

5.A Appendix: Explicit flow solutions for Fluid Droplet with Active Interface

Substituting the general solutions for the flow and pressure from equations (5.12)-(5.15) into the stress balance boundary condition in equation (5.17), we arrive at the following set of simultaneous equations to first order in the perturbations:

$$2\eta\left(a_{lm}^{(0)}(l+1)+\frac{a_{lm}^{(1)}}{R_0^2}(l-1)\right)R_0^l+2\eta^{\rm ext}\left(b_{lm}^{(0)}l+\frac{b_{lm}^{(1)}}{R_0^2}(l+2)\right)R_0^{-l-1}$$
$$=-\frac{1}{R_0}\left[2\delta c_{lm}\tilde{\zeta}\Delta\mu+\delta R_{lm}\gamma_0'(l+2)(l-1)\right]+2\left(\eta a_{lm}^{(0)}\frac{2l+3}{l}R_0^l-\eta^{\rm ext}b_{lm}^{(0)}\frac{2l-1}{l+1}R_0^{-l-1}\right) \tag{5.67}$$

$$\frac{1}{l(l+1)}\left[2\eta\left(a_{lm}^{(0)}l(l+2)+\frac{a_{lm}^{(1)}}{R_0^2}(l^2-1)\right)R_0^l-2\eta^{\rm ext}\left(b_{lm}^{(0)}(l^2-1)+\frac{b_{lm}^{(1)}}{R_0^2}l(l+2)\right)R_0^{-l-1}\right]$$
$$=-\frac{\tilde{\zeta}\Delta\mu}{R_0}\delta c_{lm} \tag{5.68}$$

$$\eta a_{lm}^{(2)}(l-1)R_0^{l-1}+\eta^{\rm ext}b_{lm}^{(2)}(l+2)R_0^{-l-2}=0\,. \tag{5.69}$$

From these conditions, and the velocity continuity condition of equation (5.16), one can determine the constants $a_{lm}^{(i)}, b_{lm}^{(i)}$. We list these below for the special case $\eta=\eta^{\rm ext}$ for brevity:

$$a_{lm}^{(0)}=\frac{l(l+1)(l+2)}{2\eta(2l+3)(2l+1)}\left[(l-1)\gamma_0'\frac{\delta R_{lm}}{R_0}-\tilde{\zeta}\Delta\mu\delta c_{lm}\right]R_0^{-l-1} \tag{5.70}$$
$$a_{lm}^{(1)}=-\frac{l(l+1)}{\eta(8l^2-2)}\left[(l+2)(l-1)\gamma_0'\frac{\delta R_{lm}}{R_0}-l\tilde{\zeta}\Delta\mu\delta c_{lm}\right]R_0^{-l+1} \tag{5.71}$$
$$b_{lm}^{(0)}=-\frac{l(l^2-1)}{\eta(8l^2-2))}\left[(l+2)\gamma_0'\frac{\delta R_{lm}}{R_0}+\tilde{\zeta}\Delta\mu\delta c_{lm}\right]R_0^{l} \tag{5.72}$$
$$b_{lm}^{(1)}=\frac{l(l+1)}{\eta(2l+3)(2l+1))}\left[(l+2)(l-1)\gamma_0'\frac{\delta R_{lm}}{R_0}+(l+1)\tilde{\zeta}\Delta\mu\delta c_{lm}\right]R_0^{l+2} \tag{5.73}$$
$$a_{lm}^{(2)}=b_{lm}^{(2)}=0\,. \tag{5.74}$$

Chapter 6

Immersed Boundary Simulations of Active Droplets

Abstract

In this chapter we will outline the constitutive equations and numerical method employed to simulate the active droplets considered in chapter 5. The simulations employ a 2D Immersed Boundary method to simulate the motion of the droplet interface. Using this method we can consider an active fluid contained within the droplet or adsorbed to its surface. We analyse the active steady states of the droplet which include persistent motility, symmetric deformations and rotational states. We also discuss direct improvements and advances that can be made on this work and outline how these could be implemented and highlight some of the key difficulties therein.

6.1 Introduction

We have developed numerical simulations to model the active droplets described in chapter 5 in 2-dimensions. Using the Immersed Boundary method [Peskin, 2002] we model a fluid droplet immersed in a surrounding fluid. In addition, we include an isotropic active fluid on the droplet interface, and also an active polar fluid confined to the drop. The modular nature of the simulations allows us to include any or none of these phenomena easily, which is useful for investigating each case individually, as well as allowing us to simulate them simultaneously.

As well as providing a check for the analytical calculations in the previous chapter, these simulations predict the steady state in these systems. In this chapter we will first describe the analytical equations governing the simulations in section 6.2. Then in sections 6.3 and 6.4 we will outline the numerical implementation we have used and some verification tests. Then, by varying the model parameters we characterise some interesting steady states in section 6.5.

In section 6.6 we will discuss potential uses for these simulations and extensions to these that could be performed in the future to investigate even more biologically relevant systems. In particular we will discuss various ways that different types of confinement can be added to this model. Finally, we will discuss the results and what we have learnt from these simulations thus far and also discuss potential experimental realisation of these simple systems *in vitro*.

6.2 Governing Equations

The majority of the equations describing the systems were outlined in chapter 5, here we will recite them briefly in a slightly different mathematical form that is useful for an understanding of the numerical implementation in section 6.3.

6.2.1 The Immersed Boundary Method

We build numerical simulations of active fluid droplets using an Immersed Boundary (IB) method for modelling fluid-fluid interactions. The IB method was originally formulated for modelling fluid-structure interactions in biological problems, where the structure can be represented by elastic fibres. In our simulations, we follow the work of [Lai et al., 2008] which adapts this to fluid-fluid interactions in a 2D domain (extensions to 3D are discussed in section 6.6.3). We begin by considering a infinitely thin, closed interface C represented by the position vector $\boldsymbol{X} = (X(s,t), Y(s,t))$ where s is a Lagrangian coordinate along the curve C and t is time. The force density on this interface due to the surface tension is given in 2D by:

$$\boldsymbol{F}_b(s,t) = \nabla_s \left[\gamma(s,t)\boldsymbol{\tau}(s,t)\right] \tag{6.1}$$

where γ is the surface tension, τ is the tangent vector to the surface and $\nabla_s = \partial/\partial s$. This acts as an external force on the fluids, which can be translated to a 2D force density via the 2D Dirac Delta function as follows

$$\boldsymbol{f}_b(\boldsymbol{x},t) = \int_C \boldsymbol{F}_b \delta(\boldsymbol{x} - \boldsymbol{X}) \mathrm{d}s \tag{6.2}$$

where $\boldsymbol{x}$ is the position vector in the medium. The 2D Dirac Delta is defined by the identity

$$\int_\Omega g(\boldsymbol{x})\delta(\boldsymbol{x} - \boldsymbol{X})\mathrm{d}^2\boldsymbol{x} = g(\boldsymbol{X})\,, \tag{6.3}$$

where $\Omega = \Omega_0 + \Omega_1$ is the total fluid domain, consisting of fluids 0 and 1. In the case of incompressible Stokes' flow, which we assume here, force balance in the fluid dictates:

$$\eta\nabla^2\boldsymbol{v} = \nabla P - \boldsymbol{f}_b \tag{6.4}$$

$$\text{where} \quad \nabla \cdot \boldsymbol{v} = 0\,. \tag{6.5}$$

Finally, if we assume that the fluids are completely immiscible, then the interface velocity will be the same as the velocity in the medium at that point, such that:

$$\frac{\partial \boldsymbol{X}}{\partial t} = \boldsymbol{V} \equiv \int_{\Omega} \boldsymbol{v}(\boldsymbol{x}, t)\delta(\boldsymbol{x} - \boldsymbol{X})\mathrm{d}^2\boldsymbol{x}\,. \tag{6.6}$$

These simple equations model the evolution of a Newtonian fluid droplet embedded in another Newtonian fluid, with a (potentially) varying surface tension $\gamma(s,t)$ at the interface. In [Lai et al., 2008] this surface tension varies according to surfactant concentration, however we consider that it depends on a concentration of active particles on the interface generating contractile stresses.

6.2.2 Active Boundary

We denote the concentration of active particles on the interface $c(s,t)$. As in chapter 5 and in reference [Joanny et al., 2013] we consider that the active fluid is contractile enough to generate a negative pressure in the (1D) boundary layer for small concentrations, and that a passive pressure will become stronger at larger concentration. This is in qualitative agreement with experiments on reconstituted crosslinked actomyosin *in vitro* which, within a range of myosin and crosslinker density, initially contracts and increases in density until a steady state size is reached [Bendix et al., 2008]. Thus, we consider that the surface tension at the interface as a function of concentration of active particles is

$$\gamma(s,t) = \gamma_0 - \zeta_c \Delta\mu c(s,t) - \frac{B}{2}c(s,t)^2\,. \tag{6.7}$$

As outlined in chapter 5 it will be useful to consider results with respect the effective activity $\tilde{\zeta}\Delta\mu = \zeta_c\Delta\mu + Bc_0$ where c_0 is the stationary steady state concentration and $B \geq 0$. Note also that there is potentially a passive pressure term linear in $c(s,t)$ absorbed into $\zeta_c\Delta\mu$, but as all of these terms are phenomenological this does not change the model. As in [Lai et al., 2008] conservation of mass on the moving interface $C(t)$ gives:

$$\frac{\mathrm{d}}{\mathrm{d}t}\int_{C(t)} c(s,t)\mathrm{d}l(s,t) = \int_{C(0)} \frac{\partial}{\partial t}\left(c(s,t)\left|\frac{\partial \boldsymbol{X}(s,t)}{\partial s}\right|\right)\mathrm{d}s = 0 \tag{6.8}$$

where $|\partial \boldsymbol{X}(s,t)/\partial s|$ is the stretching factor, relating the length of a boundary element to its initial length $\mathrm{d}s$ such that $\mathrm{d}l(s,t) = |\partial \boldsymbol{X}(s,t)/\partial s|\,\mathrm{d}s$. Equation (6.8) implies that:

$$\frac{\partial c(s,t)}{\partial t} + \frac{c(s,t)}{|\partial \boldsymbol{X}(s,t)/\partial s|}\frac{\partial}{\partial t}\left|\frac{\partial \boldsymbol{X}(s,t)}{\partial s}\right| = 0\,. \tag{6.9}$$

The second term in equation (6.8) is the Lagrangian equivalent of the advection term $((\tau\cdot\nabla)\tau)\cdot(\boldsymbol{v}c)$ in chapter 5. Diffusion of the mass on the closed interface is incorporated with the addition of the term $\partial c/\partial t = D\mathrm{d}/\mathrm{d}l\,(\mathrm{d}c/\mathrm{d}l)$ where D is the diffusion coefficient on the interface. Including this term, the evolution of the concentration c becomes:

$$\frac{\partial}{\partial t}\left(c(s,t)\left|\frac{\partial \boldsymbol{X}(s,t)}{\partial s}\right|\right) = D_f\frac{\partial}{\partial s}\left(\frac{\partial c(s,t)/\partial_s}{|\partial \boldsymbol{X}(s,t)/\partial s|}\right) + q(s,t)\,. \tag{6.10}$$

The final term q captures any binding to or unbinding from the boundary, which will be defined in the following section.

6.2.3 Coupling to an internal bulk concentration

We briefly described in the previous chapter how binding and unbinding of the active particles to and from the interface could take place. In this case we assume that these particles are only soluble in the internal droplet fluid. Then the equations describing an internal bulk concentration can be incorporated into this model by defining a level-set function H such that:

$$\nabla H(\boldsymbol{x},t) \equiv -\int_{C(t)} \hat{\boldsymbol{n}}(s,t)\delta\left[\boldsymbol{x}-\boldsymbol{X}(s,t)\right]\mathrm{d}l = \begin{cases} 1 & \text{if} \quad \boldsymbol{x}\in\Omega_0 \\ 0 & \text{if} \quad \boldsymbol{x}\notin\Omega_0 \end{cases}\,. \tag{6.11}$$

Note that length element $\mathrm{d}l = |\partial \boldsymbol{X}/\partial s|\,\mathrm{d}s$ changes as the boundary deforms. Then, following [Chen and Lai, 2014] we define the concentration field of the unbound active particles as $H\rho$ and hence the advection-diffusion equation describing this quantity is:

$$\frac{\partial\left[H(\boldsymbol{x},t)\rho(\boldsymbol{x},t)\right]}{\partial t} + \nabla\cdot(\boldsymbol{v}(\boldsymbol{x},t)H(\boldsymbol{x},t)\rho(\boldsymbol{x},t)) = D_f\nabla\cdot(H(\boldsymbol{x},t)\nabla\rho(\boldsymbol{x},t)) - Q(\boldsymbol{x},t) \tag{6.12}$$

where:

$$Q(\boldsymbol{x},t)=\int_C q(s,t)\delta(\boldsymbol{x}-\boldsymbol{X})\left|\frac{\partial \boldsymbol{X}}{\partial s}\right|\mathrm{d}s\equiv\int_C\left[k_{\mathrm{on}}\rho_b(s,t)-k_{\mathrm{off}}c(s,t)\right]\delta(\boldsymbol{x}-\boldsymbol{X})\left|\frac{\partial \boldsymbol{X}}{\partial s}\right|\mathrm{d}s\,. \tag{6.13}$$

The unbound concentration of active material at the boundary ρ_b therefore is defined as:

$$\rho_b(s,t)=\int_\Omega H(\boldsymbol{x},t)\rho(\boldsymbol{x},t)\delta(\boldsymbol{x}-\boldsymbol{X})\mathrm{d}^2\boldsymbol{x} \tag{6.14}$$

As in chapter 5, we assume for this model that the binding rates obey a linear scaling with local concentration. However it is likely that this is not a realistic assumption given the large gradients in concentration field that the simulations predict. Investigating and incorporating more realistic binding behaviour goes beyond the scope of this work and would demand one consider separate populations of active motors and filaments.

Equation (6.12) ensures that the total mass of active material is conserved such that:

$$\int_\Omega\frac{\partial\left[H(\boldsymbol{x},t)\rho(\boldsymbol{x},t)\right]}{\partial t}\mathrm{d}^2\boldsymbol{x}+\int_C\frac{\partial c}{\partial t}\left|\frac{\partial \boldsymbol{X}}{\partial s}\right|\mathrm{d}s=0\,. \tag{6.15}$$

Note that these equations are just an alternative way of describing the simple advection-diffusion inside the droplet with containing boundary conditions that was outlined in equations (5.4) and (5.5) in chapter 5.

6.2.4 Active polar fluid droplet

As mentioned in the previous chapter, we can incorporate the level-set function into the free energy for a polar liquid crystal (compare to equation (5.40) in chapter 5) inside the drop as follows:

$$F_H=\int_\Omega f_H\mathrm{d}^2\boldsymbol{x}=\frac{1}{2}\int_\Omega\left[K(\nabla\boldsymbol{p})^2+\frac{K}{2}c_b\boldsymbol{p}^2\left(\boldsymbol{p}^2-2H\right)+W_1\left(|\nabla H|+\boldsymbol{p}\cdot\nabla H\right)^2\right]\mathrm{d}^2\boldsymbol{x}\,. \tag{6.16}$$

This then looks very similar to many phase field models of (active and passive) liquid crystal emulsions in the literature [Yue et al., 2004, Ziebert et al., 2011, Tjhung et al., 2012, Giomi and DeSimone, 2014]. The key difference in the immersed boundary formulation is that the interfacial width does not depend on the surface tension and is a numerical approximation to a sharp interface, and the level-set function H is enslaved to the position of this interface. This means we can usefully change the properties of the boundary without requiring a change to any other part of the calculation. Due to issues of numerical stability, we cannot take $|\boldsymbol{p}| = 1$ so we replace the Lagrange multiplier $h_{\parallel}^{0}$ in the free energy (see equation (5.40)) with the term $Kc_b p^2(p^2 - 2H)$ where c_b is taken to be the (isotropic) filament concentration in the droplet. Thus, the magnitude of the polarisation can vary in the droplet in the simulations. We can show this by considering the passive stationary solution for the polarisation using this term. If we write the polarisation as $\boldsymbol{p} = |p|(r)\left[\cos(\beta(r,\theta))\hat{\boldsymbol{r}} + \sin(\beta(r,\theta))\hat{\boldsymbol{\theta}}\right]$ then the passive stationary state still solves for $\beta = 0$, but now $|p|$ must satisfy the equation:

$$|p|''(r) + \frac{1}{r}|p|'(r) - \frac{1}{r^2}|p|(r) = c_b|p|(r)\left(|p|^2(r) - 1\right). \tag{6.17}$$

This ordinary differential equation (ODE) is non-linear due to the $|p|^3$ term and hence we are only able to solve it numerically. Assuming that $|p| = 1$ at the droplet boundary (strong anchoring) and $|p| = 0$ near to the origin (setting $|p| = 0$ exactly at $r = 0$ leads to a solution that does not converge) we find the solutions plotted in figure 6.1.

In the limit $c_b \to \infty$ this term fulfils the role of the Lagrange multiplier $h_{\parallel}^{0}$ and strictly enforces $|p| = 1$ on Ω_0 and $|p| = 0$ on Ω_1. In the simulations, we have to use finite c_b, hence there is some finite gradient of polarisation across the interface and around the defect, which is only to ensure the numerical stability of the simulations. Thus, if we assume that activity is confined to the drop we can re-write the active stress as

$$\underline{\underline{\sigma}}^{\mathrm{act}} = -\zeta\Delta\mu H\left(\boldsymbol{pp} - \frac{\mathbb{I}}{2}\right). \tag{6.18}$$

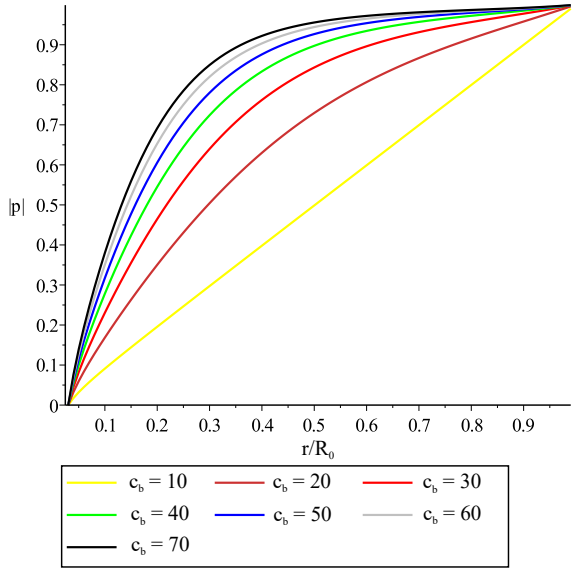

Figure 6.1: Numerical solutions to equation (6.17) for various values of c_b. As c_b increases the distribution tends towards $|p| = 1$ everywhere.

In addition, there is a stress term due to the polarisation across the interface given by (as used in [Tjhung et al., 2012]):

$$\underline{\underline{\sigma}}^{\text{int}} = \left(f_H - H\frac{\delta F}{\delta H} \right) \mathbb{I} - \frac{\partial f_H}{\partial(\nabla H)}(\nabla H)\,. \tag{6.19}$$

The stress then is incorporated into the force balance so that equation (6.4) becomes:

$$\eta\nabla^2\boldsymbol{v} = \nabla P - \nabla\cdot\left(\underline{\underline{\sigma}}^{\text{act}} + \underline{\underline{\sigma}}^{\text{dist}} + \underline{\underline{\sigma}}^{\text{int}}\right) - \boldsymbol{f}_b\,. \tag{6.20}$$

Finally the evolution of the polarisation field is governed by equation (5.45) everywhere, which we write as:

$$\frac{\partial \boldsymbol{p}}{\partial t} = -\left(\boldsymbol{v}\cdot\nabla\right)\boldsymbol{p} - \underline{\underline{\omega}}\cdot\boldsymbol{p} - \nu\underline{\underline{u}}\cdot\boldsymbol{p} + \frac{\boldsymbol{h}}{\Gamma}\,. \tag{6.21}$$

6.3 Numerical Implementation

6.3.1 Coordinate System

The bulk fluid domain Ω is defined on a staggered periodic Cartesian grid of points with spacing h in each direction. The 3 overlaid grids correspond to positions (x_i, y_j),

$(x_{i-1/2}, y_j)$, and $(x_i, y_{j-1/2})$ where $x_{i-1/2} = x_i - h/2$ and the same for y. The points x_i and y_j run from $x_0 = -(L_x - h)/2$ and $y_0 = -(L_y - h)/2$ to $x_{M_x-1} = (L_x - h)/2$ and $y_{M_y-1} = (L_y - h)/2 - h$ (where $L_{x,y}$ are the lengths of the simulation box in the x and y directions and $M_{x,y} = L_{x,y}/h$ is the total number of grid points in each direction). The interface C is described by a staggered grid of Lagrangian points s_k where $s_k = k\Delta s$ with $k = 0 \dots N(t) - 1$. These points have corresponding Cartesian coordinates (X_k, Y_k) and $(X_{k+1/2}, Y_{k+1/2}) = (X_{k+1} + X_k, Y_{k+1} + Y_k)/2$. The step size is chosen as $\Delta s = l_0/N(0)$ where l_0 is the initial boundary length and $N(0)$ the initial number of boundary points. Points can be added or removed from this mesh during the simulation, which will be outlined in section 6.3.6. Figure 6.2 gives an outline of which quantities are defined on which grid. We integrate over time with step Δt such that $t = n\Delta t$ for $n = 0 \dots T$. We will denote the time-step at which a quantity is defined by a superscript where necessary (*e.g.* $\boldsymbol{X}_k^{n+1}$), if none is given then all quantities in that equation will be at the same arbitrary time-step n.

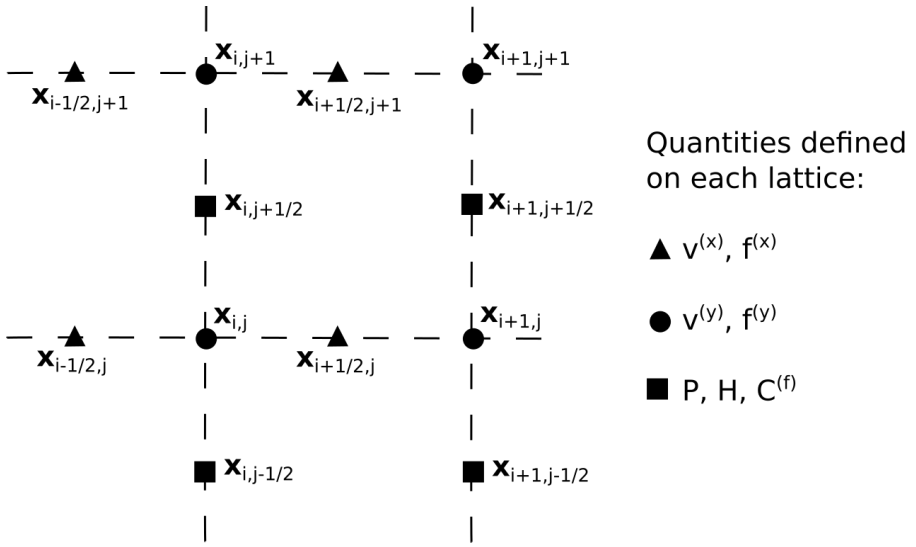

Figure 6.2: Schematic of the staggered Cartesian grid used to model the fluid domain Ω. Generally, x-components of vectors are on the $x_{i-1/2,j}$ grid, y-components of vectors are on the $x_{i,j-1/2}$ grid and scalars are on the $x_{i,j}$ grid.

Staggered grids are commonly used for fluid simulations of this nature in order to achieve consistency between first and second order gradients without the need to use a

5-point stencil in 1D (or 13-point in 2D). We define the gradient operator on the bulk fluid as $\nabla_h g_{i,j} \equiv (\partial_x, \partial_y)\, g_{i,j} = (g_{i+1,j} - g_{i,j}\,,\, g_{i,j+1} - g_{i,j})/h$ so that if $\boldsymbol{G} = \nabla_h g_{i,j}$ then the x-component of the function $\boldsymbol{G}$ is defined on the grid $(x_{i+1/2}\,,\, y_j)$ and the y-component on $(x_i\,,\, y_{j+1/2})$. Values of $\boldsymbol{G}$ can then be interpolated to other lattices where required. The Laplacian operator can then be defined as

$$\nabla_h^2 g_{i,j} \equiv \nabla_h \cdot (\partial_x g_{i-1,j}\,,\, \partial_y g_{i,j-1}) = \frac{g_{i+1,j} + g_{i,j+1} - 4g_{i,j} + g_{i-1,j} + g_{i,j-1}}{h^2} \tag{6.22}$$

such that it is on the same grid as the function g. Similarly, the boundary derivative $\partial_s g_k = (g_{k+1} - g_k)/\Delta s$ is defined on the $k + 1/2$ lattice, such that $\partial_s^2 g_k = \partial_s(\partial_s g_{k-1}) = (g_{k+1} - 2g_k + g_{k-1})\Delta s^2$.

6.3.2 Immersed Boundary Equations

We use the 2D numerical delta function $\delta_h(\boldsymbol{r} - \boldsymbol{X})$ described in [Peskin, 2002] to couple boundary quantities to the bulk fluid and vice versa. This delta function is given by the product of two 1-dimensional functions Φ:

$$\delta_h(\boldsymbol{x}_{ij} - \boldsymbol{X}_k) = \frac{\Phi\left([x_i - X_k]/h\right)\Phi\left([y_j - Y_k]/h\right)}{h^2} \tag{6.23}$$

where the function Φ acts as a numerical analogue of the 1D analytical Dirac delta function. It is desirable to use a function that is only non-zero for a few points, as this aids computational efficiency, hence a restriction regularly chosen is $\Phi(r) = 0$ if $r < -2$ or $r > 2$. In [Peskin, 2002] several constraints are imposed that one would expect from a delta function, namely that it be a continuous function in r and:

$$\sum_{i\text{even}} \Phi(r - i) = \sum_{i\text{odd}} \Phi(r - i) = \frac{1}{2} \tag{6.24}$$

$$\sum_i (r - i)\Phi(r - i) = 0 \tag{6.25}$$

$$\sum_i \left[\Phi(r - i)\right]^2 = \lambda \tag{6.26}$$

where λ is a constant. Note that the condition in equation (6.24) gives the identity $\sum_i \Phi(r-i) = 1$ but also ensures a symmetric distribution of Φ. The derivation of Φ is outlined in reference [Peskin, 2002], here we just give the resulting function:

$$\Phi(r) = \begin{cases} \left(5 + 2r - \sqrt{-4r^2 - 12r - 7}\right)/8 & \text{if} \quad -2 < r < -1 \\ \left(3 + 2r + \sqrt{-4r^2 - 4r + 1}\right)/8 & \text{if} \quad -1 \leq r < 0 \\ \left(3 - 2r + \sqrt{-4r^2 + 4r + 1}\right)/8 & \text{if} \quad 0 \leq r < 1 \\ \left(5 - 2r - \sqrt{-4r^2 + 12r - 7}\right)/8 & \text{if} \quad 1 \leq r < 2 \\ 0 \qquad \text{otherwise} \end{cases} . \tag{6.27}$$

From this it is straightforward to check that $\lambda = 3/8$. It should be noted that this distribution maintains its properties for all real values of r and is not restricted to integer values.

Using this delta function one can distribute the force density on the boundary $F_k^{(b)}$ to the fluid. First, we discretise equation (6.1) to give:

$$F_{k+1}^{(b)} = \partial_s(\gamma_k \boldsymbol{\tau}_k)\,, \tag{6.28}$$

where the tangent vector (defined on the $\boldsymbol{X}_{k+1/2}$ grid) is given by

$$\boldsymbol{\tau}_k = \frac{\partial_s \boldsymbol{X}_k}{|\partial_s \boldsymbol{X}_k|}\,. \tag{6.29}$$

The corresponding force density components in the fluid then can be defined as:

$$f_{i,j}^{(x,b)} = \sum_{k=0}^{N-1} F_k^{(x,b)} \delta(\boldsymbol{x}_{i-1/2,j} - \boldsymbol{X}_k)\Delta s \tag{6.30}$$

$$f_{i,j}^{(y,b)} = \sum_{k=0}^{N-1} F_k^{(y,b)} \delta(\boldsymbol{x}_{i,j-1/2} - \boldsymbol{X}_k)\Delta s\,, \tag{6.31}$$

where the (x) and (y) superscripts are used to denote components of the vector. Note that the x component is defined on the $\boldsymbol{x}_{i-1/2,j}$ grid and the y component on the $\boldsymbol{x}_{i,j-1/2}$, this is the same for the components of the velocity vector. We compute the velocity

components $v_{i,j}^{(x)}$ and $v_{i,j}^{(y)}$, and pressure $P_{i,j}$ by solving the incompressible Stokes equation (i.e. equation (6.4) such that $\nabla \cdot \boldsymbol{v} = 0$). To do this we employ a projection method where we first define the intermediate solutions $\boldsymbol{v}'$ and P' such that

$$\nabla^2 \boldsymbol{v}' = -\frac{1}{\eta} \boldsymbol{f}^{\text{tot}} \tag{6.32}$$

$$\nabla^2 P' = (\nabla \cdot \boldsymbol{v}'), \tag{6.33}$$

where $\boldsymbol{f}^{\text{tot}}$ is the sum of all the force densities acting on the fluid. First, we solve for $\boldsymbol{v}'$; utilising the periodicity of the lattice we can write any function $g_{i,j}$ in terms of a 2D Discrete Fourier Transform (DFT):

$$g_{i,j} = \frac{1}{\sqrt{M_x M_y}} \sum_{\alpha=0}^{M_x-1} \sum_{\beta=0}^{M_y-1} \hat{g}_{\alpha,\beta} \exp\left[2\pi I \left(\frac{i\alpha}{M_x} + \frac{j\beta}{M_y}\right)\right] \tag{6.34}$$

$$\hat{g}_{\alpha,\beta} = \frac{1}{\sqrt{M_x M_y}} \sum_{i=0}^{M_x-1} \sum_{j=0}^{M_y-1} g_{i,j} \exp\left[-2\pi I \left(\frac{i\alpha}{M_x} + \frac{j\beta}{M_y}\right)\right]. \tag{6.35}$$

Here we have used the notation $I = \sqrt{-1}$ to avoid confusion. Using equations (6.34) and (6.22) we can re-write equations (6.32) and (6.33) so that for each value of α and β:

$$\hat{v'}_{\alpha,\beta}^{(x)} = \frac{1}{\eta \hat{D}_{\alpha,\beta}^2} \hat{f}_{\alpha,\beta}^{(x,b)} \tag{6.36}$$

$$\hat{v'}_{\alpha,\beta}^{(y)} = \frac{1}{\eta \hat{D}_{\alpha,\beta}^2} \hat{f}_{\alpha,\beta}^{(y,b)} \tag{6.37}$$

$$\hat{P'}_{\alpha,\beta} = \frac{1}{\hat{D}_{\alpha,\beta}^2} \widehat{(\nabla_h \cdot \boldsymbol{v}')}_{\alpha,\beta} \tag{6.38}$$

where

$$\hat{D}_{\alpha,\beta}^2 = \left(e^{\frac{2\pi I\alpha}{M_x}} + e^{\frac{2\pi I\beta}{M_y}} - 4 + e^{-\frac{2\pi I\alpha}{M_x}} + e^{-\frac{2\pi I\beta}{M_y}}\right). \tag{6.39}$$

Using standard NAG (Numerical Algorithms Group) library functions to compute the Fast Fourier Transforms (FFTs), we find the DFTs of the components of $\boldsymbol{f}_{i,j}^{\text{tot}}$. Looping over all values of α and β we can use equations (6.36) and (6.37) to assign values to the DFT of $\boldsymbol{v}'_{i,j}$. We then compute the inverse DFT of $\hat{\boldsymbol{v}}'$ to acquire values for $\boldsymbol{v}'_{i,j}$. Following

this we calculate $\nabla_h \cdot \boldsymbol{v}'_{i,j}$ and compute its DFT. Then we can calculate $P'_{i,j}$ similarly. Finally, we relate these quantities back to the velocity and pressure as follows:

$$\boldsymbol{v}_{i,j} = \boldsymbol{v}'_{i,j} + \frac{1}{h}\left(P'_{i,j} - P'_{i-1,j}, P'_{i,j} - P'_{i,j-1}\right) \tag{6.40}$$

$$P_{i,j} = \eta \nabla_h^2 P'_{i,j}\,. \tag{6.41}$$

This is a computationally efficient method for solving the Stokes equation as each set of assignments only require $M_x M_y$ operations. The time taken for the FFT computations scales approximately as $M_x M_y \log_{10}(M_x M_y)$ so this is the limiting complexity in this process.

Once the bulk velocity is computed we can calculate the velocity of the interface using equation (6.6):

$$V_k^{(x)} = \sum_{i=i'-1}^{i'+2} \sum_{j=j'-1}^{j'+2} v_{i,j}^{(x)} \delta(\boldsymbol{x}_{i-1/2,j} - \boldsymbol{X}_k) h^2 \tag{6.42}$$

$$V_k^{(y)} = \sum_{i=i'-1}^{i'+2} \sum_{j=j'-1}^{j'+2} v_{i,j}^{(y)} \delta(\boldsymbol{x}_{i,j-1/2} - \boldsymbol{X}_k) h^2 \tag{6.43}$$

where i' is the value of $(X_k + (L_x - h)/2)/h$ rounded down to the nearest integer and j' is the same but for Y_k. Generally in IB methods this interface is updated using a simple forward first order Euler scheme, *i.e.* $\boldsymbol{X}_k^{n+1} = \boldsymbol{X}_k^n + \Delta t \boldsymbol{V}_k$. Instead we use an explicit fourth order Runge-Kutta method as outlined in section 6.4. We find that this method improves the numerical stability of the algorithm compared to a forward Euler update, particularly in the case where the boundary position is coupled to and internal polarisation field.

6.3.3 Active boundary equations

We define a concentration of active particles c_k on the boundary points $\boldsymbol{X}_{k+1/2}$ which alters the surface tension γ_k according to equation (6.7). The concentration dynamics are then governed by equation (6.10) which we discretise using the Crank-Nicholson scheme

(as in [Lai et al., 2008, Chen and Lai, 2014]):

$$c_k^{n+1}\left|\partial_s \boldsymbol{X}_k^{n+1}\right| = c_k^n\left|\partial_s \boldsymbol{X}_k^n\right| + \frac{D\Delta t}{\Delta s}\left(\frac{\partial_s c_k^{n+1}}{\left|\partial_s \boldsymbol{X}_{k+1}^{n+1}\right| + \left|\partial_s \boldsymbol{X}_k^{n+1}\right|} - \frac{\partial_s c_{k-1}^{n+1}}{\left|\partial_s \boldsymbol{X}_k^{n+1}\right| + \left|\partial_s \boldsymbol{X}_{k-1}^{n+1}\right|}\right) + \frac{D\Delta t}{\Delta s}\left(\frac{\partial_s c_k^{n}}{\left|\partial_s \boldsymbol{X}_{k+1}^{n}\right| + \left|\partial_s \boldsymbol{X}_k^{n}\right|} - \frac{\partial_s c_{k-1}^{n}}{\left|\partial_s \boldsymbol{X}_k^{n}\right| + \left|\partial_s \boldsymbol{X}_{k-1}^{n}\right|}\right) + \frac{1}{2}\left(q_k^{n+1} + q_k^n\right)\Delta t\,. \tag{6.44}$$

The quantity q contains the binding and unbinding rates for the concentration, which we will discuss in detail in section 6.3.4. We update the concentration c after updating the boundary position $\boldsymbol{X}$ so that $\boldsymbol{X}^{n+1}$ is defined. Then the set of equations in (6.44) can be represented by a periodic tridiagonal matrix:

$$\begin{pmatrix} d_0 & u_0 & & & l_0 \\ l_1 & d_1 & u_1 & & \\ & l_2 & d_2 & \ddots & \\ & & \ddots & \ddots & u_{N-2} \\ u_{N-1} & & & l_{N-1} & d_{N-1} \end{pmatrix} \begin{pmatrix} c_0^{(n+1)} \\ c_1^{(n+1)} \\ \vdots \\ c_{N-2}^{(n+1)} \\ c_{N-1}^{(n+1)} \end{pmatrix} = \begin{pmatrix} b_0^{(n+1)} \\ b_1^{(n+1)} \\ \vdots \\ b_{N-2}^{(n+1)} \\ b_{N-1}^{(n+1)} \end{pmatrix}. \tag{6.45}$$

Rearranging equation (6.44) we can read off the expressions for l,d,u, and b:

$$d_k = \left|\partial_s \boldsymbol{X}_{k+1}^{n+1}\right| + \frac{D\Delta t}{(\Delta s)^2}\left(\frac{1}{\left|\partial_s \boldsymbol{X}_{k+1}^{n+1}\right| + \left|\partial_s \boldsymbol{X}_k^{n+1}\right|} - \frac{1}{\left|\partial_s \boldsymbol{X}_k^{n+1}\right| + \left|\partial_s \boldsymbol{X}_{k-1}^{n+1}\right|}\right) \tag{6.46}$$

$$l_k = -\frac{D\Delta t}{(\Delta s)^2\left(\left|\partial_s \boldsymbol{X}_{k+1}^{n+1}\right| + \left|\partial_s \boldsymbol{X}_k^{n+1}\right|\right)} \tag{6.47}$$

$$u_k = -\frac{D\Delta t}{(\Delta s)^2\left(\left|\partial_s \boldsymbol{X}_k^{n+1}\right| + \left|\partial_s \boldsymbol{X}_{k-1}^{n+1}\right|\right)} \tag{6.48}$$

$$b_k = c_k^n\left|\partial_s \boldsymbol{X}_k^n\right| + \frac{D\Delta t}{\Delta s}\left(\frac{\partial_s c_k^n}{\left|\partial_s \boldsymbol{X}_{k+1}^n\right| + \left|\partial_s \boldsymbol{X}_k^n\right|} - \frac{\partial_s c_{k-1}^n}{\left|\partial_s \boldsymbol{X}_k^n\right| + \left|\partial_s \boldsymbol{X}_{k-1}^n\right|}\right). \tag{6.49}$$

We solve this matrix directly using standard NAG linear algebra functions. We test that the mass is conserved numerically by outputting the change in total mass in the simulation between time-steps and find that these values are randomly distributed around zero with maximum deviations on the order of machine precision.

6.3.4 Coupling to a passive bulk fluid

In order to numerically model the equations in sections 6.2.3 and 6.2.4 we need a numerical analogue for the level-set function H. Taking the gradient of both sides of equation (6.11) we see that by definition:

$$\nabla^2 H(\boldsymbol{x},t) = -\nabla \cdot \int_C \hat{\boldsymbol{n}}\delta(\boldsymbol{x}-\boldsymbol{X})\mathrm{d}l \tag{6.50}$$

Thus, as in [Unverdi and Tryggvason, 1992, Chen and Lai, 2014], to find the numerical equivalent of the function H we solve the following Poisson equation:

$$\nabla_h^2 H_{i,j} = -\nabla_h \cdot \sum_{k=0}^{N(t)-1} \left[\hat{n}_k^{(x)}\delta(\boldsymbol{x}_{i-1/2,j}-\boldsymbol{X}_{k+1/2}), \hat{n}_k^{(y)}\delta(\boldsymbol{x}_{i,j-1/2}-\boldsymbol{X}_{k+1/2})\right] |\partial_s \boldsymbol{X}_k| \,\Delta s\,. \tag{6.51}$$

We again solve this equation using the same FFT method used in to solve equations (6.36), (6.37) and (6.38). This results, for a circular boundary, in the step function shown in figure 6.3.

We can then define a concentration field that is contained within the droplet by the quantity $H\rho$. Thus, in order to conserve mass and ensure that the concentration is contained within the droplet we can use the same equations as used in [Chen and Lai, 2014] to describe a soluble surfactant. We update ρ from equation (6.12) using the following Crank-Nicholson scheme (as used in [Chen and Lai, 2014]):

$$\begin{aligned}\frac{1}{\Delta t}\left[(H\rho)_{i,j}^{n+1} - (H\rho)_{i,j}^{n}\right] = &-\frac{1}{2}\boldsymbol{D}_h \cdot \left[(\boldsymbol{v}H\rho)_{i,j}^{n+1} + (\boldsymbol{v}H\rho)_{i,j}^{n}\right] \\ &+ \frac{D_b}{2}\left[\boldsymbol{D}_h \cdot (H\boldsymbol{D}_h\rho)_{i,j}^{n+1} + \boldsymbol{D}_h \cdot (H\boldsymbol{D}_h\rho)_{i,j}^{n}\right] \\ &- \frac{1}{2}\left(\sum_{k=0}^{N-1} q_k^{n+1}\delta_h(\boldsymbol{x}_{i,j}-\boldsymbol{X}_k^{n+1}) + \sum_{k=0}^{N-1} q_k^{n}\delta_h(\boldsymbol{x}_{i,j}-\boldsymbol{X}_k^{n})\right)\end{aligned} \tag{6.52}$$

where $\boldsymbol{D}_h$ is a central difference operator on the staggered grid (as defined in [Chen and Lai, 2014]).

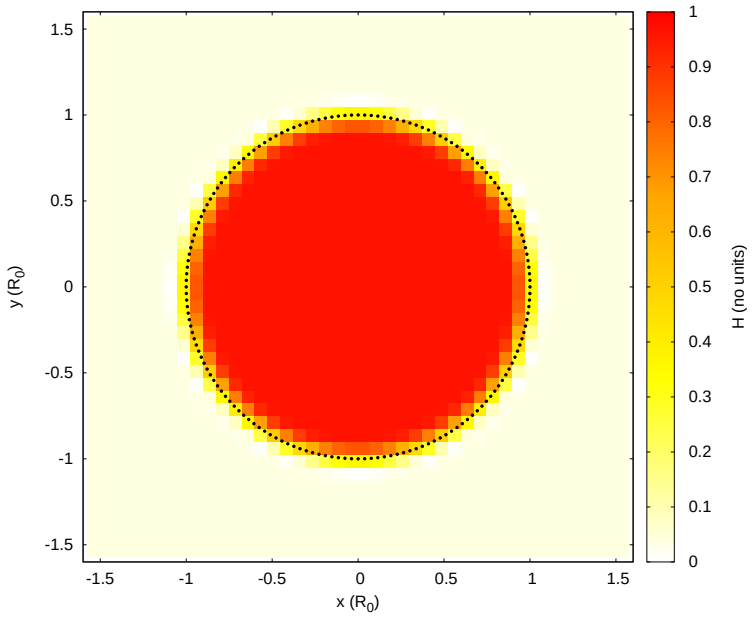

Figure 6.3: Colour plot of the level-set function H generated by solving equation (6.51) on a periodic lattice of 120 points in each dimension and grid spacing $h = 0.075$ (full fluid domain spans from -4.5 to 4.5 in each dimension). Black dots indicate boundary points.

The exchange terms q_k^n and q_k^{n+1} are given by:

$$q_k^n = k_{\text{on}} \sum_{i=0}^{M_x} \sum_{j=0}^{M_y} Hi, j^n \rho_{i,j}^n \delta_h(\boldsymbol{x}_{i,j} - \boldsymbol{X}_{k+1/2}^n) h^2 - k_{\text{off}} c_k^n \tag{6.53}$$

$$q_k^{n+1} = k_{\text{on}} \sum_{i=0}^{M_x} \sum_{j=0}^{M_y} Hi, j^{n+1} \rho_{i,j}^n \delta_h(\boldsymbol{x}_{i,j} - \boldsymbol{X}_{k+1/2}^{n+1}) h^2 - k_{\text{off}} c_k^{n+1} \,. \tag{6.54}$$

As we update the boundary positions and concentration before this step, $\boldsymbol{X}_k^{n+1}$, c_k^{n+1} and $H_{i,j}^{n+1}$ are already defined.

We can test this coupling by running some simulations with zero activity. Analytically we know that the system should reach a stable steady state where $\rho = k_{\text{off}} c_0 / k_{\text{on}}$ inside the drop and $c = c_0$ on the interface. In these simulations however, the bulk concentration evaluated at the interface is $\sum_{i=0}^{M_x - 1} \sum_{j=0}^{M_y - 1} Hi, j^n \rho_{i,j}^n \delta_h(\boldsymbol{x}_{i,j} - \boldsymbol{X}_{k+1/2}^n) h^2$, and so the

equivalent steady state for this numerical system is given by:

$$\rho_0 = \frac{k_{\text{off}} c_0}{k_{\text{on}} \left\langle \sum_{i=0}^{M_x} \sum_{j=0}^{M_y} H_{i,j} \rho_{i,j} \delta_h(\boldsymbol{x}_{i,j} - \boldsymbol{X}_{k+1/2}) h^2 \right\rangle} . \tag{6.55}$$

Where the droplet shape and position is assumed fixed in this passive case and the angled brackets indicate the average value over the boundary such that:

$$\langle f_k \rangle = \frac{\sum_{k=0}^{N-1} f_k \left| \partial \boldsymbol{X} / \partial s \right| \Delta s}{\sum_{k=0}^{N-1} \left| \partial \boldsymbol{X} / \partial s \right| \Delta s} . \tag{6.56}$$

Thus, we initialise the simulation with a concentration $c_k = c_0 = 1$ on the interface and $\rho = 0$ everywhere except at $x_i = y_j = 0$ where $\rho = \sum_{i=0}^{M_x} \sum_{j=0}^{M_y} \rho_0 H_{i,j}^0$ so that the bulk mass is all concentrated in a single point. We observe that the system reaches a steady state with constant internal and boundary concentration, as we expect, but the values inside the drop are lower than c_0 and ρ_0 (see figure 6.4). This is because the value of H in the external fluid is not exactly zero, in fact in our simulations $H \approx 0.06$ outside the droplet. This means that a significant amount of the concentration field can diffuse out of the drop over time, but this effect is limited by the periodic boundary conditions. Thus the symmetry breaking thresholds we observe are higher than predicted in chapter 5 as c_0 is effectively lower.

6.3.5 Active Polar Fluid

We define the polarisation field $\boldsymbol{p}_{i,j}$, $\boldsymbol{h}_{i,j}$ and stress components $\underline{\underline{\sigma}}_{i,j}^{(\text{act,dis,int})}$ on the centred lattice (x_i, y_j) and interpolate any gradients that are evaluated on the other lattices therein. First, we calculate the molecular field and the free energy density using (6.16) from the

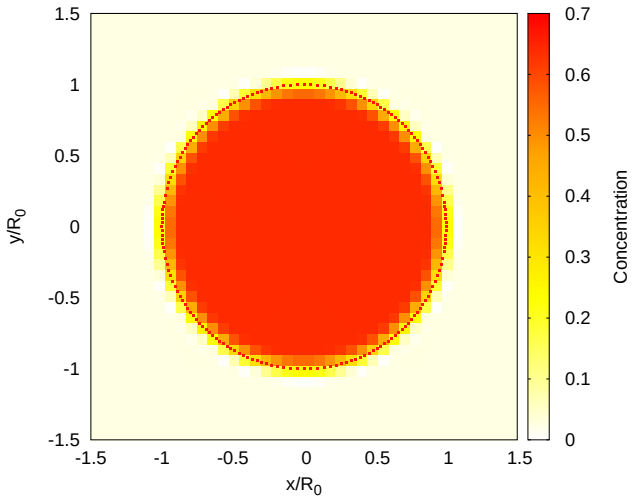

Figure 6.4: Plot of the steady state concentrations when $\zeta_c \Delta\mu = B = 0$ for $D_b = 0.005$, $D = 0.1$ and $k_{\text{off}} = k_{\text{on}} = 1$. The concentration in the bulk is scaled by ρ_0 from equation (6.55) and the concentration bound to the boundary points is scaled by $c_0 = 1$. We see that the steady state values are actually approximately 70% of these in this case.

identity $\boldsymbol{h} = -\delta F_H / \delta \boldsymbol{p}$:

$$\boldsymbol{h}_{i,j} = \frac{\delta F}{\delta \boldsymbol{p}} K \nabla_h^2 \boldsymbol{p}_{i,j} - K c_b \left(\boldsymbol{p}_{i,j}^2 - H_{i,j} \right) \boldsymbol{p} - W_1 \left[|\nabla_{hc} H_{i,j}| + \boldsymbol{p}_{i,j} \cdot (\nabla_{hc} H_{i,j}) \right] \nabla_{hc} H_{i,j} \tag{6.57}$$

$$\begin{aligned} g_{i,j}^{\text{tot}} = & \frac{K}{2} \left[\left(\nabla_{hc} p_{i,j}^{(x)} \right)^2 + \left(\nabla_{hc} p_{i,j}^{(y)} \right)^2 \right] + \frac{K}{4} c_b \boldsymbol{p}_{i,j}^2 \left(\boldsymbol{p}_{i,j}^2 - 2 H_{i,j} \right) \\ & + \frac{W_1}{2} \left[|\nabla_{hc} H_{i,j}| + \boldsymbol{p}_{i,j} \cdot (\nabla_{hc} H_{i,j}) \right]^2 \end{aligned} \tag{6.58}$$

where the central gradient operator ∇_{hc} is defined by $\nabla_{hc} g_{i,j} = \left(g_{i+1,j} - g_{i-1,j}, g_{i,j+1} - g_{i,j-1} \right) / 2h$. From these we calculate the components of the stress $\underline{\underline{\sigma}}_{i,j}^a = \underline{\underline{\sigma}}_{i,j}^{\text{act}} + \underline{\underline{\sigma}}_{i,j}^{dis} + \underline{\underline{\sigma}}_{i,j}^{int}$, and then finally the force density contribution from these stresses:

$$f^{(a,x)} = \frac{\sigma_{i,j}^{(a,xx)} - \sigma_{i-1,j}^{(a,xx)}}{h} + \frac{\sigma_{i,j+1}^{(a,yx)} - \sigma_{i,j-1}^{(a,yx)} + \sigma_{i-1,j+1}^{(a,yx)} - \sigma_{i-1,j-1}^{(a,yx)}}{4h} \tag{6.59}$$

$$f^{(a,y)} = \frac{\sigma_{i,j}^{(a,yy)} - \sigma_{i,j-1}^{(a,yy)}}{h} + \frac{\sigma_{i+1,j}^{(a,xy)} - \sigma_{i-1,j}^{(a,xy)} + \sigma_{i+1,j-1}^{(a,xy)} - \sigma_{i-1,j-1}^{(a,xy)}}{4h} . \tag{6.60}$$

As with the velocity field, the x-component of the force density is defined on the $\boldsymbol{x}_{i-1/2,j}$ lattice and the y-component on the $\boldsymbol{x}_{i,j-1/2}$ lattice. This force density is then added to the boundary force density in equation (6.32) before calculation of the velocity. Once the velocity is computed, the polarisation update equation can be computed from equation (6.21) as:

$$\frac{\partial p_{i,j}^{(x)}}{\partial t} = -\left(\boldsymbol{v}_{i,j}\cdot\nabla_{dw}\right)p_{i,j}^{(x)} - \omega_{i,j}p_{i,j}^{(y)} - \nu\left(u_{i,j}^{(xx)}p^{(x)} + u_{i,j}^{(xy)}p^{(y)}\right) + \frac{1}{\Gamma}h_{i,j}^{(x)} \tag{6.61}$$

$$\frac{\partial p_{i,j}^{(y)}}{\partial t} = -\left(\boldsymbol{v}_{i,j}\cdot\nabla_{dw}\right)p_{i,j}^{(y)} + \omega_{i,j}p_{i,j}^{(x)} - \nu\left(u_{i,j}^{(yx)}p^{(x)} + u_{i,j}^{(yy)}p^{(y)}\right) + \frac{1}{\Gamma}h_{i,j}^{(y)} \tag{6.62}$$

where

$$\begin{aligned}
\boldsymbol{v}_{i,j} =& \left(v_{i-1/2,j}^{(x)} + v_{i+1/2,j}^{(x)},\, v_{i,j-1/2}^{(y)} + v_{i,j-1/2}^{(y)}\right)\\
\omega_{i,j} =& \frac{1}{4}\Big[\left(\partial_x v_{i,j-1/2}^{(y)} + \partial_x v_{i,j+1/2}^{(y)} + \partial_x v_{i-1,j-1/2}^{(y)} + \partial_x v_{i-1,j+1/2}^{(y)}\right)\\
&- \left(\partial_y v_{i-1/2,j}^{(x)} + \partial_y v_{i+1/2,j}^{(x)} + \partial_y v_{i-1/2,j-1}^{(x)} + \partial_y v_{i+1/2,j-1}^{(x)}\right)\Big]\\
u_{i,j}^{(xx)} =& \partial_x v_{i-1/2,j}^{(x)}\\
u_{i,j}^{(xy)} = u_{i,j}^{(yx)} =& \frac{1}{4}\Big[\left(\partial_x v_{i,j-1/2}^{(y)} + \partial_x v_{i,j+1/2}^{(y)} + \partial_x v_{i-1,j-1/2}^{(y)} + \partial_x v_{i-1,j+1/2}^{(y)}\right)\\
&+ \left(\partial_y v_{i-1/2,j}^{(x)} + \partial_y v_{i+1/2,j}^{(x)} + \partial_y v_{i-1/2,j-1}^{(x)} + \partial_y v_{i+1/2,j-1}^{(x)}\right)\Big]\\
u_{i,j}^{(yy)} =& \partial_y v_{i,j-1/2}^{(y)}\,.
\end{aligned}$$

The polarisation is updated using the coupled fourth order Runge-Kutta method at the same time as the boundary is updated using equations (6.42) and (6.43), this procedure is outlined in section 6.4.

6.3.6 Adding and Removing Boundary Points

As the immersed boundary in these simulations is the interface between two fluids, there is no resistance to neighbouring points getting too close or too far apart, as there would be in an elastic boundary. Therefore, it is necessary to add and remove points from the simulation to keep the boundary well defined and maintain accuracy. We remove the point $\boldsymbol{X}_k$ whenever $|\partial_s \boldsymbol{X}_{k-1}| < 0.65$ and add a point between $\boldsymbol{X}_k$ and $\boldsymbol{X}_{k+1}$ when

$|\partial_s \boldsymbol{X}_k| > 1.35$. See figure 6.5 for a visual guide to this process.

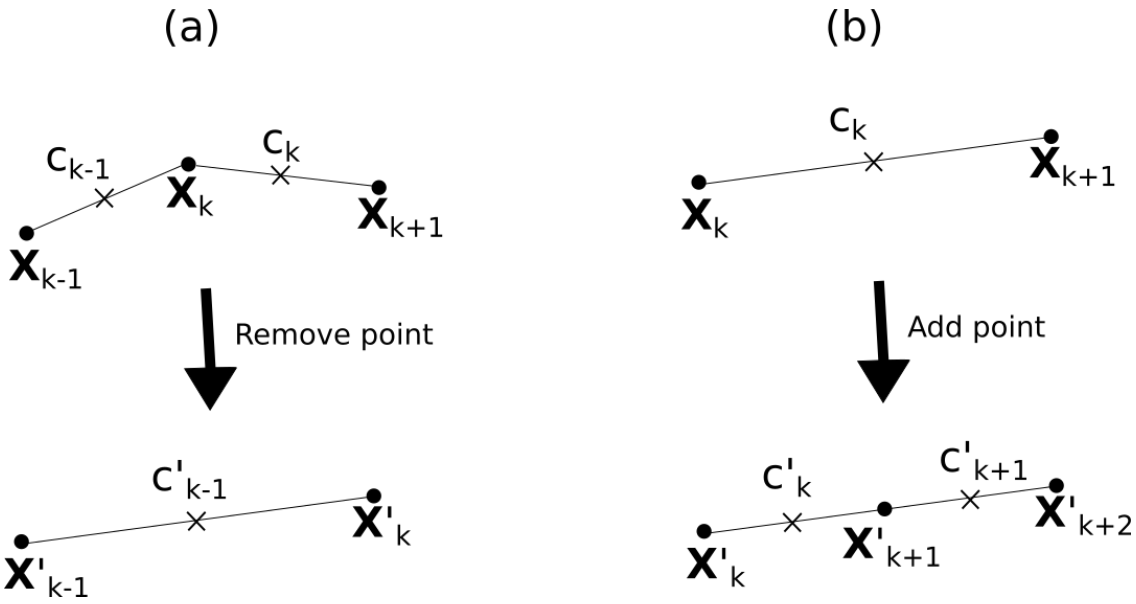

Figure 6.5: Schematic of **(a)** removing the point $\boldsymbol{X}_k$ and **(b)** adding a point between $\boldsymbol{X}_k$ and $\boldsymbol{X}_{k+1}$. Circular points denote the boundary position nodes and crosses denote the concentration defined on the half-integer lattice.

To remove a point $\boldsymbol{X}_k$ we reassign $\boldsymbol{X}'_m = \boldsymbol{X}_{m+1}$ for all $k \leq m < M-1$, then reduce the total number of boundary points to $N' = N - 1$. Conservation of mass then dictates:

$$c'_{k-1} = \frac{c_k \left|\partial_s \boldsymbol{X}_k\right| + c_{k-1} \left|\partial_s \boldsymbol{X}_{k-1}\right|}{\left|\partial_s X'_{k-1}\right|} \tag{6.63}$$

and again $c'_m = c_{m+1}$ for all $k \leq m < N-1$. The dashed quantities all denote the new values after removal of the boundary point.

To add a point between $\boldsymbol{X}_k$ and $\boldsymbol{X}_{k+1}$ we reassign $\boldsymbol{X}'_{m+1} = \boldsymbol{X}_m$ for all $k < m < N$ then add the point $\boldsymbol{X}'_{k+1} = (\boldsymbol{X}_{k+1} + \boldsymbol{X}_k)/2$ with concentration $c'_{k+1} = c_k$ to conserve mass (c_k remains unchanged).

We notice that when large flow fields are generated in the simulations, inaccuracies in the boundary positions can accumulate that need to be addressed. Firstly, we observe 'buckling' of neighbouring boundary points in areas where the boundary flow converges,

which results in points not being removed from the simulation even though they are overlapping. Thus, we also add a condition for the removal of a boundary point if $\left|\nabla_s^2 R_k\right| > d_{\max}$ where, after some testing of different boundary shapes, we arrived at $d_{\max} = 0.05R_0/\Delta s^2$, where we have defined R_k to be the distance of the boundary point from the droplet centre of mass. Therefore any excessive second order gradients in the boundary position are effectively smoothed out. Of course though we choose the limit so that smooth boundary deformations are still permitted, such as those observed in section 6.5.3.

6.3.7 Droplet Area Conservation

We observe that the droplets can lose significant area over the whole simulation time, despite the fluid incompressibility. This effect is observed in the fluid immersed boundary simulations presented in [Lai et al., 2008] and [Chen and Lai, 2014] but is very slight and gradual (on the order of 10^{-4}% area loss over a whole simulation) as the size of the flows is imposed externally. It is possible to observe much more rapid area loss in our simulations, and so to prevent this, and be consistent with the incompressibility condition, we calculate the area at each time step as

$$A^n = \sum_{i=0}^{M_x-1} \sum_{j=0}^{M_y-1} H_{i,j}^n h^2 \,. \tag{6.64}$$

We subtract this from the initial droplet area at time $n = 0$ to get $\mathrm{d}A = A_0 - A_n$. In order to keep the shape fixed, we then alter the values of $\boldsymbol{X}_k$ with a constant in the normal direction: $\delta\boldsymbol{X} = (\sqrt{(A^n - dA)/\pi} - \sqrt{(A^0/\pi)})\hat{\boldsymbol{n}}$. We then iterate this process, recalculating the area after this alteration and updating the value of $\delta\boldsymbol{X}$ accordingly until the area is conserved within a certain tolerance. We choose this tolerance to be $10^{-6}A^0$ and find that this step rarely takes more than 2 iterations, and in an individual step $\delta\boldsymbol{X}$ is at most the order of $10^{-6}R_0$, which is several orders of magnitude below the average velocity of the points in these simulations. Thus this area conservation step makes little difference to the evolution of the droplet.

6.4 Overview of the Algorithm

The final simulation code is modular in nature, so that we can turn features on or off. The bare code contains the simulation of a passive fluid drop in a periodic domain, then one can choose whether to add an active boundary and an active polar fluid separately. On initialisation we define the fluid boundary points $\boldsymbol{X}_k$, the concentration on the boundary $c_{k+1/2}$ (if included) and the filament polarisation $\boldsymbol{p}_{i,j}$ (if included). The order of execution of the algorithm is given below:

1. Boundary forces calculated according to equations (6.28).

2. Bulk forces calculated as outlined in section 6.3.5 (if active polar fluid is included).

3. Solve the Stokes' equation following section 6.3.2.

4. Calculate boundary velocity using equations (6.42) and (6.43).

5. Simultaneously update boundary and polarisation field using an explicit fourth-order Runge-Kutta method (outlined below).

6. Correct the boundary position for area conservation as outline in section 6.3.7.

7. Update concentration at the interface by solving the system in equation (6.45).

8. Update the bulk concentration ρ using the Crank-Nicholson scheme of equation (6.52).

9. Add or remove fluid boundary points as outlined in section 6.3.6.

In step 5 we apply a coupled fourth order Runge-Kutta method where we update the boundary and the polarisation field. At the start of the update we store $\boldsymbol{p}_{i,j}^n$ and $\boldsymbol{X}_{i,j}^n$, the update them for a half time-step such that $\boldsymbol{p}_{i,j}^{n+1/4} = \boldsymbol{p}_{i,j}^n + \Delta t \boldsymbol{k}_1/2$ and $\boldsymbol{X}_k^{n+1/4} = \boldsymbol{X}_k^n + \Delta t \boldsymbol{V}_k^n/2$ where $\boldsymbol{k}_1$ is the vector given by the right hand sides of equations (6.61) and (6.62). We then repeat steps 1-4 for this new polarisation and boundary position.

Repeating this process we can define:

$$\boldsymbol{p}_{i,j}^{n+1/2} = \boldsymbol{p}_{i,j}^{n} + \frac{\Delta t}{2}\boldsymbol{k}_2 \qquad \boldsymbol{X}_{k}^{n+1/2} = \boldsymbol{X}_{k}^{n} + \frac{\Delta t}{2}\boldsymbol{V}_{k}^{n+1/4} \tag{6.65}$$

$$\boldsymbol{p}_{i,j}^{n+3/4} = \boldsymbol{p}_{i,j}^{n} + \Delta t\boldsymbol{k}_3 \qquad \boldsymbol{X}_{k}^{n+3/4} = \boldsymbol{X}_{k}^{n} + \Delta t\boldsymbol{V}_{k}^{n+1/2} \tag{6.66}$$

where $\boldsymbol{k}_2$ and $\boldsymbol{k}_3$ are again the right hand sides of equations (6.61) and (6.62) evaluated at the $n + 1/4$ and $n + 1/2$ time-steps respectively. We also define $\boldsymbol{k}_4$ similarly as this vector evaluated for the $n + 3/4$ values of the polarisation and boundary condition. In between each fractional update we repeat steps 1-4. Then finally the updated polarisation and boundary are given by:

$$\boldsymbol{p}_{i,j}^{n+1} = \boldsymbol{p}_{i,j}^{n} + \frac{\Delta t}{6}\left(\boldsymbol{k}_1 + 2\boldsymbol{k}_2 + 2\boldsymbol{k}_3 + \boldsymbol{k}_4\right) \tag{6.67}$$

$$\boldsymbol{X}_{k}^{n+1} = \boldsymbol{X}_{k}^{n} + \frac{\Delta t}{6}\left(\boldsymbol{V}_{k}^{n} + 2\boldsymbol{V}_{k}^{n+1/4} + 2\boldsymbol{V}_{k}^{n+1/2} + \boldsymbol{V}_{k}^{n+3/4}\right) \tag{6.68}$$

We run the simulation, iterating over steps 1-9 usually 10^6 times, unless we deem that longer is required.

6.5 Results and Analysis

In this section we will look at some preliminary tests performed to check the accuracy of the simulations and some results that are pertinent to the research questions posed in the introduction.

We normalise the length and time scales of the simulations with respect to the initial droplet radius R_0 and the viscosity η and following some checks of accuracy choose step sizes of $h = 0.075$, $\Delta s \approx h/2$ and $\Delta t = 5 \times 10^{-4}$. We choose a grid length of $L_x = L_y = 9$, which gives $M_x = M_y = 120$, which has prime factors of 2, 3, and 5, resulting in efficiency savings in the FFT algorithm. Below is a table of parameters used in the code and the values or range of values that we test throughout this section. We relate these to SI units by setting the length, time and energy scales to biologically relevant values such that

$R_0 = 10\,\mu$m and $\eta = 10\,$kPa s, and $\zeta\Delta\mu = -10 \ldots 10$kPa.

Parameter name	Simulation values	SI units
Fluid viscosity η	1	10 k Pa s
Passive surface tension γ	0.1 - 10	1 - 100 k Pa μm
Initial droplet radius R_0	1	10 μm

Table 6.1: Fluid simulation parameters

Parameter name	Simulation values	SI units
Interface activity $\zeta_c\Delta\mu$	-2.5 - 0	-25 - 0 k Pa μm^2
Interface concentration c^0	1	0.1 μm^{-1}
Interface diffusion coefficient D	0.1 - 0.5	1 - 5 μm^{2}s^{-1}
Interface passive pressure B	0 - 1	0 - 100 k Pa μm^3
Bulk diffusion parameter D_f	0.001 - 0.1	0.01 - 1 μm^{2}s^{-1}
Unbinding rate k_{off}	0.01 - 2.0	10^{-3} - 0.2 s^{-1}
Binding rate k_{on}	0.01 - 1.0	0.01 - 1 μm s^{-1}

Table 6.2: Active boundary parameters

Parameter name	Simulation values	SI units
Rotational viscosity Γ	1.0	10 k Pa s
Bulk activity $\zeta\Delta\mu$	-10 - 10	-10 - 10 k Pa
Elastic constant K	0.01 - 0.5	1 - 50 nN
Anchoring constant W_1	0 and 1.25	0 - 12.5 nN μm^{-1}
Effective concentration c_b	50	0.05 μm^{-2}
Liquid crystal coupling constant ν	$\pm$1.1	dimensionless

Table 6.3: Active polar fluid parameters

6.5.1 Fluid Droplet Deformation

In order to test that the IB code for a fluid drop outlined in section 6.3.2 works correctly we consider a simple fluid droplet initialised with a shape given by:

$$\boldsymbol{X}_k^0 = (1 + \frac{1}{2}\cos(2\theta_k^0))\left[cos(\theta_k^0), \sin(\theta_k^0)\right] \tag{6.69}$$

where $\theta_k^0 = k\Delta s$ (see figure 6.6). We can then measure the evolution of this shape at time n using the Fourier coefficients:

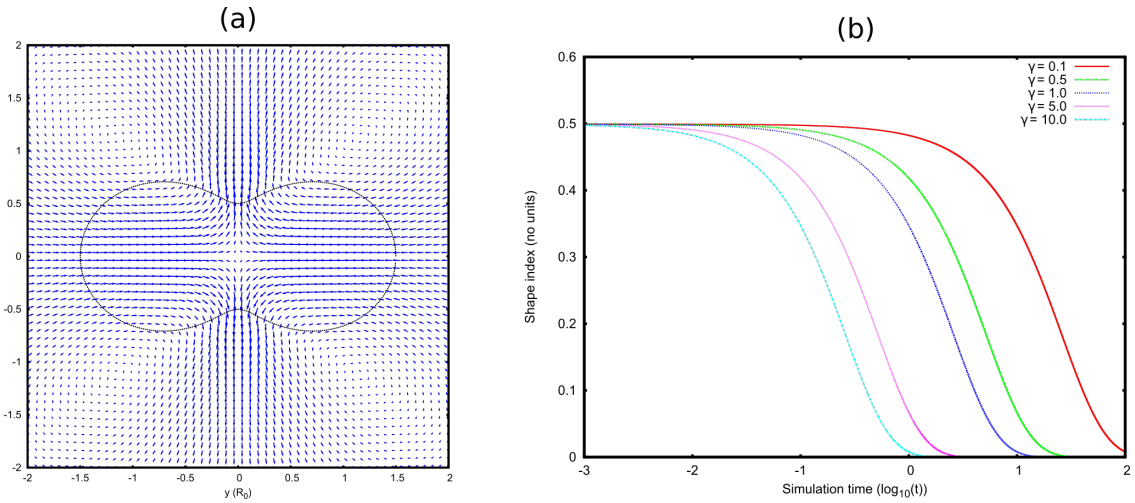

Figure 6.6: **(a)** Black line shows the boundary conformation at time $t = 0$ given by equation (6.69). Blue arrows show the initial flow field, scaled for visibility. **(b)** Evolution of the shape factor a_2^n (see equation (6.70)) with respect to the simulation time t (log scale) for values of the surface tension γ (in simulation units) spanning two orders of magnitude.

$$a_l^n = \sum_{k=0}^{N-1} \frac{1}{2} \left(\left| \tilde{\boldsymbol{X}}_k^n \right| + \left| \tilde{\boldsymbol{X}}_{k+1}^n \right| \right) \cos(l\theta_k^n) \left(\theta_{k+1}^n - \theta_k^n \right) \tag{6.70}$$

$$b_l^n = \sum_{k=0}^{N-1} \frac{1}{2} \left(\left| \tilde{\boldsymbol{X}}_k^n \right| + \left| \tilde{\boldsymbol{X}}_{k+1}^n \right| \right) \sin(l\theta_k^n) \left(\theta_{k+1}^n - \theta_k^n \right) \tag{6.71}$$

Generally, we compute the first few orders of Fourier coefficients $l = 2, 3, 4$, but in this particular test we just present a_2^n as the shape index as this is initially set to $1/2$ by equation (6.69). The evolution of this shape index is presented in figure 6.6(b) for several values of surface tension γ. As one would expect the droplet returns to a spherical shape, and the time it takes to do so is linearly proportional to the surface tension. Reducing the grid spacing from $h = 0.075$ to $h = 0.025$ makes no discernible difference to the droplet evolution (see figure 6.7). We test whether the droplet interaction with itself via the periodic boundaries affects evolution by varying the grid size $L_{x,y}$. Figure 6.7 shows that our choice of $L_{x,y} = 9R_0$ appears sufficient to render interactions with the droplet's periodic image negligible.

We also note that once the droplet reaches steady state, there is still some flow in the system even though analytically the flow should be zero. This arises due to inaccuracies in the mapping to the Cartesian mesh. We find that these flows are very small and do not

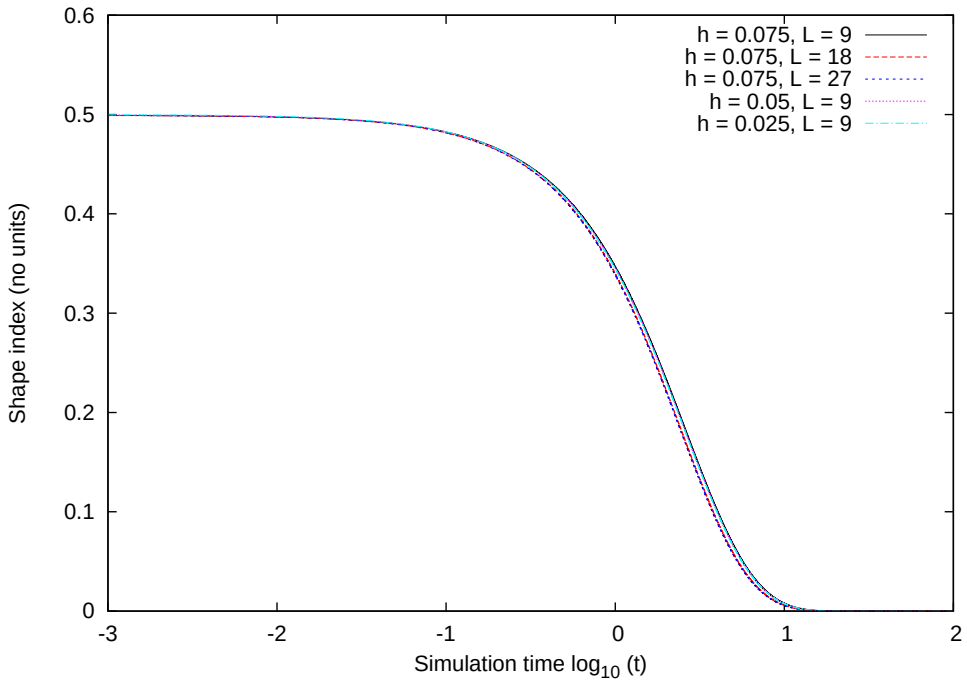

Figure 6.7: Evolution of the droplet shape with a surface tension value of $\gamma = 1$ for 3 grid spacings ($h = 0.025, 0.05, 0.075$) and 3 grid sizes ($L = 9, 18, 27$)

affect the droplet shape. However, these flow are on average only an order of magnitude smaller than those produced by the random perturbation that we apply, so they could affect the symmetry breaking direction.

6.5.2 Active Boundary Simulations

In this section we will study the steady states observed in the active boundary model discussed in sections 6.2.2 and 6.3.3. First, we will consider the case of contractile activity and diffusion only. Then we will move on to introduce the effects of the passive repulsion term proportional to B and also exchange of matter with the solvent inside the droplet. Finally we will consider how confinement affects the observed flow profile and deformation of the droplet.

In all of these cases, in order to enable the droplet to break symmetry we apply a perturbation to the system at time $t = 2.5$. We do this by altering the concentration at the interface at the beginning of the time-step by a small amount. In order to conserve

mass, we perturb the concentration using a Fourier series:

$$c_k^{5000} = c_k^{5000} + c^0 \sum_{l=1}^{N/4} [a_{kl} \cos(l\theta_k) + b_{kl} \sin(l\theta_k)] \tag{6.72}$$

where θ_k is as defined in section 6.5.1 and the coefficients a_{kl} and b_{kl} are assigned randomly generated values between -10^{-3} and 10^{-3}.

Activity and diffusion only

We find that for all values of contractile activity tested above a threshold value, a swimming steady state is observed with the droplet remaining circular see figure 6.8. Generally, almost all of the active contractile matter concentrates itself to a small section of the droplet surface. The width in this peak is determined by the balance of the advection (driven by activity) and diffusion terms in equation (6.10).

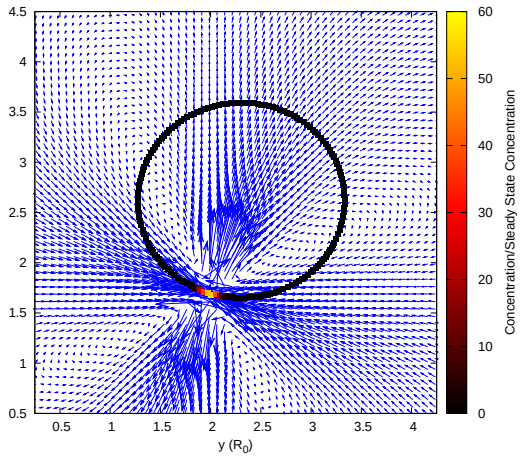

Figure 6.8: Snapshot of a simulation with $\zeta_c \Delta\mu = -1.5$ and $D = 0.1$. Arrows show the velocity field, scaled for visibility, and the interface points are coloured corresponding to the concentration field there. We see that the peak at the droplet rear is very narrow and concentrated.

In section 5.2 of chapter 5 we analysed the symmetry breaking threshold in this system, in this section we will measure the steady state droplet velocity. This velocity at the interface drives the instability, so if this is slightly underestimated by the simulations then the activity threshold will be increased. Figure 6.9(a) shows the centre of mass velocity of the droplets for several activity values.

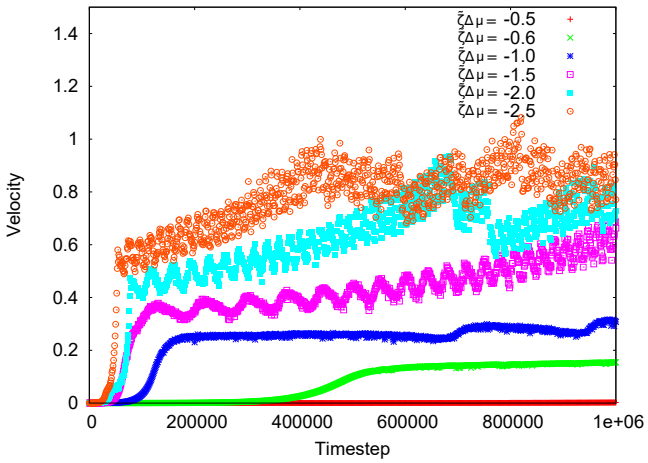

Figure 6.9: Evolution of the droplet centre of mass velocity over time for different values of the activity and a diffusion coefficient of $D = 0.1$. The time-step size used is $\Delta t = 5 \times 10^{-4}$.

We see that the velocity increases exponentially as the droplet breaks symmetry but after this transition the speed is not steady, and the graph is quite noisy. This is due to the active particle concentration being condensed to only a few boundary points leading to very high gradients there (see figure 6.8). The concentration profile seems to fluctuate not settling to a steady state. Thus, we see the importance of including higher order terms into the model (such as the passive repulsion term $Bc^2/2$ in the surface tension definition) as this prevents an unphysically large concentration build up. In addition, in this regime the linear active term is also a poor approximation due to these large gradients in c. Therefore, clearly just including activity and diffusion terms in this way does not lead to a numerically stable solution, nor does it appear a reasonable approximation to any real system.

Steady state swimming speeds

Including a non-zero value of B we see that the stability threshold is governed by the effective activity $\tilde{\zeta}\Delta\mu = \zeta_c\Delta\mu + Bc^0$. The threshold in $\tilde{\zeta}\Delta\mu$ for symmetry breaking is the same regardless of B, as predicted in the linear stability analysis in chapter 5. When this passive term is included the system steady state shows a broader concentration profile on the droplet boundary (see figure 6.10) and the system reaches a stable swimming speed.

Plotting this swimming speed against effective activity (figure 6.11)(a) we that it increases non-linearly, and that there is only a very weak negative dependence on the parameter B.

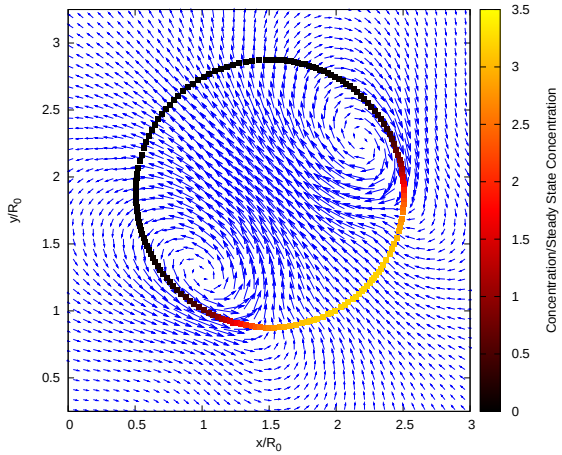

Figure 6.10: Snapshot of a simulation with $\zeta_c \Delta\mu = -1.5$, $D = 0.1$ and $B = 1.5$. Arrows show the velocity field, scaled for visibility, and the interface points are coloured corresponding to the concentration field there. We see that the peak at the droplet rear is much broader than in figure 6.8.

The initial trajectory of the droplet should be completely random, due to the random perturbation on the boundary that is applied, however it is possible that the direction of symmetry breaking may be affected by directions of the Cartesian grid, as this does have a small effect on the flow profile (see section 6.5.1). Plotting the trajectories of the droplets we see that the steady state swims in a straight line. This is contrary to what is observed when $B = 0$, where the droplet swims in circular paths, however this could be related to these simulations not reaching a stable steady state.

As mentioned in Chapter 5, we also observe that above a certain activity threshold, as predicted by the linear stability analysis, the active concentration initially forms two peaks, which then converge to form one. This manifests in an overshoot in the velocity evolution (see figure 6.11(b) as the two peaks converge and the concentration then spreads into one broader peak.

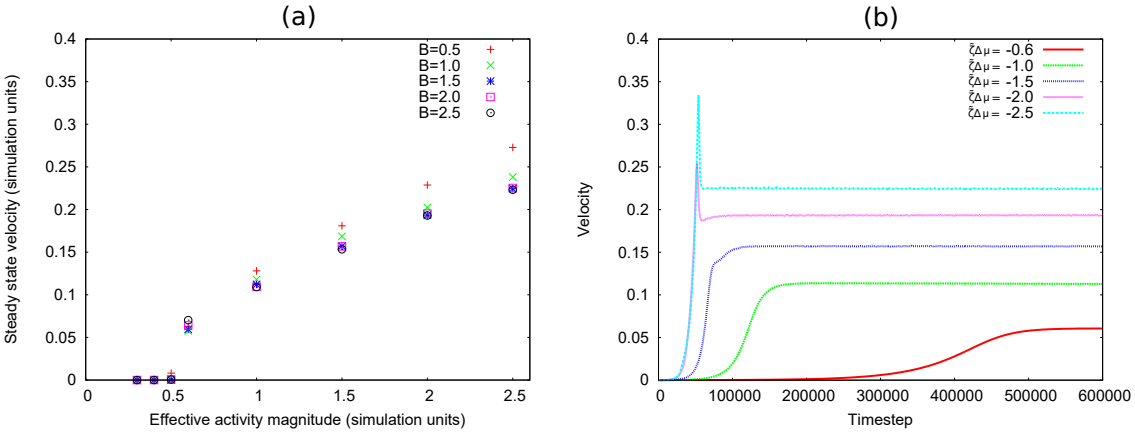

Figure 6.11: **(a)** Final droplet velocity plotted against the effective activity $\tilde{\zeta}\Delta\mu$ for different values of B. **(b)** Evolution of droplet velocity against simulation time-step for different values of the effective activity and $B = 1.5$.

Coupling to a bulk concentration

Due to the problems in numerical accuracy when $B = 0$, we choose to set $B = 1$ in order to test the case where we include a coupled concentration field in the bulk fluid as outlined in section 6.3.4. We test two interesting limits of this system, one where the binding rates k_{on} and k_{off} are slow compared the rate of diffusion in the bulk ($D_f \gg k_{\text{on,off}}$) and the other where the bulk diffusion is slow compared to the binding rates ($D_f \ll k_{\text{on,off}}$). The other important time-scale in these simulations is set by the cortical velocity which determines the divergence of the concentration at the interface.

We observe that in both cases, the steady state velocity of the droplet increases with the ratio $k_{\text{on}}/k_{\text{off}}$ although this change is much more pronounced in the slow diffusion case (see figure 6.12(a)). When diffusion is slow, we see that the steady state concentration inside the droplet follows that on the boundary, with high concentration at the droplet rear (see figure 6.13). This is because unbinding of the active concentration occurs more here (as it is proportional to concentration on the interface) and at a faster rate than it can diffuse away. We also occasionally see that in this case these simulations crash due to the calculation of the bulk concentration update. This happens when the iterative solution method fails to converge to within the tolerance value. This is related to the fact the concentration in the bulk is highly non-uniform, and the main source terms in this limit

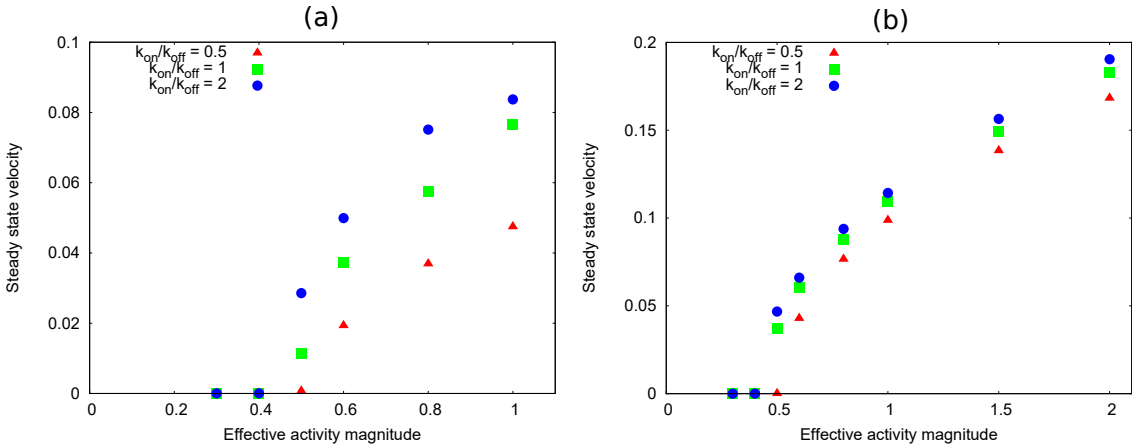

Figure 6.12: Steady state velocity versus $\left|\tilde{\zeta}\Delta\mu\right|$ for bulk diffusion and binding rate values of **(a)** $D_b = 0.005$, $k_{\text{on}} = 1.0$ and **(b)** $D_b = 0.5$, $k_{\text{on}} = 0.01$. The other values used are $B = 1$, $c_0 = 1$, $\eta = 1$, $\gamma = 1$, and $D = 0.1$. Note the difference in axes, in case (a) the simulations for higher activity values failed to run until the end, this is also why the final circular point in (a) does not fit the trend, as this simulation failed to reach steady state.

are from only a few points (those near the boundary) and are large in comparison to the other terms. This slow diffusion means that the velocity is comparable to the no binding simulations, even though the concentration profile is more evenly distributed along the interface. This is because there is positive feedback from the concentration inside the droplet that maintains the asymmetry.

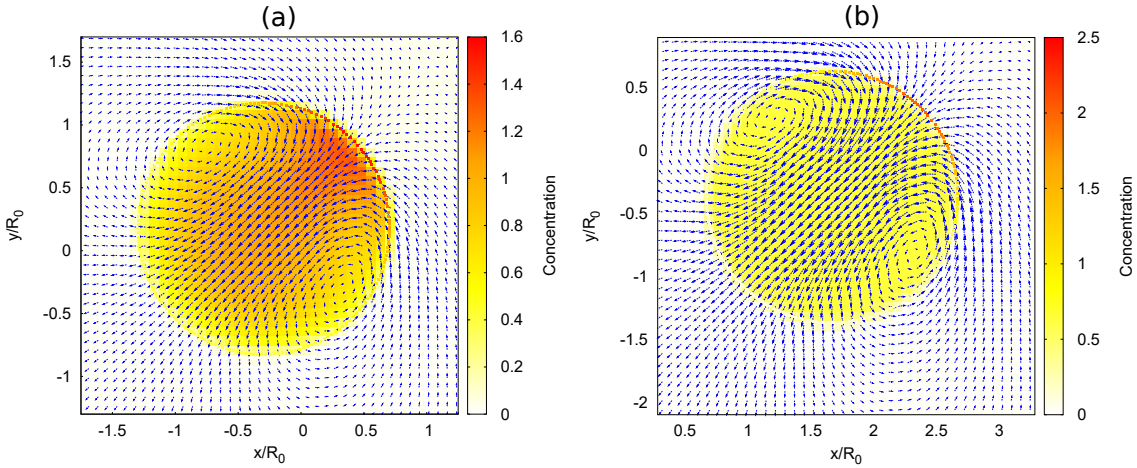

Figure 6.13: Steady state profiles for bulk diffusion and binding rate values of **(a)** $D_b = 0.005$, $k_{\text{on}} = 1.0$ and **(b)** $D_b = 0.5$, $k_{\text{on}} = 0.01$. The other values used are the same as in figure 6.12 and we have selected the $\tilde{\zeta}\Delta\mu = -0.8$ and $k_{\text{on}}/k_{\text{off}} = 1$ cases to show in both (a) and (b). The blue arrows show the fluid velocity (same scales used for both), note also the difference in concentration scales.

In the fast diffusion case the bulk concentration appears roughly constant (figure 6.13(b)). This means that any unbound active particles are quickly redistributed, resulting in a broader concentration profile on the boundary than when there was no binding. Note however, that because binding and unbinding is slow compared to the cortical velocity, there is little effect on the symmetry breaking threshold and the difference in velocities between the different binding values is small. We see also that because binding is slow the concentration profile is narrower than in the fast binding case. Also the droplet velocity in both of these simulations is only slightly slower than the no binding case.

If we take both diffusion and binding to be fast on the simulation time-scales then we see this has a very large impact on the symmetry breaking threshold (data not shown). In that case a much higher activity is required to overcome the fast recirculation of active particles in the drop.

6.5.3 Active Polar Fluid

Comparison with published results

We can test that the simulations of a droplet of active polar fluid are working by comparing to the hybrid lattice Boltzmann simulations published in [Tjhung et al., 2012]. By adjusting our simulation parameters to be the same as in the hybrid LB simulations of an active polar fluid we can compare the steady states directly. As in reference [Tjhung et al., 2012] we set the following parameters as: $K = 0.04$, $c_b = 2.5$, $R_0 = 17$, $\Delta t = 1$, $h = 1$, $W_1 = 0$, $\eta = 1$, $\Gamma = 1$ and $\nu = -1.1$. We initialise both sets of simulations with a small polarisation in the positive x direction inside the droplet, and perturb the systems by applying a small normal anchoring $W_1 = 0.0001$ for the first 5000 time-steps. We set the surface tension to $\gamma = 0.2$ which is approximately the effective surface tension in the phase field model in [Tjhung et al., 2012]. We also need to note that, the active stress in the hybrid LB simulations is proportional to $\zeta\Delta\mu\phi$ where $\phi = 2$ inside the droplet, and $\phi = 0$ outside. Therefore, when we compare activity values in figure 6.14(a), the activity values used in the hybrid LB simulations are multiplied by 2 for consistency.

We can see from figure 6.14 that we have good agreement between the two sets of simulations, with similar steady state velocity trends and droplet shape over a range of contractile activity values. It appears that, while the symmetry breaking threshold is approximately the same in both sets of simulations, the steady state velocity is a little larger in the IB simulations. We think that this is because of the non-zero values of H in the external fluid, as discussed in section 6.3.4. In the IB model the polarisation field and activity is coupled to H and so there will be small, non-physical active forces generated in the external fluid due to the error in H.

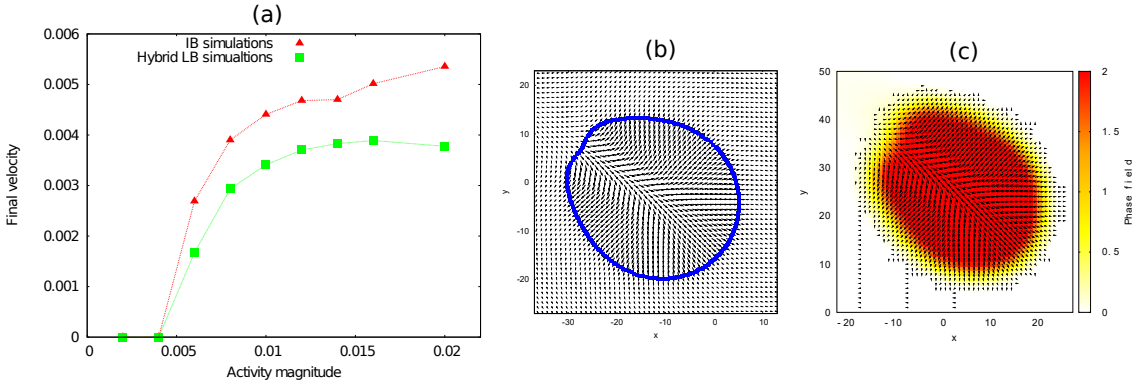

Figure 6.14: **(a)** Steady state droplet velocity for an active polar fluid drop simulated using the Immersed Boundary method (red triangles) and using hybrid lattice Boltzmann simulations used in [Tjhung et al., 2012]. All parameters used are listed in the text. **b** Snapshot of the system steady state using the IB method, where the blue line is the Lagrangian droplet interface and the black arrows show the polarisation. **(c)** Snapshot of the system steady state using hybrid LB simulations, the colour gradient shows the value of the phase field ϕ and the black arrows show the polarisation field.

Steady state shapes and velocities

As in chapter 5, we focus on the case of strong polar anchoring at the interface in order to investigate the effect of this coupling between internal polarisation and shape. We observe that with this boundary condition we only see an active motile state for extensile activity $\tilde{\zeta}\Delta\mu > 0$. This is in contrast to simulations by Giomi [Giomi and DeSimone, 2014] which show that, with normal anchoring an active *nematic* droplet shows swimming states for contractile activity. This suggests that it is the difference between nematic and polar order that is responsible for the difference. The stationary state of the system with polar

order consists of an aster with defect $q = +1$ at the droplet centre, whereas in the nematic case it consists of an elongated droplet with $q = \pm 1/2$ defects along the long-axis of the droplet. This difference in stationary state therefore must change the geometry such that the stability threshold for motion changes sign. This change appears to be robust for the values of ν we ave tested (one corresponding to 'rod-like' and one to 'disc-like') particles.

As predicted in chapter 5, the activity threshold for the onset of motion does not depend on the surface tension, however the droplet steady state speed does. As we can see in figure 5.8 the motile steady state is elongated and the amount of asymmetry in the shape depends on the surface tension. In figure 6.15 we plot the $k = 2$ mode shape parameter (essentially measuring droplet elongation) and final droplet velocity against the surface tension. Clearly, due to the strong anchoring at the interface, the polarisation profile is coupled to the boundary shape, so when the surface tension is small the polarisation profile is able to deform the droplet more and reach a faster steady state. As surface tension is increased the deformation reduces and goes towards a circular droplet, and in this limit the droplet velocity begins to plateau at its minimum value. This shows a positive feedback between the shape and the motion in these droplets, but in this case it doesn't appear to affect the symmetry breaking threshold.

For contractile activity we see that the lowest order symmetry breaking mode corresponds to a non-motile state where the droplet appears to initiate division. The rate of deformation of the droplet interface is exponential and is modelled well by the linear stability analysis at small times. In some cases we see that this deformation is halted at some steady state 'dumbbell' shape, where the defect is elongated into a line defect along the long axis of the droplet. At larger activity values we see that the opposite sides of the immersed boundary are almost brought into contact. However, these simulations do not yet have the capability of modelling division of the droplet as this is not a part of the IB model, which is a shortcoming in comparison to phase field models.

In principle one could impose conditions that would allow division of the boundary,

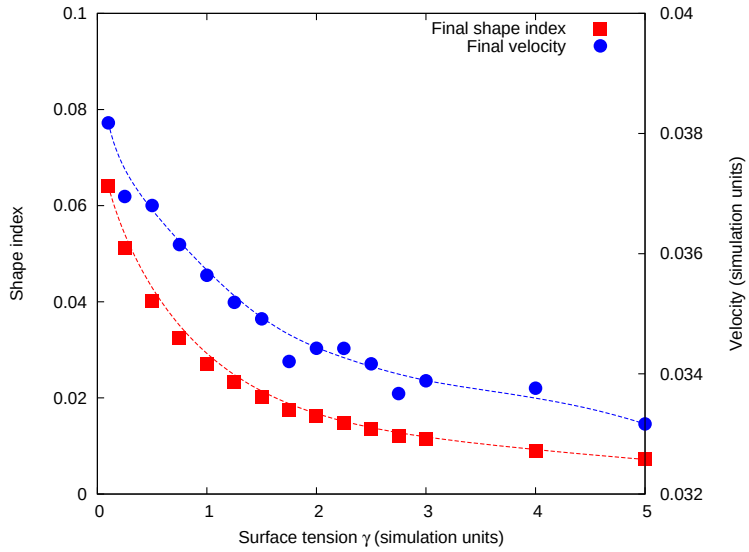

Figure 6.15: Final droplet speed (right axis) and $k = 2$ mode shape parameter (calculated as $\sqrt{(a_2^T)^2 + (b_2^T)^2}$, left axis) plotted against droplet surface tension. Dotted lines show a Bezier curve fit to the data. These simulations used $\zeta\Delta\mu = 1.5$ and $\nu = -1.1$ with the remaining parameters the same as used in section 5.3.2

such that there were two separate immersed boundaries in the simulation. To do this, one would need to calculate the separation between non-neighbouring boundary points k_1 and k_2, and once they were within a certain distance (say $\mathrm{d}s$) separate the boundary into 2 boundaries one from $k_1 + 1 \ldots k_2$ the other from $k_2 \ldots k_1$.

6.6 Future Directions

6.6.1 Coupling between internal and boundary activity

An interesting possibility that could be explored in these simulations is the case where there is an active polar liquid crystal inside the droplet coupled to an active interface. Currently, one can explore that directly with the simulations as they stand, if we assume that the concentration field ρ does not interact with the internal active polar fluid. Then we can explore coupling between these two systems via the flow alone. This could be a good estimate for a system with an active actin gel on the interface, and an active microtubule gel inside the droplet, where we assume that the filaments and motors only interact with their related species (*i.e.* microtubules with kinesin and actin with myosin).

A more thorough model of such a system, and indeed an important extension to our model, would be to consider filament and motor populations individually. Then one could consider coupling between a motor population bound to filaments in the droplet bulk and to those adsorbed on the droplet interface. The difficulty with such a system is the number of physical parameters, many would need to be fixed to realistic values that may not be easily attainable from experiments.

6.6.2 Elasticity in interface and external medium

One can easily change the properties of the droplet interface by modifying the expression for the boundary force in equation (6.1). We can use this to model different interface properties, such as bending and stretching elastic moduli. Original immersed boundary methods were designed for elastic biological fibres, with tension in the fibre defined as:

$$T = \varepsilon \left| \frac{\partial \boldsymbol{X}}{\partial s} \right| \tag{6.73}$$

such that the force exerted by the boundary on the fluid is

$$\boldsymbol{F} = \frac{\partial}{\partial s} \left(T \boldsymbol{\tau} \right) . \tag{6.74}$$

Suitably changing the boundary properties we could use these simulations to model an active lipid membrane immersed in a fluid. However, in this case the force would depend on the stretching factor $|\partial \boldsymbol{X}/\partial s|$, so any adding or removing of boundary points would change the force. For an elastic boundary one should not need to add and remove boundary points as the elasticity should stabilise the boundary shape. It may be useful to systematically add boundary points to change the effective elasticity to simulate a change in boundary composition, such as deposition of cell wall material in bacteria.

6.6.3 3D generalisation

The immersed boundary method is formulated for simulating 1D object-fluid interactions, such as fibres. Thus, any surfaces are generally represented as a mesh of 1D fibres. This

method is unsuitable for fluid interfaces such as the one simulated here because the surface tension force should be proportional to the sum of curvatures in the two orthogonal surface directions. In a mesh of Lagrangian fibres the fibre directions at vertices are not necessarily perpendicular and hence the method we use here does not generalise to 3D in a straight-forward way. However, a generalisation of the fluid IB model known as the immersed interface method (IIM) has been used to model surfactant flow on a 3D fluid drop interface [Xu, 2014]. In this case one has to explicitly consider the stress jump in the normal direction at the interface in order to impose the boundary force. The boundary is implicitly defined by the surrounding Cartesian mesh points, for which the flows are solved separately using the stress jump relation. The rest of the fluid flow can be solved using a standard 3D Stokes' solver.

Firstly, 3D generalisation would be very informative so that we can observe the predicted coupling between concentration of active points on the interface and curvature (in section 5.2). Moving forward, 3D simulations would be necessary to quantitatively relate these simulations to most relevant experimental systems.

6.6.4 External Boundaries

We are interested in the effects of confinement on active droplets and specifically how this affects motion and spontaneous symmetry breaking. This has relevance to cell motility in confinement. For example, a common migration mechanism, observed when cells are confined but non-adhering, is driven by high actomyosin concentration in the cortex at the cell rear [Poincloux et al., 2011, Heuze et al., 2013, Bergert et al., 2015]. Friction with the channel walls allows the cell to push itself forward via cortical flow and/or directed polymerisation. We would like to investigate how the active droplets we study here compare, and how interaction with walls can direct or prevent motion.

There are several possible methods to incorporate walls and confinement into the simulation; the most direct method is to set a boundary condition on the flow. We have implemented this in the simulations but found a significant problem using the delta func-

tion to interpolate the flow at the droplet interface when it is near to a wall. If we simply assume that the velocity is zero at any grid points in the wall, then two problems arise. First is that the flow calculated on the interface may no longer conserve the droplet area (area is approximately conserved in the periodic simulations by the flow incompressibility). Second, the interface is able to pass through the wall. Solving both of these problems would be difficult. In order to stop the droplet entering the walls one would need a velocity field defined within the walls that was a reflection of the flow inside, but this would only be consistent in the case of flat walls. Secondly, the area conservation condition outlined in 6.3.6 could be used to ensure area conservation but could also result in the droplet overlapping the walls.

Another method could be to confine the droplet using a spatially dependent force potential as in [Camley and Rappel, 2014]. This could be a good approximation to interactions with soft walls, but to approximate interaction with hard (and spatially resolved) walls this potential well would have to be very sharp, which could cause issues numerically.

The most consistent way is to simulate the boundary as an array of immersed boundary points. We have implemented these in the simulations but have found some problems with this method, which we will discuss in the following. We define $\boldsymbol{X}_l^w(s^w, t)$ to be the position vector of a wall point where $l = 0..N_w - 1$ and N_w is the number of points that constitute the walls. In order to simulate the interaction with the walls we consider that the wall points are independent and exert a force on the medium given by:

$$\boldsymbol{F}_m^w = A_w \left(\boldsymbol{X}_l^{w0} - \boldsymbol{X}_l^w \right) , \tag{6.75}$$

where $\boldsymbol{X}_l^{w0}$ is the initial position vector of wall point l. This means that if a wall point is displaced from it's initial location it will exert a restoring force. The evolution of the wall points is then described in the same way as the fluid boundary (equation (6.6)) by the fluid velocity around it. Therefore, if we choose A_w to be large then the wall should react on shorter time-scales than the active droplet and hence we should find an approximate

non-slip solution at the interface. We generally choose to confine the fluid in the y-direction with symmetric walls, the positions of which are given by the function $\pm w(x)$.

$$w(x) = \begin{cases} w_0/2 & \text{if} \quad |x| \leq L_x/8 \\ w_0/2 - 2(w_0 - w_c)(|x| - Lx/8)/L_x & \text{if} \quad L_x/8 < |x| \leq 3L_x/8 \\ w_c/2 & \text{if} \quad |x| > 3L_x/8 \end{cases} \tag{6.76}$$

where w_0 is the channel width at the centre of the simulation and w_c the width of channel at the simulation edges. Thus if we choose $w_c < 2 * R_0$ then there will be a constriction at the simulations edges which the droplet could only migrate though if suitably deformed. We have tested two layouts for the wall points to simulate this confinement. The first consists of two lines line of wall points with spacing $h/2$ along $y = \pm w(x)$ (see figure 6.16(a)) immersed in the periodic fluid. The second we try is a 2D array of points with spacing $h/2$ in all of the fluid where $y > w(x)$ and $y < w(x)$ (see figure 6.16(b)).

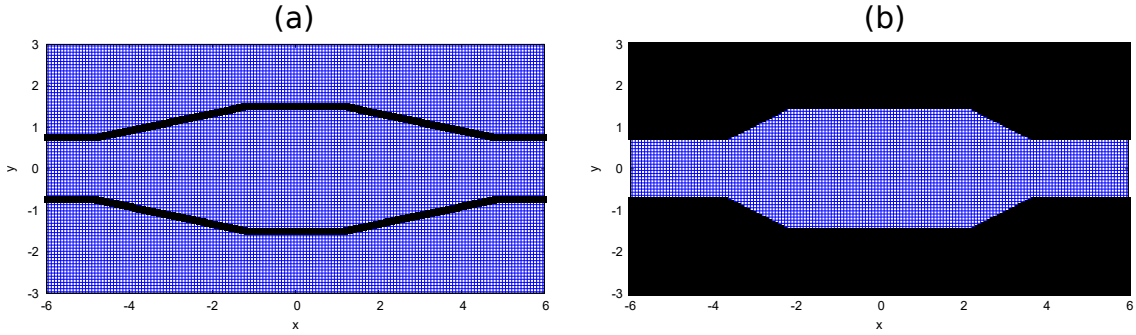

Figure 6.16: Plot of the wall points for **(a)** the case where the wall consists of a single line of points and **(b)** where the wall consists of a 2D array of points. Walls points are in black, blue crosses label the points of the Cartesian mesh. In both examples we have chose the channel widths as $w_0 = 3$ and $w_c = 1.5$.

A problem with this wall point method is that the resulting flow profile is different from the solutions with a strict non-slip condition. We can test this by applying an external force to a fluid in a single width channel ($w_0 = w_c$). Choosing $\boldsymbol{f}_{\text{ext}} = cos(\pi y_j/2w_0)$ we can calculate the non-slip solutions analytically also. We see from figure 6.17 that the solutions, while all non-slip at the interface, have a very different flow profile. It appears that the force from the wall points only cancels the flow locally around the walls. Furthermore, the

damping of the steady state flow from the wall points appears even more severe in the case where the walls consist of a 2D array of points (figure 6.17), rather than a single line. We do not yet know how to resolve these issues, hence we do not present any results from these simulations here.

A potentially unproblematic use for such external boundaries may be to consider a mesh of elastic fibres within the walls. This may then give an environment more relevant to cell motility *in vivo*, as one could tune the elasticity to be comparable to that of the extra cellular matrix. We outlined the simulation of immersed elastic fibres in the previous section, so this could be an interesting future route to simulating confinement in a physically consistent way.

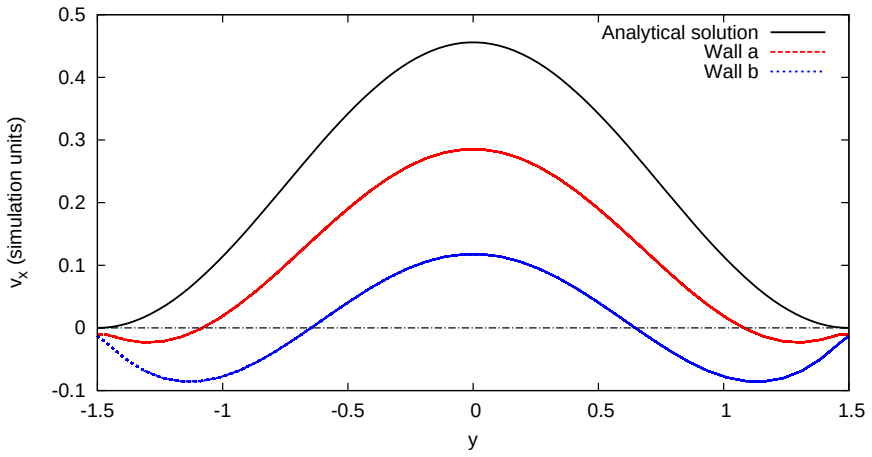

Figure 6.17: Steady state velocity in a single width channel ($w_0 = 3$) with non-slip walls. We apply the external force profile described in the text and run simulations for a wall consisting of a single line of points with wall force $A_w = 100$ (wall a) and a 2D array of points with wall force $A_w = 1$ (wall b).Note that, as the density of wall points in the fluid is increased, the velocity profile is damped further from the non-slip analytical solution.

6.7 Discussion and Conclusions

In this chapter we have detailed the numerical method that we have used to simulate the evolution of active droplets in 2D. We have used an Immersed Boundary (IB) method to

model the fluid boundary as a Lagrangian mesh of points. This allows us to explicitly simulate a concentration of isotropic active contractile particles on the interface that alter the surface tension. Further, we use the immersed boundary to define a level-set function which defines the inside and outside of the drop. Using this we can define an active polar liquid crystal phase in the droplet interior with anchoring at the droplet interface.

Using the Immersed Boundary simulations we find steady state migrating states in both types of active droplet. In both cases the steady state droplet velocity scales non-linearly with activity, levelling off at larger activity values. We also investigate the effect on motion when we simulate binding and unbinding of the active particles from the droplet surface. We see that this reduces the droplet velocity, but in the limits of low diffusion rate or slow binding that this effect is only slight. When diffusion is slow compared to the binding rate we observe some positive feedback the bound and unbound concentration fields. In the case of an active polar fluid drop, we observe steady state rotation and deformation, as discussed in chapter 5.

We also discuss various ways to take these simulations forward and simulate even more biologically relevant problems. We identify the most important challenge as generalising these simulations to 3D, however most of this challenge is technical, as the constitutive equations scale to 3D in a straight-forward way. In addition we discuss our attempts to simulate droplets interacting with confining hard walls, and the pros and cons of various approaches. This would enable us to simulate environments more applicable to *in vivo* cell migration.

Chapter 7

Discussion and Outlook

Abstract

In this chapter we will summarise the research presented in this thesis, and its relevance to the physics of *in vitro* and *in vivo* cytoskeletal systems. we will also discuss some future directions for this research.

7.1 Summary

In this thesis we have presented models of active contractile fluids confined to droplets in order to understand and predict aspects of cytoskeletal dynamics and cell deformation. We have used the hydrodynamic approach modelling these systems with continuous quantities following the models derived in [Kruse et al., 2004, Kruse et al., 2005, Joanny et al., 2007, Fürthauer et al., 2012] and used in many other studies.

In chapter 3 we considered a droplet with its internal symmetry broken by a splayed polarisation field. We were able to analytically calculate the flow in the droplet, the forces on the drop interface (assuming a linear friction at the interface) and the centre of mass velocity (in the case of the drop immersed in an external fluid). In combination with the simulations presented in [Tjhung et al., 2012] and later in [Marth et al., 2014] we characterise the resulting droplet motion resulting from directed active contraction. This analytical calculation also shows how reasonable approximations of the flows and forces can be obtained in this system despite the difficult geometry. The spherical droplet is best described in polar coordinates, whereas the polarisation is assumed to be splayed around a Cartesian axis. Thus, the system cannot be reduced to a single coordinate, and hence only approximate solutions can be obtained that satisfy the boundary constraints and physical laws.

Chapter 4 studied the inverted case of a passive droplet immersed in an active polar fluid from work performed with collaborators at Edinburgh University [De Magistris et al., 2014]. In this system we see that, if we assume strong anchoring at the interface, we can use the work of [Lubensky et al., 1998] to approximate the steady state polarisation field. If the anchoring at the interface is polar, this always results in a system with broken symmetry, even in the passive limit. Thus, when the polar liquid crystal is active the droplet is propelled by the medium. In chapter 4 we quantify this motion analytically, first we show that the direction of the active force around the droplet agrees with the motion observed in simulations. Plus, we can estimate how the droplet centre of mass velocity will scale

with system size by approximating the flow at the boundaries by the expression we derive for the far field flow in an infinite active fluid.

In chapters 5 and 6 we model two different examples of coupling between interface morphology and active fluid dynamics. First, we model a fluid droplet with an isotropic active contractile fluid dispersed on the interface. In this system, contraction of the active fluid increases the droplet surface tension. Any inhomogeneity in concentration of active particles on the interface creates a surface tension gradient and hence fluid flow. This flow can create a divergent current of active concentration on the interface and give rise to instabilities in the stationary steady state of the system. We can predict these analytically based on the assumptions in the model. We consider all spherical harmonic modes of the perturbation in 3D and see that the activity threshold increases for higher order modes. Furthermore, we see that the activity thresholds for symmetry breaking are not coupled to boundary deformation, however the evolution of these states do show coupling with the curvature for a 3D system. This shows that the initial instability can be described well by considering a completely spherical drop. In 2D the droplet is not deformable due to surface tension gradients alone, and we see that our calculations in this geometry agree well with the results of the simulations outlined in chapter 6.

An interesting observation from simulations of this active interface is that when multiple peaks in concentration form they are unstable. This is related to the problem of stability in cytokinesis of animal cells. It can be reasoned that perfectly symmetric cleaving of cell by the active contractile forces around the droplet middle should be a physically unstable system. Firstly, any asymmetry in the position of the 'contractile ring' should reduce the volume in one half of the cell, and in turn increase the pressure there. This should then create a flow from the small to the larger daughter cell and perpetuate the asymmetry [Sedzinski et al., 2011]. Moreover, our model shows that even in a 2D incompressible system, when the droplet shape remains fixed, this form of instability still exists due to the cortical flow. As the peaks become closer together, the cortical flow in between them reduces as the flows from the two peaks cancel slightly, this also means an increase in

flow speed on the other side of the peaks, promoting the asymmetry and resulting in the coalescence of the two peaks.

The other system we consider in chapters 5 and 6 is a fluid drop containing an active polar liquid crystal of constant density. Here, we assume that the polarisation is strongly coupled to interface dynamics by an anchoring term, which we show constrains the behaviour to certain forms of instability. Similar to the system in chapter 3, we see that symmetry breaking can occur regardless of surface tension value (and hence amount of deformation) by an asymmetric distortion of the polarisation field, or by a rotation of the polarisation field (the latter is the same instability predicted in [Kruse et al., 2004]). We also see that there is coupled modes of symmetry breaking, the lowest order of this leads to the onset of droplet division by contractile active stresses. Interestingly, while this system has much in common with an active nematic, the symmetry breaking observed that results in motion actually occurs for extensile activity, rather than contractile. This difference comes from the equilibrium steady state consisting of a single $q = +1$ defect in the polar case, whereas two $q = +1/2$ defects are present in the nematic case. We are able to predict the onset of division and higher modes of deformation within the assumptions made in the linear stability analysis. However these cannot predict the symmetry breaking mode that results in persistent droplet motion, as the assumptions break down in this case.

The active polar drop system has a rich variety of steady state behaviours. When we reduce the value of the single elastic constant K, such that $K/R_0^2 \ll \gamma$, we begin to see that for large enough activity, the symmetry can break internally in complex ways without any initial boundary deformation. This effect would also be observed by increasing the droplet size, because this effectively makes bulk free energy smaller in comparison to the active energy in the system. This means that small changes in boundary conformation are not propagated through the elastic interactions of the filaments and the polarisation far from the boundary is somewhat independent of the anchoring. When this is the case we begin to see deformation of the defect for larger activity and the creation of new

defects. These all break the internal symmetry and create flow in the system. It would be interesting to study these states in more detail in the future as they appear to exist in the regime between the ordered steady states one observes for small, highly constrained systems and the pseudo-chaotic steady states observed in large active nematic and polar gels [Giomi et al., 2012].

7.2 Experimental Realisation and Limitations

The models presented in this thesis are highly idealised systems that display distinct aspects of cytoskeleton dynamics, namely active stress generation. Thus, direct experimental realisation of these systems would require suitable active gels be synthesised *in vitro* from active cytoskeletal components. The behaviour observed in such *in vitro* active gels greatly depends on the ratios of components included and the synthesis process. An example of an *in vitro* active gel that maintains long range nematic order are the microtubule bundle systems created in [Sanchez et al., 2012] and [Keber et al., 2014]. In these gels the bundles are stabilised by the addition of polyethylene glycol (PEG) which also enables the microtubules to adsorb onto the inside surfaces of vesicles or emulsion droplets. Kinesin motors are added to the system which are observed to generate propulsion of the filaments in a way that is consistent with the generation of extensile stresses [Giomi et al., 2013]. [Sanchez et al., 2012] observe that this can lead to the creation and annihilation of defects in the active gel, consistent with behaviour observed in the high activity limit of these continuum models. In [Keber et al., 2014] the system size is smaller and stable defects form in the microtubule gel, however the extensile stresses generated by the kinesin motors can change the configuration of the defects on the surface from a tetrahedral arrangement (the equilibrium configuration) to a planar configuration. Depending on the microtubule concentration, the vesicles may not be evenly covered with microtubules and a band of microtubules tend to form around the droplet middle. These banding effects can be captured by active gel continuum models, however when the filament count becomes small the continuum approximation breaks down and microscopic models may be more relevant.

The droplets that we consider that contain an active gel with strong polar order $|\boldsymbol{p}| = 1$ may be experimentally realisable in such an *in vitro* active gel where the components generate contractile stresses. However in such a system there would need to suitable buffering by the solvent or passive polymers to prevent rapid clumping or adsorption onto a droplet interface. Furthermore the filament concentration would need to be large enough to observe nematic effects, as in [Coppin and Leavis, 1992] and [Viamontes et al., 2006] for passive actin filament solutions. This may require introducing bundling proteins such as α-actinin or fimbrin to the active gel so that the actin forms thicker fibres, meaning larger elastic interactions between filaments making it easier to achieve stronger ordering. In cells these proteins are associated with stress fibres and filopodia formation but in less adhesive environments, such as immersed in a fluid or gel, these structures cannot form in the same way. However, the introduction of these proteins not necessary for actin bundle formation, this has been observed in experiments in a 2D system where bundle formation and nematic ordering can be induced by concentrations of polymer crowding agents [Popp et al., 2006].

The model we present in chapter 3 then will be relevant to an *in vitro* system such as the one proposed above if there is little or no anchoring of the actin at the interface that could result in large density gradients or defect formation. Thus, we predict that in the low ATP concentration case (corresponding to low activity) it should be possible to observe a transition from an aligned nematic or polar state to a splayed configuration of broken symmetry. It would be interesting to observe in such a system how suitable a constant density approximation is in this case for the motors and actin network. In chapters 4 and 5 we consider the case where this polar actin fluid is anchored in a normal direction to the interface. For this to occur, one may require a surfactant or membrane protein dispersed on the interface that strongly prefers a particular actin filament end (barbed or pointed). In these cases we are able to make predictions about symmetry breaking and motion. In particular, we can predict the activity required to break symmetry for a simple fluid drop using the simulations, and what steady states can be observed. However, these models still lack some of the details of these simplified exper-

iments, such as varying motor density and viscoelasticity, which may change the behaviour.

The contractile isotropic active gel that we consider in chapters 5 and 6 is most similar physically to reconstituted actomyosin systems created *in vitro* such as [Bendix et al., 2008]. In this example the addition of passive crosslinkers is vital to stabilise the actin network. Within a range of myosin motor concentration and crosslinker density this *in vitro* system contracts until the density of filaments is high enough to prevent further contraction [Bendix et al., 2008]. Assuming that this kind of gel could be adsorbed onto a droplet surface, it should be possible to observe the steady state behaviour we predict. The second order passive term that we include in this model is a phenomenological parameter that prevents the system continuing to contract at very high density [Joanny et al., 2013], but nonetheless even when this system reaches steady state there still exists a surface tension gradient on the surface. Again, for these experiments it may be useful to stabilise the gel with a polymer buffer, or introduce branching proteins such as ARP2/3. In order to mimic the cell cortex, and resemble the model here, ideally one would construct a system where the actin network either covers a fluid droplet or coats the inside of a vesicle. Then, if one could capture large filaments of myosin motors inside these droplets these could bind and unbind to the underside of the actin network and produce contractile stresses at the interface. In this case the one component model we have used here is only relevant if we assume that the actin network is not very dynamic, and the dynamic concentration c is that of the motor protein filaments.

If this could be achieved then we predict that at low ATP concentrations, there will be a transition to a motile state, with a single peak in motor concentration. Comparing predicted activity dependence of the swimming velocity to experimental values with respect to ATP concentration, it would be possible to assess some of the merits and limitations of these models. In particular, in relating the activity parameter to experimental values. In addition, by comparing these measurements to concentration profiles, it should be possible to distinguish within what range the surface tension is approximately linearly dependent on concentration.

Currently, the groups of Andreas Bausch, Gijsje Koenderink and Zvonimir Dogic are making rapid advances in constructing active cytoskeletal networks and techniques to deposit or encapsulate these in droplets or vesicles (see [Keber et al., 2014],[Tsai et al., 2011] and [Sanchez et al., 2012] for examples respectively). Thus we anticipate that our understanding of the physics of these systems will greatly advanced as more experimental data is acquired, and a wider range of active gels are synthesised.

Despite the models presented here being far removed from the complex biology of cells *in vivo*, the physics explored can inform us about the physical instabilities that could exist in these systems. In some cases continuum active gel models can provide an overall physical description and understanding of the motion of particular cell types in specific geometries [Hawkins et al., 2009], [Hawkins et al., 2011]. In some active gel models cell motility and deformation is approached from a more generic point of view [Kruse et al., 2006], [Callan-Jones and Voituriez, 2013] ,[Turlier et al., 2014]. In this way there are generic behaviours displayed in the models presented here such as the persistent motion of droplets driven by active stresses and droplet deformation coupled to internal polarisation dynamics.

7.3 Further work and extensions

Chapters 5 and 6 demonstrate some of the interesting physical states that can be observed via the immersed boundary simulations that we construct. Due to the modular nature of the simulation it is possible for them to be extended in various useful ways as discussed in chapter 6. Firstly, in order to capture more aspects of cytoskeletal dynamics one could incorporate more physically allowed active terms that give rise in filament sorting and banding and directed polymerisation forces. In addition one could incorporate a friction on the flow imposed by a substrate parallel to the simulation plane, to incorporate changes in geometry in this 2D model. Furthermore one can easily alter the boundary properties to simulate different droplet interfaces, and impose external boundaries to confine the

system.

One major drawback of these simulations is that the method does not scale in a straight forward way to 3D. However, as discussed in section 6.6.3 this can be achieved by a similar immersed boundary method where normal and tangential force continuity is explicitly considered near the interface. In addition the simulations would currently be too slow to run effectively on a 3D system and so parallelisation of the source code might be necessary.

In future work it would be interesting to investigate where the instabilities we predict may occur in cytoskeletal networks in nature and in what regimes the approximations of these models are valid. Further, the similarities between the simple models of an active interface presented here, and the dynamics of droplets moving under reaction and diffusion of chemicals that alter surface tension [Yoshinaga, 2014], suggest that our stability analysis technique could be adopted here to predict the thresholds for different modes of symmetry breaking.

7.4 Conclusion

In this thesis we have probed at the physics of active systems of filaments and motors in various regimes where the behaviour is constrained by system geometry. We use analytical calculation to predict and understand behaviour observed in simulations as far as possible. We have also introduced some insights and techniques to approximating behaviour in these systems successfully. Finally, we have also produced useful simulations that can be extended to model an even wider range of active fluid droplet systems. Corrections such as droplet area conservation and interface smoothing have made this immersed boundary method more robust for these systems with high activity and large local flows.

To conclude, the calculations and numerical simulations presented in this thesis further the understanding of the physics of self-propelled motion by active stress generation. Further, the simulations we have written can potentially be utilised to simulate more

complex systems relevant to the phenomena of cell motility and polarisation due to the activity of the cytoskeleton.

Bibliography

[Ahmadi et al., 2005] Ahmadi, A., Liverpool, T. B., and Marchetti, M. C. (2005). Nematic and polar order in active filament solutions. *Phys. Rev. E*, 72(6):60901.

[Ahmadi et al., 2006] Ahmadi, A., Marchetti, M. C., and Liverpool, T. B. (2006). Hydrodynamics of isotropic and liquid crystalline active polymer solutions. *Phys. Rev. E*, 74(6):1–23.

[Alberts et al., 2008] Alberts, B., Johnson, A., Lewis, J., Raff, M., Roberts, K., and Walter, P. (2008). *Molecular Biology of the Cell*. Garland Science, New York, 5th edition.

[Ananthakrishnan and Ehrlicher, 2007] Ananthakrishnan, R. and Ehrlicher, A. (2007). The forces behind cell movement. *Int. J. Biol. Sci.*, 3(5):303–317.

[Aranson and Tsimring, 2006] Aranson, I. S. and Tsimring, L. S. (2006). Theory of self-assembly of microtubules and motors. *Phys. Rev. E*, 74(3):031915.

[Bendix et al., 2008] Bendix, P. M., Koenderink, G. H., Cuvelier, D., Dogic, Z., Koeleman, B. N., Brieher, W. M., Field, C. M., Mahadevan, L., and Weitz, D. a. (2008). A quantitative analysis of contractility in active cytoskeletal protein networks. *Biophys. J.*, 94(8):3126–3136.

[Bergert et al., 2015] Bergert, M., Erzberger, A., Desai, R. a., Aspalter, I. M., Oates, A. C., Charras, G., Salbreux, G., and Paluch, E. K. (2015). Force transmission during adhesion-independent migration. *Nat. Cell Biol.*, 17(4).

[Blake, 1971] Blake, J. R. (1971). A spherical envelope approach to ciliary propulsion. *J. Fluid Mech.*, 46:199–208.

[Bornens, 2008] Bornens, M. (2008). Organelle positioning and cell polarity. *Nat. Rev. Mol. Cell Biol.*, 9(11):874–886.

[Bray, 2001] Bray, D. (2001). *Cell Movements: From Molecules to Motility*. Garland, New York, 2nd edition.

[Callan-Jones et al., 2008] Callan-Jones, A. C., Joanny, J.-F., and Prost, J. (2008). Viscous-Fingering-Like Instability of Cell Fragments. *Phys. Rev. Lett.*, 100(25):258106.

[Callan-Jones and Voituriez, 2013] Callan-Jones, A. C. and Voituriez, R. (2013). Active gel model of amoeboid cell motility. *New J. Phys.*, 15(2):025022.

[Cameron et al., 1999] Cameron, L. A., Footer, M. J., van Oudenaarden, A., and Theriot, J. a. (1999). Motility of ActA protein-coated microspheres driven by actin polymerization. *Proc. Natl. Acad. Sci.*, 96(9):4908–4913.

[Camley and Rappel, 2014] Camley, B. A. and Rappel, W.-J. (2014). Velocity alignment leads to high persistence in confined cells. *Phys. Rev. E*, 89(6):062705.

[Carlsson, 2006] Carlsson, A. E. (2006). Contractile stress generation by actomyosin gels. *Phys. Rev. E*, 74(5):1–6.

[Chan et al., 2000] Chan, a. Y., Bailly, M., Zebda, N., Segall, J. E., and Condeelis, J. S. (2000). Role of cofilin in epidermal growth factor-stimulated actin polymerization and lamellipod protrusion. *J. Cell Biol.*, 148(3):531–42.

[Charras and Paluch, 2008] Charras, G. and Paluch, E. (2008). Blebs lead the way: how to migrate without lamellipodia. *Nat. Rev. Mol. Cell Biol.*, 9(9):730–736.

[Chen and Lai, 2014] Chen, K.-Y. and Lai, M.-C. (2014). A conservative scheme for solving coupled surface-bulk convection-diffusion equations with an application to interfacial flows with soluble surfactant. *J. Comput. Phys.*, 257(PA):1–18.

[Chen and Doolen, 1998] Chen, S. and Doolen, G. D. (1998). Lattice Boltzmann Method for Fluid Flows. *Annu. Rev. Fluid Mech.*, 30:329–364.

[Coppin and Leavis, 1992] Coppin, C. M. and Leavis, P. C. (1992). Quantitation of liquid-crystalline ordering in F-actin solutions. *Biophys. J.*, 63(3):794–807.

[Cross et al., 2007] Cross, S. E., Jin, Y.-S., Rao, J., and Gimzewski, J. K. (2007). Nanomechanical analysis of cells from cancer patients. *Nat. Nanotechnol.*, 2(12):780–783.

[Cukierman et al., 2001] Cukierman, E., Pankov, R., Stevens, D. R., and Yamada, K. M. (2001). Taking cell-matrix adhesions to the third dimension. *Science*, 294:1708–1712.

[Dai and Sheetz, 1999] Dai, J. and Sheetz, M. P. (1999). Membrane Tether Formation from Blebbing Cells. *Biophys. J.*, 77(6):3363–3370.

[de Gennes and Prost, 1993] de Gennes, P. G. and Prost, J. (1993). *The Physics of Liquid Crystals*. Clarendon Press, Oxford, 2nd edition.

[De Magistris et al., 2014] De Magistris, G., Tiribocchi, A., Whitfield, C. A., Hawkins, R. J., Cates, M. E., and Marenduzzo, D. (2014). Spontaneous motility of passive emulsion droplets in polar active gels. *Soft Matter*, 10:7826–7837.

[Discher et al., 2005] Discher, D. E., Janmey, P., and Wang, Y.-L. (2005). Tissue cells feel and respond to the stiffness of their substrate. *Science*, 310:1139–1143.

[Dombrowski et al., 2004] Dombrowski, C., Cisneros, L., Chatkaew, S., Goldstein, R. E., and Kessler, J. O. (2004). Self-Concentration and Large-Scale Coherence in Bacterial Dynamics. *Phys. Rev. Lett.*, 93(9):98103.

[Doyle et al., 2013] Doyle, A. D., Petrie, R. J., Kutys, M. L., and Yamada, K. M. (2013). Dimensions in cell migration. *Curr. Opin. Cell Biol.*, 25(5):642–649.

[Edwards and Yeomans, 2009] Edwards, S. A. and Yeomans, J. M. (2009). Spontaneous flow states in active nematics: A unified picture. *Europhys. Lett.*, 85(1):18008.

[Ehrbar et al., 2011] Ehrbar, M., Sala, A., Lienemann, P., Ranga, A., Mosiewicz, K., Bittermann, A., Rizzi, S. C., Weber, F. E., and Lutolf, M. P. (2011). Elucidating the role of matrix stiffness in 3D cell migration and remodeling. *Biophys. J.*, 100(2):284–293.

[Euteneuer and Schliwa, 1984] Euteneuer, U. and Schliwa, M. (1984). Persistent, directional motility of cells and cytoplasmic fragments in the absence of microtubules. *Nature*, 310:58–61.

[Even-Ram and Yamada, 2005] Even-Ram, S. and Yamada, K. M. (2005). Cell migration in 3D matrix. *Curr. Opin. Cell Biol.*, 17(5):524–532.

[Fackler and Grosse, 2008] Fackler, O. and Grosse, R. (2008). Cell motility through plasma membrane blebbing. *J. Cell Biol.*, 181(6):879–884.

[Fidler, 2003] Fidler, I. J. (2003). The pathogenesis of cancer metastasis: the 'seed and soil' hypothesis revisited. *Nat. Rev. Cancer*, 3(6):453–458.

[Fielding et al., 2011] Fielding, S. M., Marenduzzo, D., and Cates, M. E. (2011). Nonlinear dynamics and rheology of active fluids: Simulations in two dimensions. *Phys. Rev. E*, 83(4):1–14.

[Foffano et al., 2012] Foffano, G., Lintuvuori, J. S., Stratford, K., Cates, M. E., and Marenduzzo, D. (2012). Colloids in Active Fluids: Anomalous Microrheology and Negative Drag. *Phys. Rev. Lett.*, 109(2):028103.

[Fürthauer et al., 2012] Fürthauer, S., Neef, M., Grill, S. W., Kruse, K., and Jülicher, F. (2012). The Taylor-Couette motor: spontaneous flows of active polar fluids between two coaxial cylinders. *New J. Phys.*, 14(2):023001.

[Gardel et al., 2008] Gardel, M. L., Kasza, K. E., Brangwynne, C. P., Liu, J., and Weitz, D. A. (2008). Mechanical Response of Cytoskeletal Networks. In *Methods Cell Biol.*, pages 487–519.

[Giomi et al., 2013] Giomi, L., Bowick, M. J., Ma, X., and Marchetti, M. C. (2013). Defect annihilation and proliferation in active nematics. *Phys. Rev. Lett.*, 110(22):1–5.

[Giomi and DeSimone, 2014] Giomi, L. and DeSimone, A. (2014). Spontaneous Division and Motility in Active Nematic Droplets. *Phys. Rev. Lett.*, 112(14):147802.

[Giomi et al., 2012] Giomi, L., Mahadevan, L., Chakraborty, B., and Hagan, M. F. (2012). Banding, excitability and chaos in active nematic suspensions. *Nonlinearity*, 25(8):2245–2269.

[Gittes et al., 1993] Gittes, F., Mickey, B., Nettleton, J., and Howard, J. (1993). Flexural Rigidity of Microtubules and Actin Filaments Measured from Thermal Fluctuations in Shape. *J. Cell Biol.*, 120(4):923–934.

[Goldberg and Theriot, 1995] Goldberg, M. B. and Theriot, J. a. (1995). Shigella flexneri surface protein IcsA is sufficient to direct actin-based motility. *Proc. Natl. Acad. Sci.*, 92(14):6572–6576.

[Gomes et al., 2005] Gomes, E. R., Jani, S., and Gundersen, G. G. (2005). Nuclear movement regulated by Cdc42, MRCK, myosin, and actin flow establishes MTOC polarization in migrating cells. *Cell*, 121(3):451–463.

[Guck et al., 2005] Guck, J., Schinkinger, S., Lincoln, B., Wottawah, F., Ebert, S., Romeyke, M., Lenz, D., Erickson, H. M., Ananthakrishnan, R., Mitchell, D., Käs, J., Ulvick, S., and Bilby, C. (2005). Optical deformability as an inherent cell marker for testing malignant transformation and metastatic competence. *Biophys. J.*, 88(5):3689–3698.

[Harada et al., 2014] Harada, T., Swift, J., Irianto, J., Shin, J.-W. W., Spinler, K. R., Athirasala, A., Diegmiller, R., Dingal, P. C. D. P., Ivanovska, I. L., and Discher, D. E. (2014). Nuclear lamin stiffness is a barrier to 3D migration, but softness can limit survival. *J. Cell Biol.*, 204(5):669–682.

[Hatwalne et al., 2004] Hatwalne, Y., Ramaswamy, S., Rao, M., and Simha, R. (2004). Rheology of Active-Particle Suspensions. *Phys. Rev. Lett.*, 92(11):118101.

[Hawkins and Liverpool, 2014] Hawkins, R. J. and Liverpool, T. B. (2014). Stress reorganization and response in active solids. *Phys. Rev. Lett.*, 113(2):1–5.

[Hawkins et al., 2009] Hawkins, R. J., Piel, M., Faure-Andre, G., Lennon-Dumenil, A. M., Joanny, J. F., Prost, J., and Voituriez, R. (2009). Pushing off the Walls: A Mechanism of Cell Motility in Confinement. *Phys. Rev. Lett.*, 102(5):58103.

[Hawkins et al., 2011] Hawkins, R. J., Poincloux, R., Bénichou, O., Piel, M., Chavrier, P., and Voituriez, R. (2011). Spontaneous Contractility-Mediated Cortical Flow Generates Cell Migration in Three-Dimensional Environments. *Biophys. J.*, 101(5):1041–1045.

[Head et al., 2011] Head, D. A., Gompper, G., and Briels, W. J. (2011). Microscopic basis for pattern formation and anomalous transport in two-dimensional active gels. *Soft Matter*, 7(7):3116–3126.

[Hemingway et al., 2015] Hemingway, E. J., Maitra, a., Banerjee, S., Marchetti, M. C., Ramaswamy, S., Fielding, S. M., and Cates, M. E. (2015). Active Viscoelastic Matter: From Bacterial Drag Reduction to Turbulent Solids. *Phys. Rev. Lett.*, 114(9):098302.

[Heuzé et al., 2011] Heuzé, M. L., Collin, O., Terriac, E., Lennon-Duménil, A.-M., and Piel, M. (2011). Cell migration in confinement: a micro-channel-based assay. *Methods Mol. Biol.*, 769:415–34.

[Heuze et al., 2013] Heuze, M. L., Vargas, P., Chabaud, M., Le Berre, M., Liu, Y. J., Collin, O., Solanes, P., Voituriez, R., Piel, M., and Lennon-Dumenil, a. M. (2013). Migration of dendritic cells: physical principles, molecular mechanisms, and functional implications. *Immunol. Rev.*, 256(1):240–254.

[Hill, 1980] Hill, T. L. (1980). Bioenergetic aspects and polymer length distribution in steady-state head-to-tail polymerization of actin or microtubules. *Proc. Natl. Acad. Sci.*, 77(8):4803–4807.

[Hirokawa, 1998] Hirokawa, N. (1998). Kinesin and Dynein Superfamily Proteins and the Mechanism of Organelle Transport. *Science*, 279:519–526.

[Joanny et al., 2007] Joanny, J. F., Jülicher, F., Kruse, K., and Prost, J. (2007). Hydrodynamic theory for multi-component active polar gels. *New J. Phys.*, 9(11):422.

[Joanny et al., 2013] Joanny, J.-F. F., Kruse, K., Prost, J., and Ramaswamy, S. (2013). The actin cortex as an active wetting layer. *Eur. Phys. J. E*, 36(5):52.

[Joanny and Ramaswamy, 2012] Joanny, J.-F. F. and Ramaswamy, S. (2012). A drop of active matter. *J. Fluid Mech.*, 705(April):46–57.

[Keber et al., 2014] Keber, F. C., Loiseau, E., Sanchez, T., DeCamp, S. J., Giomi, L., Bowick, M. J., Marchetti, M. C., Dogic, Z., and Bausch, A. R. (2014). Topology and Dynamics of Active Nematic Vesicles. *Science*, 345:1–19.

[Kim et al., 2003] Kim, J., Park, Y., Kahng, B., and Lee, H. Y. (2003). Self-organized patterns in mixtures of microtubules and motor proteins. *J. Korean Phys. Soc.*, 42(1):162–166.

[Konstantopoulos et al., 2013] Konstantopoulos, K., Wu, P., and Wirtz, D. (2013). Dimensional control of cancer cell migration. *Biophys. J.*, 104(2):279–280.

[Kovács et al., 2004] Kovács, M., Tóth, J., Hetényi, C., Málnási-Csizmadia, A., and Seller, J. R. (2004). Mechanism of blebbistatin inhibition of myosin II. *J. Biol. Chem.*, 279(34):35557–35563.

[Kruse et al., 2001] Kruse, K., Camalet, S., and Jülicher, F. (2001). Self-Propagating Patterns in Active Filament Bundles. *Phys. Rev. Lett.*, 87(13):138101.

[Kruse et al., 2006] Kruse, K., Joanny, J. F., Jülicher, F., and Prost, J. (2006). Contractility and retrograde flow in lamellipodium motion. *Phys. Biol.*, 3(2):130–137.

[Kruse et al., 2004] Kruse, K., Joanny, J. F., Jülicher, F., Prost, J., and Sekimoto, K. (2004). Asters,Vortices, and Rotating Spirals in Active Gels of Polar Filaments. *Phys. Rev. Lett.*, 92(7):78101.

[Kruse et al., 2005] Kruse, K., Joanny, J. F., Prost, J., Sekimoto, K., Recherche, S. D., Jülicher, F., Prost, J., and Sekimoto, K. (2005). Generic theory of active polar gels: a paradigm for cytoskeletal dynamics. *Eur. Phys. J. E*, 16(1):1–28.

[Kruse and Jülicher, 2000] Kruse, K. and Jülicher, F. (2000). Actively contracting bundles of polar filaments. *Phys. Rev. Lett.*, 85(8):1778–1781.

[Kumar et al., 2014] Kumar, A., Maitra, A., Sumit, M., Ramaswamy, S., and Shivashankar, G. V. (2014). Actomyosin contractility rotates the cell nucleus. *Sci. Rep.*, 4:3781.

[Laan et al., 2012] Laan, L., Pavin, N., Husson, J., Romet-Lemonne, G., van Duijn, M., López, M. P., Vale, R. D., Jülicher, F., Reck-Peterson, S. L., and Dogterom, M. (2012). Cortical dynein controls microtubule dynamics to generate pulling forces that position microtubule asters. *Cell*, 148(3):502–514.

[Lai et al., 2008] Lai, M.-C., Tseng, Y.-H., and Huang, H. (2008). An immersed boundary method for interfacial flows with insoluble surfactant. *J. Comput. Phys.*, 227(15):7279–7293.

[Lamb, 1945] Lamb, S. H. (1945). *Hydrodynamics*. Courier Corporation.

[Lautenschläger and Piel, 2013] Lautenschläger, F. and Piel, M. (2013). Microfabricated devices for cell biology: All for one and one for all.

[Lee and Kardar, 2001] Lee, H. Y. and Kardar, M. (2001). Macroscopic equations for pattern formation in mixtures of microtubules and molecular motors. *Phys. Rev. E*, 64(5):056113.

[Liverpool and Marchetti, 2003] Liverpool, T. B. and Marchetti, M. C. (2003). Instabilities of Isotropic Solutions of Active Polar Filaments. *Phys. Rev. Lett.*, 90(13):138102.

[Liverpool and Marchetti, 2005] Liverpool, T. B. and Marchetti, M. C. (2005). Bridging the microscopic and the hydrodynamic in active filament solutions. *Europhys. Lett.*, 69(5):7.

[Liverpool et al., 2008] Liverpool, T. B., Marchetti, M. C., Joanny, J. F., and Prost, J. (2008). Mechanical response of active gels. *Europhys. Lett.*, 85:18007.

[Lo et al., 2000] Lo, C.-M., Wang, H.-B., Dembo, M., and Wang, Y.-l. (2000). Cell Movement Is Guided by the Rigidity of the Substrate. *Biophys. J.*, 79(1):144–152.

[Lubensky et al., 1998] Lubensky, T. C., Pettey, D., and Currier, N. (1998). Topological defects and interactions in nematic emulsions. *Phys. Rev. E*, 57(1):610–625.

[Lutolf and Hubbell, 2005] Lutolf, M. P. and Hubbell, J. a. (2005). Synthetic biomaterials as instructive extracellular microenvironments for morphogenesis in tissue engineering. *Nat. Biotechnol.*, 23(1):47–55.

[Maiuri et al., 2012] Maiuri, P., Terriac, E., Paul-Gilloteaux, P., Vignaud, T., McNally, K., Onuffer, J., Thorn, K., Nguyen, P. a., Georgoulia, N., Soong, D., Jayo, A., Beil, N., Beneke, J., Lim, J. C. H., Sim, C. P.-Y., Chu, Y.-S., Jiménez-Dalmaroni, A., Joanny, J.-F., Thiery, J.-P., Erfle, H., Parsons, M., Mitchison, T. J., Lim, W. a., Lennon-Duménil, A.-M., Piel, M., and Théry, M. (2012). The first World Cell Race. *Curr. Biol.*, 22(17):R673–5.

[Marchetti et al., 2013] Marchetti, M. C., Joanny, J. F., Ramaswamy, S., Liverpool, T. B., Prost, J., Rao, M., and Simha, R. A. (2013). Hydrodynamics of soft active matter. *Rev. Mod. Phys.*, 85(3):1143–1189.

[Marenduzzo et al., 2007] Marenduzzo, D., Orlandini, E., and Yeomans, J. (2007). Hydrodynamics and Rheology of Active Liquid Crystals: A Numerical Investigation. *Phys. Rev. Lett.*, 98(11):118102.

[Marth et al., 2014] Marth, W., Praetorius, S., and Voigt, A. (2014). A mechanism for cell motility by active polar gels. pages 1–20.

[Mattila and Lappalainen, 2008] Mattila, P. K. and Lappalainen, P. (2008). Filopodia: molecular architecture and cellular functions. *Nat. Rev. Mol. Cell Biol.*, 9(6):446–54.

[Medalia et al., 2002] Medalia, O., Weber, I., Frangakis, A. S., Nicastro, D., Gerisch, G., and Baumeister, W. (2002). Macromolecular architecture in eukaryotic cells visualized by cryoelectron tomography. *Science*, 298:1209–1213.

[Mitchison and Cramer, 1996] Mitchison, T. J. and Cramer, L. P. (1996). Actin-Based Cell Motility and Cell Locomotion. *Cell*, 84(3):371–379.

[Mitchison and Kirschner, 1984] Mitchison, T. J. and Kirschner, M. (1984). Dynamic Instability of Microtubule Growth. *Nature*, 312(5991):237–242.

[Mogilner, 2009] Mogilner, A. (2009). Mathematics of cell motility: Have we got its number? *J. Math. Biol.*, 58(1-2):105–134.

[Mogilner and Oster, 1996] Mogilner, A. and Oster, G. (1996). Cell motility driven by actin polymerization. *Biophys J.*, 71(6):3030–3045.

[Mogilner and Oster, 1999] Mogilner, A. and Oster, G. (1999). The polymerization ratchet model explains the force-velocity relation for growing microtubules. *Eur. Biophys. J.*, 28(3):235–242.

[Mogilner and Oster, 2003] Mogilner, A. and Oster, G. (2003). Force Generation by Actin Polymerization {II}: The Elastic Ratchet and Tethered Filaments. *Biophys. J.*, 84(3):1591–1605.

[Mullins et al., 1998] Mullins, R. D., Heuser, J. A., and Pollard, T. D. (1998). The interaction of Arp2/3 complex with actin: nucleation, high affinity pointed end capping, and formation of branching networks of filaments. *Proc. Natl. Acad. Sci.*, 95(11):6181–6186.

[Nédélec, 2002] Nédélec, F. (2002). Computer simulations reveal motor properties generating stable antiparallel microtubule interactions. *J. Cell Biol.*, 158(6):1005–1015.

[Nédélec et al., 1997] Nédélec, F. J., Surrey, T., Maggs, A. C., and Leibler, S. (1997). Self-organization of microtubules and motors. *Nature*, 389(6648):305–308.

[Neuhaus et al., 1983] Neuhaus, J. M., Wanger, M., Keiser, T., and Wegner, A. (1983). Treadmilling of actin. *J. Muscle Res. Cell Motil.*, 4(5):507–527.

[Nobili and Durand, 1992] Nobili, M. and Durand, G. (1992). Disorientation-induced disordering at a nematic-liquid-crystalsolid interface. *Phys. Rev. A*, 46(10):R6174–R6177.

[Ohta and Ohkuma, 2009] Ohta, T. and Ohkuma, T. (2009). Deformable self-propelled particles. *Phys. Rev. Lett.*, 154101(April):1–4.

[Paluch et al., 2006] Paluch, E., Sykes, C., Prost, J., and Bornens, M. (2006). Dynamic modes of the cortical actomyosin gel during cell locomotion and division. *Trends Cell Biol.*, 16(1):5–10.

[Pellegrin and Mellor, 2007] Pellegrin, S. and Mellor, H. (2007). Actin stress fibres. *J. Cell Sci.*, 120(Pt 20):3491–3499.

[Peskin, 2002] Peskin, C. S. (2002). The immersed boundary method. *Acta Numer.*, 11(January 2002):479–517.

[Peskin et al., 1993] Peskin, C. S., Odell, G. M., and Oster, G. F. (1993). Cellular motions and thermal fluctuations: the Brownian ratchet. *Biophys. J.*, 65(1):316–324.

[Poincloux et al., 2011] Poincloux, R., Collin, O., Lizárraga, F., Romao, M., Debray, M., Piel, M., Chavrier, P., R.Poincloux, O.Collin, F.Lizárraga, M.Romao, M.Debray, M.Piel, and P.Chavrier (2011). Contractility of the cell rear drives invasion of breast tumor cells in {3D} Matrigel. *Proc. Natl. Acad. Sci.*, 108(5):1943–8.

[Popp et al., 2006] Popp, D., Yamamoto, A., Iwasa, M., and Maéda, Y. (2006). Direct visualization of actin nematic network formation and dynamics. *Biochem. Biophys. Res. Commun.*, 351(2):348–353.

[Prass et al., 2006] Prass, M., Jacobson, K., Mogilner, A., and Radmacher, M. (2006). Direct measurement of the lamellipodial protrusive force in a migrating cell. *J. Cell Biol.*, 174(6):767–772.

[Ramaswamy, 2010] Ramaswamy, S. (2010). The Mechanics and Statistics of Active Matter. *Annu. Rev. Condens. Matter Phys.*, 1:323–345.

[Ridley et al., 2003] Ridley, A. J., Schwartz, M. A., Burridge, K., Firtel, R. A., Ginsberg, M. H., Borisy, G., Parsons, J. T., and Horwitz, A. R. (2003). Cell migration: integrating signals from front to back. *Science*, 302:1704–1709.

[Robinson and Spudich, 2004] Robinson, D. N. and Spudich, J. A. (2004). Mechanics and regulation of cytokinesis. *Curr. Opin. Cell Biol.*, 16:182–188.

[Rodionov and Borisy, 1997] Rodionov, V. I. and Borisy, G. G. (1997). Microtubule treadmilling in vivo. *Science*, 275:215–218.

[Sanchez et al., 2012] Sanchez, T., Chen, D. T. N., DeCamp, S. J., Heymann, M., and Dogic, Z. (2012). Spontaneous motion in hierarchically assembled active matter. *Nature*, 491(7424):431–434.

[Sankararaman et al., 2004] Sankararaman, S., Menon, G. I., and Kumar, P. B. S. (2004). Self-organized pattern formation in motor-microtubule mixtures. *Phys. Rev. E*, 70(3 1):1–18.

[Sarkar and Basu, 2015] Sarkar, N. and Basu, A. (2015). Role of interfacial friction for flow instabilities in a thin polar-ordered active fluid layer. *Phys. Rev. E*, 92(5):052306.

[Sedzinski et al., 2011] Sedzinski, J., Biro, M., Oswald, A., Tinevez, J.-Y., Salbreux, G., and Paluch, E. (2011). Polar actomyosin contractility destabilizes the position of the cytokinetic furrow. *Nature*, 476(7361):462–6.

[Selinger, 2015] Selinger, J. V. (2015). *Introduction to the Theory of Soft Matter: From Ideal Gases to Liquid Crystals*. Springer.

[Shitara et al., 2011] Shitara, K., Hiraiwa, T., and Ohta, T. (2011). Deformable self-propelled domain in an excitable reaction-diffusion system in three dimensions. *Phys. Rev. E*, 83(6):066208.

[Small et al., 1978] Small, J. V., Isenberg, G., and Celis, J. E. (1978). Polarity of actin at the leading edge of cultured cells. *Nature*, 272:638–639.

[Small et al., 1998] Small, J. V., Rottner, K., Kaverina, I., and Anderson, K. I. (1998). Assembling an actin cytoskeleton for cell attachment and movement. *Biochim. Biophys. Acta - Mol. Cell Res.*, 1404(3):271–281.

[Soares e Silva et al., 2011] Soares e Silva, M., Depken, M., Stuhrmann, B., Korsten, M., MacKintosh, F. C., and Koenderink, G. H. (2011). Active multistage coarsening of actin networks driven by myosin motors. *Proc. Natl. Acad. Sci.*, 108(23):9408–9413.

[Straight et al., 2003] Straight, A. F., Cheung, A., Limouze, J., Chen, I., Westwood, N. J., Sellers, J. R., and Mitchison, T. J. (2003). Dissecting temporal and spatial control of cytokinesis with a myosin II Inhibitor. *Science*, 299:1743–1747.

[Surrey et al., 1998] Surrey, T., Elowitz, M. B., Wolf, P. E., Yang, F., Nédélec, F., Shokat, K., and Leibler, S. (1998). Chromophore-assisted light inactivation and self-organization of microtubules and motors. *Proc. Natl. Acad. Sci.*, 95(8):4293–4298.

[Surrey et al., 2001] Surrey, T., Nédélec, F., Leibler, S., and Karsenti, E. (2001). Physical Properties Determining Self-Organization of Motors and Microtubules. *Science*, 292:1167–1171.

[Svitkina et al., 1997] Svitkina, T. M., Verkhovsky, A. B., McQuade, K. M., and Borisy, G. G. (1997). Analysis of the ActinMyosin {II} System in Fish Epidermal Keratocytes: Mechanism of Cell Body Translocation. *J. Cell Biol.*, 139(2):397–415.

[Thampi et al., 2014] Thampi, S. P., Golestanian, R., and Yeomans, J. M. (2014). Instabilities and topological defects in active nematics. *Europhys. Lett.*, 105(1):18001.

[Thoresen et al., 2011] Thoresen, T., Lenz, M., and Gardel, M. L. (2011). Reconstitution of contractile actomyosin bundles. *Biophys. J.*, 100(11):2698–705.

[Thoumine et al., 1999] Thoumine, O., Cardoso, O., and Meister, J.-J. J. (1999). Changes in the mechanical properties of fibroblasts during spreading: a micromanipulation study. *Eur. Biophys. J.*, 28(3):222–234.

[Tilney and Portnoy, 1989] Tilney, L. G. and Portnoy, D. a. (1989). Actin Filaments and the Growth, Movement, and Spread of the Intacellular BActerial Parsite, Listeria monocytogenes. *J. Cell Biol.*, 109(October):1597–1608.

[Tjhung et al., 2012] Tjhung, E., Marenduzzo, D., and Cates, M. E. (2012). Spontaneous symmetry breaking in active droplets provides a generic route to motility. *Proc. Natl. Acad. Sci.*, 109(31):12381–6.

[Toner and Tu, 1995] Toner, J. and Tu, Y. (1995). Long-range order in a two-dimensional dynamical XY model: how birds fly together. *Phys. Rev. Lett.*, 75(23):4326–4329.

[Toner and Tu, 1998] Toner, J. and Tu, Y. (1998). Flocks, herds, and schools: A quantitative theory of flocking. *Phys. Rev. E*, 58(4):4828–4858.

[Toyota et al., 2012] Toyota, T., Wakamoto, Y., Hayashi, K., and Ohnuma, K. (2012). Controlling Cell Migration with Micropatterns. In *Innov. Biotechnol.*, pages 187–208.

[Tsai et al., 2011] Tsai, F. C., Stuhrmann, B., and Koenderink, G. H. (2011). Encapsulation of active cytoskeletal protein networks in cell-sized liposomes. *Langmuir*, 27(16):10061–10071.

[Turlier et al., 2014] Turlier, H., Audoly, B., Prost, J., and Joanny, J.-F. (2014). Furrow constriction in animal cell cytokinesis. *Biophys. J.*, 106(1):114–123.

[Unverdi and Tryggvason, 1992] Unverdi, S. O. and Tryggvason, G. (1992). A Front-Tracking Method for Viscous Incompressible Multifuid Flows. *J. Comput. Phys.*, 100:25–37.

[Uyeda et al., 2000] Uyeda, T. Q., Kitayama, C., and Yumura, S. (2000). Myosin II-independent cytokinesis in Dictyostelium: its mechanism and implications. *Cell Struct. Funct.*, 25(1):1–10.

[Verkhovsky et al., 1999] Verkhovsky, A. B., Svitkina, T. M., and Borisy, G. G. (1999). Self-polarization and directional motility of cytoplasm. *Curr. Biol.*, 9(1):11–20.

[Viamontes et al., 2006] Viamontes, J., Oakes, P., and Tang, J. (2006). Isotropic to Nematic Liquid Crystalline Phase Transition of F-Actin Varies from Continuous to First Order. *Phys. Rev. Lett.*, 97(11):118103.

[Voituriez et al., 2005] Voituriez, R., Joanny, J. F., and Prost, J. (2005). Spontaneous flow transition in active polar gels. *Europhys. Lett.*, 70(3):404–410.

[Voituriez et al., 2006] Voituriez, R., Joanny, J. F., and Prost, J. (2006). Generic Phase Diagram of Active Polar Films. *Phys. Rev. Lett.*, 96(2):28102.

[Wang and Wolynes, 2012] Wang, S. and Wolynes, P. (2012). Active contractility in actomyosin networks. *Proc. Natl. Acad. Sci.*, 109(17):6446–6451.

[Webb and Horwitz, 2003] Webb, D. D. J. and Horwitz, A. A. F. (2003). New dimensions in cell migration. *Nat. Cell Biol.*, 5(8):690–692.

[Weeds and Maciver, 1993] Weeds, a. and Maciver, S. (1993). F-actin capping proteins. *Curr. Opin. Cell Biol.*, 5(1):63–69.

[Wegner, 1976] Wegner, A. (1976). Head to tail polymerization of actin. *J. Mol. Biol.*, 108(1):139–150.

[Weinberg, 2013] Weinberg, R. (2013). *The Biology of Cancer, Second Edition*. Garland Science.

[Whitfield et al., 2014] Whitfield, C. A., Marenduzzo, D., Voituriez, R., and Hawkins, R. J. (2014). Active polar fluid flow in finite droplets. *Eur. Phys. J. E*, 37(2).

[Wirtz et al., 2011] Wirtz, D., Konstantopoulos, K., and Searson, P. C. (2011). The physics of cancer: the role of physical interactions and mechanical forces in metastasis. *Nat. Rev. Cancer*, 11(7):512–522.

[Wolf et al., 2013] Wolf, K., te Lindert, M., Krause, M., Alexander, S., te Riet, J., Willis, a. L., Hoffman, R. M., Figdor, C. G., Weiss, S. J., and Friedl, P. (2013). Physical limits of cell migration: Control by ECM space and nuclear deformation and tuning by proteolysis and traction force. *J. Cell Biol.*, 201(7):1069–1084.

[Woodhouse and Goldstein, 2012] Woodhouse, F. G. and Goldstein, R. E. (2012). Spontaneous circulation of confined active suspensions. *Phys. Rev. Lett.*, 109(16):168105.

[Wottawah et al., 2005] Wottawah, F., Schinkinger, S., Lincoln, B., Ananthakrishnan, R., Romeyke, M., Guck, J., and KÃs, J. (2005). Optical rheology of biological cells. *Phys. Rev. Lett.*, 94(9):098103.

[Xu, 2014] Xu, J.-J. (2014). A Coupled Immersed Interface and Level Set Method for Three-Dimensional Interfacial Flows with Insoluble Surfactant. *Commun. Comput. Phys.*, 15(2):451–469.

[Yabunaka et al., 2012] Yabunaka, S., Ohta, T., and Yoshinaga, N. (2012). Self-propelled motion of a fluid droplet under chemical reaction. *J. Chem. Phys.*, 136(7):074904.

[Yarar et al., 1999] Yarar, D., Wayne, T., Arie, A., and Welch, M. D. (1999). The Wiskott-Aldrich syndrome protein directs actin-based motility by stimulating actin nucleation with the Arp2/3 complex. *Curr. Biol.*, 9(10):555–558.

[Yoshinaga, 2014] Yoshinaga, N. (2014). Spontaneous motion and deformation of a self-propelled droplet. *Phys. Rev. E*, 89(1):012913.

[Yue et al., 2004] Yue, P., Feng, J. J., Liu, C., and Shen, J. (2004). A diffuse-interface method for simulating two-phase flows of complex fluids. *J. Fluid Mech.*, 515:293–317.

[Ziebert and Aranson, 2014] Ziebert, F. and Aranson, I. S. (2014). Modular approach for modeling cell motility. *Eur. Phys. J. Spec. Top.*, 223(7):1265–1277.

[Ziebert et al., 2011] Ziebert, F., Swaminathan, S., and Aranson, I. S. (2011). Model for self-polarization and motility of keratocyte fragments. *J. R. Soc. Interface*, 9(70):1084–1092.

[Zumdieck et al., 2005] Zumdieck, A., Lagomarsino, M., Tanase, C., Kruse, K., Mulder, B., Dogterom, M., and Jülicher, F. (2005). Continuum Description of the Cytoskeleton: Ring Formation in the Cell Cortex. *Phys. Rev. Lett.*, 95(25):258103.